University of Stavanger

FACULTY OF SCIENCE AND TECHNOLOGY

MASTER'S THESIS

Study program/Specialisation: **Engineering Structures and Materials, Mechanical systems**	**Spring** semester, 2021 **Open** / ~~Confidential~~
Author: **Pravesh Kumar Yadav**	 **(Author's signature)**

Programme coordinator: **Associate Professor Knut Erik Teigen Giljarhus**

Programme Supervisor: **Professor Vidar Folke Hansen**

Title of master's thesis:

Microstructure and Mechanical Properties of SLM Printed Super Duplex Stainless Steel (EN 1.4410)

Credits: **30**

Keywords: **EN 1.4410/ AISI SAF 2507/ UNS S32750** **Super Duplex Stainless Steel** **Selective Laser Melting** **Microstructure** **Mechanical Properties**	Number of pages: **127** + Appendix: **46** **Stavanger, 14.06.2021**

Page intentionally left blank

Abstract

The purpose of this study is to investigate the microstructural and mechanical characterization of super duplex stainless steel of grade EN 1.4410 / AISI SAF 2507 manufactured by selective laser melting (SLM). The findings offer insights on the phase arrangement of as-built conditions as well as various heat-treated temperatures. It also studies the effect of cooling rate on microstructure and mechanical properties of the material after heat treatment at different temperatures.

The heat treatment was applied on SDSS from 1000 ° C to 1300 ° C at the interval of 100 ° C for 1-hour duration to restore the balanced duplex microstructure. Then, the material was cooled by two different methods, i.e., water quenching and air cooling, after heat treatment to check the effect of cooling rate. The microstructural analysis has performed using a Light optical microscope, scanning electron microscope (SEM), and transmission electron microscope (TEM). The material's mechanical properties are studied by performing Vickers hardness test and pitting corrosion test of type ASTM G48.

The as-printed material was entirely ferritic, with barely a trace of austenite. All the elemental composition was within the standard SAF 2507 range in powder and in the as-printed sample except chromium, which was found out of range (about 27.5% wt.). Because of the specific laser scanning pattern, a unique macroscopic texture was formed. A mosaic-type macrostructure with tesserae of 123–126 µm was obtained after SLM in an as-printed sample. The grains inside each tessera had a different crystallographic orientation than grains in adjacent tesserae. The nano-sized dislocation loops were abundant in the as-printed material, both within the tesserae and within smaller recrystallized micron grains between the mosaic boundaries. TEM result also shows a decrease in dislocation density after heat treatment of SLM manufactured parts. The as-printed microstructure has a ferrite of about 94% and 99.6% using a light microscope and EBSD respectively. The nitrogen concentration ranged from 0.56-0.88 percent in the as-printed sample, indicating that nitride phases or nitrogen-enriched regions in the ferrite matrix might occur after fast cooling in heat-treated material.

At 1000 ° C, the sigma phase was found about 14-15% in both water-quenched and air-cooled samples. But the sigma phases vanished after heat treatment temperature above 1100 ° C. The chromium nitride was observed inside ferrite grain and at the grain boundary in all water quenched samples. As heat treatment temperature increased from 1000 ° C to 1300 ° C, the volume fraction of chromium nitrides has also increased from 1% to 5.5% approximately. It was challenging to avoid chromium nitrides precipitation even at higher temperatures by the water quenching method. So, heat treatment

temperature should be kept as low as possible without risking precipitation of intermetallic phases.

The air cooling method provides precipitation-free and pure dual-phase microstructure at a temperature ranging from 1100-1300 ° C, so air cooling is preferred for this material. The best phase balance was found at 1200 ° C with about 61% δ-ferrite and 39% austenite. In water quenched sample, as HT temperature increases from 1000-1300 ° C, the grain size of austenite grows larger, and the surrounding δ-ferrite band becomes wider. Similar was the case in the air-cooled sample too. But grain size of austenite was a little bigger in the air-cooled sample than the water quenched sample at the same temperature due to slow cooling.

The solid part of the sample was found harder than the hollow part. The sample surface parallel to the build direction is harder than the sample surface perpendicular to the build direction. The average hardness of as-built SAF 2507 is 417, and it decreases with heat treatment. The average hardness decreased in the material by 30-35% after heat treatment was carried out. The hardness of the material increases with an increase in the percentage of ferrite content and precipitates like sigma and chromium nitride.

No visible pits were observed in any sample while performing the ASTM G48 pitting corrosion test at room temperature of 22±2 ° C for 72 hours.

It can be stated that the sample is not in a satisfactory dual-phase super duplex structure straight from production but rather an approximately fully ferritic microstructure. It clearly states that the material had to be processed before use, which leads to loss of time and money. The material holds more surprises, and it shows great promise as a standard engineering material.

Acknowledgments

I consider myself fortunate to acknowledge and thank everyone who helped to complete this thesis work.

I am grateful to my supervisor, **Professor Vidar Folke Hansen**, Department of Mechanical and Structural Engineering and Materials Science, for his guidance, assistance, expertise, and patience throughout the thesis. He has been supportive and encouraging me throughout this period.

I want to express my gratitude to **Morten Kollerup BAK** and **Mechatronics Innovation Lab AS**, who offered me an exciting thesis topic and provided SLM printed sample.

I want to thank Head Engineer Johan A. Thorkaas and Senior Engineer Wakshum M. Tucho for their guidance and for helping me with specimen preparations and operating SEM & TEM Microscopes. I would also like to thank Senior Engineer Mats Ingdal for helping me prepare different etchant and chemical solutions for the pitting corrosion test.

I want to express my heartfelt appreciation to everyone for their assistance with technical matters and their moral encouragement and helpful advice in the thesis work. Finally, I would like to express my gratitude to my family member and my wife, Mrs. Sabita Yadav, for always encouraging and inspiring me.
Thank you, Everyone.

Sincerely,

Pravesh Kumar Yadav

Stavanger, Norway

Table of Contents

List of Figures

List of Tables

List of Abbreviation

AM	Additive Manufacturing
3D	3-Dimensional
SLM	Selective Laser Melting
CAD	Computer Aided Engineering
SS	Stainless Steel
DSS	Duplex Stainless Steel
SDSS	Super Duplex Stainless Steel
SCC	Stress Corrosion Cracking
EN	European Number
SEM	Scanning Electron Microscope
TEM	Transmission Electron Microscope
OM	Optical Microscope
STL	STereoLithography
PBF	Powder Bed Fusion
DED	Directed Energy Deposition
SLS	Selective Laser Sintering
EBF	Electron Beam Freeform
EBM	Electron Beam Machining
RS	Residual Stress
EDM	Electrical Discharge Machining
NDT	Non-Destructive Testing
EBSD	Electron Backscatter Diffraction
HR-EBSD	High Angular Resolution Electron Backscatter Diffraction
UT	Ultrasonic Testing
XRD	X-Ray Diffraction

ASTM	American Society for Testing and Materials
PREN	Pitting Resistance Equivalent Number
FCC	Face Centric Cubic
BCC	Body Centric Cubic
APF	Atomic Packing Factor
BCT	Body Centered Tetragonal
HT	Heat Treatment
TTT	Time Temperature Transformation
CCT	Continuous Cooling Transformation
HV	Vickers Hardness Number
AISI	American Iron and Steel Institute
HSE	Health, Safety and Environment

List of Symbols

σ	Sigma
δ	Ferrite
$\gamma 2$	Secondary Austenite
γ	Austenite
v	Scan Speed
h	Hatch Spacing
t	Layer Thickness
α'	Alpha Prime
χ	Chi
a, c	Lattice Parameter

Page intentionally left blank

1. Introduction

1.1 Background and Motivation

Additive Manufacturing (AM) is an ever-growing industry, and one sees more and more markets begin to explore opportunities to implement the technology. In today's time, additively manufactured metallic materials have drawn attention from academia & industry [1]. With the potential to produce items directly in their desired geometry and with the corresponding mechanical properties in a fast, efficient, and secure way, it opens the possibility of implementing a digital warehouse for spare parts in the form of computer-generated models. In this way, one can reduce, and potentially eliminate, the need to hold on spare parts on-site in favor of now being able to produce the desired parts when needed [2]. In addition, one can produce prototypes or custom parts faster and more efficiently than with the conventional methods. One can use this technology because it can reliably recreate parts with the expected mechanical properties and the desired shape. It is with the intention that research and investigations are done around 3D printing (Additive Manufacturing) methods and 3D printer machines so that one can produce the materials with the most faithful properties, making the process more economically and practically beneficial [3].

SLM is an AM technology, which is accepted as beneficial and versatile [4]. Selective laser melting is one of the most mature metal AM technologies belonging to the powder bed fusion technology. Today, the technology is used to produce end-use parts – not only for small series production but also for medium-to-large scale production. SLM is still evolving, especially when it comes to the industrialization of technology and the processing of new materials [5]. SLM allows design freedom and a high density of manufactured components in a single production step [6]. The AM process begins with slicing a CAD file into a series of layers. The data is modified before being sent to the SLM machine. A focused high-power laser successively scans under an inert gas atmosphere and respectively melts each layer's contour until the parts are finally materialized [6].

Duplex stainless steels (DSS) are essential and versatile class of steel currently in use worldwide. They have a two-phase microstructure consisting of roughly equal proportions of ferrite and austenite [7]. DSS are notable in that they improve the corrosion properties of more traditional stainless steels (304, 316L) but have about twice the strength [8]. The resistance to pitting corrosion for duplex stainless steels tends to be superior to the traditional 300 series [9]. This is a result of the chemical composition, particularly the amount of chromium [7]. The combination of high strength and good corrosion resistance makes duplex stainless steel notably resistant to

stress corrosion cracking (SCC) [7]. Additionally, they can be cost-competitive due to their high strength, as less material may be used [9]. Although duplex stainless steel has been in use since the 1930s, researchers are always looking for methods to innovate, such as discovering alternative production procedures for certain components [9].

Super duplex stainless steels are widely used in the marine, petrochemical, oil, and gas industries because of their superior strength and corrosion resistance. The proper ratio of austenite to ferrite phase balance (50/50) guarantees these remarkable properties [10]. But, the accurate thermomechanical processing of DSS-wrought products has led to higher costs. Therefore, it is essential to examine proper production processes for the fabrication of SDSS structural parts. SDSS is more difficult to process than other types of stainless steel, and the SLM process is still not adequately developed for this group of materials. The demand for the 3D-printed Super duplex SS is increasing, and therefore industries want to grow further and mature the SLM process for this material group [10].

1.2 Aims and Objectives

This thesis aims to study the microstructures and mechanical properties of as-printed and heat-treated super duplex stainless steel (EN 1.4410) produced by an SLM process. At the start, the optimization will preferably be done by performing test prints with a systematic variation of the most critical process parameters such as laser power and scanning speed. The properties that are aimed to be investigated include:

1. Study effect of heat treatment at various temperatures on the microstructure of SLM manufactured SDSS.
2. Study of phase content of as printed and heat-treated SDSS.
3. Effect of heat treatment on hardness.
4. Effect of heat treatment on pitting corrosion resistance

The microstructures are studied with the help of an optical microscope, scanning electron microscope, and transmission electron microscope. The optical microscope is used to investigate material macrostructures. At the same time, SEM is used to observe the grain structure and existence of any intermetallic phases and other precipitates. TEM is used to investigate the precipitate phases and dislocation. The hardness test is done to analyze the mechanical properties, and a pitting corrosion test is performed to study the corrosion behavior of a material.

1.3 Importance of this research

Super duplex stainless steel has even higher corrosion resistance and is especially popular in the offshore/maritime industry and widely used worldwide. So, the demand for the 3D-printed SDSS is increasing day by day. SDSS is more difficult to process than other types of stainless steel, and the SLM process is still not developed for this group of materials. The changes in microstructure before and after heat treatments are not clearly defined till now. The changes in mechanical properties like hardness, yield strength, and elongation before and after heat treatments are not well studied for EN 1.4410 material. The microstructures and mechanical properties at different laser power and scanning speed are not well examined. There is always room for improvement of these products, so this research is necessary.

Understanding these mechanical and microstructural properties is essential for using nickel alloy in manufacturing components for several industries like offshore, aerospace, turbines, etc. Information about microstructural changes in the alloy after heat treatment is also studied, which is vital for using alloys in parts exposed to high temperatures. The research also provides an insight into the changes in the properties of alloy from top to bottom of the specimen that is important for durability and strength.

1.4 Limitation

Due to the Covid-19 situation, it was challenging to perform all the tests and experiments that have prohibited studying all the properties of the material properly. It was intended to explore the specimens in more detail, but the research was restricted due to restrictions on the use of lab and equipment. Due to technical failure, the scanning electron microscope wasn't in working condition. So, microstructural analysis, EDS analysis, and EBSD analysis using SEM were not performed on all samples.

The size of the sample material has also made it impossible to conduct all surveys according to current standards. Attempts have been made to perform all the surveys as close to the standards as possible, and it is ensured that the results presented are precise.

2. Literature Review

The reviewed publications were evaluated by comparing their observation and results against each other. The published data related to the topic was studied to understand the problem.

2.1 Additive Manufacturing

Additive manufacturing (AM) is one of the processes used to manufacture three-dimensional objects by layering material one upon one based on the digital CAD model. Additive Manufacturing is also called as 3D-Printing [11]. The specimen of superalloy that was used in this study was produced using AM.

Additive manufacturing is old technology; sewing cloths and gluing wood are also considered additive manufactured products. With additive manufacturing, complicated and extensive assembly products can be produced with fewer pieces, reducing time and weight. Mobile AM facilities can also be used to reproduce or repair defective parts worldwide [11]. Hence, AM also contributes to increasing a product's lifetime and reduce the usage of resources.

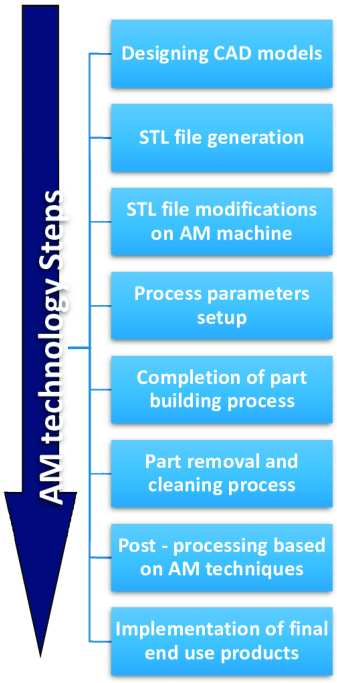

Figure 1: Additive manufacturing processing steps [12]

The procedure of an additive manufactured part consists of several steps, as shown in figure 1. The process starts with the concept design, where the idea is first generated and further modeled using 3D modeling software to visualize the 3D structure. The 3D model is then saved in STL format, where the desired set-up is applied in the AM software. The AM software controls the printing process, such as the scaling, build

volume, orientation for printing, producing support material, etc. The 3D model is sliced into layers and sent further for printing. Post-processing is performed by removing the support material, machining, or assembling parts [12].

2.1.1 Additive Manufacturing of Metals

There are multiple processes developed for additive manufacturing. The two most important aspects of any metal AM processes are input raw material and the energy source used to form the part. Input raw material may be employed in metal powder or wire, and laser beam may be employed as an energy source [13].

Metal AM processes can be broadly classified into four major groups (figure 2), powder bed fusion-based technologies (PBF), binder jetting, sheet lamination, and directed energy deposition (DED) based technologies. These technologies may be further categorized depending on the type of energy source employed. In PBF based technology, heat energy selectively fuses portions of a powder bed. Selective laser sintering/melting (SLS/SLM), laser fusing, and electron beam melting (EBM) are the leading representative processes of PBF based technologies. In DED-based technologies, concentrated thermal energy is used to fuse materials by melting as they are deposited. Wire-Laser AM, electron beam freeform fabrication (EBF), and Wire-arc AM are popular DED-based technologies [13].

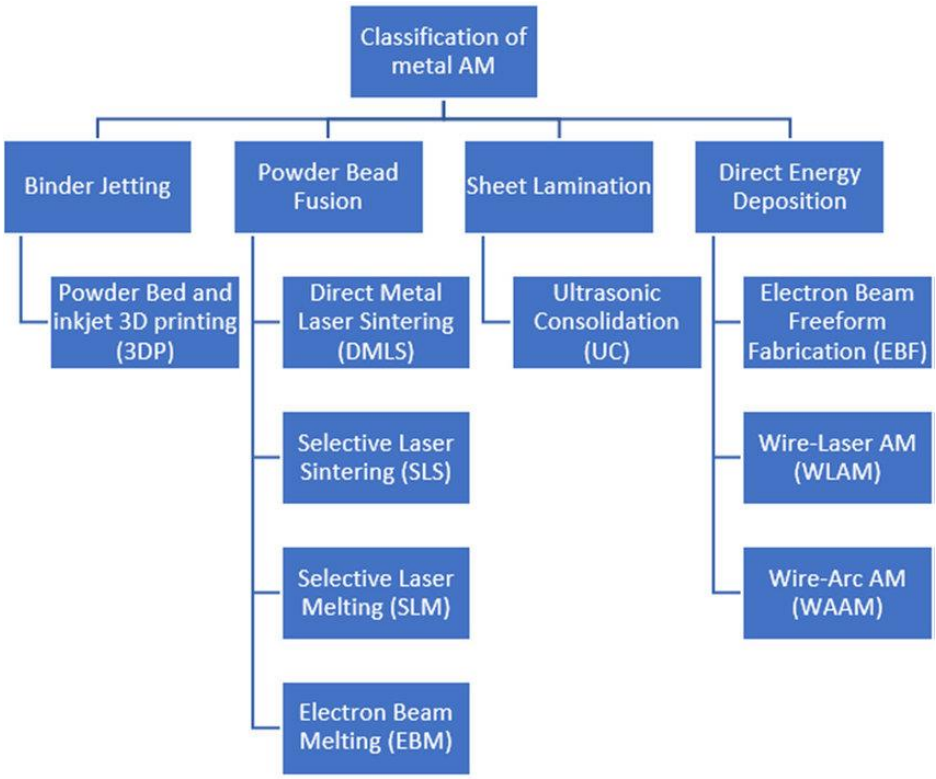

Figure 2: Classification of metal additive manufacturing technologies [13]

The selective Laser Melting (SLM) method is used to manufacture Super duplex stainless steel EN 1.4410 in this thesis.

2.1.2 Selective Laser Melting (SLM)

Selective Laser Melting is a method in which material in powder form is deposited in layers on a working platform and then fused selectively, using a high-power laser [14].

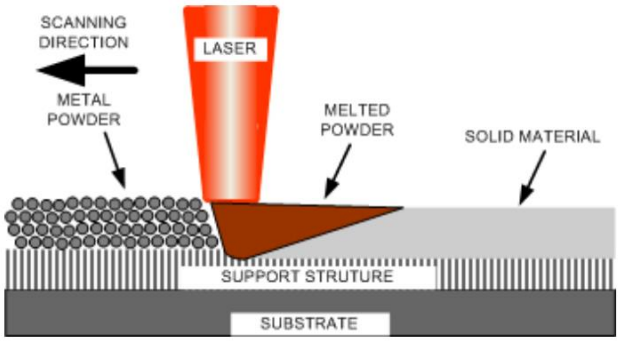

Figure 3: Principle of the SLM method [14]

The principle of the SLM process is visualized in figure 3. The first step in the SLM process is to construct the model in CAD software and then divide it layer by layer with one two-dimensional geometry that is programmed in the SLM machine. Metallic powder is dispersed in a thin layer over a substrate. A high-powered laser is used to melt the layer of metallic powder. The thickness of the coating varies between 20 µm - 100 µm [11]. The process takes place in a chamber with an atmosphere of argon or nitrogen to avoid oxidation. Then the substrate is lowered, and the next thin layer of metal powder is spread on top of the first layer, which is laser melted again; the process is repeated until the object corresponds to the CAD model. The unmelted powder is removed, and the model is now an independent solid object. Since the powder melts completely where the laser beam has passed, the object will have an almost 100% density. The remaining powder that the laser beam has not melted can be reused for 3D printing of other models. The laser continuously emits radiation with a wavelength of 1060–1080 nm. The laser spot sizes are between 50–180 µm as per requirement [11]. The SLM technique is represented in Figure 4.

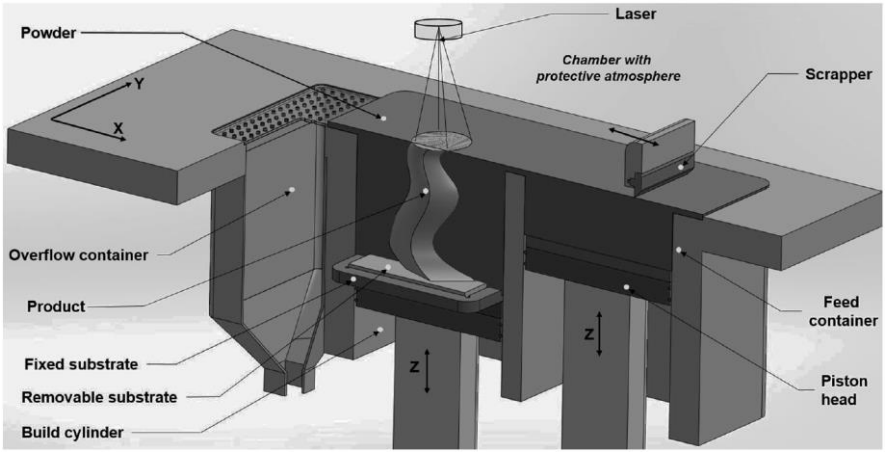

Figure 4: Schematic illustration of SLM [15]

Few defects can be found in the SLM-produced products, such as tiny pores, holes, and cracks. These defects can be reduced by adjusting the process parameters and conducting stress relief annealing [16]. The advantages and disadvantages of the SLM method are listed in table 1.

Table 1: Advantages and Disadvantages of SLM process [16] [17]

Advantages	• Can print medium to high surface qualities. • Good repeatability. • Suitable for manufacturing highly dense parts directly. • Highly complex geometry (thin walls, hidden holes) can be produced. • Can build almost every type of material.
Disadvantages	• Lower scanning speed • Build structures are required due to the weight of the metallic parts and distortion at high temperatures. • Sensitive to corrosion. • Post heat treatment is required for parts that have been stressed. • Melt pool instabilities and higher residual stresses.

2.1.3 Process Parameter of SLM

The SLM process parameters can be classified broadly into powder-related, laser-related, and powder-bed-related variables according to the properties, as shown in Figure 5. The powder-related process parameters, such as surface morphology, chemical composition, size, and shape of the particles, are constant in an actual production environment [18]. The laser-related properties that influence the SLM process are the laser power, laser type, and spot size. The scanning parameters like scanning strategy, hatch spacing, and scanning speed affect SLM-produced material characteristics [19].
The final classification of SLM process parameters is powder-bed characteristics. The powder is applied onto the building platform through a raking mechanism in powder bed processes, called recoating. Several factors define the powder delivery system,

including the recoated type, number of recoating passes, powder characteristics, and quantity of recovered powder during each pass. The significant process parameter that controls the part properties is the thickness of the recoating layer. The laser-material interaction is influenced by Layer thickness, particle size distribution (PSD), and laser parameters [20].

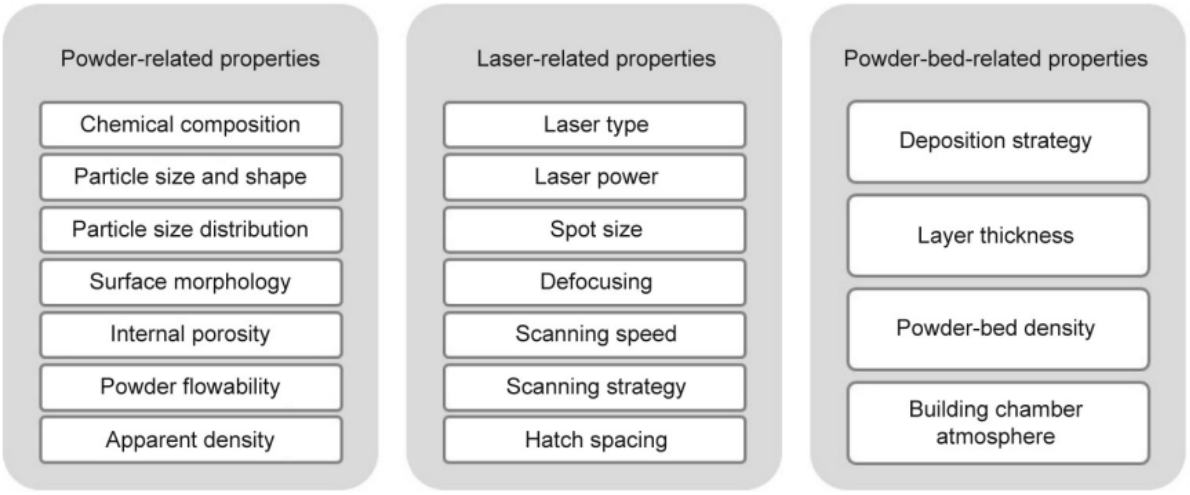

Figure 5: Summary of SLM process parameters [20]

All the parameters are essential and affect the process. The main influence variables in the SLM process and the varying process parameters of the specimens are explained in brief below (also shown in figure 6a).

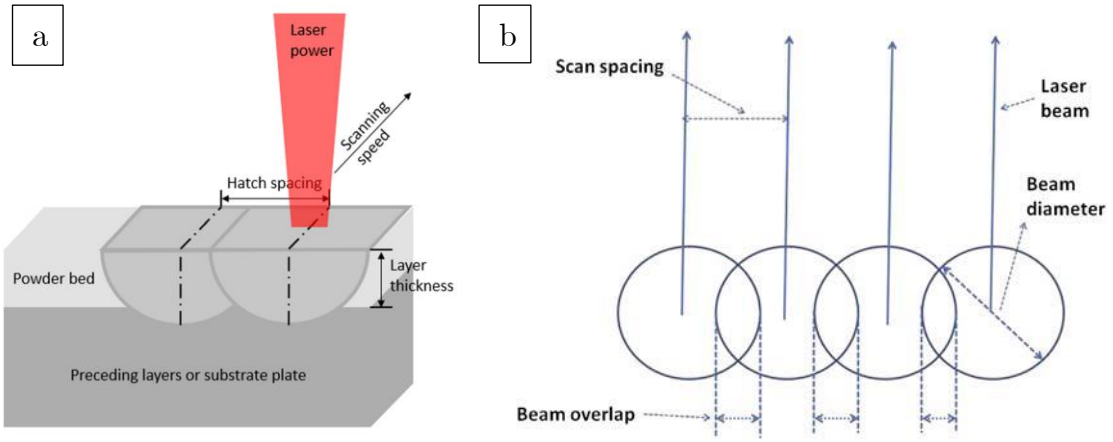

Figure 6: (a) SLM process parameters (b) Beam overlap [21]

2.1.3.1 Laser Power

The main parameter in the process is laser power. Its magnitude depends on the type of processed materials. SLM machines are built with 50 to 400 W of laser capacity. Power selection is not performed separately but relies on other parameters of the process and spot size. For the same laser power, with a reduction in spot size, higher laser energy density is attained, which could be used to process higher melting point materials [22].

Laser power also relies upon our purpose with powders. It needs more power if we want to melt it completely. If the intention is to melt the powder partly, then less energy is

required. The higher laser power may ablate metal powder and degrade polymer powder, demanding the identification of a process window for a given material. If the width of the melt pool differs from the default value, the laser power varies automatically to control the size of the melt pool. This results in consistency in the mechanical properties and dimension of the component produced by the melting powder [23, 24].

2.1.3.2 Hatch Spacing

The distance between two consecutive laser beams is called Hatch spacing [25]. It's also called Scan spacing or hatch distance. Hatch spacing is directly proportional to the speed of production. It would take less time for the laser to scan the layer if it is high, while if it is low, several scans must be done to process the whole layer. Smaller hatch spacing is required to make thin features [22].

To allow a large scanning spacing, a large laser spot size is necessary. Or else, there remains a gap between two consecutive scans resulting in porous materials. Higher laser power is needed to provide the required laser energy for processing with larger spot size. This means that the maximum scanning spacing obtained is constrained in the SLM method. As seen in figure 6(b), some overlaps are made to prevent any porosity from forming at the boundary of the scans. Overlap is necessary because the laser power at the center of the scan is higher than at the scan boundary in the typical Gaussian beam, resulting in melting at the center of the scan while heating at the boundary. The formation of overlaps compensates this less heat production at the boundary [22].

2.1.3.3 Scanning Speed

The rate at which the laser beam scans the line in the powder bed is called scanning speed. With an increase in the speed of scanning, the production speed increases. The scanning speed and laser energy density are related as follows [26]:

$$\text{Laser energy density} = \frac{\text{Laser Power}}{\text{Hatch Spacing x scan speed x layer thickness}} \qquad [1]$$

The equation [1] demonstrates that laser energy density is limited at high scan speed and may not be adequate to process the powder bed. An increase in laser power could compensate for this. However, there is not enough time for heat to disperse over the whole powder bed; it could lead to inadequate melting and removal of the powder. Therefore, the above equation is applicable only within a range defined by the types of materials and other process parameters, such as temperature and environmental strain. The value of the scanning speed used is between 0.1 mm/s and 15 m/s [22].

In SLM, scan speed determines the length of the melt pool. Higher scanning speed gives rise to a longer and thinner melt pool, which is more prone to split into several smaller melt pools due to Rayleigh instability [26].

2.1.3.4 Layer Thickness

Layer thickness is the thickness of the 3D CAD model of the component, which is translated into a physical layer by laser processing. It is the same as the powder layer used in the process, which is fixed by adjusting the height of the platform. Layer thickness is another significant parameter directly related to the production speed. Higher production speed is achieved with increased layer thickness, while high precision is achieved with its reduction [22].

Higher laser energy is required for the processing of thicker layers. However, there is a limit to how much laser energy may be increased since excessive energy may produce surface distortion and inaccuracies. This can be avoided by scanning the same surface twice with less energy [22].

The thinner layer requires low energy density but offers dense products with low surface roughness. The thin powder size is needed to create a thin layer. The use of thin layers increases manufacturing time and raises manufacturing costs. Lower layer thickness also means lower shrinkage after melting by moving laser beam, which improves dimensional accuracy and smoothness of the surface [22].

2.1.3.5 Scanning Strategy

Scanning strategy is a method of scanning powder beds with a laser beam to increase the production speed, density, and product quality. A good scanning strategy eliminates distortion, warp, anisotropy, inaccuracy, and porosity from printed products. In general, it consists of two types: fill scan and contour scan. Fill scan is used for scanning in all areas, and contour scanning is used for boundary scanning [22]. The direction of scan tracks can either be unidirectional or bidirectional, as in Figures 7A and 7B, respectively.

Scanning in a parallel line produces shrinkage stress as well as anisotropic strength. The shrinkage stress gives rise to warp and distortion. This might be avoided by splitting the plane into many tiny islands, as seen in figure 7D, and scanning each island separately. Island-shift is a scanning technique in which the cross-section is separated into smaller regions. These areas help to minimize vector length [27]. This also eliminates heat build-up from a larger area (whole plane) to a small area (an island). Each island may be scanned using a different line strategy, reducing the non-uniform distribution of heat [22]. For each layer, these islands are moved a small

amount transversely in both x and y-direction (Fig. 7E). The shift is done to ensure that no two layers are identical (prevent pattern repetition) [27].

For building a parallel-line scan mode, the scanning direction in every successive layer is rotated by 90° to decrease the anisotropic buildup [22]. Such rotation is illustrated in Fig. 7C. But, the scanning strategy used in this sample printing is stripe scanning with each layer rotation of 67° using the SLM method.

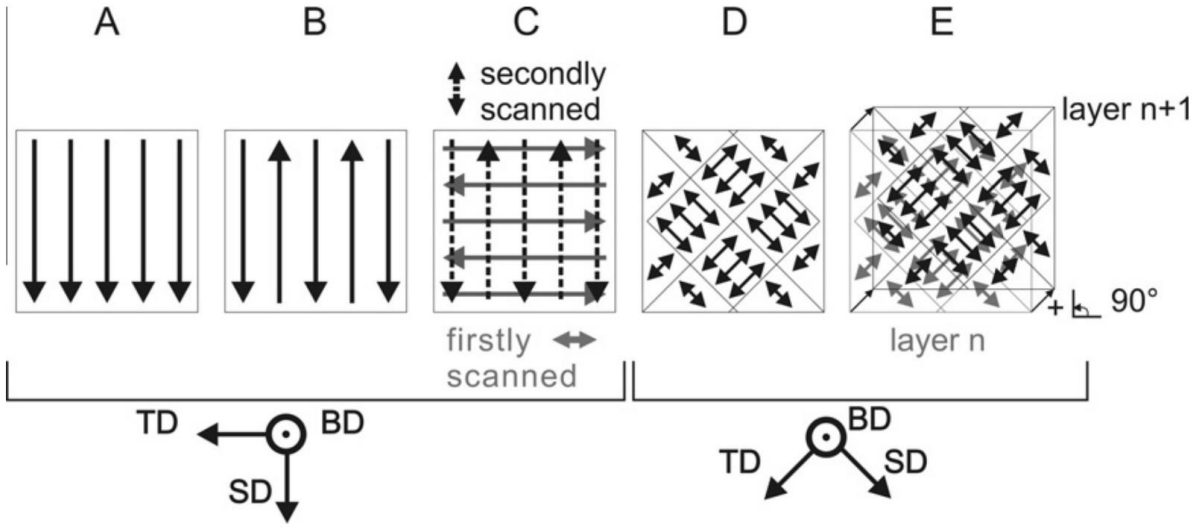

Figure 7: Scanning strategies for SLM. (A) is unidirectional, (B) is bidirectional, (C) shows bidirectional scans rotated by 90°, (D) illustrates dividing areas into islands, (E) illustrates rotation and island-shift between layers. The transverse (TD), scanning (SD) and building direction (BD) are indicated [27].

2.1.4 Typical defects in the material produced using SLM

The most common defects in SLM produced materials are as follows: -

2.1.4.1 Cracks

The cracks in the microstructure may be during solidification or subsequent heating. Microstructure cracking is often material-dependent, and there may be certain instances of processing where cracking is inevitable [18].

In AM material, there are various material-dependent processes where the cracks form [28]. Solidification cracking may occur for certain materials if excessive energy is applied and appears from the stress-induced between solidified areas of the melt pool and areas that are yet to solidify. This form of cracking depends on the material's solidification composition (dendritic, cellular, planar) and are caused by high pressure on the melt pool or inadequate liquid flow to solidified grains to provide insufficient supply or flow obstruction [29]. Higher applied energy contributes to higher thermal gradients, explaining the more significant thermal stress required for solidification cracking. The Grain boundary crack nucleates along the grain boundary of the material. The sources

of this method of crack are based on material and rely on the formation or dissolution of precipitate phases & the morphology of the grain boundary [29].

The process variables needed to minimize the induced porosity of the process may vary from those required to reduce crack formation [28]. Solidification cracking and grain boundary cracking are both processes found within the microstructure. Generally, cracking is often used to describe the macroscopic cracking of the material. These cracks can nucleate due to other visible defects, such as delamination, which are not linked to excess energy input [30].

2.1.4.2 Porosity

Porosity might be generated during the casting process. Porosity may be either inter-layer porosity or intra-layer porosity. If there is a lack of input energy needed to melt the input material, this phenomenon can produce some un-melted regions, leading to inter-layer porosity. Inter-layer porosity develops close to the substrate. Due to the rapid cooling rate, this type of porosity can also occur. Pores formed due to inter-layer porosity are irregularly shaped and large [31].

On the other hand, Intra-layer porosity is related to inert shielding gas entrapment. This porosity is randomly distributed, and the pores formed by this type of porosity are round-shaped. Intra-layer porosity typically occurs in regions with lower cooling speeds [31].

The characteristics of the initial powder also have an impact on the porosity values. If the initial powder has a variable grain size, the porosity of the final material can increase. It is crucial to control the size and shape of the powder to produce a homogeneous alloy with less porosity [32].

2.1.4.3 Melt ball formation

The formation of melt ball is due to the solidification of the melted material into spheres instead of solid layers, wetted on the underlying part. Surface tension is a physical phenomenon that induces melt balling, which is directly related to the melt pool dimensions [33]. If the length-to-diameter ratio is greater than 2·1, the melt pool will shift from a welded bead (half-cylinder) to a melted ball (sphere). It should be mentioned that these conditions are strictly theoretical, based on assumptions of smooth surfaces, chemical homogeneity, and other ideal conditions. The purpose of countering this problem is to minimize the length-to-diameter ratio of the melt pool [33]. The formation of the Melt Ball is shown in Figure 8(a), and the extreme condition is usually found only during material development. It appears with higher temperatures or alongside delamination with lower temperatures [18].

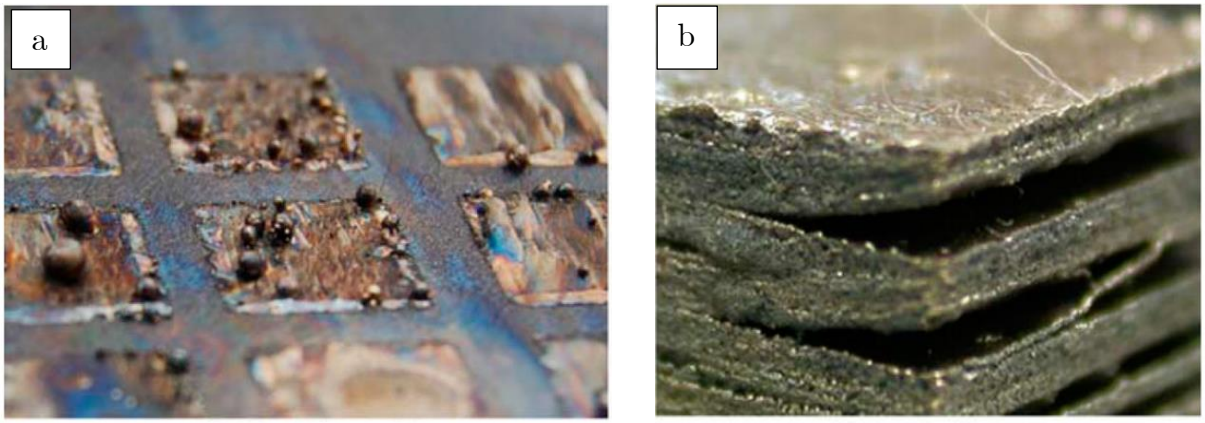

Figure 8: (a) Melt Ball Formation and (b)Delamination [34]

2.1.4.4 Delamination

Delamination is the separation of the neighboring layers within parts due to a lack of proper melting between the layers, as in Figure 8(b). This may occur as a result of insufficient powder melting or insufficient re-melting of the underlying solid. Whereas the effects of lack-of-fusion defects can be found and mitigated with post-processing within the component's interior, delamination results are macroscopic and cannot be corrected by post-processing. By using substrate heating, reduction in visible cracking has been illustrated in SLM [30].

2.1.4.5 Swelling

Excess energy input will lead to the material being overheated. This can happen due to small features or overhangs in the geometry of the component. Overhangs in PBF are usually rendered using support structures such as wafers. Recently, lattice support systems have been explored [35]. Two types of support are available: mechanical support and thermal support. Mechanical supports help protect overhangs from deformation due to gravity or growth stress. Thermal supports enable the applied energy to follow a conductive path away from the melt surface of the PBF. Swelling is the growth of solid material above the degree of distribution and melting of the powder. This is analogous to the humping phenomena, which happens due to the surface tension effects associated with the melt pool geometry [36].

2.1.4.6 Substrate adherence & warping

To achieve mechanical adhesion of the first layers of the melted component, metal AM processes are constructed on top of a metal substrate surface [36]. The substrate can be held at room temperature, warmed by internal heaters, or heated by an electron beam. Many metal deposits form ductile interfaces and should be cut off during post-processing. Ti-6Al-4V deposited on the layer of stainless steel 304 creates a more brittle

interface that can be separated without cutting by applying energy. Such an interface can minimize the number of post-processing steps.

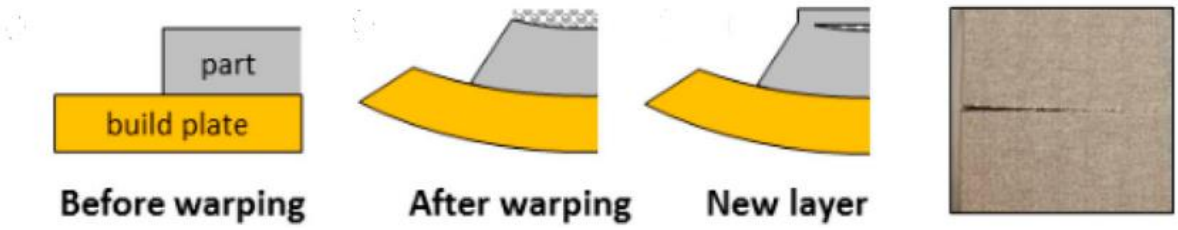

Figure 9: Build plate warping effect during processing & resultant damage [18]

Substrates may warp during use, as shown in Figure 9. This may be due to the operating temperature of the AM procedure, the heating of the substrate before use, or the differential coefficients of thermal expansion. To avoid this effect, some processes use a substrate of the same metal as the build, such as stainless steel. The ultimate impact of the deformation of the substrate is the distortion of the geometry of the component inside the affected layers and the potential loss of fusion or delamination in the transition region back to the unaffected part. Substrate warping is a type of stress relief resulting in irreversible plastic deformation. The latest work on modeling the distortion of the substrate has simplified the evolution of stress in thermal history in EBM [37]. The same processes that induce deformation of the substrate may also lead to significant problems with residual stress [18].

2.1.4.7 Residual stress

Residual stress is typical in metal AM materials due to extensive thermal gradients during manufacturing which can adversely affect mechanical properties and serve as a driving force for changes in grain structure. If this stress exceeds the local material yield stress, warping or plastic deformation may arise. Cracking or other defects can occur if this stress exceeds the local ultimate tensile strength of the material [38]. Residual stress is explained in detail as a separate heading below. The different methods of measurement of residual stresses are also described in brief.

2.2 Residual Stress

The repeated thermal cyclic effect, which applies to both DED and SLM, causes residual stress (RS) in the alloys produced by the AM process. This results in adverse changes in the mechanical properties that decrease the lifespan of the products. Three types of residual stresses can be detected: Macro -, Micro- and Sub-micro residual stress, depending on which AM system is used. Macro RS results in a change in the final dimension of the component, Micro residual stress results in changes in the size of grains, and Sub-micro RS contributes to dislocations [39].

There are two reasons for the formation of residual stress in AM metals. The first cause is where both the top layer and the previously solidified layer melt during the printing process, allowing the behavior and microstructure of the material to change. The second cause for residual stress formation is the repeated temperature change during the heating and cooling processes. During the heating process, the metal is required to expand, but the material is partly shrinking due to the low temperature in the surrounding region. These cases can induce defects like porosity, cracks, and inclusions give undesired mechanical properties [40].

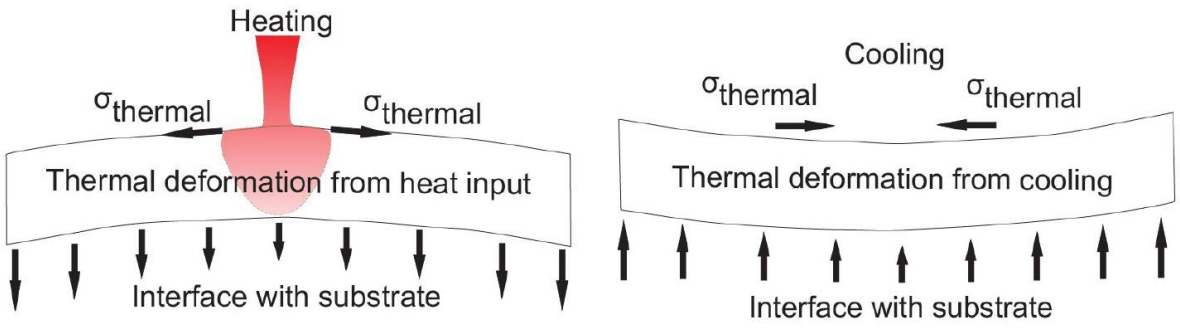

(a) heating phase. (b) cooling phase.

Figure 10: Thermal deformation at each cycle on a deposited layer [40]

The heating and the cooling stage of the AM process are shown in Figure 10. As the laser is applied to the surface during the heating process (a), the upper layer increases its strain (length) and stress. After eliminating the laser, the cooling process (b) allows the material to experience compression stress at the welded spot resulting in the production of residual stress [40].

This RS results in problems like distortion, reduction in fatigue life, and corrosion resistance. The RS is a complicated problem to analyze and solve. Residual stress can be measured using various techniques: micro-hardness, the contour method, X-ray diffraction, neutron diffraction, or other methods. Micro-hardness only shows stress details close to the surface being examined. After cutting, the contour process depends on the deflection of surfaces, and this technique gives similar results to those of diffraction of the neutron [41]. In addition, it is noted that the contour process is less

relying on chemistry than neutron diffraction. X-ray diffraction and neutron diffraction can be used to calculate the variance in bulk stress, but they are more costly and requires advanced equipment [42].

2.2.1 Method of Residual Stress Measurement

There are various methods available for measuring residual stress, as shown in Figure 11. The residual stress measurement methods can be categorized in three ways: destructive, non-destructive, and semi-destructive. Various techniques have been developed over the period, but the most developed methods are X-Ray Diffraction, Neutron Diffraction, Ultrasonic, Indentation, and the Magnetic method [43].

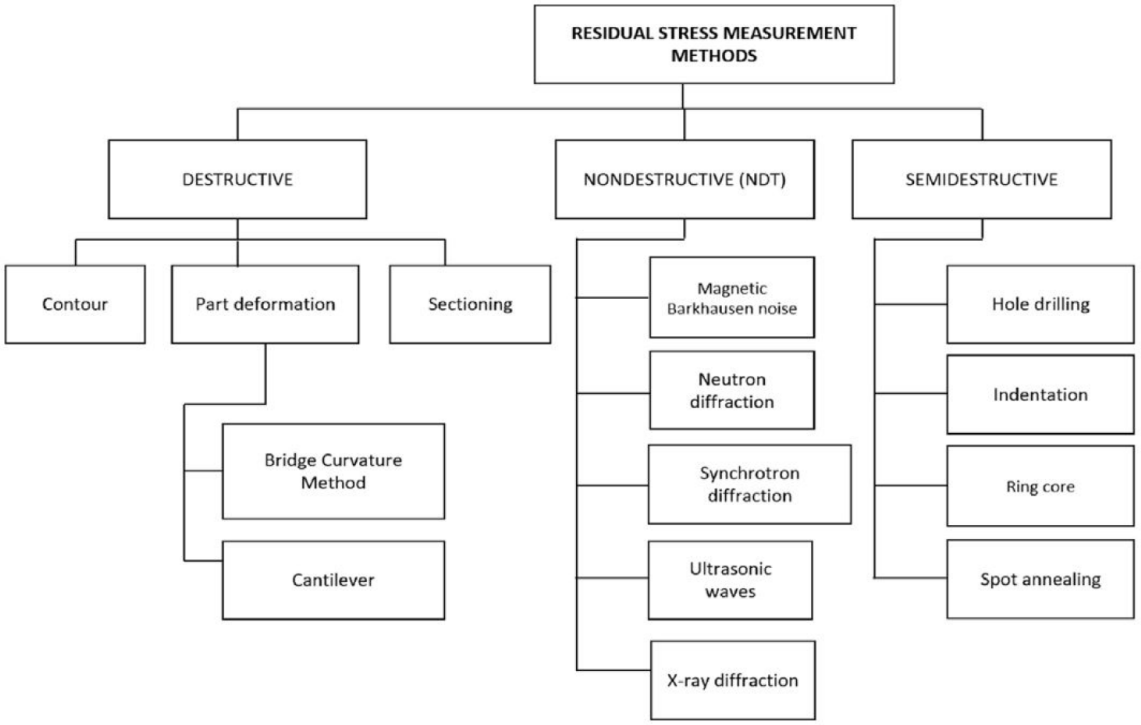

Figure 11: Residual stress measuring methods [43]

Some measurement methods have advantages such as reliability, consistency, affordability, and other methods have disadvantages such as high cost, complexity, non-standardized, slow operation, and low accuracy. The most commonly used measurement method is X-Ray diffraction [44].

2.2.2 X-Ray Diffraction Method

X-ray diffraction is a non-destructive method of study based on the theory of Bragg's law. There is currently no protocol for this form of testing available. The X-Ray beam reaches the specimen at an angle that complies with Bragg's law, interacts with the lattice planes, and is reflected in the detector. Measurements of planes are taken at various angles, and strains are then measured using those equations. The X-ray

interacts at a small distance under the surface of the specimen, depending on the material and the angle of incident [45].

X-ray diffraction evaluates residual stress by analyzing the distance between the crystallographic planes. The spacing between planes can differ from when it is in a stress-free state, if residual stress is present in a material. The lattice spacing increases in the planes parallel to the stress direction if there is tensile residual stress present in a component. Conversely, the lattice spacing perpendicular to the residual stress of the tensile will decrease [46]. This is shown in figure 12.

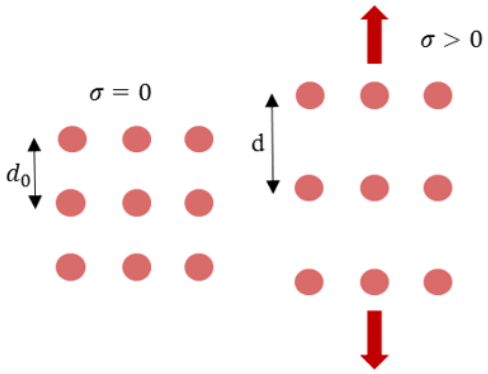

Figure 12: Lattice structure without (left) & with (right) residual stress [47]

If the crystalline is inhomogeneously strained (Figure 13), the angle of the Bragg is changed, causing the diffraction peaks to widen. The precipitates, vacancy layer defects, and dislocations cause inhomogeneous strain in the crystalline. Bragg's law equation is shown below.

$$\lambda = 2d\sin\theta \qquad [2]$$

where λ is the wavelength, d is the lattice distance, θ is the diffraction angle.

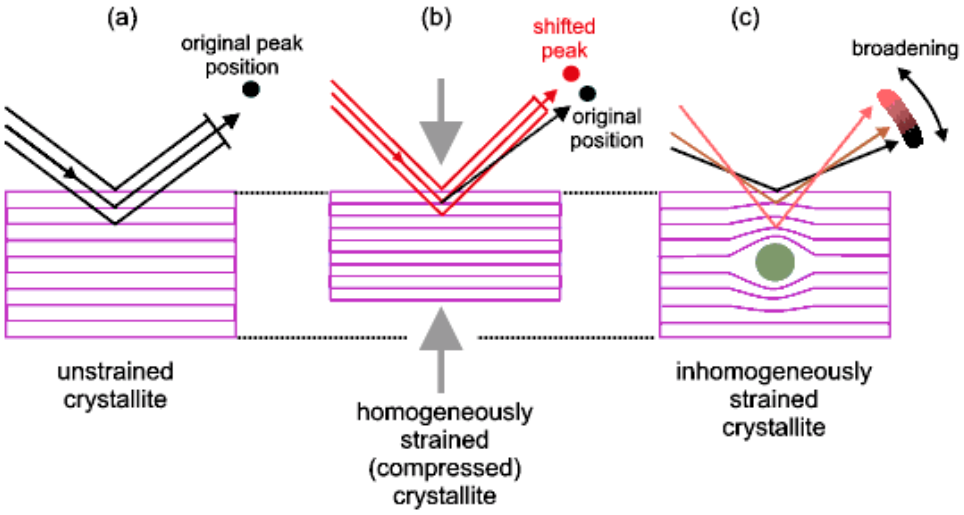

Figure 13: Inhomogeneous crystallite strain [48]

2.3 Super Alloys

The microstructure and mechanical characteristics of common metals change at high temperatures. When working at high temperatures, such as in power plants, aircraft, oil and gas extraction, and processing units, this allows the metal to lose its strength. In metals working at high temperatures, these kinds of flaws can be avoided by designing an alloy that can survive high-temperature conditions [49]. A superalloy is outstandingly heat resistant, has high dimensional stability, maintains rigidity, has high strength and toughness [50]. A superalloy is created by mixing alloy metals to heat and wear-resistant metals to improve their properties. Superalloy materials are resistant to high temperatures, corrosion, oxidation, creeping, abrasion and are resistant to high temperatures [51].

Super Alloys are broadly classified into three classes [50]. They are mentioned below: -

1. Nickel base.

2. Nickel-iron base.

3. Cobalt base.

This thesis deals with the properties of nickel-iron base superalloys, i.e., Super duplex stainless steel.

2.3.1 Duplex Stainless Steel

Duplex stainless steel (DSS) is a type of steel with a primary phase composition of ferritic (δ) and austenitic (γ) microstructure. When melting DDS steel, it will solidify from the liquid phase to an approximately 100% ferritic structure. When cooling to room temperature, parts of the ferritic structure will be transformed to austenite. The most common and preferred type of DSS consists of a ratio of about 50/50 between ferrite and austenite. With such an even distribution, DSS steel will benefit from both the higher yield strength of ferrite and retain some of the work-hardened properties that result in tensile strength. This property comes from the austenitic microstructure. Hence, DSS steel fills a gap in the market between austenitic and ferritic stainless steel. [52]. The typical duplex stainless steels contain ~20-25 % Cr, ~0.05-5 % Mo, ~1-8 % Ni, and ~0-6 % Mn.

Duplex stainless steels were initially produced as a low-nickel alternative to austenitic stainless steels in some applications. Super duplex stainless steels demonstrate a strong trend towards higher alloys. Nickel content has risen from 4 to 7 weight % in super

duplex stainless steel. DSS has some apparent benefits compared to austenitic stainless steel, such as greater mechanical strength and higher corrosion resistance. DSS benefits against austenitic stainless steels can be expanded by use in areas where normal austenitic stainless steels are unsuitable due to stress corrosion cracking [53].

The austenitic phase tends to be cathodically shielded by the ferritic phase, which is typically mechanically more robust in commercial DSSs with low interstitial nitrogen content. Recent concern in DSS is related to the high resistance to chloride-induced stress corrosion of recently produced super duplex steels, which continues to be a significant problem in marine and petrochemical applications [53].

However, the austenitic phase in the DSS, compared to that of ferritic stainless steels, dramatically increases the impact toughness of the alloys. Super DSS reveals a value of 230J and above after appropriate heat treatment, which can be considered a very high value for this steel class [53].

2.3.2 Classification of DSS

DSS is usually selected to produce the desired volume fraction of the ferrite constituent, chemical compositions, and thermomechanical treatments. The chemical composition is used for DSS classification by measuring the pitting resistance equivalent number, referred to as PREN, because the nitrogen content is considered [54].

$$\text{PREN} = [\text{wt.\% Cr}] + 3.3\cdot [\text{wt.\% Mo}] + 30\cdot [\text{wt.\% N}] \qquad [3]$$

DSS are classified into four types based on PREN value, as shown in Table 2 [55, 56]. They are: -

1) **Lean duplex SS:** Usually, the EN 1.4362 grade has been produced more recently for less demanding applications, especially in the building and construction industry. Their corrosion resistance is comparable to normal austenitic grade EN 1.4401, and their mechanical properties are better. When strength is necessary, this can be a great advantage. The PREN range is 22–27 [55, 56].
2) **Standard duplex SS:** It is characteristic of the mid-range of properties and is perhaps the most used today. The PREN range is 28-38 [55, 56].
3) **Super duplex SS:** It is designed to satisfy the specific requirements of the oil and gas industry and those of the chemical industry. They provide superior resistance and strength to corrosion. Still, They are more challenging to process because the higher contents of Cr, Ni, Mo, N, and even W facilitate the development of intermetallic phases that significantly decrease the steel's impact resistance. The PREN range is 38-45 [56].

4) **Hyper duplex SS:** It was created as a more robust alternative to 2507 for usages in even more aggressive environments, such as hot seawater, acidic chloride solutions, and organic acids. A new form of duplex steel that provides pitting resistance numbers higher than 45 is hyper-duplex stainless steel (HDSS). These duplex stainless steels show both the highest rate of corrosion pitting resistance as well as mechanical strength [56].

Table 2: Chemical Composition of different types of Duplex stainless steel [56]

Type	Cr %	Ni %	Mo %	N %	PRE No
Lean	20-24	1-5	0.1-0.3	0.1-0.22	22-27
Standard	21-23	4.5-6	2.5-3.5	0.1-0.22	28-38
Super Duplex	24-29	4.5-8	2.7-4.5	0.1-0.35	38-45
Hyper Duplex	27	6.5	5	0.4	> 45

2.3.3 Super Duplex Stainless Steel

The type and compositions of alloying elements may be used to characterize super duplex stainless steel. The high chromium and molybdenum content of Super Duplex makes it very resistant to uniform corrosion by organic acids such as formic acid and acetic acid. Super Duplex is also more resistant to inorganic acids, particularly those containing chlorides. The Super Duplex pitting resistance equivalent, determined by PREN, will exceed 38 in most material types [8].

This thesis focuses on the study of super duplex stainless steel of grade EN 1.4410. Alloy SAF 2507 (EN 1.4410 / ASTM S32750) is a super-duplex chromium-nickel stainless steel with copper in addition. The chemical composition of EN 1.4410 material is presented in table 3 below [57].

Table 3: Chemical Composition of EN 1.4410 (ASTM S32750) [57]

Chemical	Weight Percentage (wt. %)
Chromium (Cr)	24-26
Nickel (Ni)	6-8
Molybdenum (Mo)	3-5
Copper (Cu)	0.5
Manganese (Mn)	≤ 1.2
Silicon (Si)	≤ 0.8
Nitrogen (N)	0.24-0.32
Carbon (C)	≤ 0.03
Phosphorus (P)	≤ 0.035
Sulphur (S)	≤ 0.02

Each alloy element has specific physical and chemical properties. Each factor affects the properties of the superalloy depending on these characteristics. The importance of alloying elements of super duplex stainless steel is described briefly in section 2.4.

2.4 Role of alloying elements in DSS

It is crucial to understand the impact of the various alloying elements when producing SDSS. The role of each element in the overall composition is critical for the microstructure and, again, for the corrosion resistance and the mechanical properties. The main alloy elements and their properties are discussed below.

2.4.1 Chromium

Chromium over 12% enables forming a passive film, a core component of all stainless steel. It also serves as a ferrite stabilizer. Adding Cr increases corrosion resistance and oxidation against nitric and chromic acids. It also increases resistance to high-temperature oxidation and hot sulfur gas [51].

2.4.2 Molybdenum

Molybdenum provides a protective film on the iron and increases the corrosion resistance of SDSS. It is also a ferrite former and will, especially in combination with chromium, contribute to the precipitation of secondary phases in stainless steel. It also increases the strength of high-temperature supplies for metallic materials. It also increases resistance to pitting and crack corrosion. The incorporation of carbon and molybdenum can regulate ductility, but the contents should be controlled to avoid the creation of intermetallic phases [51].

2.4.3 Nickel

Nickel stabilizes the austenite and is needed to maintain the phase balance between austenite and ferrite in duplex steel. If the content is too high, the proportion of austenite will exceed 50% and lead to the enrichment of chromium and molybdenum in the ferrite. Increased nickel content leads to a greater toughness of the material and has a small effect on corrosion resistance. Nickel improves corrosion resistance to stress cracking and gives metallurgical stability. It also strengthens plastic performance at high temperatures and increases resistance to carburization, oxidation, and nitridation [51].

2.4.4 Manganese

Manganese is an austenite formation but has little effect on stabilizing the duplex structure in DSS. On the other hand, the element helps increase wear and tension resistance without compromising the material's ductility. Manganese also increases the

solubility of nitrogen, which makes it possible to add more nitrogen and utilize its property as a corrosion protector [58].

2.4.5 Nitrogen

Another essential alloy agent is nitrogen. Nitrogen contributes positively as an alloying element in stainless steel in several ways. It significantly improves the material's corrosion resistance and strength. Nitrogen is a cheap alloying element and can replace nickel in the alloy because it acts as an austenite former. This property also makes that nitrogen delays and reduces the precipitation of intermetallic phases, such as the σ phase and chromium nitrides in DSS, which has a high chromium and molybdenum content. SDSS contains more significant amounts of nitrogen because it is rich in ferrite-forming alloying elements, and nitrogen contributes to the material retaining the duplex structure [59].

2.4.6 Carbon

Carbon is found interstitially in steel, but it is desirable to keep the level low, all the way down to 0.03% in SDSS. Carbon is an interstitial element in steel and contributes to strength, but it also leads to a risk of sensitization (precipitation of chromium carbides). This is because carbon contributes to the precipitation of chromium-rich precipitates, which can further lead to areas with corrosion. Carbons help prevent corrosion and provide strength at high temperatures [51].

2.4.7 Sulphur

It reduces grain boundary cohesion and decreases tensile ductility. It can also be harmful to the metal, but it is controlled by the addition of manganese and magnesium [58].

2.4.8 Tungsten

Tungsten has been added to duplex alloys up to 2% to improve pitting resistance by expanding the potential range of the passive layer. Tungsten also increases resistance to crevice corrosion in heated chloride solutions [51, 60].

2.4.9 Copper

The properties of DSS are beneficially influenced by copper alloying. Copper lowers the high-temperature limit for precipitation of the sigma and chi phases, as well as the volume of the precipitated chi phase [51].

2.5 Selective Laser Melting of Duplex Stainless Steel

The selective laser melting of duplex stainless steel from powder feedstock is a new area of research. There are just a handful of papers that have been published very recently, once this thesis has begun. Davidson printed 2507 super duplex stainless steel [61]. The optimization of parameters was accomplished by fixing all parameters apart from laser power. An almost pure ferritic microstructure was found after the SLM process due to high cooling rates instead of an austenitic-ferritic microstructure. After complete solution annealing, the equilibrium microstructure (45% austenite) was retrieved, while the morphology of the austenite was ¨needle-like¨. The densities achieved were between 85-90% [61].

Davidson ran a matrix skew of laser power and laser volumetric energy densities (VED) in a follow-up paper [62]. The volumetric energy density (E in (J/mm^3), is a typical parameter studied during selective laser melting, but it does not capture complex physics [63].

$$E = \frac{P}{vht} \tag{4}$$

Here, P is power (W), v is scan speed (mm/s), h is hatch spacing (mm), and t is powder layer thickness (mm).

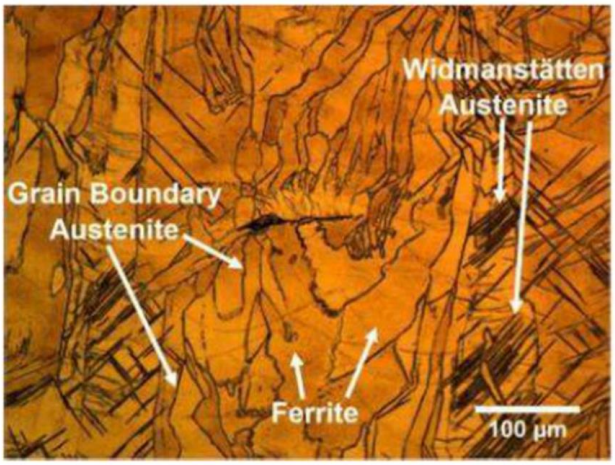

Figure 14: Microstructure of as-built duplex stainless steel 2507 [62]

Davidson's fascinating observation was that the duplex stainless steel treated by the SLM showed white, spherical precipitates in the microstructure [62]. Davidson suggested these precipitates be CrN, which can shape under high-temperature conditions (>1273 K) and rapid cooling speeds (>20 K/s) [62]. These precipitates will minimize ductility and increase pitting corrosion rates, the authors hypothesized. The hardness of 408.4 HV, which was 125.9 HV higher than their forged measurement, was another fascinating finding. The CrN precipitates can clarify this high hardness, but the reason may also be the microstructure. The samples analyzed were mainly ferrite,

and the grains were elongated and columnar as seen in Figure 14 (mean length ~370 µm, mean width ~35 µm) [62].

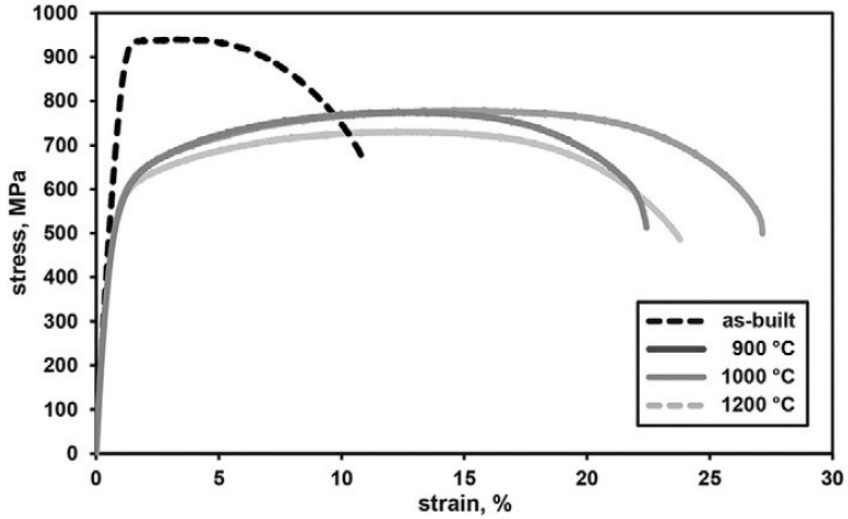

Figure 15: Mechanical properties for SLM produced Duplex SS 2205 by heat treatment [5]

Hengsbach produced SLM samples with 99% ferrite and a density of >99% [5]. This density is a big improvement over previous work and is possibly due to the right choice of processing parameters (275W, scan speed of 775 mm/s, and energy density of 59 J/mm^3). The predicted mechanical properties of the DSS can be restored after heat treatment, according to Hengsbach, as shown in Figure 15. They showed that as-built samples with high dislocation densities and nitride involvement were brittle, but ductility and hardness were restored by heat treatment of 900-1200°C. The findings were clarified in light of the recovery of the duplex microstructure (up to 34 % austenite) [5].

Papula published another very recent analysis [64]. They also found that the as-built sections were fully ferritic, hard, and brittle, but the duplex microstructure was restored by the annealed solution (up to 46.4 % of the austenite recovered). A particularly high relative density of 99.97% was claimed and backed by an ultimate tensile strength of >800 MPa and an elongation of >40%. The elongation is shocking, as the criteria normally mention 25%. Papula proposed high power (>250W) and a 67° scan rotation technique to achieve optimum density [64]. Initial research on pitting corrosion suggested that the as-built condition was vulnerable to pitting when the annealed condition was not present [64].

2.6 Microstructure of Super Duplex Stainless Steel

2.6.1 Primary Phase

DSS alloys can have two different primary phases. The iron-carbon alloy may exist as ferritic or austenitic. These phases have different lattice structures, which affects the mechanical properties and solubility of other elements. The Delta Ferrite phase has a body-centered cubic (BCC) crystal structure, while the austenite phase has a face-centered cubic (FCC) crystal structure, as shown in Figure 16. It is seen that there are more atoms in an FCC structure than in a BCC structure. The Atomic packing factor (APF) for FCC and BCC corresponds to 0.74 and 0.68, respectively. This means that the FCC structure is more tightly packed. Furthermore, it can also be seen that the FCC and BCC have different coordination numbers, i.e., for the FCC and BCC are 12 and 8, respectively. Both APF and the coordination numbers indicate that the atoms are denser in FCC cells [65].

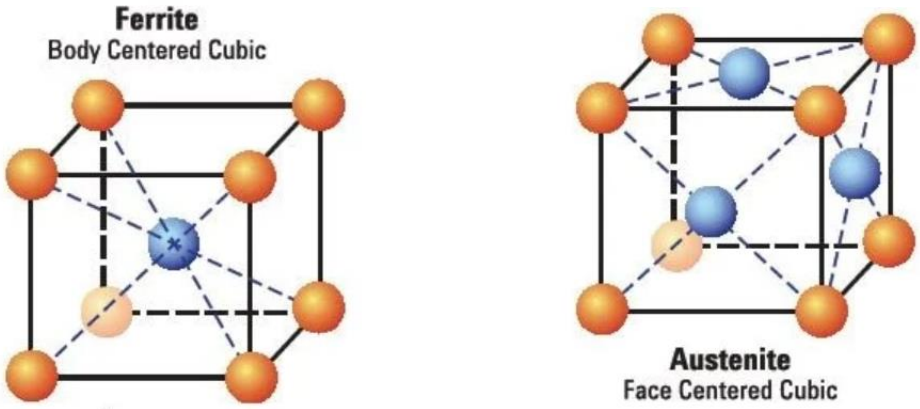

Figure 16: Crystal structure of Ferrite and Austenite [66]

Super duplex stainless steels have a microstructure with a ferritic-austenitic structure, and hot-rolled material has grains elongated in the rolling. The ferrite/austenite ratio can affect the characteristics of the DSS. According to the American Petroleum Industry research, the ferrite concentration of the DSS ranges between 30 and 65% [67]. However, it has been reported that the best properties are acquired when the ferrite content is about 50% [68]. The three different microstructures: ferritic, duplex, and austenitic, are shown in figure 17. An austenite stabilizer clearly shows the transformation in the microstructure from ferritic to duplex and finally to austenitic after adding nickel [69].

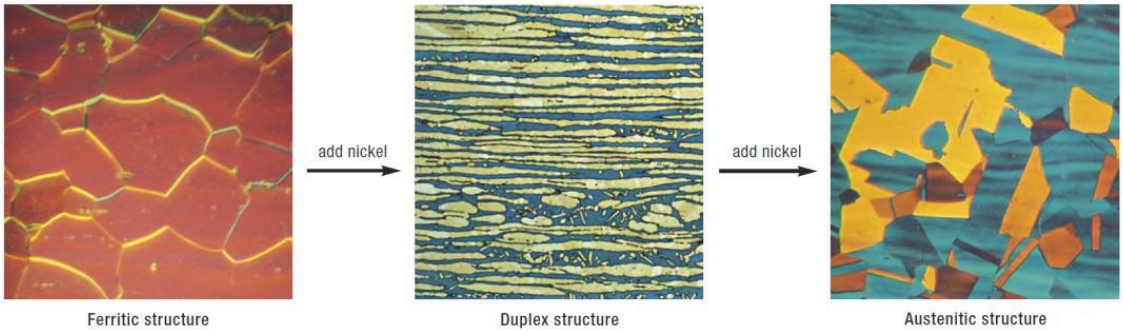

Figure 17: Increasing the nickel content changes the microstructure of stainless steel from ferritic (left) to duplex (middle) to austenitic (right) [70]

2.6.2 Secondary Phase

Secondary phases occur outside of ferrite & austenite and are often precipitated in connection with heat treatment and cooling of the material. In DSS steel, precipitates are often correlated to the ferrite phase and its less dense BCC structure due to its significantly higher diffusion rate than in austenite [71].

The precipitates are usually undesirable as they will affect the alloying elements and influence the material's mechanical properties, which decreases its toughness and corrosion resistance [71].

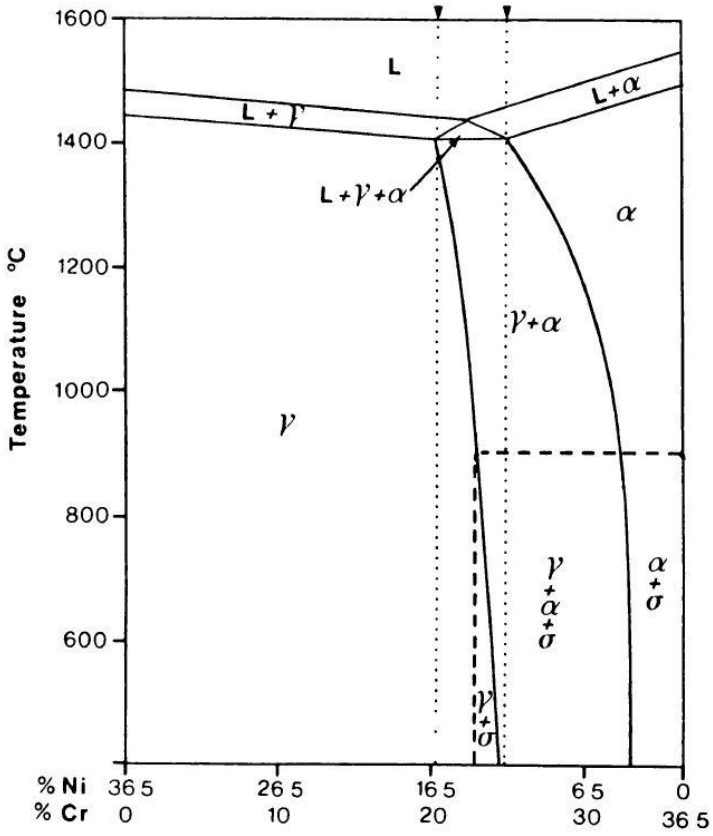

Figure 18: Fe-Cr-Ni phase diagram for 63.5 wt.% Fe [72]

A Fe-Cr-Ni phase diagram for 63.5 weight % Fe is illustrated in Figure 18. A possible DSS alloy composition is indicated in the phase diagram by the vertical dashed line[72]. DSS alloys solidify mostly at about 1425°C as ferrite and partly convert into a solid-state reaction to austenite at lower temperatures. If the cooling rate is rapid, relatively little ferrite may transform to austenite at ambient temperature, leading to an excessive ferrite phase. As a result, the cooling rate of duplex steel must be slow enough to enable roughly 50% of the ferrite to be transformed to austenite while yet being rapid enough to prevent the formation of intermetallic phases. When welding various part sizes or heavy parts with very low heat input, unnecessary phases can occur during fabrication [68].

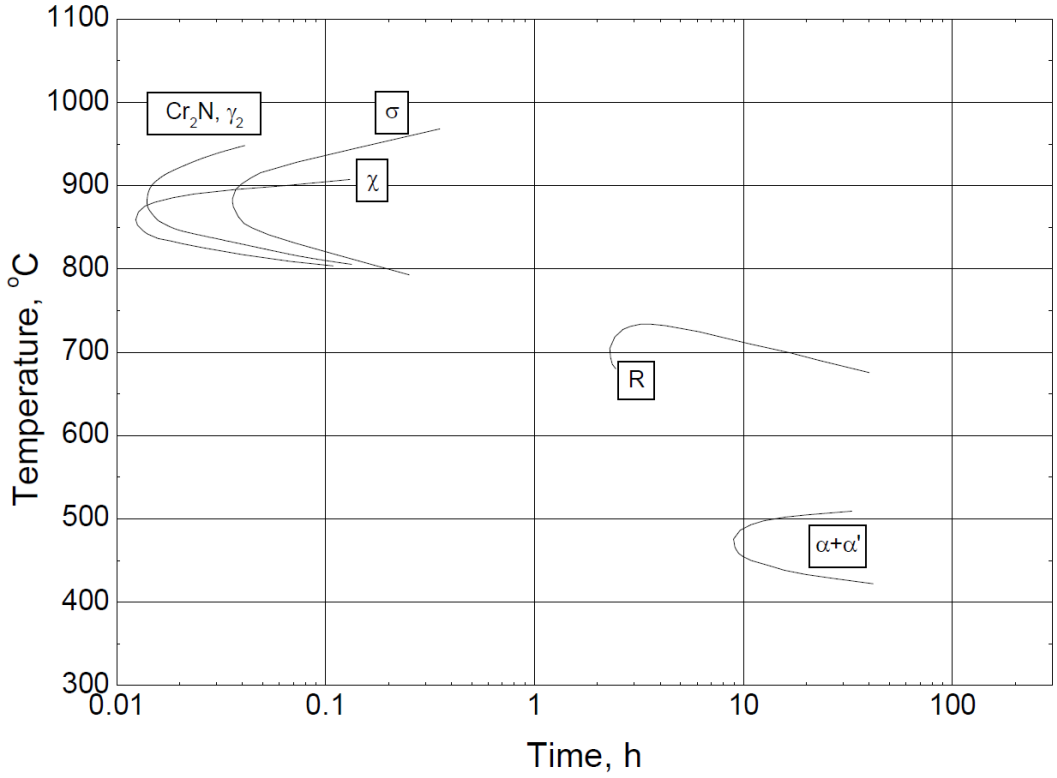

Figure 19: TTT diagram for various precipitates appearing in SAF 2507 [71]

The presence of a ferrite matrix makes the DSS susceptible to embrittlement and loss of mechanical properties, especially toughness, due to long-term exposure at high temperatures. The deposition of carbides, nitrides, and intermetallic phases, both of which may be detrimental, can occur for short periods as cooling continues to lower temperatures in the range of 475-955°C (887-1750°F). The most noticeable phases are the alpha prime (α′) phase, sigma (σ) phase, chi (χ) phase, chromium nitrides, secondary austenite, carbides, R phase, π phase, and τ phases. For this purpose, DSS is usually not used at temperatures above 315°C (600°F) [68]. Some parameters of the phases are listed in Table 4. A schematic TTT diagram of precipitation occurring in SAF 2507 is given in Figure 19. In addition, a spinodal decomposition of ferrite will

occur in the 300-500°C range. The sigma phase is the most important phase described above due to its toughness and corrosion behavior [71]. The different types of precipitation of secondary phases are explained in detail in the next heading, 2.6.3.

Table 4: Phases observed in duplex stainless steels [71] [73]

Type of precipitate	**Nominal composition**	**Lattice type**	**Temperature range in DSS, °C**	**The lattice parameter, nm**
σ	Fe 35-55, Cr 25-40, Mo 11-25	BCT	600-1000	a=0.880, c=0.454
Chromium nitride	Cr_2N	Hexagonal	700-900	a=0.480, c=0.447
	CrN	Cubic	N/A	a=0.413-0.447
χ	$Fe_{36}Cr_{12}Mo_{10}$, Fe 35-50, Cr 20-35, Mo 20-22	BCC	700-900	a=0.892
R	Fe 30-40, Cr 17-20, Mo 25-45	Hexagonal	550-650	a=1.0903, c=1.9342
		Rhombohedral		a=0.9011, α=74°27´30´´
π	$Fe_7Mo_{13}N_4$	Cubic	550-600	a=0.636-647
τ	Not determined	-	550-650	a=0.405, b=0.484, c=0.286
Carbide	M_7C_3		950-1050	a=0.452, b=0.699, c=1.211
	$M_{23}C_6$	FCC	600-950	a=1.0560-1.065

2.6.3 Characteristics of Precipitation of Secondary Phases

2.6.3.1 Sigma (σ) phase

The sigma phase is the most well-known deleterious phase precipitation in the DSS. It precipitates at the nose temperature of the TTP diagram in SDSS at less than 30 seconds. It is a rich Fe-Cr-Mo phase with a tetragonal structure. Atomic lattice sites can be packed with various components depending on the chemical structure of the DSS alloy. The δ/γ phase boundaries are common sites for σ precipitation [74]. The stability range is between roughly 600°C and 1000°C based on the composition of the steel [73]. A more coral-shaped morphology is observed at low temperatures, while σ precipitates are blockier at extreme temperatures [75]. Figure 20 shows how the sigma phase is formed along the phase boundaries between ferrites and austenite.

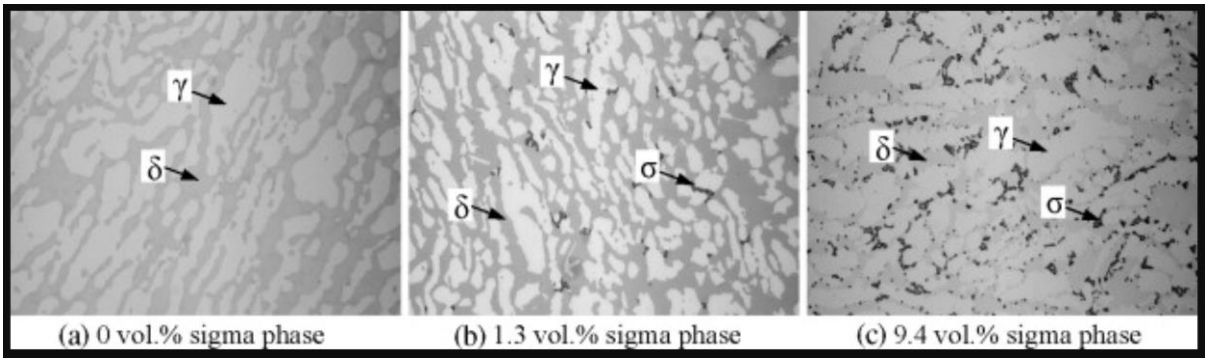

Figure 20: Sigma phase in duplex stainless steel [76]

2.6.3.2 Chi (χ) phase

Chi (χ) is a cubic Mo-rich intermetallic phase precipitating in the temperature range between 700°C to 900°C. It can contain up to 28 wt. % Cr and 22 wt. % Mo and precipitate in smaller amounts relative to sigma. The nucleation of chi is quick due to its cubic form, while its growth rate is sluggish. Chi is typically considered an intermediate process, replaced by a sigma phase during longer aging cycles [75]. It is important to remember that the higher molybdenum content in the chi phase, along with its strong atomic scattering factor, makes it possible to distinguish the chi phase on scanning electron microscope images captured with backscattered electrons, where it appears with a brighter contrast than that of sigma phase [71]. Chi-phase has a similar effect on corrosion and toughness properties as the sigma phase, but, as the two phases mostly co-exist, it is impossible to examine their impact on an individual basis.

2.6.3.3 Chromium Nitrides

Chromium nitrides can precipitate with two different mechanisms: equilibrium and non-equilibrium mechanisms. Equilibrium nitrides mostly precipitate during isothermal aging. They are CrN (cubic) or Cr2N (hexagonal) and precipitate on δ/γ or δ/δ boundaries. They can also be found within austenite near phase boundary due to the development of secondary austenite into ferrite [77]. On the other hand, Non-equilibrium nitride precipitate in samples heated to high peak temperatures accompanied by fast cooling, which is often found inside ferrite grains. An isothermal exposure to a temperature range of 700-900°C creates intergranular Cr_2N at δ/δ grain boundary as thin plates at the sub-grain boundary, triple point, inclusion, and dislocation arrays [78].

2.6.3.4 Secondary Austenite (γ_2)

The decomposition of ferrite to intermetallic and chromium nitride leads to precipitation of austenite. It shapes at lower temperatures as the duplex microstructure is formed. There are two precipitation sites of this form of austenite seen in old wrought structures: within ferrite grains and in austenite grains [79].

A variety of temperature-based mechanisms can form secondary austenite. By the temperature range 700-900 ℃, the secondary austenite will absorb large amounts of nickel while, to some extent repelling chromium and molybdenum. As a result, secondary austenite often occurs in connection with the sigma phase, rich in chromium and molybdenum [78]. At high temperatures above 1000°C, austenite will be transformed into ferrite, and DSS steel will be approximately 100% ferritic. Rapid cooling of this structure will lead to a metastable microstructure with a higher ferrite content due to inhibition of the reprecipitation of the austenite phase [79].

A metastable microstructure is a stable structure; however, when reheated to over 800℃, precipitation of austenite will occur in the form of secondary austenite. With chromium nitrides occurring at the grain boundary, secondary austenite grows from grain boundaries and into the ferrite phase, where the solubility of nitrogen is low. Secondary austenite will increase the material's toughness but decrease the corrosion resistance due to its low chromium content, which is an essential element for corrosion resistance [79].

2.6.3.5 R, π and τ phases

Laves or R phase (Fe2Mo) precipitate in small concentrations between 550 and 650°C after several hours of exposure. They occur at intra- and intergranular locations, have

a high molybdenum content and diminish pitting corrosion resistance. However, since those precipitating at intergranular sites contain significantly more molybdenum (40% compared to 35 % Mo), their effect on pitting resistance is more prominent [74].

The π-nitride has been detected at intragranular sites in duplex weld metal after isothermal heat treatment at 600°C for several hours. It is Cr and Mo rich and so has been previously mistaken with the σ-phase [74].

Heat treatment for several hours in the temperature range from 550 to 650°C can lead to the development of the severely defected needle-like τ-phase on δ/δ boundaries [80].

2.6.3.6 Carbides $M_{23}C_6$ and M_7C_3

Both forms of carbide, M_7C_3 & $M_{23}C_6$, have been found to precipitate at temperatures of 950-1050 °C and below 950 °C, respectively. Precipitation in all forms of carbide arises preferably at the δ/γ phase boundary. But precipitates have also been found at the δ/δ and γ/γ margins [81, 82]. However, carbide precipitation is becoming less significant in modern DSS, where the carbon content is very limited. For example, SAF 2507 did not detect any form of carbide precipitate. Thus, intergranular corrosion induced by carbide precipitation and Cr depletion near grain boundary seems impossible in modern DSS [71].

2.6.3.7 Alpha prime (α') and G-phase

The minimum temperature decomposition within duplex steel is alpha prime, which occurs between 300 and 525°C and is the primary cause of hardening and '475 embrittlement' in ferritic stainless steels. It is recommended that α'-formation is a result of the miscibility gap in the Fe-Cr system, whereby ferrite undergoes spinodal decomposition into Fe-rich δ-ferrite and a Cr-rich α', or, just outside the spinodal. But still within the gap, classical nucleation and development of α' occurs. Alpha prime is often associated with the co-precipitation of Cr-N in the form of sub-grain networks of Cr_2N needles interspersed within a film of α' [78].

At temperatures below 400°C, the Arrhenius equation is mainly used to explain embrittlement kinetics [83]. The activation energy characteristic of '475 embrittlement' is like Cr-diffusion in ferrite, while other factors affect α' formation, such as Cr, Mo, and Cu contents and high ferrite levels. In addition, G-phase develops at α/α' interfaces after several hours of exposure between 300 and 400°C, due to enrichment of Ni and Si at these sites [84].

2.7 Heat Treatment

Various structural changes occur in duplex stainless steel during isothermal or anisothermal heat treatment [78]. Much of them involve ferrite since the diffusion rates in the BCC structure are much higher than in the FCC austenite. In addition, the α-phase is enriched with chromium and molybdenum, which have a high potential to enable the formation of intermetallic compounds. The element solubility in ferrite reduces with a drop in temperature, increasing the possibility of precipitation during heat treatment [85] [78].

The structural changes encountered in the duplex alloys can be classified into three groups. The classification is done depending on whether they occur at temperatures above 1050 °C, from 600 to 1050 °C, or below 600 °C [85].

2.7.1 Temperature above 1050 °C

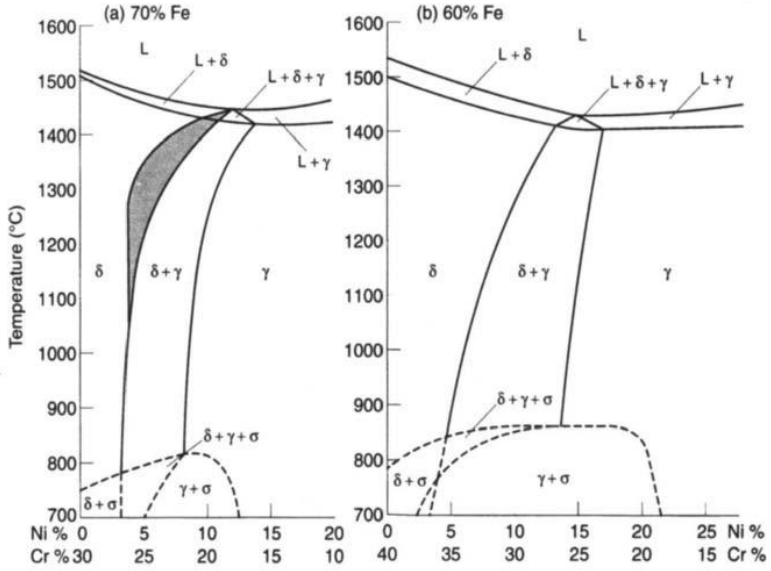

Figure 21: Concentration profiles in the ternary Fe-Cr-Ni constitution diagram at 70% and 60% Fe [86] [78]

or typical grades and typical cooling rates, duplex stainless steels solidify fully in the ferrite field. A solid-state transformation accompanies this to austenite (Figure 21), which is naturally reversible, such that any significant rise in temperature (from l050°C to 1300°C) corresponds to an increase in ferrite content (Figure 22). The schematic impact of nitrogen additions is shown in Figure 21(a). Furthermore, when the temperature rises, the partitioning of the substitutional components between the phases decreases. Additionally, ferrite is enriched by interstitial elements such as carbon and nitrogen [78].

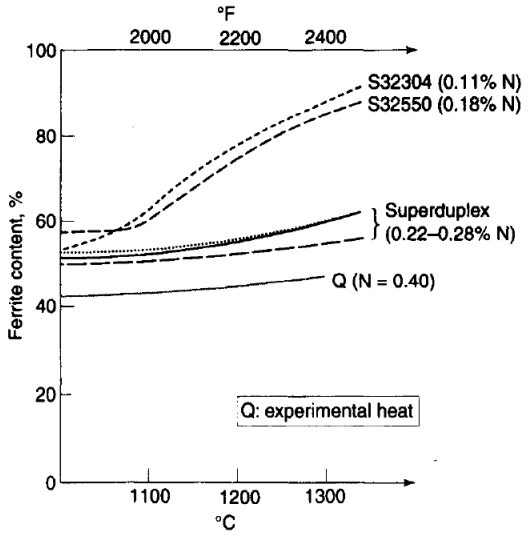

Figure 22: Difference in ferrite content with temperature for different DSS [86] [87]

The variation in ferrite content with temperature for different duplex grades is presented in Figure 22. The considerable influence of the chemical composition on the shape of the curves should be observed. This is notably true for nitrogen additions, with high concentrations (0.25-0.4%) enhancing the integrity of the two-phase structure. At 1250°C, the volume fractions of ferrite and austenite in these alloys remain nearly equal, whereas the grades of less than 0.2% N produce 80 to 85 % of ferrite. This finding has a substantial impact on the structure of the heat-affected areas of welds [78].

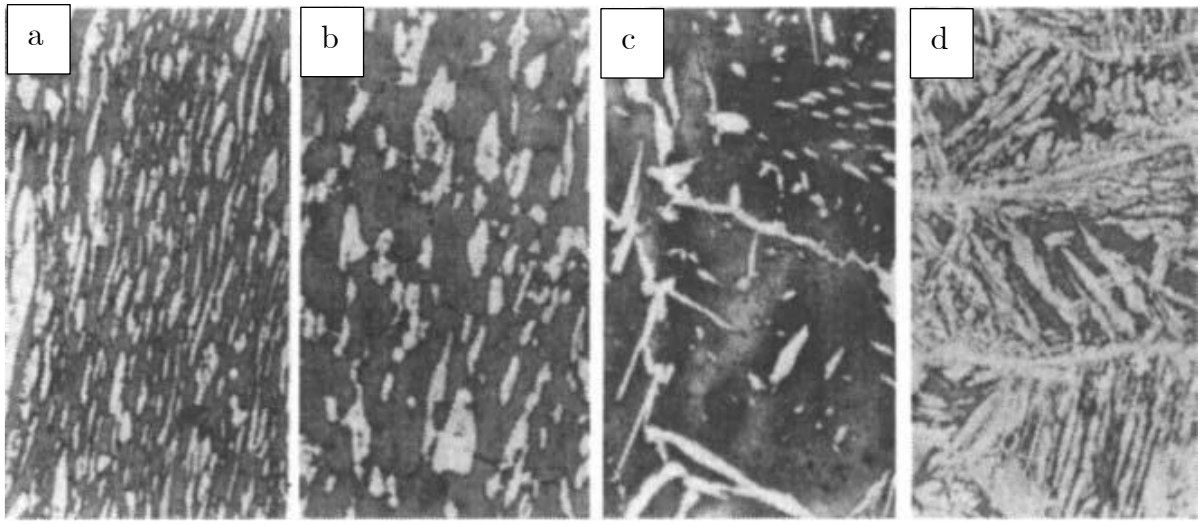

Figure 23: Effect of heat treatment on the ferrite/austenite microstructure [78] [86]

Heat treatment in the 1100-1200°C temperature range may dramatically affect the microstructure of the wrought product, as shown in Figure 23(a). The grains may be equiaxed by treating them for an extended period of time at high temperatures (Figure 23(b)) or can be made acicular, with a Widmannstatten type structure by cooling at medium rates, as in Fig. 23(c). The dual structure, consisting of both coarse and fine

austenite grains, can be achieved (as in Figure 23(d)) by step quenching, with or without simultaneous mechanical strain [78].

2.7.2 Temperature from 600 to 1050 °C nose

The lean grade S32304 alloy is the least prone to the development of intermetallic phases and needs exposure of at least 10 to 20 hours to initiate precipitation at temperatures below 900 °C (Figure 24). For this purpose, it is best to pick a solution annealing temperature below 1000°C for this material [88].

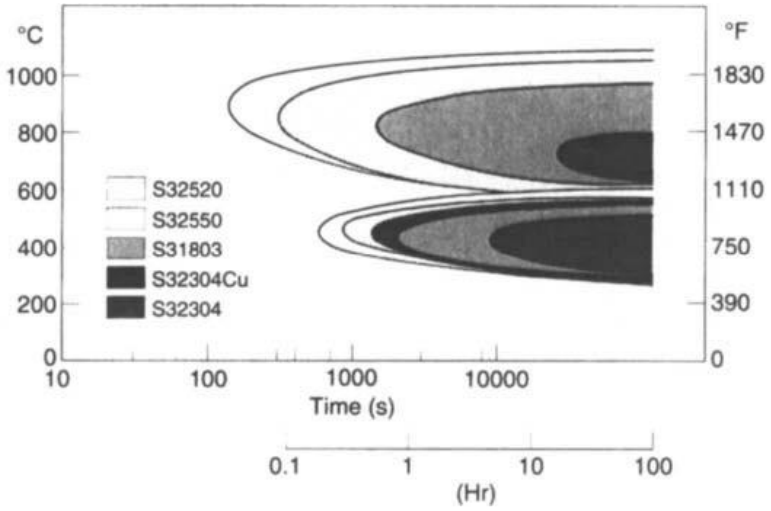

Figure 24: TTT diagrams of DSS derived by optical metallography between 600 and 1050°C and measure of hardness between 300 and 600°C [86]

Alloy S32205/S31803 is more vulnerable to precipitation than grade S32304 due to molybdenum content. Molybdenum increases the rate of intermetallic precipitation and expands the stability range to higher temperatures. Due to this, higher temperatures for solution annealing, i.e., above 1000 ° C, are required [88].

Super duplex grades have the strongest potential for intermetallic precipitation owing to their higher Cr, Mo, and W contents. However, it should be remembered that precipitation kinetics in these high alloy grades are, at worst, equal to super austenitic or super ferritic stainless steel (Figure 25). And, as in the case of the last two stainless steel, the super duplex alloys can be used satisfactorily in industrial applications by taking care during heat treatment, including quick removal from the furnace followed by water quenching [88].

Precipitates redissolve during a solution anneal, which for the super duplex grades must be performed at 1050°C or above. A few minutes at 1050-1070°C is sufficient for grades S32550 and S32750, whereas 1100°C has been advised for tungsten-bearing grades such as S32760. Similar high temperatures are required for welding, as consumables appear to have higher Ni, Si, and Mn contents than base materials. Higher Ni-content induces

high levels of austenite when annealed and helps in the enrichment of Cr and Mo in the leftover ferrite. This fact, combined with higher levels of Si and Mn, improves intermetallic phase stability. And still, for welds made with corresponding consumables, lower annealing temperatures (1040°C as opposed to 1100°C) can be used [88].

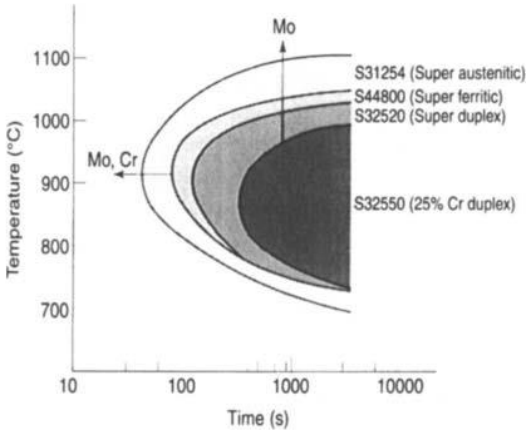

Figure 25: TTT diagrams for super stainless steels [87]

2.7.3 Temperature between 300-600 °C nose

In this temperature range, the lean alloy grade S32304 is the least prone to hardening, and a significant effect is not noted until about three hours of exposure to 400°C (Fig. 24). For grades S32205 and S31803, containing molybdenum, a much shorter incubation time is found, which would appear to accelerate hardening [88].

The 25% Cr and super duplex alloys have a broad temperature range for hardening and the shortest incubation times. This is the consequence of both the higher content of Cr and Mo and copper additions (if present) [88].

As in the high chromium ferrite steels, an embrittling reaction can occur in the duplex grades at a temperature below 600 °C. This phenomenon is accompanied by a marked hardening of ferrite, due, at least partly, to the formation of chromium-rich BCC α′ or α-Cr phase. In addition to the formation of α′, other precipitation processes can occur in the ferrite. Thus, intermetallic compounds, M6C type carbides, or Cr2N nitrides can occur for very long exposure [85].

2.7.4 Continuous Cooling Diagrams

For industrial treatments, it is important to note that precipitate nucleation is slow at temperatures near the solvus, and their development is quick. At the same time, the reverse is true at lower temperatures, near the nose of the transformation curve. Hence, it isn't easy to prevent phase transformations, such as sigma precipitation, during the reheating of heavy segment materials. Therefore the solution treatment should be

carried out at a sufficiently high temperature to dissolve any such phase. On the other hand, the slow nucleation rate at high temperatures and the slow growth rate at lower temperatures make it relatively possible to prevent the sigma phases during cooling, even in the case of air cooling of some castings heavy plates [88].

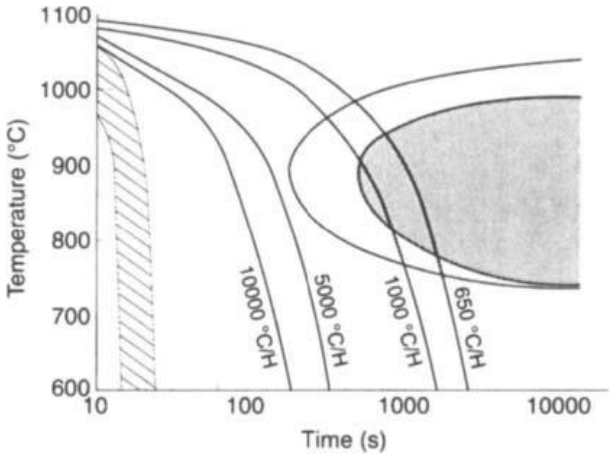

Figure 26: Continuous cooling diagram from 1080°C for S32520 grade [87]

For the S32520 grade, Figure 26 indicates a continuous cooling transition (CCT) diagram. Typical HAZ cooling rates are denoted by the hashed area, while in super duplex alloys, the two shaded areas represent various sensitivities to intermetallic formation. A significant shift in time can be seen in the precipitation 'nose' position between the TTT (Fig. 23) and CCT (Fig. 26) diagrams. The cooling rates as low as around 2000°C per hour are possible without precipitation with a 1080°C solution. However, quicker cooling is advised for higher annealing temperatures as the chance of precipitation of nitride rises. In general, the cooling rates determined in the heat-influenced weld zones are faster than can be accomplished during quenching, negating intermetallic formation [88].

2.7.5 Effect of Cooling Rates on Microstructure

The aim of maintaining the proper phase balance in duplex stainless steel is mainly accomplished by controlling the chromium, molybdenum, nickel, and nitrogen content, followed by thermal history control. However, because the cooling rate influences the quantity of ferrite that may transform to austenite, cooling rates after high-temperature exposures affect the phase balance. It is possible to have more ferrite than the equilibrium level since high cooling rates increase ferrite retention [70].

There has been minimal research on the effect of cooling rate on the ferrite concentration in duplex stainless steel. In 1987, S.A. David investigated the impact of fast solidification on stainless steel microstructures and their implications for the Schaeffler Diagram [89]. It was established in this article that quick cooling rates have

a considerable impact on metal microstructures, making constitution diagrams (Schaeffler and Delong diagrams) incorrect for estimating ferrite concentration [89]. Figure 27(a) depicts a modified constitution diagram based on David's work that accounts for varied cooling rates. This schematic is intended for use with stainless steel weld metal. The ferrite percentage varies greatly depending on the cooling rate. Lines representing the two-phase ferrite & austenite area, for example, converge as the cooling rate increases. The ferrite to austenite transformation reaction process is slowed as the cooling rate increases [90]. The ferrite content of DSS studied in the article [89] was observed to rise as cooling rates increased. It has also been discovered that a simple depiction, such as the Schaeffler diagram (Figure 27(b)), does not work for varying cooling rates [89].

a

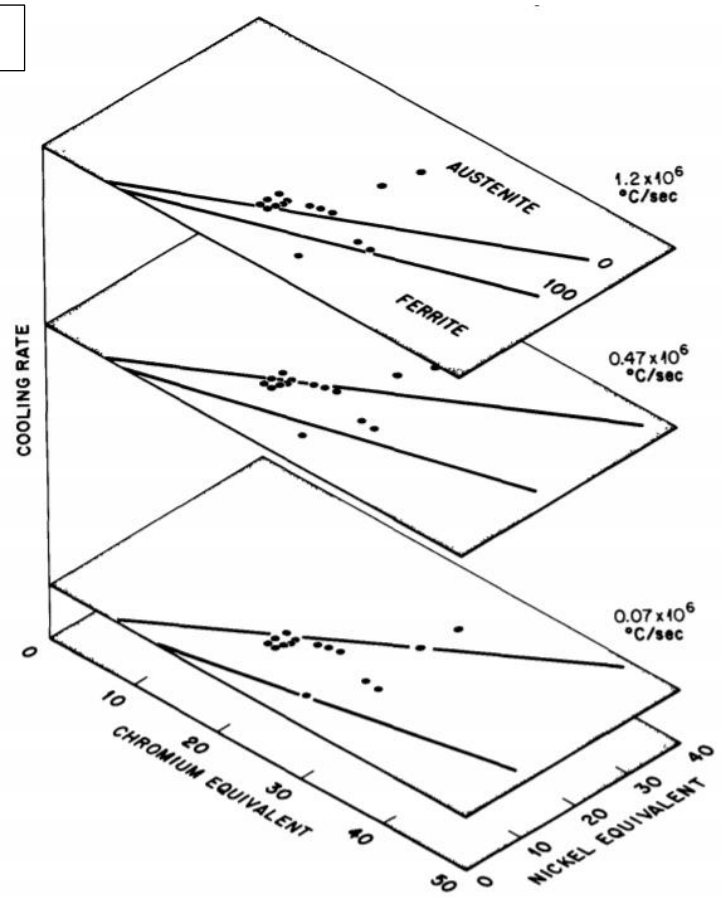

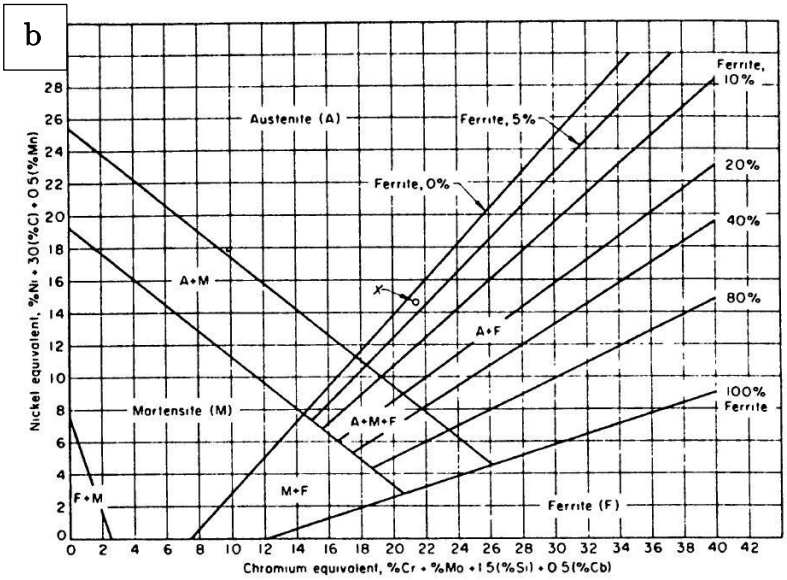

Figure 27: (a) Composite constitution diagram for DSS using cooling rate as a third dimension (b) A Schaeffler diagram [89]

2.7.6 Effect of heat treatment on Microstructure

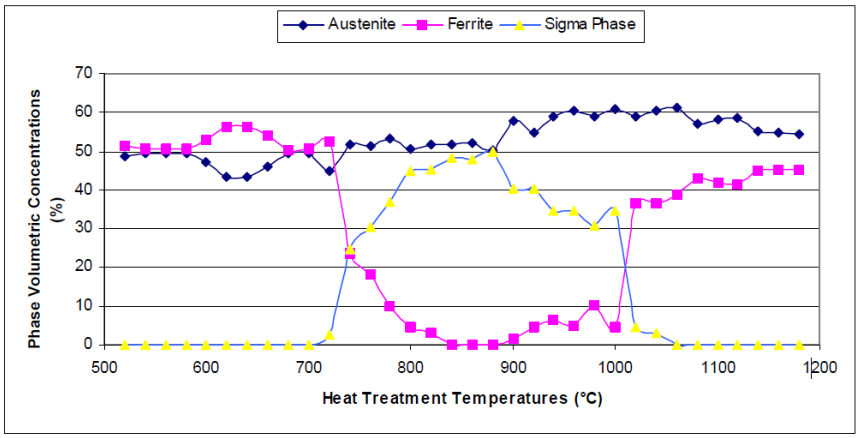

Figure 28: Concentration of phases versus H.T. temperature for ASTM A890 Gr6A Super Duplex Stainless Steel [91]

As can be seen from figure 28 (results of water quenched heat treatment), the sigma phase starts to precipitate at 720°C, and its concentration increases sharply to 880°C when it exceeds around 50% in volume. At temperatures above 1060°C, the sigma process steadily vanishes from the microstructure of the material. The curve showing the difference of ferrite volumetric concentration shows an opposite behavior indicating the sigma phase concentration. An increasing sigma phase concentration allows the ferrite concentration to decrease when the intermetallic phase forming elements (Cr and Mo) are removed from the ferrite, where they are more soluble. Thus, the eutectoid reaction: $\delta \rightleftharpoons \sigma + \gamma_2$ is unbalanced toward the right [91].

2.8 Mechanical Properties

Super duplex stainless steels have 2-3 times more yield strength than standard stainless steels, ferritic and austenitic steels. It has significantly higher tensile strength than traditional stainless steel such as 304L and 316L. Smaller grain size is usually produced in dual austenite-ferrite microstructures, which are not easily generated in single-phase steels, resulting in superior mechanical properties. Duplex steels were found to follow the Hall-Petch relationship [78]. The specific grade of material under study in this thesis is SDSS EN 1.4410. The allowable mechanical properties of SDSS EN 1.4410 (ASTM UNS S32750) are shown in Table 5.

Table 5: ASTM specifications on mechanical properties for SDSS EN 1.4507 [92]

Specification	Microhardness (HV)	Yield Strength (MPa)	Tensile Strength (MPa)	Elongation (%)
ASTM UNS S32750	≈ 270	≈ 550	≈ 800	≈ 25

2.8.1 Hardness Measurement

Hardness is the material's ability to withstand localized plastic deformation. Hardness tests may provide an impression of the low-cost and non-destructive deformation behavior of a material. Hardness measurement can be classified into three distinct methods: scratch hardness, indentation hardness, and rebound hardness [93]. Here, indentation hardness is of concern for this analysis.

Indentation hardness measurements are carried out by indenting the surface of the metal by applying force to the indenter over a given period, which creates an impression on the surface. The indentation geometry is determined, and the hardness value is derived from this in different ways. The hardness of the material is determined by the depth or size of the impression, with a softer material having a deeper impression than a harder material under the same test circumstances [65].

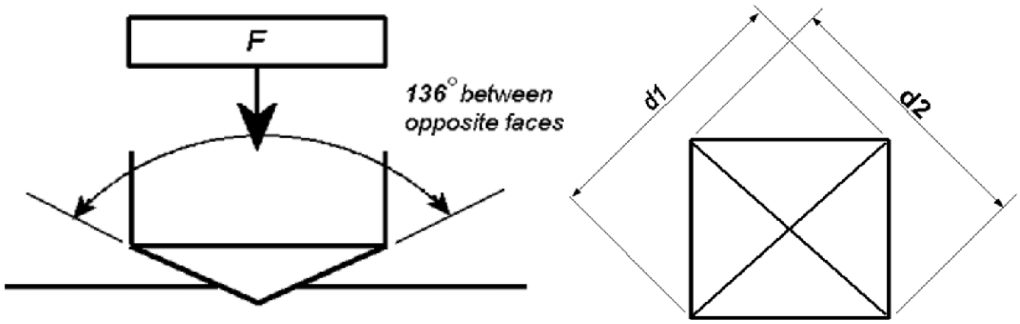

Figure 29: Schematic illustrates Vickers hardness test [94]

Vickers hardness measurement is a simple, feasible test that uses a small diamond pyramid. The diamond pyramid forms an angle of 136° between opposite side surfaces, as shown in figure 29. A known force is applied perpendicularly on the pyramid into the test material. Then the diagonals in the leading impression and Vickers hardness (HV) can be calculated via equation 5.

$$HV = 1.854 \frac{F}{d^2} \qquad [5]$$

Where F= load in kgf, d = mean value of d_1 and d_2 in mm.

2.8.2 Effect of heat treatment on hardness

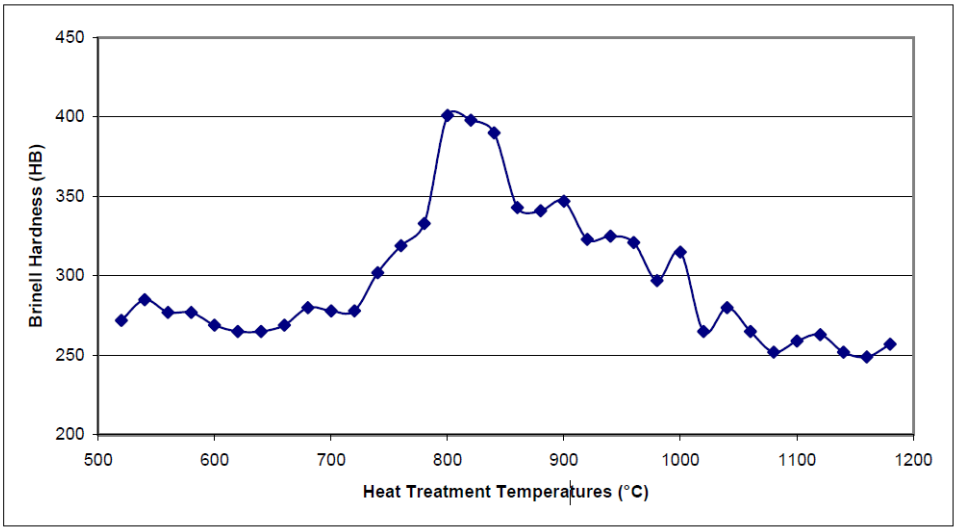

Figure 30: Material hardness as a function of heat treatment temperatures for ASTM A890 Gr6A Super Duplex Stainless Steel [91]

The hardness is closely related to the volume fraction of δ-ferrite and austenite in duplex stainless steel. Figure 30 shows that the steel hardness continues to increase successfully from 720°C to a peak in the order of 400 Brinell at 840°C and then declines as the temperature increases. In the temperature range 720-840°C, the volume of the sigma phase increases (i.e., δ-ferrite content decreases), which increases the hardness of the material in a parabolic pattern (Figure 31). This intermetallic precipitate is hard, resulting in a huge increase in hardness from a macroscopic perspective. In the temperature range 1060-1300°C, the microstructure is ferritic-austenitic and almost free from other precipitation. The hardness was found to decrease with increasing heat treatment temperature. This is due to an increase in the volume percentage of δ-ferrite, which is the harder of the two phases. [91].

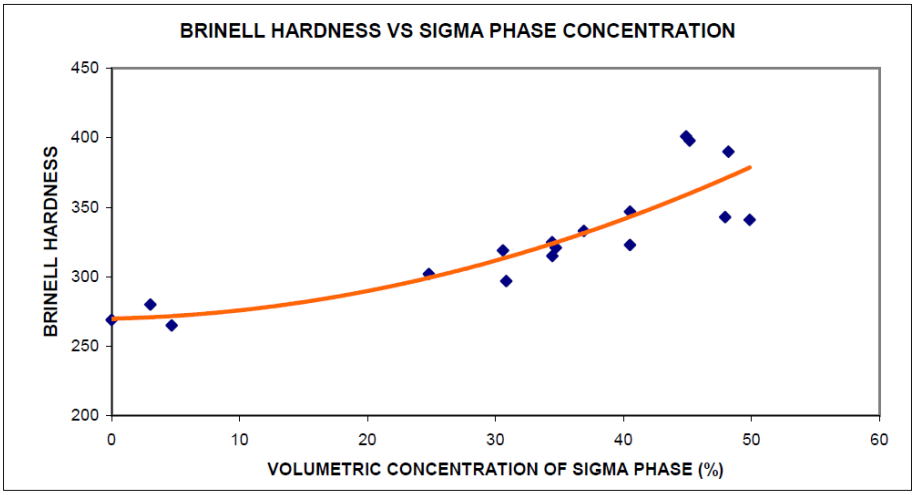

Figure 31: Correlation between Brinell hardness and sigma phase volume for ASTM A890 Gr6A Super Duplex Stainless Steel [91]

While comparing as-built and heat-treated materials above 950°C, as-built materials have the highest microhardness, as shown in Table 6. After various heat treatments (above 950°C), the microhardness is decreased, with a larger reduction at higher annealing temperatures and longer holding time [64].

Table 6: Microhardness (HV1) and its standard deviation of the SLM duplex stainless steel grade 2205 for different annealing treatments [64]

Sample	As-Built	Annealed 950/5	Annealed 1000/5	Annealed 1050/5	Annealed 1100/5	Annealed 1000/60	Annealed 1050/60
Hardness (HV1)	336.6±6.4	279.9 ± 10.3	279.8 ± 11.2	270.5 ± 8.8	255.2 ± 4.2	262.6 ± 9.6	265.0 ± 8.5

2.8.3 Effect of grain orientation on the hardness

The results demonstrate that specific grain orientation patterns may be identified in the as-built and annealed state related to the processing conditions (Figure 32). Ferrite and austenite grains align in certain orientations, implying that layerwise building and the +45°/-45° scan approach impact the position of ferrite grain boundaries. This influences the nucleation and development of austenite after heat treatment. According to general ideas of heterogeneous nucleation, the austenite would prefer to nucleate and grow near the grain boundaries. The impacts of layering and grain elongation along the build direction are most visible when evaluated parallel to the build direction (Figure 32(a)(c)), whereas the impacts of the scan strategy are most visible when evaluated perpendicular to the build direction (Figure 32(b)(d)). The fact that the microstructure remains after the heat treatment demonstrates that austenite crystallizes at grain boundaries [95].

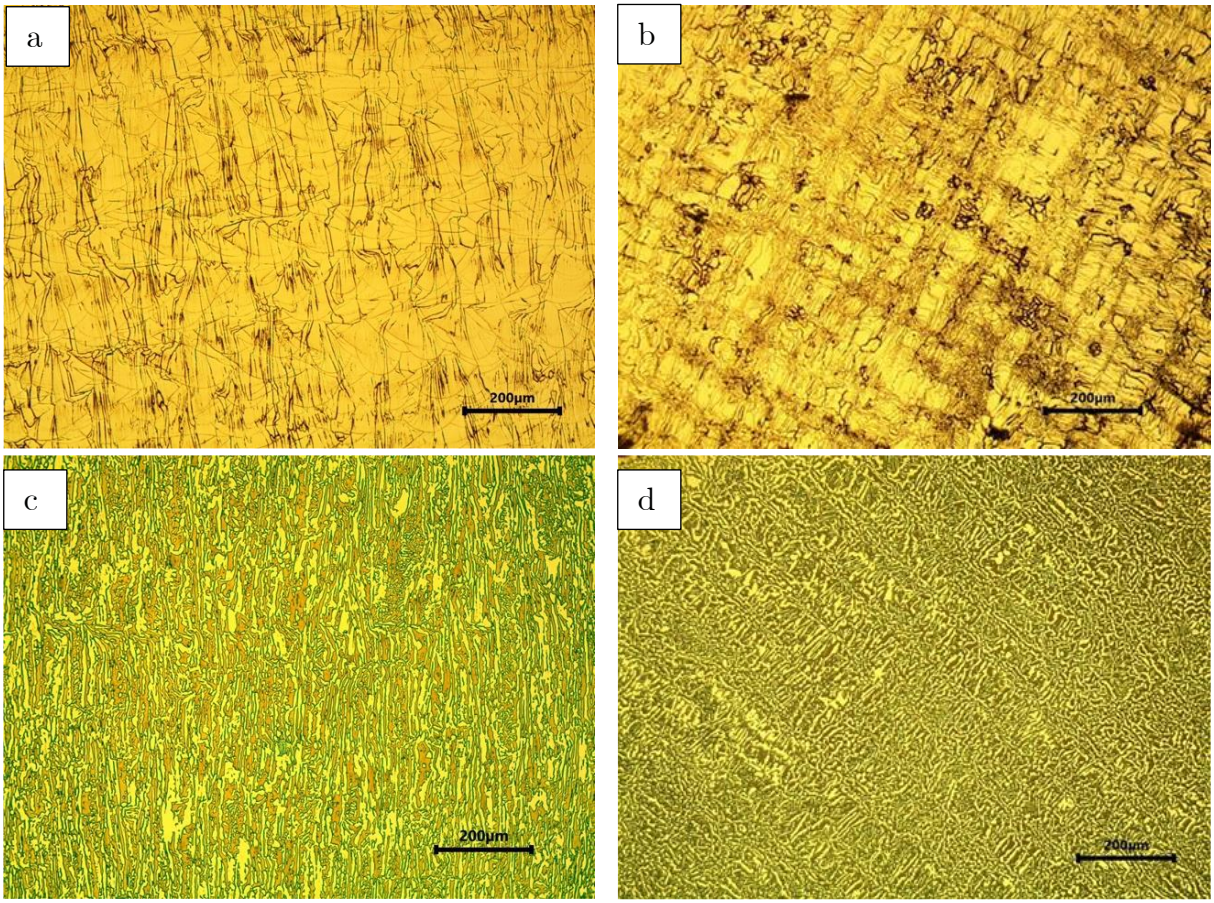

Figure 32: DSS SAF 2205 processed by SLM of (a) as-built parallel to build direction, (b) as-built perpendicular to build direction, (c) heat-treated parallel to build direction, and (d) heat-treated perpendicular to build direction [95]

When grains are studied parallel to the build direction, it is obvious that a considerable percentage of them are elongated along the build direction, as seen in Figure 32. The grain size measurements back this up. As-built grains measured 32.7±4.3 µm and 18.8±3.4 µm in length and width, respectively. The annealed grains measured 12.7±4.7 µm and 5.4±0.8 µm in length and width, respectively. On the other hand, figures 32(b) and (d) demonstrate the effect of the +45°/-45° scan method on grain orientation. The grain size measurements also revealed that the heat treatment resulted in a net decrease in grain size. This is most likely a consequence of transitioning from a single-phase to a dual-phase material. The observed grain sizes from the perpendicular cross sections confirm this theory even more. The width and length of the as-built grains were measured to be 15.1±4.3 µm and 15.1±8.0 µm, respectively. The width and length of the annealed grains were measured to be 5.1±0.3 µm and 5.0±0.5 µm, respectively [95].

Anisotropic properties are well recognized in SLM manufactured components. As illustrated in Table 7, the as-built components printed in this investigation showed a difference of +60 HV when inspected parallel and perpendicular to the build direction. The explanation is most likely the grain orientation, which reveals elongation along the

build direction. After the heat treatment, the microhardness anisotropy vanishes. The grains continue to elongate in the build direction. The anisotropy in the as-built samples is probably caused by layering defects rather than grain orientation [95].

Table 7: Hardness measurement for DSS SAF 2205 processed by SLM [95]

Sample	Microhardness (HV) Parallel to build direction	Microhardness (HV) perpendicular to build direction
As-built	362.74±14	419±7
Heat-treated	265±4	258±8

2.8.4 Pitting Corrosion of SDSS

Pitting is a form of corrosive localized attack that creates pits. Metals with passive films are more resistant to corrosion of this kind. It is characteristic that these pits only develop on small areas while not affecting the bulk of the surface, which means that the weight loss caused by this type of corrosion is minimal. However, the consequence of the attack may cause significant failures [96].

Pitting is thought to begin when the pitting potential approaches a critical value (Ep), which varies depending on the chemical composition of the alloy and the atmosphere (temperature and chloride concentration). Potentiodynamic anodic polarization tests are frequently used to measure Ep (figure 33). The initiation of pitting degradation is detected as an inevitable rise in current density in these measurements. The greater the Ep value, the more excellent the resistance of the alloy against pitting corrosion in the given environment. [97].

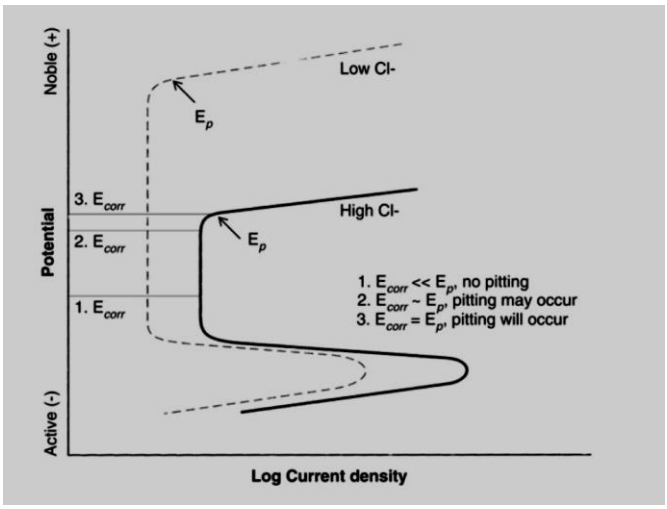

Figure 33: Schematic illustration of a polarization curve, determining the pitting corrosion risk [97]

- **Mechanism of pitting Corrosion**

Pitting corrosion occurs as a consequence of the breakdown of the passive layer. Metal is dissolved as an anode, while the remaining surface acts as a cathode where oxygen is formed into hydroxyl groups. The accumulation of positive metal ions in the pit will provoke a self-stimulating and self-propagating effect called hydrolysis. As seen in Figure 34, the presence of Cl^- and H^+ ions will prevent the metal from re-passivating, and the pH in the pit will become very low. When the pitting process is in progress, the metal is perforated, and the reaction is stopped. The presence of Cr and Mo in an SDSS will increase the pitting resistance, and the PRE number is used to categorize the pitting resistance of super duplex stainless steel [98].

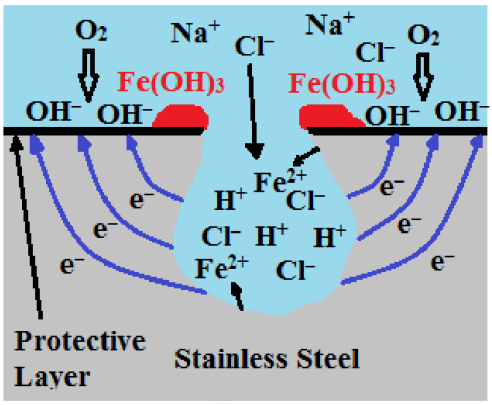

Figure 34: Mechanism of Pitting Corrosion [99]

The pitting process begins with metal dissolution. When metal is found in the environment that is an electrolyte and contains chlorine ion and molecules of oxygen, the following reaction happens [100, 101]:

Reaction for metal dissolution on the bottom of the pit (anodic reaction),

$$M \rightarrow Mn^{+} + ne^{-} \qquad [6]$$

is balanced by the reaction on the nearby surface:

$$O_2 + 2H_2O + 4e^{-} \rightarrow 4OH^{-} \qquad [7]$$

As the result of these reactions, there is an increase in the concentration of Mn^{+} inside the pits, and for neutrality, the chloride ions migrate into the pit. That is how metal chloride ($M^{+}Cl^{-}$) is formed. Further, metal chloride is hydrolyzed by water:

$$M^{+}Cl^{-} + H_2O \rightarrow MOH + H^{+}Cl^{-} \qquad [8]$$

From this equation, the product of this reaction is free acid that lowers the pH values in the pit. In the hole, pH values are around 1.5 to 1.0, while pH values are neutral in the bulk solution.

Metal hydroxide that is formed is also not stable, and it reacts with oxygen and water to form the final corrosion product:

$$2M(OH)_2 + \tfrac{1}{2}\, O_2 + H_2O \rightarrow 2M(OH)_3 \qquad [9]$$

The initiation of pitting in duplex stainless steels may occur at the high sulfur content grain boundary, oxide/sulfide inclusions, or in Cr-depleted regions nearby at high precipitate Cr phases such as σ phase or α´ [7]. These phases of precipitation are avoided by sufficient heat treatment. Duplex stainless steels have outstanding resistance to localized forms of corrosion [102].

2.9 Microscopy

2.9.1 Optical Microscopy

The optical microscope, also known as the ¨light optical microscope¨, is a microscope that magnifies small sample images using visible light and a lens set. It is an inexpensive method to study the macrostructure of a material. Optical microscopes are the simple and oldest kind of microscope, yet many complicated designs strive to increase resolution and sample contrast. Historically, optical microscopes were simple to create and common because they utilize visible light, allowing samples to be seen directly through the naked eye.

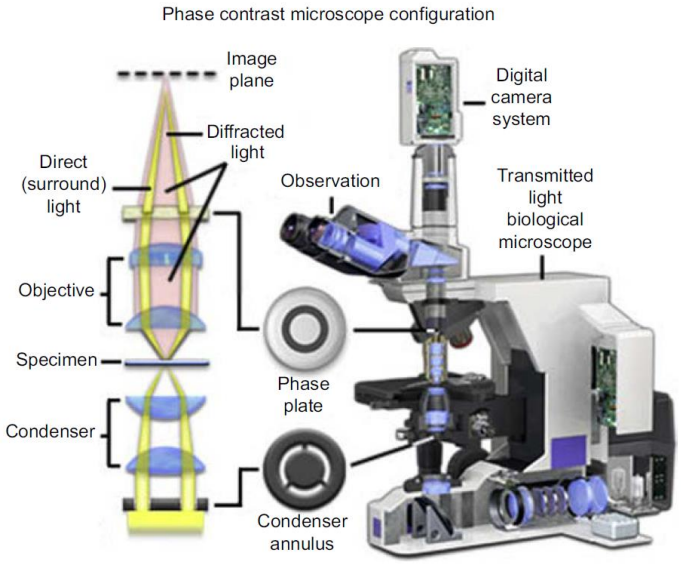

Figure 35: Light Microscope [103]

A micrograph can be created by capturing an image from an optical microscope using normal light-sensitive cameras. Images were initially taken on photographic film, but improvements in complementary metal-oxide-semiconductor (CMOS) and charge-coupled device (CCD) cameras have enabled digital image recording (figure 35). Purely digital microscopes are now available, which employ a CCD camera to observe a sample and show the resulting image immediately on a computer screen without the necessity of eyepieces [103].

2.9.2 Scanning Electron Microscopy (SEM)

A scanning electron microscope is an electron microscope that creates pictures by scanning a material with a focused beam of electrons. Electrons interact with atoms in the sample, creating a range of visible signals that carry information about the sample's surface topography and composition. In general, the electron beam is scanned in a raster scan pattern, and the direction of the beam is coupled with the detected signal to create an image. SEM has a resolution of about 1-10 nm [103].

SEM generates images by scanning the surface with a focused beam of high-energy electrons that interact with atoms on the surface of the samples. An electron gun, condenser and objective lenses, objective aperture, scanning coils, sample stage, control system, and pumping system are required for a typical SEM. The electron gun is mounted on top of a microscope chamber. Electrons are accelerated to energies ranging from 1-30 keV. The electron beam is then de-magnified by passing through the condenser and objective lenses before hitting the sample. The electron beam is detected by scanning coils, which scan the specimen in X and Y directions, resulting in surface imaging produced by various electron detectors, as illustrated in Figure 36 [103].

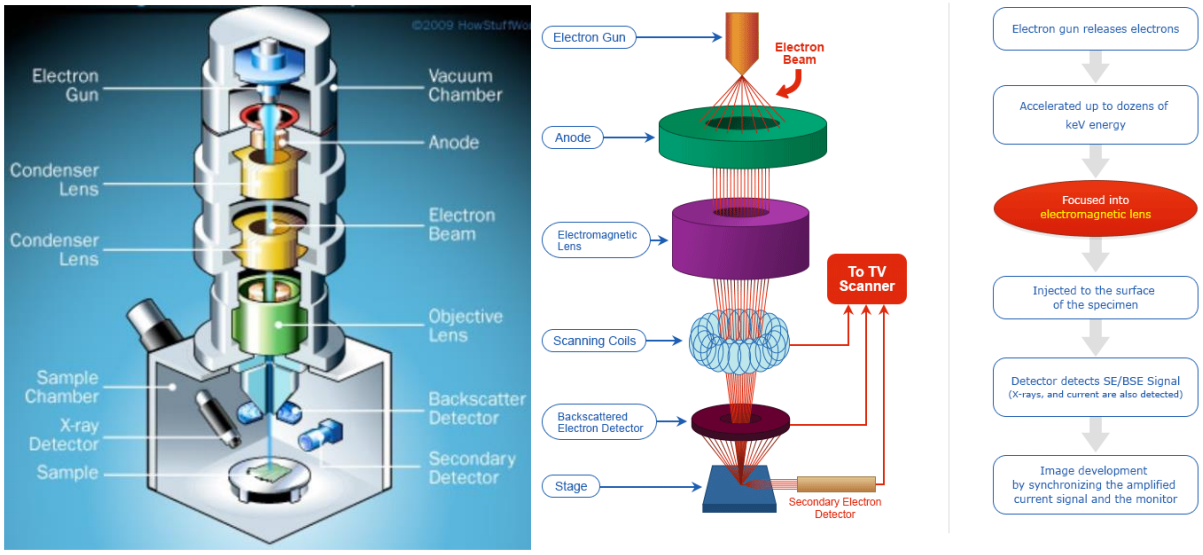

Figure 36: Schematic illustration of SEM [103, 104]

As the incident beam interacts with the specimen, various detectors are used to capture the reflected electrons. These detectors are mounted in a solid angle range where various signals can be accepted and obtained. The detectors can be effective by allowing a greater percentage of the signal to be detected. Secondary electrons (3eV - 5eV) and backscattered beam electrons are the electrons collected by the detectors [105].

As the incident beam strikes the surface and penetrates the specimen, electrons are absorbed and uniformly dispersed in a balloon-shaped volume known as the interaction volume (Figure 37(b)). When the beam energy increases, so does the interaction volume. Different portions of the interaction volume emit SE, BSE, and X-ray signals (Figure 37(b)). The signals that reflect & make it to the surface are detected, while the others stay inside or are lost [105].

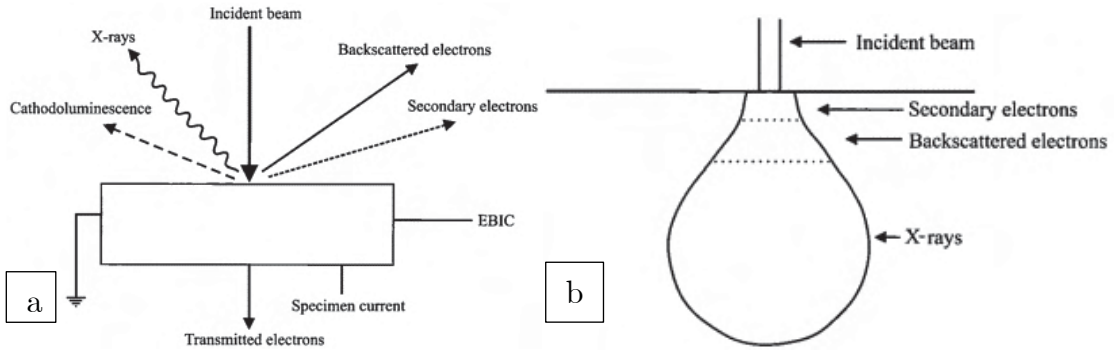

Figure 37: (a) Different Signal generated from sample surface (b) Interaction volume of the electron beam within the specimen [105]

- **Electron backscattered diffraction (EBSD)**

SEM is used in various modes based on secondary electron, backscattered electron, or diffracted backscattered electron signals. Secondary electrons are used to display images to detail a sample's morphology and topography, while backscattered electrons reveal contrast in various phases by calculating the atomic number in multiphase samples. Diffracted backscattered electrons are widely used to collect information on a solid crystalline sample's crystal structure and orientation [106]. EBSD detectors usually include a phosphor screen, a compact lens, and a couple-charged device camera. A polished and even-surfaced specimen should be placed into the SEM chamber and angled 70 degrees to the diffraction camera. This configuration increases the contrast in a diffraction pattern. The electrons collide with the surface of the specimen, interacting with the atomic lattice planes. Some of these interactions satisfy Bragg's Law and undergo backscatter diffraction, resulting in diffraction patterns. Miller indices can then be used to identify the diffraction patterns separately [105].

- **Energy-dispersive X-ray spectroscopy (EDS)**

The elemental analysis of a sample is performed using EDS. As an electron from the emission gun inelastically interacts with an electron in the specimen, the secondary electron is forced out of its position. An electron from an outer shell will move to a lower energy state and emit an X-ray with a characteristic wavelength. These X-rays are converted to voltage signals, which can then be used to generate an EDS spectrum. Since the energies and wavelengths of different elements vary, a chemical analysis may be done by measuring them [105].

2.9.3 Transmission Electron Microscopy (TEM)

Transmission electron microscopy is a technique in which a beam of electrons is transmitted through a sample to generate an image. An electron beam transmits information about the composition of a sample via an ultra-thin specimen. An electron

gun, a condenser, an objective, projector lenses, apertures, a fluorescent screen, a pump system, a monitor, and a control system are common components of a TEM (Figure 38(a)). The electron gun consists of a filament (usually V-shaped and made of LaB_6), a Wehnelt cylinder, and an anode mounted on the microscope column's top [107].

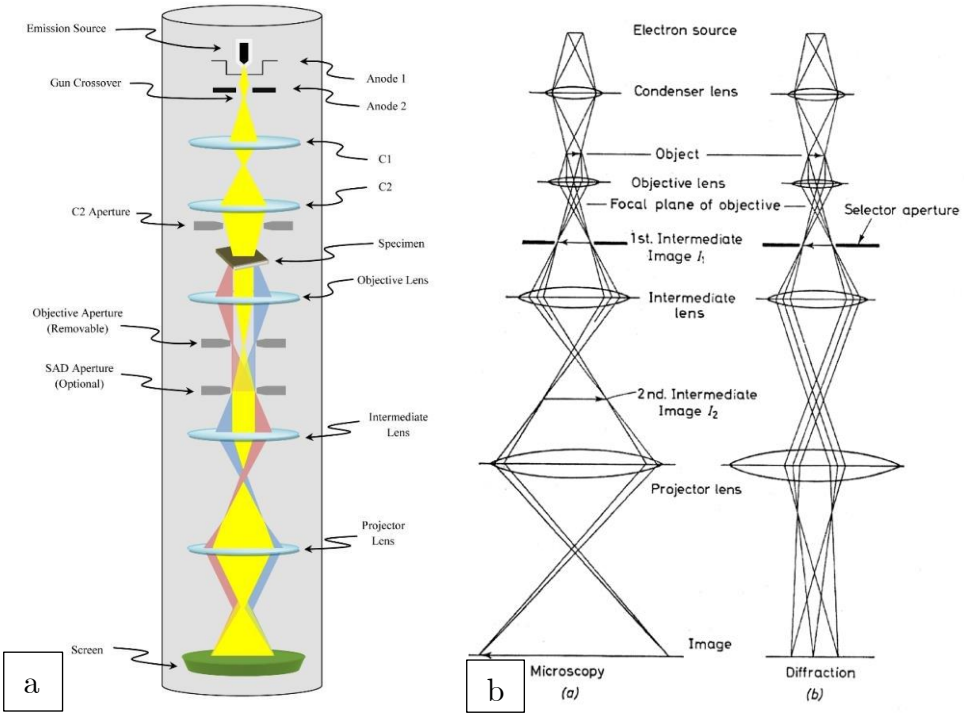

Figure 38:(a) Components and structure of TEM (b) Beam path in Imaging mode and Diffraction mode [106, 108]

When a high voltage is applied to the filament, electrons are emitted and accelerated toward the anode. The electrons then travel further through the hole in the anode to the condenser lenses, which enable the image's area and intensity to be controlled. A condenser aperture is located between the condenser lenses and is responsible for the convergence angle. It is worth noting that the size of the condenser aperture affects the image's quality and intensity. A specimen chamber can be found further down. The special TEM holder inserts the TEM specimen (3mm in diameter) between the pole pieces of the objective lenses. The latter is primarily used to generate first intermediate or diffraction images. The intermediate lenses will switch between two modes: image and diffraction (Figure 38(b)). They are focused on the image plane in the image mode and on the back focal plane in the diffraction mode. The objective aperture is located between the objective and intermediate lenses, allowing for image contrast control (to be inserted in the image mode). The projector lenses are the final group of lenses; they magnify the image (diffraction pattern) created by the objective lenses and visualize it on the fluorescent screen [106, 107, 109].

3. Experimental Details

Several experiments have been conducted to gather the requisite data for this thesis to examine and further understand the microstructural and mechanical properties of the SLM manufactured super duplex stainless steel. The experiments and research studies were carried out in the laboratories at the University of Stavanger. The data obtained were used for quantitative and qualitative analysis. The full description of the experimental methods used is explained in this section.

3.1 Manufacturing of Specimen

The sample material used in this study is SLM manufactured with SDSS alloy. The SLM-made sample used in theses thesis is super duplex stainless steel of European grade EN 1.4410 (AISI SAF 2507). The design of the sample is shown in figure 39 (Photo credit: Mechatronics Innovation Lab AS). It is produced with the SLM 280 2.0 machine from SLM Solutions. Mechatronics Innovation Lab A/S provided the sample material.

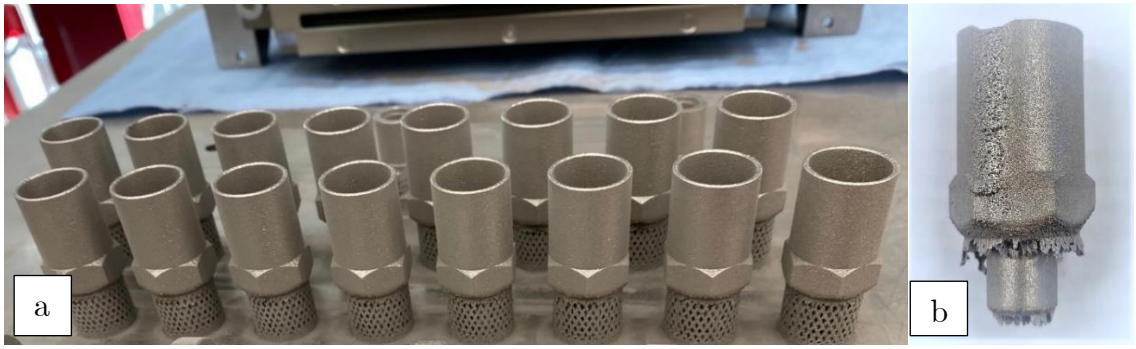

Figure 39: SLM Printed SDSS Sample (a) with support (b) after removing support

The production parameters of the SLM printed sample used in this thesis are given in Table 8. The scanning strategy used in this sample printing is stripe scanning with each layer rotation of 67°, as shown in Figure 40.

Table 8: Process parameters for the SLM 280 machine from SLM Solutions

Production Parameter	Laser Power	Scanning Speed	Hatch Distance	Layer Thickness	Laser Spot Size	Shielding Gas
Value	250 Watt	950 mm/s	0.1 mm	0.05 mm	0.08 mm	Argon

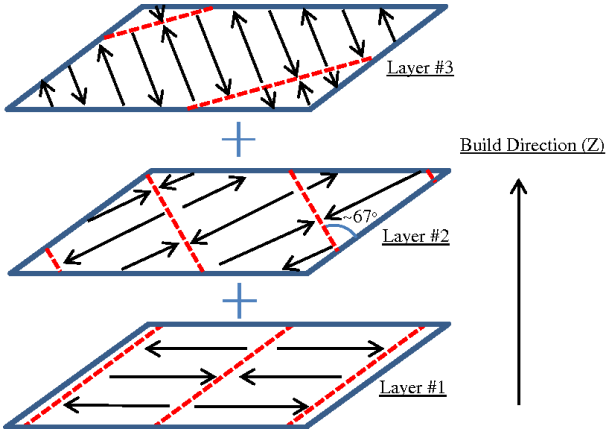

Figure 40: Stripe scanning strategy with 67° layer rotation [110]

3.2 Specimen Characterization

Before grinding and polishing, the printed samples were cut into two pieces (see Fig. 41b) with an abrasive cutting machine, Struers Disctom-10, using diamond-rimmed wheels. These pieces were again further sliced for grinding and polishing using Struers Accutom-2. The samples were labeled on the specimen they were cut from, represented in figure 41(c). The pink shaded face in figure 41(c) illustrates the face used for grinding, polishing, and observation. The sample is supposed to be divided into five sections. The sample consists of a hollow part and a solid part. The as-printed part will be represented as ¨AP¨, heat-treated sample as ¨HT¨. The XY-plane of sample is termed as surface perpendicular to build direction, and YZ-plane of sample is termed as surface parallel to build direction.

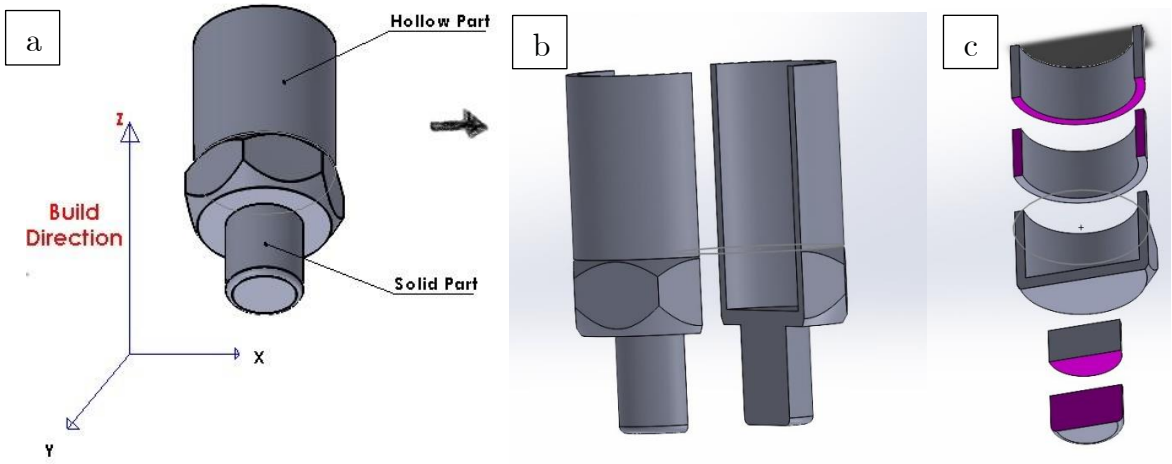

Figure 41: An illustration of how the specimens were divided into section (a) Single Specimen (b) Splitted into 2 section (c) splitted into 5 sub-section.

As seen in figure 41(c), the pink surface of the split sample is also used for hardness measurement and Optical Microscopy study. The pink-colored face of the solid part of the sample is only used to study in SEM and TEM. One section of the hollow part of the sample is used for the pitting corrosion test.

3.3 Heat Treatment

A High-temperature furnace Nabertherm HTCT, 01-14 with a P310 controller, was used for heat treatment of the specimens for different time intervals. The heat treatment is done at a higher temperature so that all the precipitates get dissolved. Samples were inserted in a preheated furnace leading to a small drop in temperature at insertion. Therefore, the timing was delayed until the furnace had reached the desired temperature, approximately 4 min after sample insertion.

If the cooling rate is rapid, relatively little ferrite may transform to austenite at ambient temperature, leading to an excessive ferrite phase. As a result, the cooling rate of duplex steel must be slow enough to enable roughly 50% of the ferrite to be transformed to austenite while yet being rapid enough to prevent the production of intermetallic phases. So, two different cooling methods, i.e., water quenching and air cooling, are used to analyze the difference between their microstructure and phase content. The heat treatment temperature, time, and cooling methods are used as per Table 9. The heat-treated samples are shown in Figure 42.

Table 9: Heat treatment temperature, time duration and cooling method details

Temperature	Time Duration	Cooling Method
1000ºC	60 minutes	Water Quenching
1000ºC	60 minutes	Air Cooling
1100ºC	60 minutes	Water Quenching
1100ºC	60 minutes	Air Cooling
1200ºC	60 minutes	Water Quenching
1200ºC	60 minutes	Air Cooling
1300ºC	60 minutes	Water Quenching
1300ºC	60 minutes	Air Cooling

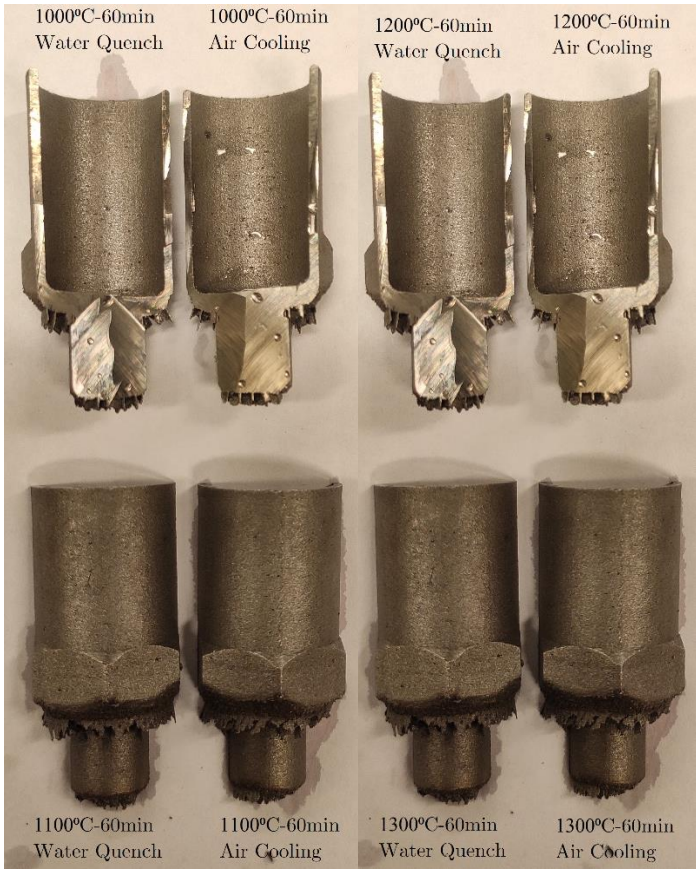

Figure 42: Heat-treated Samples

3.4 Sample Preparation

The samples are prepared in the following steps to analyze the material's micro-structure under the Optical microscope and electron microscopes.

3.4.1 Cutting Process

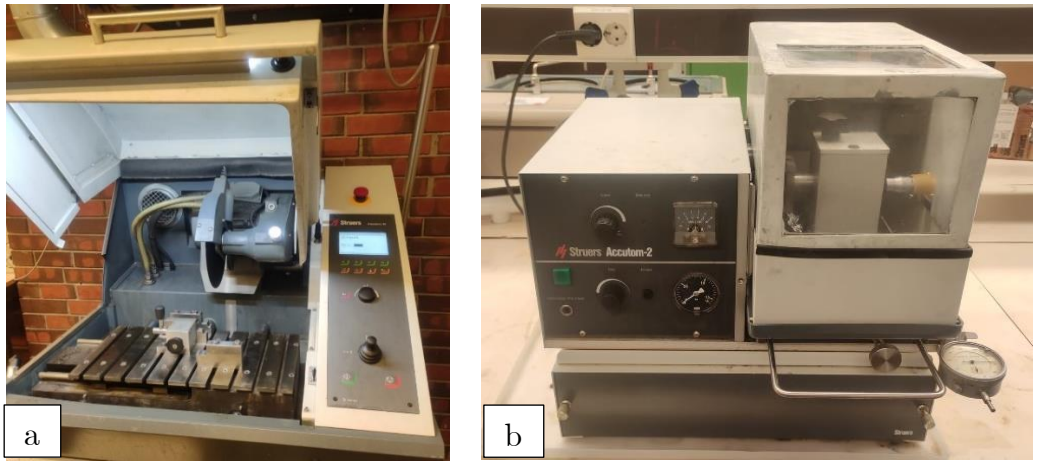

Figure 43: (a) Struers Discotom-10 (b) Struers Accutom-2

The material was initially cut into two parts using Struers Discotom-10, as shown in figure 43(a). In a way like this, this was done that one part became approximately hollow cylinder, while the second part was mainly a solid cylinder with support structure as shown in figure 44(b). Struers Discotom-10 has a quick process with a 2mm thick cut-off wheel and can cut large sections. Struers Accutom-2 [Figure 43(b)] is a slow process that uses a 1 mm thick cut-off wheel to cut thin specimens with minimum material waste. Struers Accutom-2 was used to prepare OM, SEM, TEM, hardness test, and pitting corrosion test specimens, as shown in Figure 44(c).

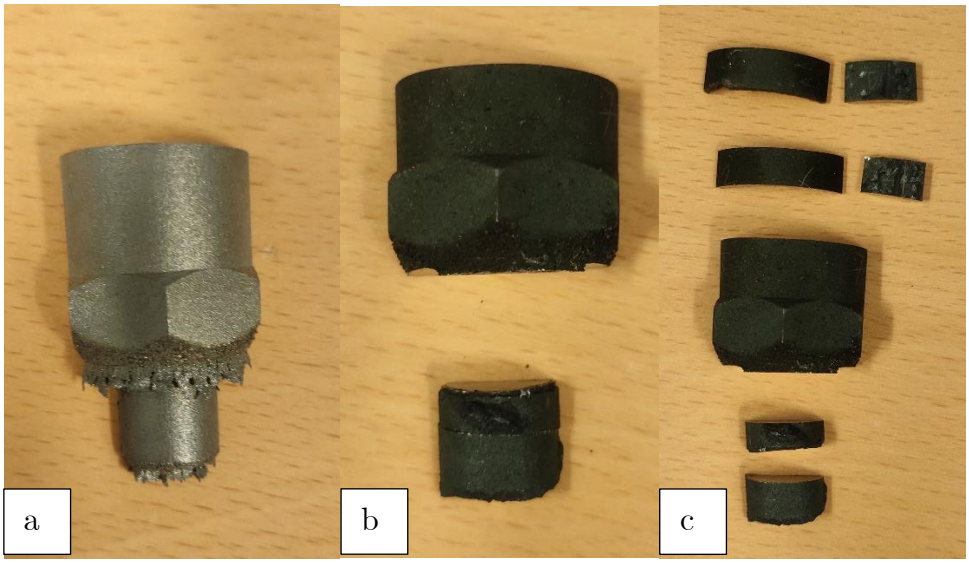

Figure 44: (a) EN 1.4410 Sample (b) Specimen cut by Discotom-10 (c) Specimen cut by Accutom-2

3.4.2 Hot Mounting

Figure 45: (a) Struers Citopress-30 (b) Hot mounted sample

After cutting the specimen, the hot mounting process is used to make it easier to handle the specimens when conducting metallurgical procedures, including grinding, polishing, OM analysis, SEM analysis, and hardness analysis. Struers CitoPress-30 was used to cast the test discs with condofact, a synthetic resin that is cast quickly and is suitable for electrolytic etching because it is electrically conductive. The amount of resin used for sample preparation for Optical microscopy and SEM is explained in Table 10. Struers Citopress-30 and hot mounted samples are shown in Figures 45(a) and (b), respectively.

Table 10: Amount of mounting resin used

Hot mounting for OM Sample		Hot mounting for SEM Sample	
Mounting Resin	**Volume (ml)**	**Mounting Resin**	**Volume (ml)**
Clarofast	6	Clarofast	5
Condofast	9	Polyfast	10
Total	15	Total	15

3.4.3 Grinding and Polishing

Grinding and polishing is a process performed to obtain a clear, scratch-free, and reflecting surface of the specimen for microscopic examination. Struers Tegraforce-35 with a dispenser of the Struers Tegradoser-5 machine was used for grinding and polishing purposes, as in Figure 46(a). Samples were grinded with MD-Piano of grits sizes P220, P600, and P1200. Then the specimen was polished using polishing clothes with 9 µm, 3 µm, and 1 µm diamond suspension as described in Table 11. After each grinding & polishing step, the specimens were cleaned properly with the Struers Lavamin machine (Figure 46(b)) and distilled water to remove impurities that could contaminant the sample surface. Struers Tegraforce-35 machine was also quickly cleaned with water and paper after each step to avoid dragging any traces from previous

steps. Finally, the samples were rinsed with ethanol and dried with a hot air dryer to remove water from the surface.

Table 11: Grinding and Polishing Procedure

Step	Surface/Abrasive	RPM	Load	Applied Time	Lubricant/Suspension
1.	MD-Piano 220	300	40 N	2 min	Water
2.	MD-Piano 600	300	40 N	2 min	Water
3.	MD-Piano 1200	300	40 N	2.5 min	Water
4.	MD-Allegro 9µm	300	30 N	3 min	DiaPro All/Lar
5.	MD-Dac 3µm	150	30 N	6 min	DiaPro Dac
6.	MD-Mol 1µm	150	15 N	8 min	DiaPro Nap-B

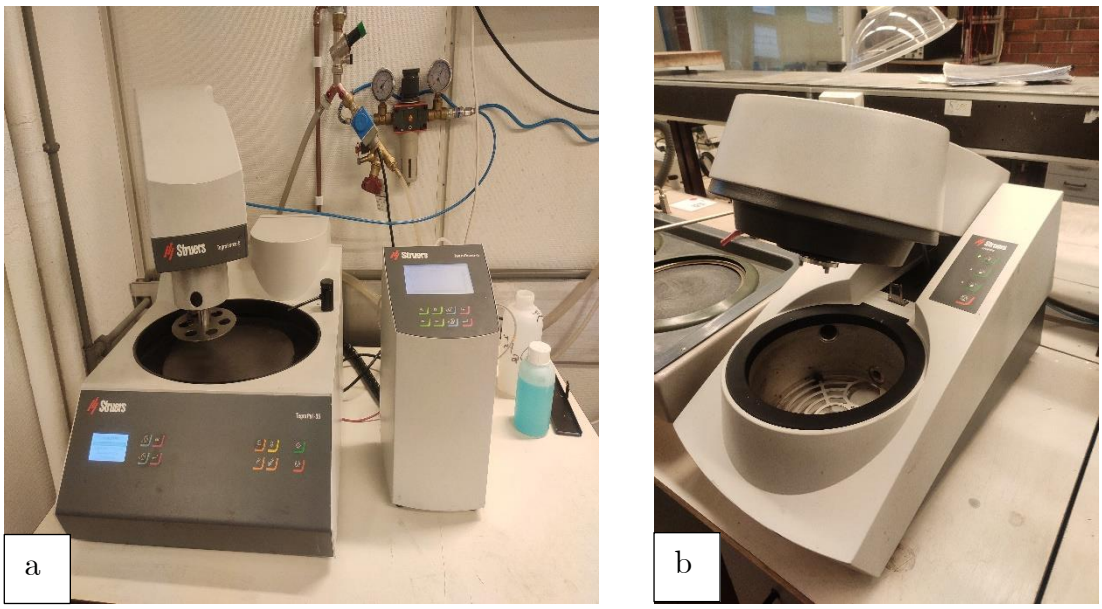

Figure 46: (a) Struers Tegraforce-35 with a dispenser Struers Tegradoser-5 machine (b) Struers Lavamin machine

3.4.4 Electrolytic polishing and Etching

The samples were electrolytically etched with Struers Lectropol-5 to bring out clearer images in the light microscope of phase variations, grain boundaries, precipitates, and other potentials details on the surface. The as-printed SDSS samples were electrolytically etched by 10% oxalic acid at 5.5 V for 30 seconds to observe melt pool & grain boundary. Similarly, it was etched with 20% NaOH at 5V for 10 seconds for phase analysis. The heat-treated specimens were electrolytically etched in two steps, as listed in Table 12. After the material had been subjected to etching, it was rinsed with water, cleaned with ethanol, and dried with hot air.

Oxalic acid effectively delineates intragranular chromium nitride precipitates by revealing a high density of small etching pits in the ferrite phase where nitride precipitates are present. The second step in the etching process provides a strong

contrast between the individual phases in the specimen, making subsequent microstructure study in a microscope easier.

Table 12: Parameters used in the electrolytic etching procedure for heat-treated sample [111]

	Etchant	Voltage	Time	Application
Step 1	10% oxalic acid	5 V	8 sec	Delineates microstructure.
Step 2	20% NaOH	2 V	6 sec	Colours ferrite and intermetallic

3.5 Sample Preparation for Optical Microscope

The sample was grinded, polished, and etched using the process explained in section 3.4. After the polishing and etching process, the material was examined in the light microscope OLYMPUS GX53 to get a general overview of the microstructure and phase distribution of the sample. The surface of the samples was examined at between 2.5 - 100 times magnification, and they were documented using the computer program Olympus Stream Essentials. Phase Analysis was also performed using the same computer program.

3.6 Sample preparation and experimental setup for SEM

Figure 47: SEM Zeiss SUPRA 35VP

The sample was prepared in the same way as for the optical microscopy, and there was no need to change etch from the optical light microscope for the SEM analysis of the first sample. But the second sample was final polished with 0.04 µm OP-S suspension instead of etching. Then both samples were cleaned in an ultrasonic bath before being studied in SEM. This is to get a clean surface for a more precise examination and analysis of the material and avoid contamination of the vacuum chamber in the microscope. The SEM machine of Zeiss SUPRA 35VP with Gemini optics was used for analysis, as shown in figure 47. The working distance used was between 10 - 12 mm, the accelerating voltage applied was 15-20kV, an aperture size of 60 µm for the QBSD

detector and 30 µm for the SE2 detector was used. The EDS analysis is carried out during SEM analysis and has no additional preparation than stated for the SEM.

Before performing the EBSD analysis, the specimens need new polish to remove the etch applied for the light and scanning microscope preparations. After new polish, the sample was finally ultra-polished with OPS colloidal silica. Then the sample was tightened on the inclined sample holder, and then aperture size of 300µm for the EBSD detector was used.

3.7 Sample preparation for TEM

The sample preparation for TEM is a time-consuming and complicated process. The transmission electron microscope JEOL-2100(LaB6 filament) running at 200 kV was used for analysis, as shown in figure 48. It was fully equipped with EDS, as well as annular bright and dark-field detectors.

At first, 1 mm thin specimen is cut using Accutom-2, then the specimen was mounted to a Plexiglas block, and it was grinded with different grit sizes of 120P, 220P, 500P, 1000P, and 2000P on both sides of the specimen. The grinding is continued till the thickness of the specimen is about 0.1-0.15 mm. Liquid nitrogen at a very low temperature is used to extract the very thin sample from the block and the tape, followed by a pure ethanol bath to clean and remove the adhesive residue. After that, the Gatan stamping tool was used to punch circular disks of diameter 3mm. Finally, the punched specimen was twin-jet electro polished with 10% perchloric acid, 20% glycerol, and 70% ethanol solution at temperatures ranging from -20 to -30°C and a 20V etching potential. The specimen is then immediately soaked in multiple ethanol baths to eliminate the electrolyte. The Jet polishing method creates a circle in the center of the sample with a nanometer thickness on the edge of the circle used for TEM analysis.

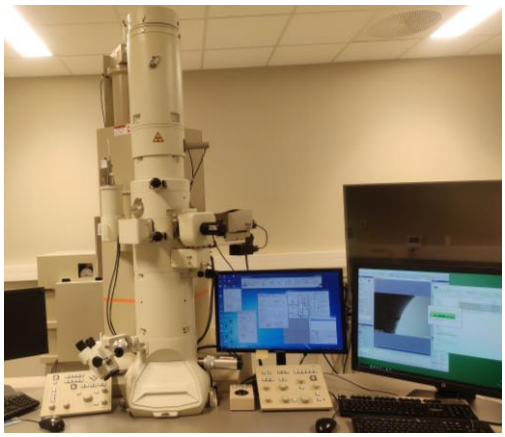

Figure 48: Transmission electron microscope JEOL-2100

3.8 Pitting Corrosion test

ASTM G48 Test states, "Standard Test Methods for Pitting and Crevice Corrosion Resistance of Stainless Steels and Related Alloys by Use of Ferric Chloride Solution." Method A is Ferric Chloride pitting test, and it is the one being used for the experiment [112].

3.8.1 Sample Preparation

The sample was cut by using Struers Accutom-2 machine. Then the sample was grinded and polished by SiC paper of grits P220, P320, and P500, as shown in Fig.49 (a). The sample was hollow semi-circular shape, so it was challenging to polish uniformly. The sharp edges of the sample were also rounded by grinding and polishing.

Then the dimension of the sample was measured, and the total exposed area was calculated. After that, the specimen was rinsed well with water, dipped in acetone, and air-dried. Then the sample was weighed to the nearest 0.0001g.

3.8.2 Preparation of Ferric Chloride Test Solution

The 100 g of reagent grade ferric chloride, $FeCl_3 \cdot 6H_2O$, was dissolved in 900 ml of Type IV reagent water (about 6 % $FeCl_3$ by mass). Filter through glass wool or filter paper to remove insoluble particles, if present [112].

3.8.3 Apparatus Required

The apparatus required for ASTM G48; Method A test is:

- Beaker
- Plastic Rod for Supporting Specimen
- Nylon Wire
- Temperature measurement device
- Plastic cover

3.8.4 Procedure

In 900 ml of distilled water, 100 g of Reagent grade ferric chloride $FeCl_3.6H_2O$ was dissolved (6% $FeCl_3$ by mass). For each specimen tested, the solution volume was ensured to be at least 5 ml/cm^2 of surface area. A new solution was prepared for each new test. Since the corrosion test was carried out at room temperature, there was no water bath required. The solution was poured into the beaker, and samples were tied with thin nylon wire and hung on plastic rods. After the solution reached the desired temperature of 22 ± 2 ° C, the samples were immersed in the solution [112].

After immersing the specimens in ferric chloride solution in beakers, plastic covers were used to cover the beakers to prevent evaporation of the test solution, as shown in Fig.49(d). It was left there for 72 hours.

After completing the test, the specimens were rinsed with water, and a nylon brush was used to remove corrosion products. After cleaning, they were dipped in acetone for 15 minutes and left for drying a room temperature for 24 hours.

Dried specimens were first visually inspected for pits; then, their weight loss was measured. In the end, a Microscope was used for better examination of the specimen surface [112]. The corrosion rate can be calculated using the formula as shown below.

$$\text{Corrosion rate} = \frac{Wt_i - Wt_f}{A} \qquad [10]$$

Wt_i and Wt_f are the weights of the sample measured before and after the test, respectively, and A is the exposed surface area.

Deviation from G48 Test

A glass cradle or hook was supposed to be used according to G48 Test, but nylon wire was used due to its unavailability. Since the specimen was too small, it was easy to tie the sample and hang it with nylon wire.

A test specimen 25 by 50 mm (1 by 2 in.) is recommended as a standard size. But my sample is a small hollow tube, so it was impossible to cut in standard size. All specimens in a test series should have the same dimensions when comparisons are to be made. I tried my best to make it of the same dimension, but there were still a few variations in size.

The water bath was supposed to be used for maintaining the constant temperature throughout the test. But the test was conducted at room temperature of $22 \pm 2^\circ$ C, so a water bath was not necessary.

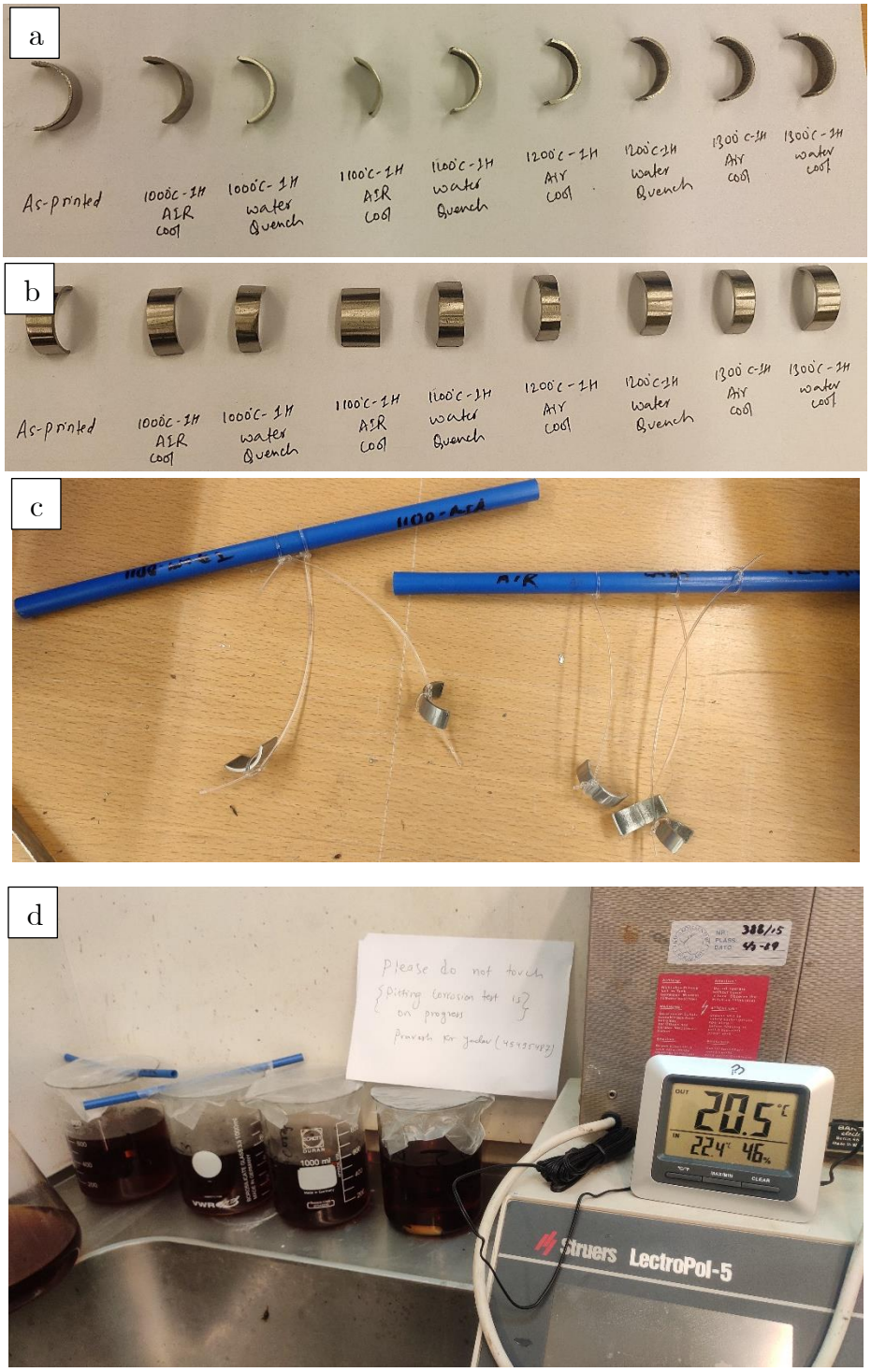

Figure 49: Pitting corrosion set up (a) Side view of Samples (b) Top view of samples (c) Samples tied with nylon wire (d) Samples Immersed in Ferric chloride solutions

3.9 Hardness Test

The hardness test is an excellent way to see how well a material can resist plastic deformation. Hardness measurements of the sample material were performed both before and after heat treatment to see how a change in the microstructure affected Vickers hardness. The samples were polished to a smooth finish to measure the indentation mark. The grinding and polishing procedure was the same as of optical microscope sample. Hardness tests were recorded using a Vickers Struers DuraScan test machine (Figure 50(a)) with a load of 5 kg, i.e., HV5 with a dwell time of 10 seconds. The indent centers were separated by 3 mm from the edge and 2-3 mm between them. Each specimen was measured at 9 to 10 different indentation points. Struers DuraScan has automatic focusing and hardness measurement (via measuring the diagonals of the impression), but this was set manually to obtain more precise measurements.

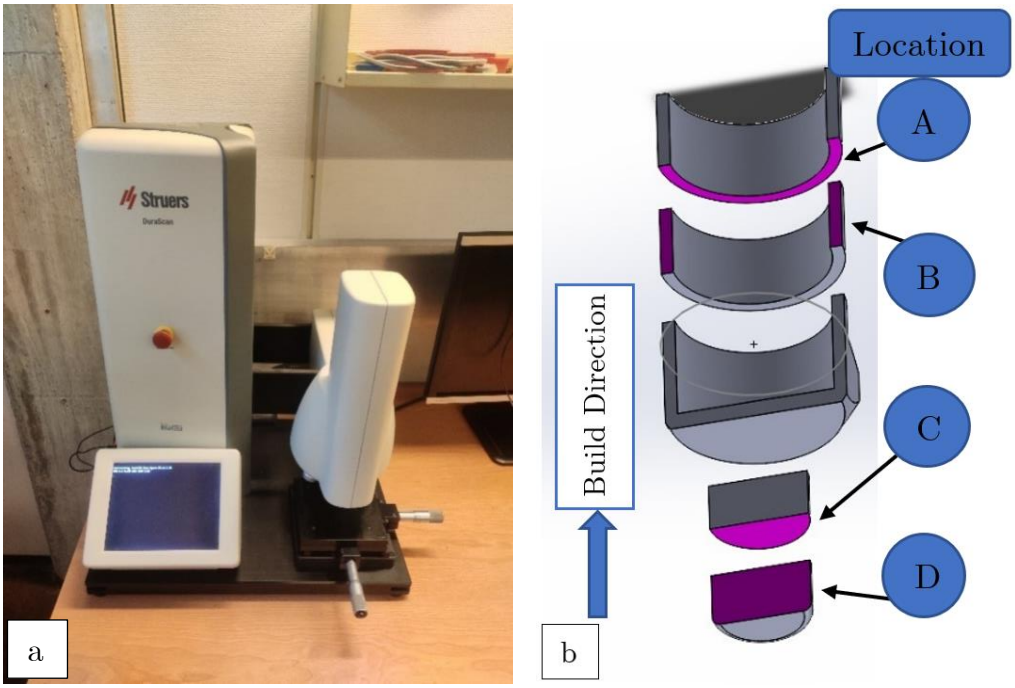

Figure 50: (a) Struers DuraScan (b) Pink Colored faces of Specimen where hardness test is done

The two-section from the hollow part (Location A and B) and two-section from the solid part (Location C and D) of a specimen are used for the hardness test, as shown in Figure 50(b).

Here, Location A is surface perpendicular to Build Direction in hollow Part.

Location B is surface parallel to Build Direction in hollow Part.

Location C is surface perpendicular to Build Direction in solid Part.

Location D is surface parallel to Build Direction in solid Part.

4. Results

This section presents the result of performed material tests into two categories, i.e., Microstructure and Mechanical Properties. Only the results that showed significant changes in mechanical and microstructural properties are presented and compared. Relevant images, graphs, and tables that were not included in this part are presented in the Appendix.

4.1 Optical Light Microscope

4.1.1 Macrostructure

4.1.1.1 As-Printed Specimen

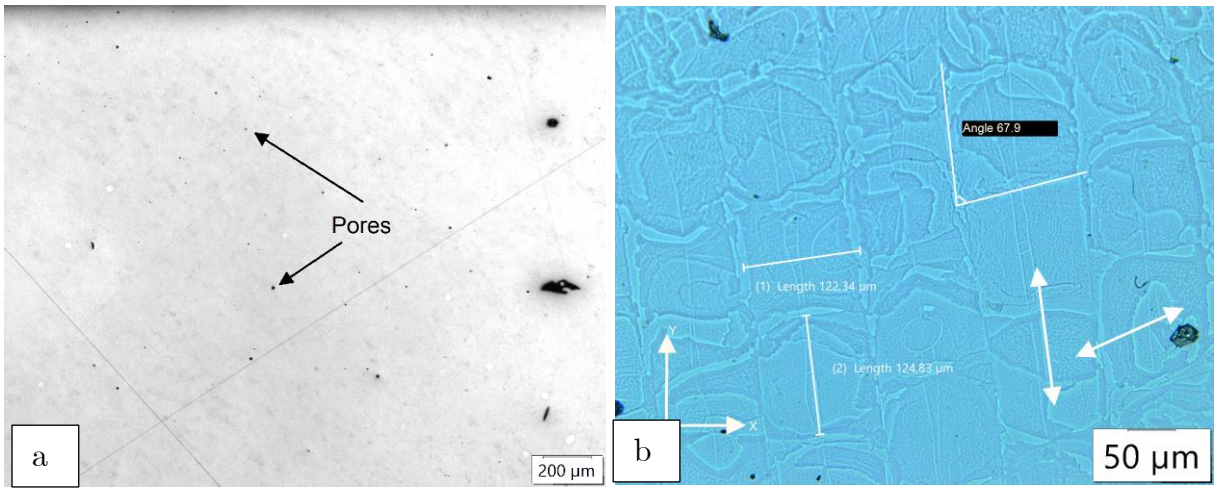

Figure 51: (a) As-printed Sample after Polishing (b) As-printed sample perpendicular to build direction (XY-plane) etched with OP-S

The As-printed sample after grinding and polishing was observed, then a lot of pores were seen in the sample, as shown in figure 51(a). After OP-S polishing, the XY-plane of a polished sample, grains and grain boundary was visible as in fig. 51(b). The grains are seen to be arranged in a unique mosaic structure (square-type). The length and width of grains were measured and found to be 126.08 ± 7.65 µm and 125.95 ± 7.82 µm, respectively. Two arrows in fig.51(b) are assumed as scanning direction and represent deposition and melted layer. Since two different layers can be observed, the polished surface is not parallel to the fabrication plane. The scanning strategy used in this sample printing is stripe scanning with each layer rotation of 67°. The angle between two different mosaic-type stripes is measured and found to be 67.9°, which matches the layer rotation angle.

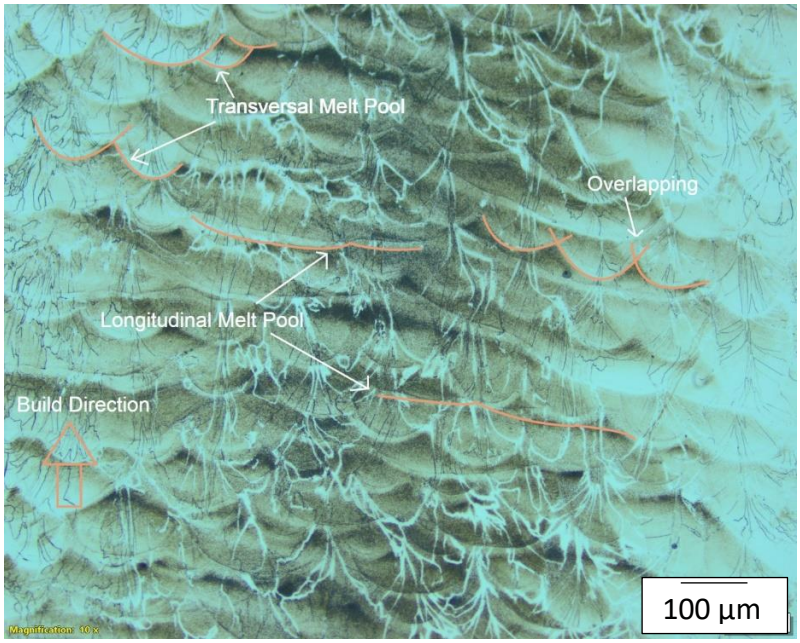

Figure 52 Melt Pool observed in as-printed parallel to build direction etched with 10% Oxalic Acid

When the sample's yz-plane was etched, the melt pool, grain boundaries, and solidification structures can be visible, as shown in figure 52. A melt pool is formed when the laser radiates on the surface of a powder bed. There are two types of melt pool observed, i.e., transversal and longitudinal melt pool. The small semi-circular and semi-elliptical shapes are observed as transversal melt pools, and large semi-elliptical shapes are termed longitudinal melt pools. A longitudinal melt pool is evidence of layer rotation. Large Melt pools are formed due to high laser energy density, which allows deeper penetration of laser. The hatch spacing determines the overlap rate between adjacent tracks. Certain areas were exposed to the second scan and melted twice to join neighboring tracks and produce a thick layer known as overlapping of the melt pool. The presence of overlapping melt pools implies a good fusion of metal powder with no holes. The build direction is from bottom to top in Figure 52.

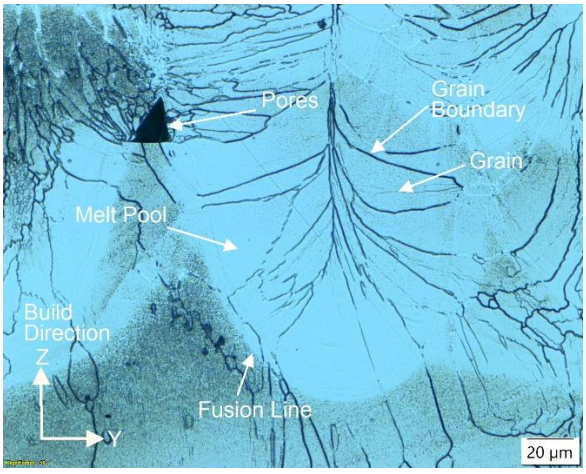

Figure 53: Magnified image of the melt pool

As shown in Figure 53, the fusion line is defined as the melt pool boundary formed during melting powder. This fusion line is dark-colored, which contains accumulated alloy elements. The melt pool depth was measured (see Appendix A), and it was found that it varies from about 50 µm to 132 µm, i.e., an average depth of 90 µm. The fusion penetration is found to be deeper than layer thickness. The average melt pool depth is about 90 µm, whereas the layer thickness is about 50 µm. This deviation in depth is due to high laser density and also because the sample was not cut exactly parallel yz-plane, which makes melt pool inclined and depth dimension increased.

The Grain boundaries are observed inside melt pools and across the fusion boundary, as in Figure 53. When the grain grows across the fusion boundary, it is the solidification growth of epitaxial columnar grains. These grains are considered anisotropic because they grow along the printing direction or heat flow direction. The as-printed sample consists of δ-ferrite and Austenite. The 20% NaOH etchant attacks δ-ferrite while austenite remains unattacked, as shown in Figure 54. So, δ-ferrite is tanned, which is dark blue, and austenite is light blue. The austenite is mainly formed at the grain boundaries, which is finer grain. But δ-ferrite has coarser grains morphology. The fine particles inside the ferrite grains are austenite.

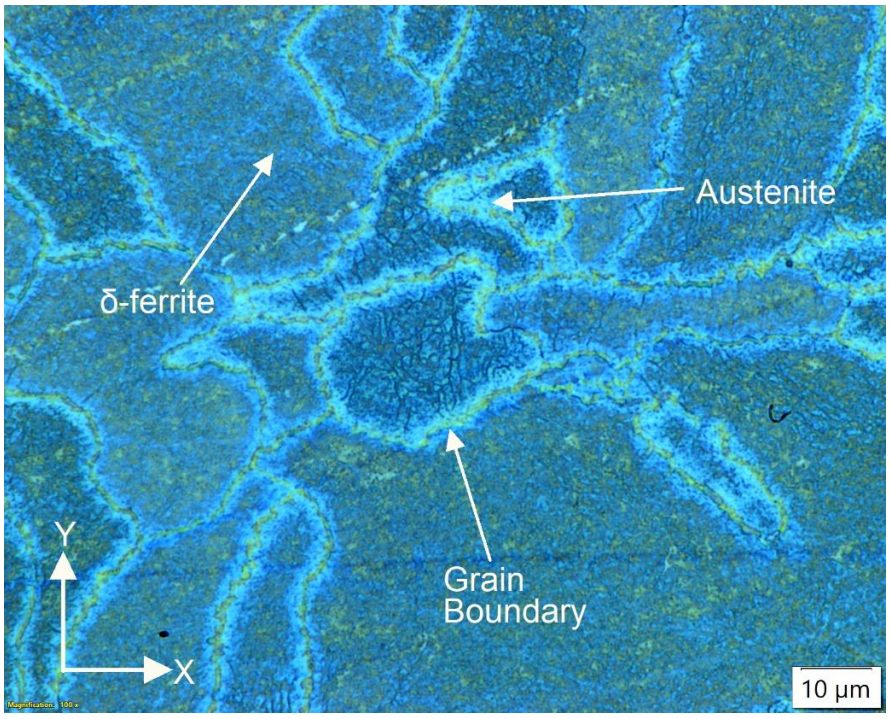

Figure 54: Plane perpendicular to build direction of the as-printed sample

4.1.1.2 Heat-treated sample at 1000 ° C for 1hour and water Quenched & Air Cooled

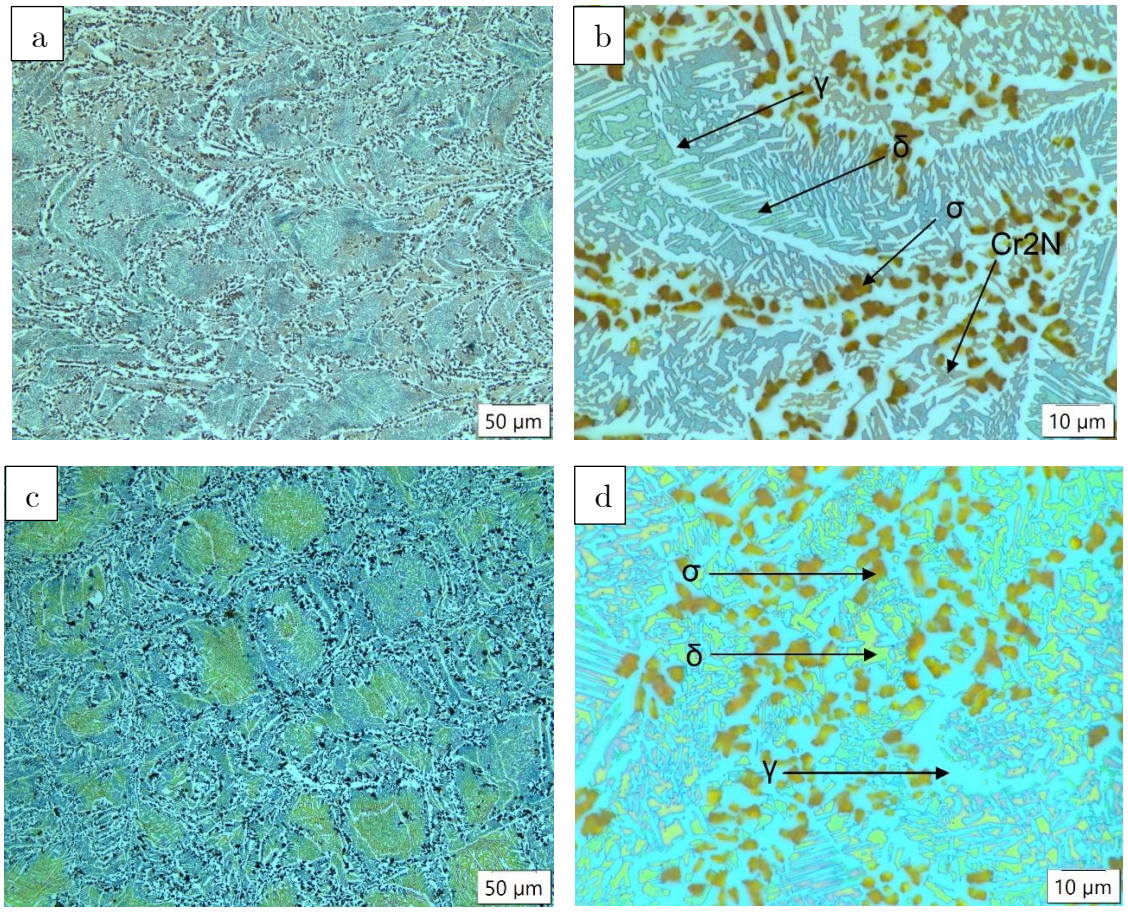

Figure 55: Microstructure of heat-treated sample for 1hour (a) at 1000 ° C water quenched, Magnification 20x (b) at 1000 ° C water quenched, Magnification 100x (c) at 1000 ° C air-cooled, Magnification 20x (d) at 1000 ° C air-cooled, Magnification 100x

The heat-treated sample at 1000 ° C for 1-hour duration and then water quenched was observed in a light microscope for microstructure study. From Figure 55(a) & (b), it can be observed that there are intermetallic phases, i.e., sigma and chromium nitride, along with austenite(γ) and δ-ferrite phases. The dotted pattern inside δ-ferrite is chromium nitrides, but it is difficult to observe in lower magnification images (Fig. 55b). Both sigma and chromium nitride phases have been formed inside the δ-ferrite and at the boundary of δ/γ.

The light blue color indicates austenite(γ) phase, reddish-brown indicates sigma phase, and tanned dark blue indicates δ-ferrite phase, as shown in Figure 55(d). The chromium nitrides were not observed in an air-cooled sample. The sigma (σ) phase has precipitated in the high Cr-concentrated region of δ-ferrite and has formed directly in δ-ferrite particles.

4.1.1.3 Heat-treated sample at 1100 ° C for 1hour and Water Quenched & Air cooled

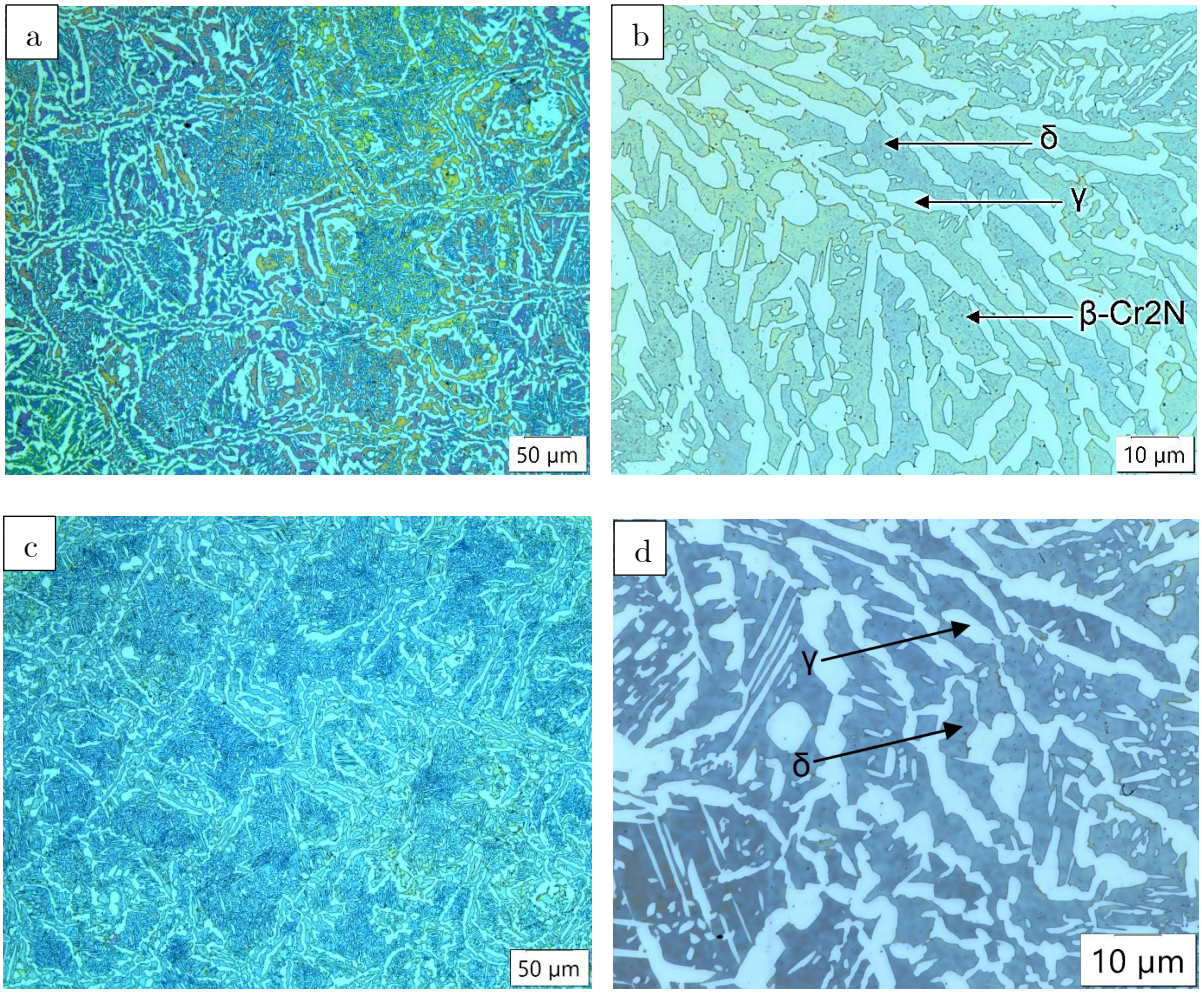

Figure 56: Microstructure of heat-treated sample for 1hour (a) at 1100 ° C water quenched, Magnification 20x (b) at 1100 ° C water quenched, Magnification 100x (c) at 1100 ° C air-cooled, Magnification 20x (d) at 1100 ° C air-cooled, Magnification 100x

The light blue color indicates the austenite(γ) phase, while tanned dark blue indicates the δ-ferrite phase, as shown in Figure 56. Secondary phases were observed at this temperature too, due to rapid cooling (water quenching). The dotted pattern inside δ-ferrite is chromium nitrides, as in Figure 56(b).

The sample heat-treated at 1100 ° C for 1 hour and then air-cooled to room temperature were investigated, and then no secondary phases were found. The primary phases δ-ferrite and austenite were only observed (Fig. 56(d)).

4.1.1.4 Heat-treated sample at 1200 ° C for 1hour and Water Quenched & Air cooled

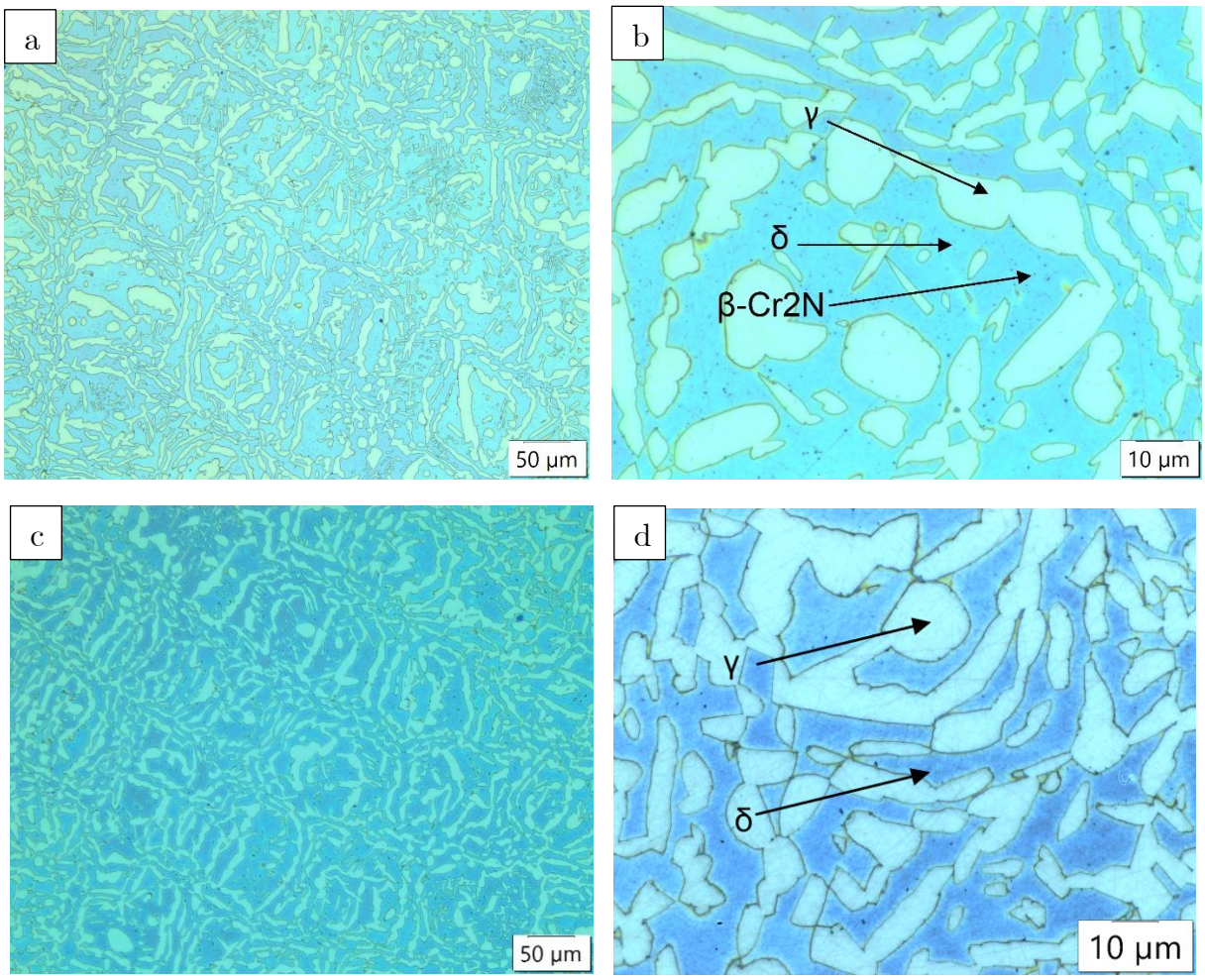

Figure 57: Microstructure of heat-treated sample for 1hour (a) at 1200 ° C water quenched, Magnification 20x (b) at 1200 ° C water quenched, Magnification 100x (c) at 1200 ° C air-cooled, Magnification 20x (d) at 1200 ° C air-cooled, Magnification 100x

The light blue colour indicates the austenite(γ) phase, while tanned dark blue indicates the δ-ferrite phase, as shown in Figure 57(b). Secondary phases, i.e., chromium nitride was observed at this temperature due to rapid cooling.

The heat-treated samples cool slowly with the air cooling method than water quenched, so it gets enough time to transform from ferrite to austenite. So, the grain size of austenite is bigger than the water quenched sample at the same temperature. There were no secondary phases visible.

4.1.1.5 Heat-treated sample at 1300 ° C for 1hour and Water Quenched & Air cooled

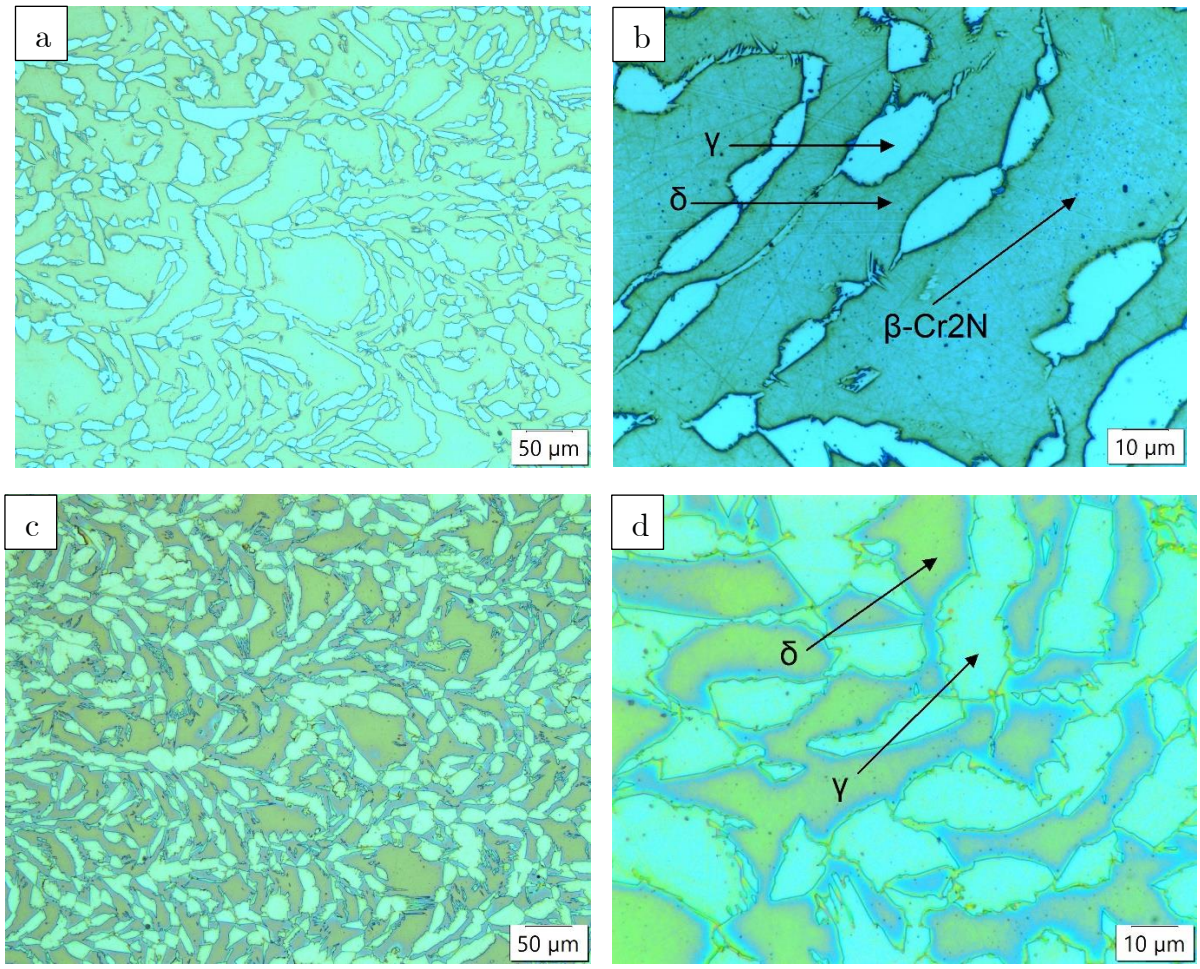

Figure 58: Microstructure of heat-treated sample for 1hour (a) at 1300 ° C water quenched, Magnification 20x (b) at 1300 ° C water quenched, Magnification 100x (c) at 1300 ° C air-cooled, Magnification 20x (d) at 1300 ° C air-cooled, Magnification 100x

The samples heat-treated at 1300 ° C and cooled by water quenching have more δ-ferrite than austenite in proportion, as seen in Figure 58(a)&(b). The grain size of δ-ferrite is much bigger than austenite. The chromium nitrides are formed at the ferrite and austenite grain boundary and also within the ferrite grain. Nitrogen is mostly partitioned to austenite, but the nitrogen content of ferrite increases as temperature rises. Chromium nitrides are prone to forming after rapid cooling from high temperatures because ferrite is supersaturated with nitrogen.

No precipitates were formed at this temperature by the air cooling method, which can be observed in Figure 58(c)(d). The light blue colour indicates the austenite(γ) phase, while dark blue indicates the δ-ferrite phase. The grain size of austenite is bigger than the water quenched cooling method.

4.1.2 Phase Analysis

Here, only a few images and graphs of phase balance are presented and compared. Relevant photos, graphs and tables that were not included in this part are shown in Appendix B.

4.1.2.1 As-Printed Specimen

The as-printed sample consists of δ-ferrite and Austenite. The 20% NaOH etchant attacks δ-ferrite while austenite remains unattacked. So, δ-ferrite is dark blue and austenite is light blue in the color. The austenite is mainly observed near the grain boundary, which is finer grain. But δ-ferrite has coarser grains morphology.

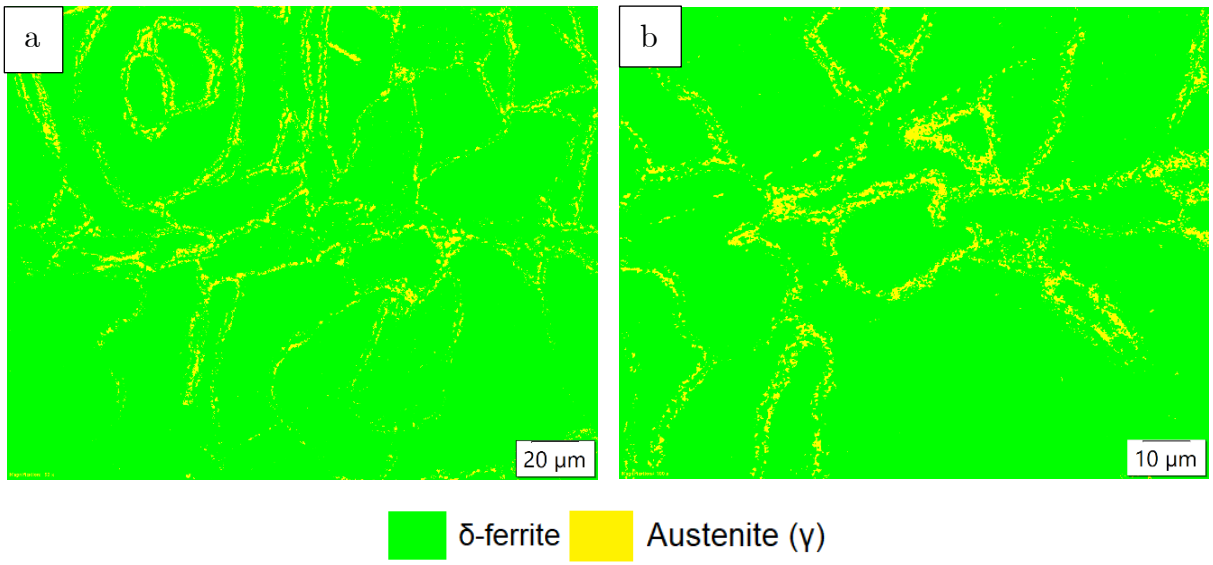

Figure 59: Phase Analysis of As-printed sample (a) Magnification 20x (b) Magnification 100x

After Performing phase analysis, the percentage of δ-ferrite was about 93.55 ± 2.14%, and austenite was about 6.45 ± 2.14% (Appendix B1, Table III). Here, the green color indicates δ-ferrite, and the yellow color represents the austenite phase (Figure 59). Hence, it can be concluded that the as-printed sample was mostly ferritic in composition.

4.1.2.2 Heat-treated sample at 1000 ° C for 1hour and Water quenched & Air cooled

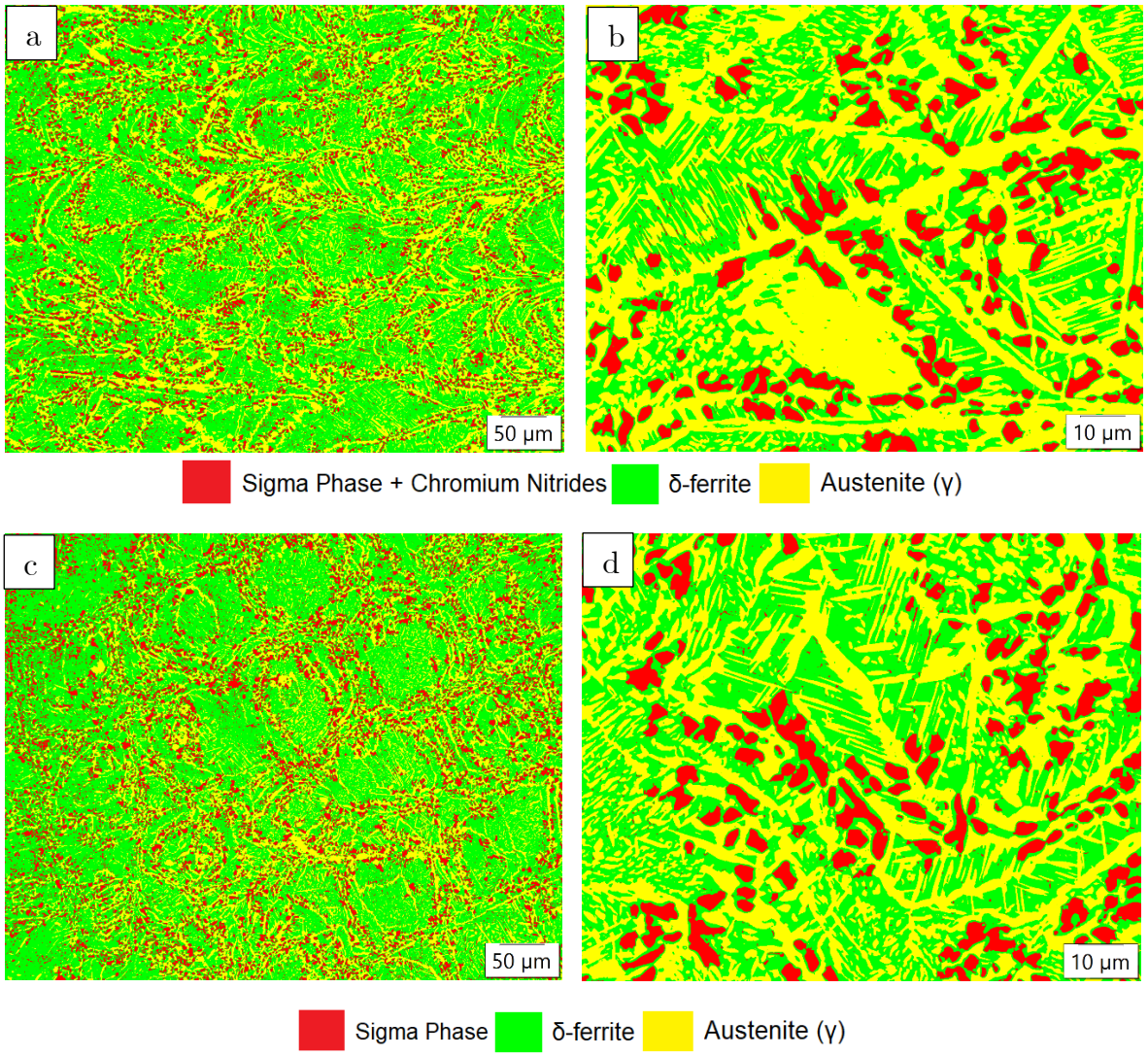

Figure 60: Phase Analysis of heat-treated sample at 1000 ° C for 1hour then water quenched (a) Magnification 20x (b) Magnification 100x. Phase Analysis of heat-treated sample at 1000 ° C for 1hour then Air-cooled (c) Magnification 20x (d) Magnification 100x

In the water-cooled sample, the sigma phase and chromium nitrides have been found as a secondary phase, but the sigma phase was only found in the air-cooled sample (Fig. 60). The bigger grain size of the red color represents the sigma phase. After the phase analysis, the percentage of precipitate, δ-ferrite, and austenite phase was about 14.02 ± 2.17%, 50.82 ± 4.55%, and 35.16 ± 3.87%, respectively (Appendix B2). While in an air-cooled sample, the percentage of sigma, δ-ferrite, and austenite phase was about 15.58 ± 1.71%, 48.72 ± 3.2%, and 35.70 ± 3%, respectively (Appendix B3).

Due to rapid cooling, the percentage of precipitate is less in water quenched sample than in the air-cooled sample. The percentage of the austenite phase is found more in an air-cooled sample because the cooling rate is slower, and δ-ferrite gets more time to transform into the austenite phase.

4.1.2.3 Heat-treated sample at 1100 ° C for 1hour and Water quenched & Air cooled

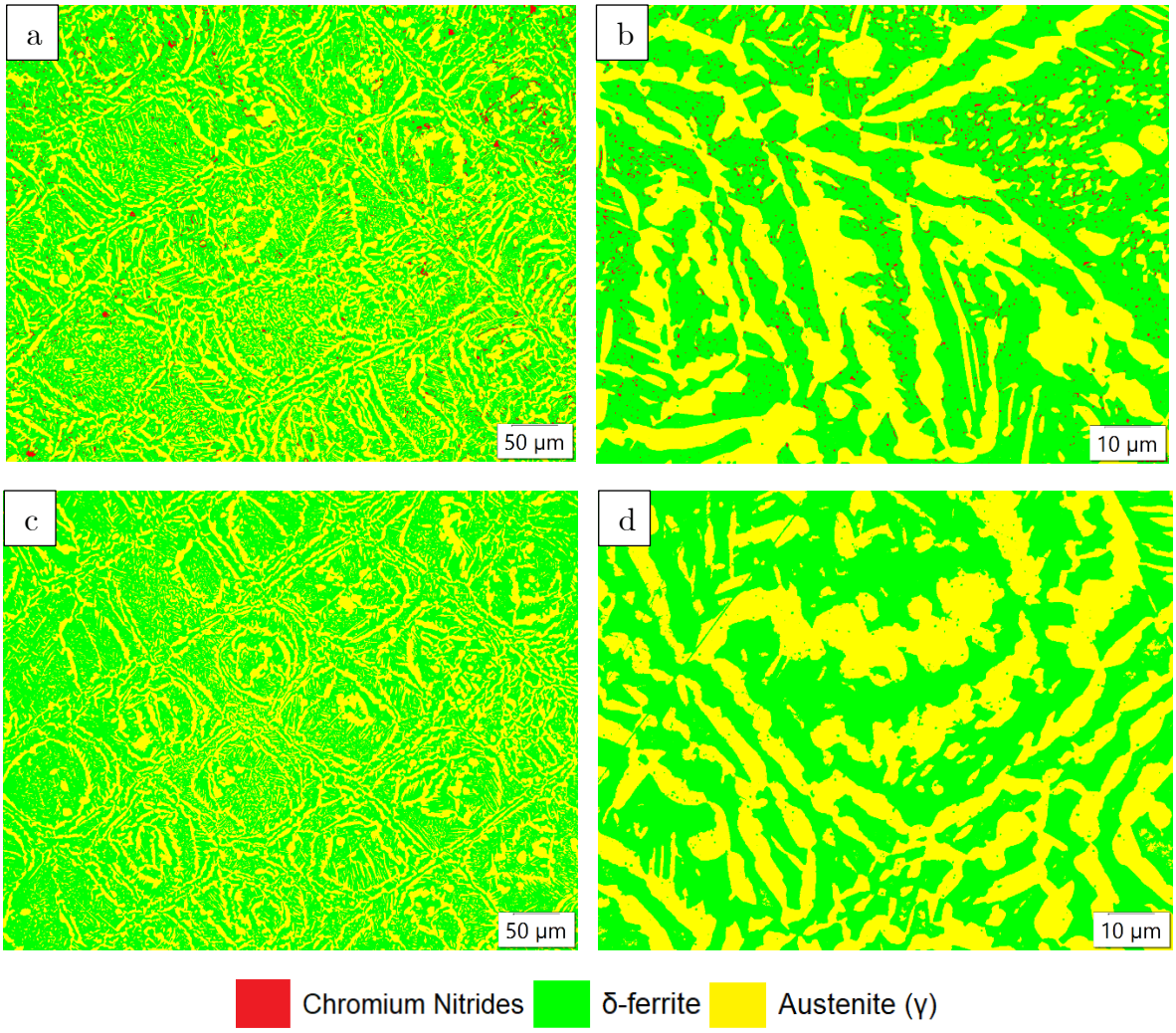

Figure 61: Phase Analysis of heat-treated sample at 1100 ° C for 1hour then water quenched (a) Magnification 20x (b) Magnification 100x. Phase Analysis of heat-treated sample at 1100 ° C for 1hour then Air-cooled (c) Magnification 20x (d) Magnification 100x

Chromium nitrate was observed due to rapid cooling in the water quenched sample, as in Figure 62(a)(b). But there were no secondary phases observed in heat-treated at 1100 ° C then air-cooled sample. The percentage of chromium nitrate, δ-ferrite, and austenite phase was about 3±1.06%, 60.69±2.73%, and 36.31±2.78% respectively in water quenched sample (Appendix B4). While in an air-cooled sample, the percentage of δ-ferrite and austenite phases was about 63.03±3.09% and 36.97±3.09%, respectively (Appendix B5).

4.1.2.4 Heat-treated sample at 1200 ° C for 1hour and water quenched & Air cooled

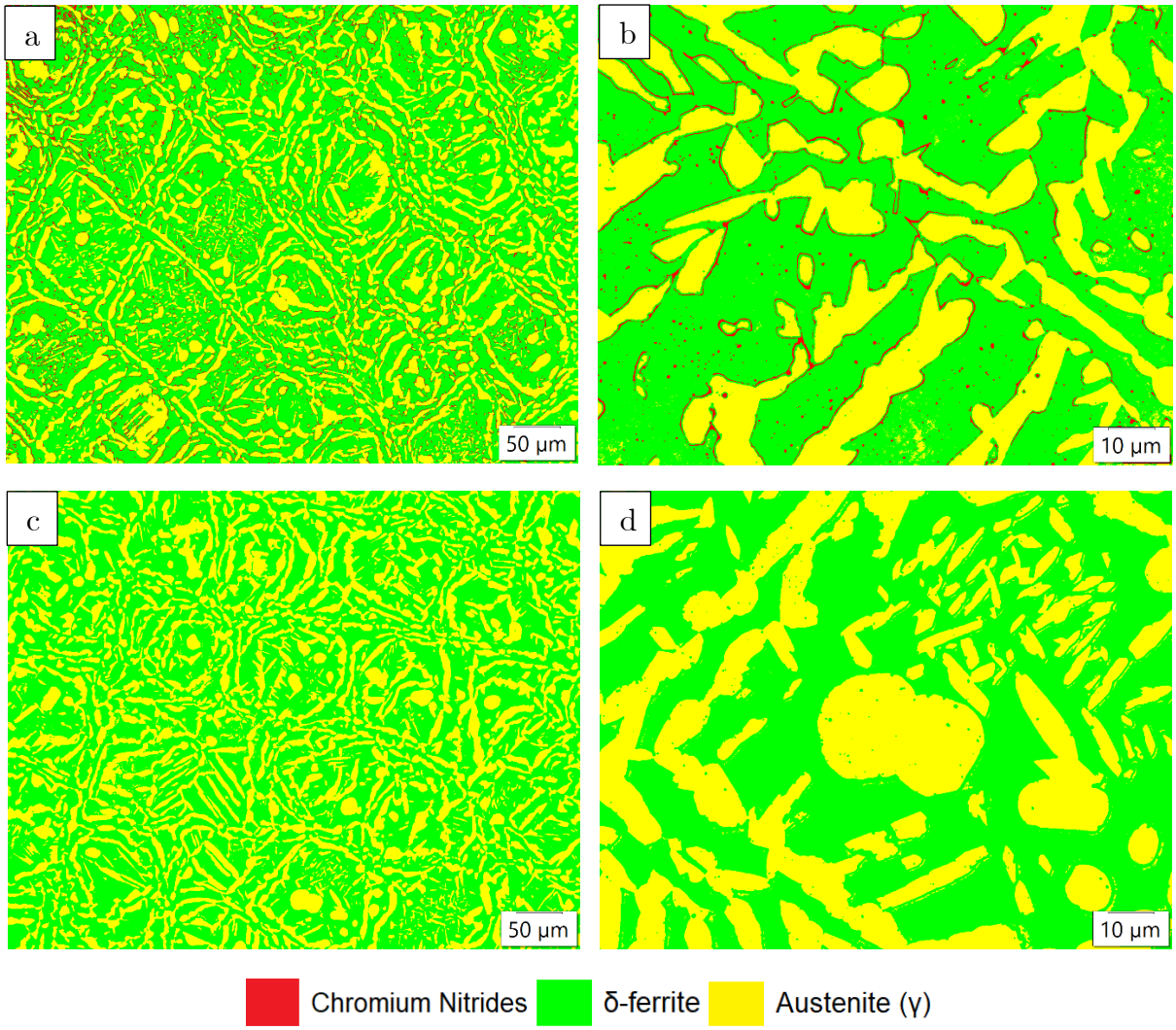

Figure 62: Phase Analysis of heat-treated sample at 1200 ° C for 1hour then water quenched (a) Magnification 20x (b) Magnification 100x. Phase Analysis of heat-treated sample at 1200 ° C for 1hour then Air-cooled (c) Magnification 20x (d) Magnification 100x

Similarly, the sample heat-treated at 1200 ° C and then water quenched also has chromium nitride present due to the high cooling rate. But the air-cooled sample was found in the pure duplex phase (δ-ferrite and austenite phase only) as in Figure 63(c)&(d).

The percentage of chromium nitrate, δ-ferrite, and austenite phase was about 4.18 ± 1.04%, 64.36 ± 2.09%, and 31.46 ± 2.29% respectively in water quenched sample (Appendix B6). While in an air-cooled sample, the percentage of δ-ferrite and austenite phases was about 61.34 ± 2.72% and 38.66 ± 2.72%, respectively (Appendix B7).

4.1.2.5 Heat-treated sample at 1300 ° C for 1hour and water Quenched

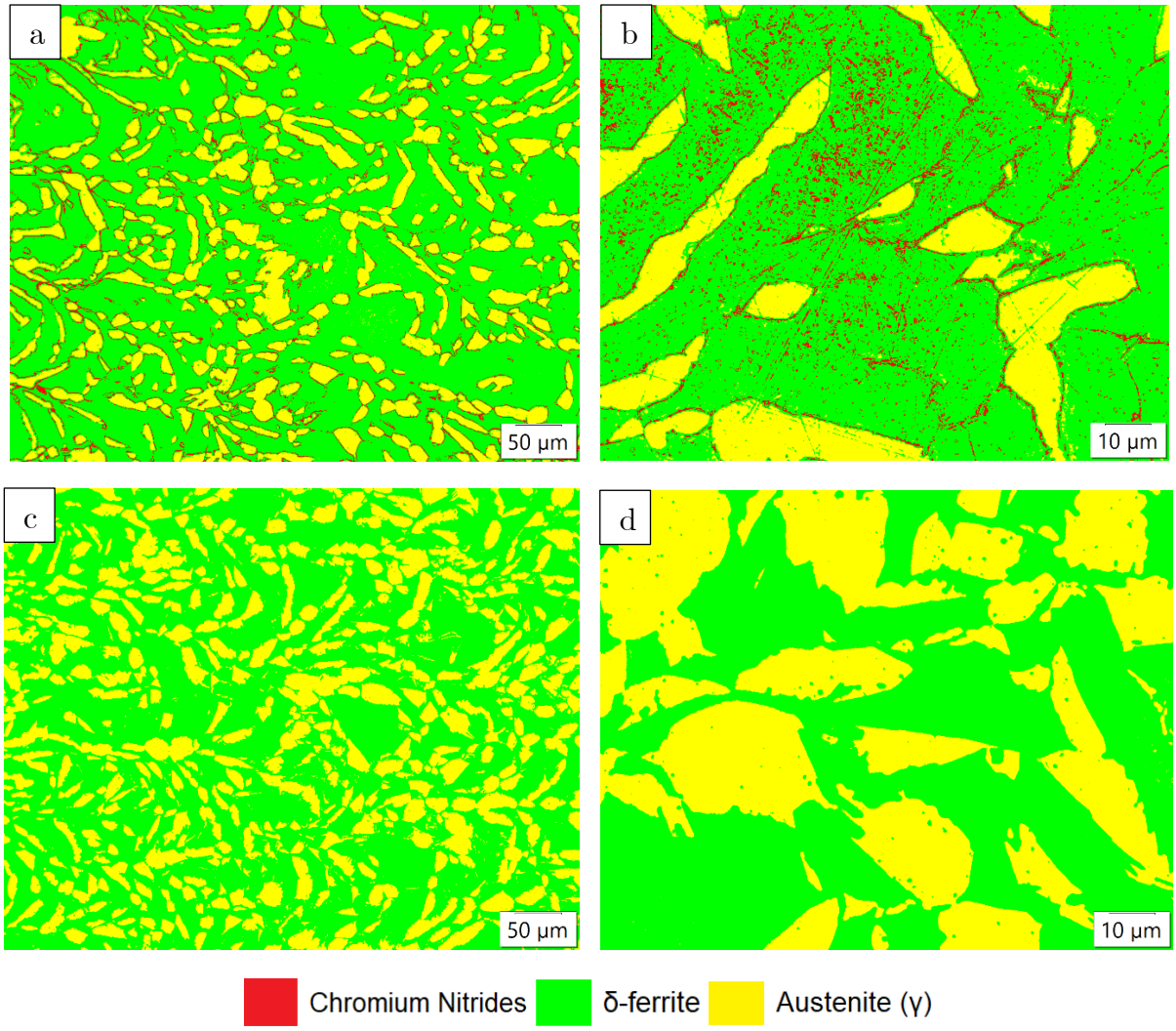

Figure 63: Phase Analysis of heat-treated sample at 1300 ° C for 1hour then water quenched (a) Magnification 20x (b) Magnification 100x. Phase Analysis of heat-treated sample at 1300 ° C for 1hour then Air-cooled (c) Magnification 20x (d) Magnification 100x

The percentage of chromium nitrate, δ-ferrite, and austenite phase was about 5.52 ± 1.51%, 72.29 ± 2.21%, and 22.20 ± 1.77% respectively in water quenched sample (Appendix B8). While in an air-cooled sample, the percentage of δ-ferrite and austenite phases was about 63.46 ± 3.12% and 36.54 ± 3.12%, respectively (Appendix B9).

At this higher temperature, the percentage of chromium nitrite was increased, and the grain size of austenite was also much bigger, as shown in Figure 64.

4.1.2.6 Summary of Phase Analysis

Table 13: Summary of Phase Analysis

Sample Name	% Precipitate (σ & Cr_2N)	% of δ-Ferrite	% of Austenite (γ)
As Printed	-	93.55 ± 2.14	6.45 ± 2.14
HT at 1000 ° C for 1hr then water quenched	14.02 ± 2.17	50.82 ± 4.55	35.16 ± 3.87
HT at 1000 ° C for 1hr then air-cooled	15.58 ± 1.71	48.72 ± 3.2	35.70 ± 3
HT at 1100 ° C for 1hr then water quenched	3.00 ± 1.06	60.69 ± 2.73	36.31 ± 2.78
HT at 1100 ° C for 1hr then air-cooled	-	63.03 ± 3.09	36.97 ± 3.09
HT at 1200 ° C for 1hr then water quenched	4.18 ± 1.04	64.36 ± 2.09	31.46 ± 2.29
HT at 1200 ° C for 1hr then air-cooled	-	61.34 ± 2.72	38.66 ± 2.72
HT at 1300 ° C for 1hr then water quenched	5.52 ± 1.51	72.29 ± 2.21	22.20 ± 1.77
HT at 1300 ° C for 1hr then air-cooled	-	63.46 ± 3.12	36.54 ± 3.12

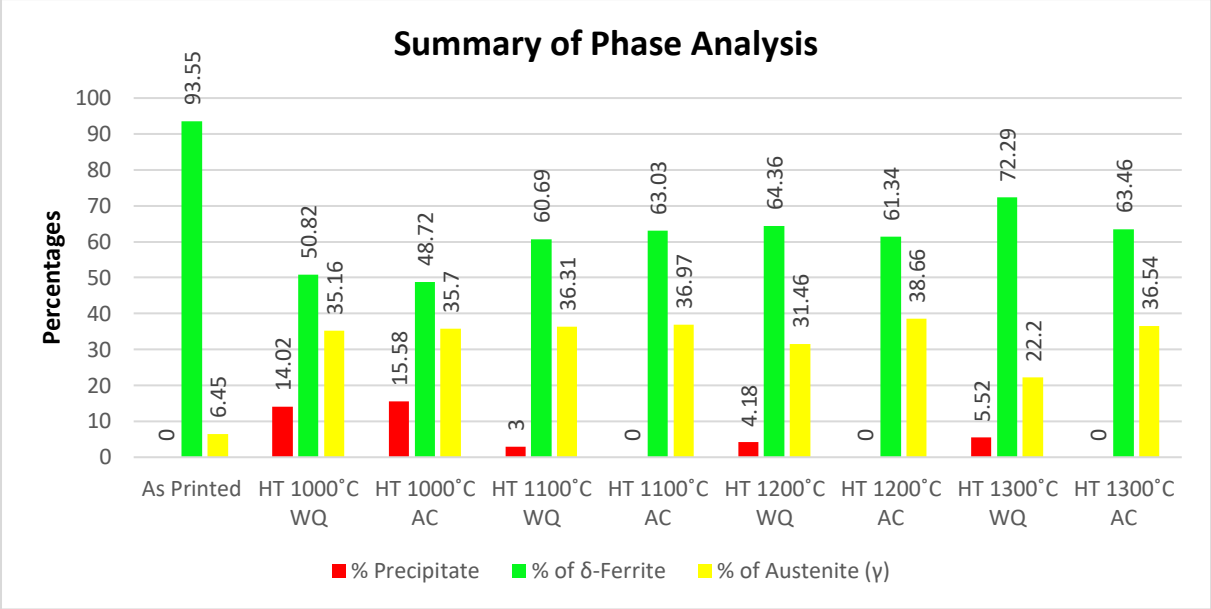

Figure 64: Summary of Phase Analysis

The result of phase analysis performed using an optical light microscope is summarized in table 13 and graphically illustrated in Figure 65. In Fig. 65, the WQ indicates water quenched, and AC indicates the air-cooled method. The precipitates like the sigma phase and chromium nitride are represented by red color in the graph. In contrast, δ-ferrite and austenite phases are represented by green and yellow colors in the diagram.

4.2 SEM

A scanning electron microscope was used to study microstructure, EDS, and EBSD of the powder and SLM printed EN 1.4410 sample. The heat-treated samples weren't analyzed because the scanning electron microscope wasn't working due to technical failures. The results are presented below.

4.2.1 Microstructure Study

4.2.1.1 SAF 2507 Powder Study

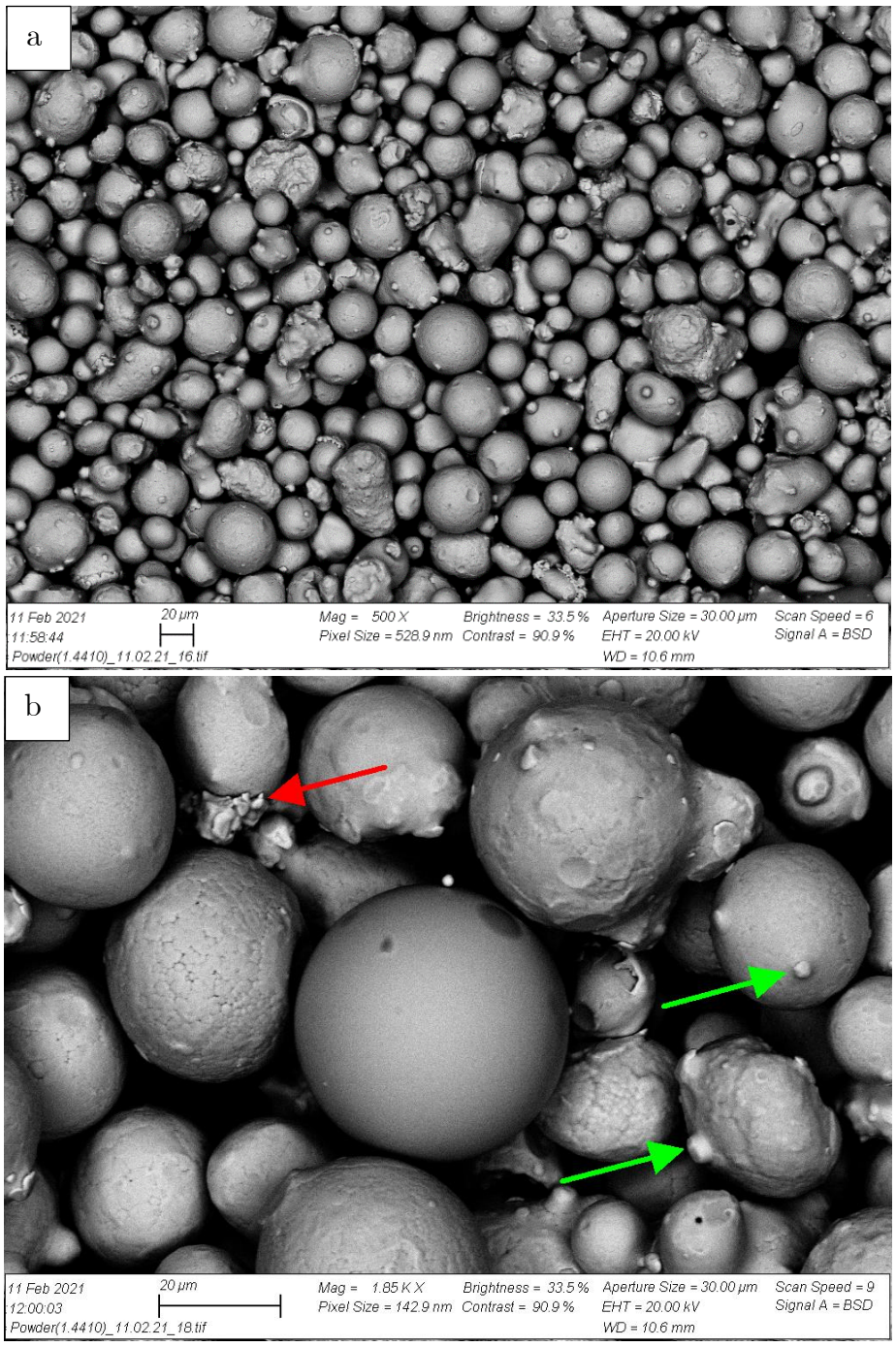

Figure 65: Powder Morphology (a) Magnification 500x (b) Magnification 1850x

Super-duplex stainless-steel powder of grade UNS S32750 (SAF 2507) is used in this study. The powder is of spherical morphology, and few powders are irregularly shaped, as shown in Figure 65(a). While observing irregularly shaped powder particles, it was found that molten powder had splat over solidified spherical particle and then had covered it (see red arrow in Figure 65(b)). Some irregular-shaped particles also seem to bulge out in different directions (see green arrow in Figure 65(b)). This may be due to smaller-sized particles sticking to bigger particles during the solidification process.

The powder particles diameter ranged from 7.36 to 53.72 µm and with a mean diameter of 26.644 µm, as shown in figure 66.

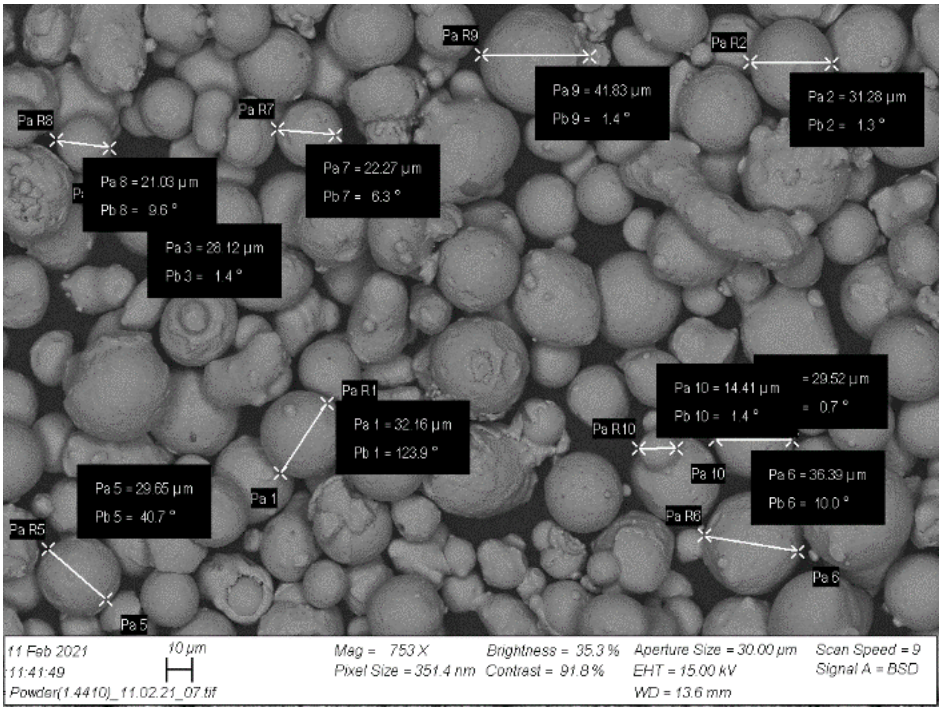

Figure 66: Powder particles size measurement

4.2.1.2 As-printed Sample

At lower magnification (Fig. 67 (a)&(c)), the macrostructure seems to be a mosaic type (square-like) structure. The formation of mosaic texture is due to the specific scanning strategy used for manufacturing the sample. The scanning strategy used in this sample printing is stripe scanning with each layer rotation of 67°. The angle between two different mosaic-type stripes is measured and found to be 67.19°, which matches the layer rotation angle. The grains and grain boundary are visible in etched images, as shown in Figures 67(a)&(b).

The macrostructure seems to be uniform, and the average length and width of each tessera are about 123.2 & 125.5 µm, respectively. At the mosaic boundaries, the small re-crystallized grains are observed at higher magnification (Fig. 67 (b)&(d)). In the as-

printed sample, lots of tiny pores were also observed at higher magnification, as shown in Figure 67(e). The porosity may be formed due to entrapment of shielding gases, unmelted powder, or due to a large hatch distance.

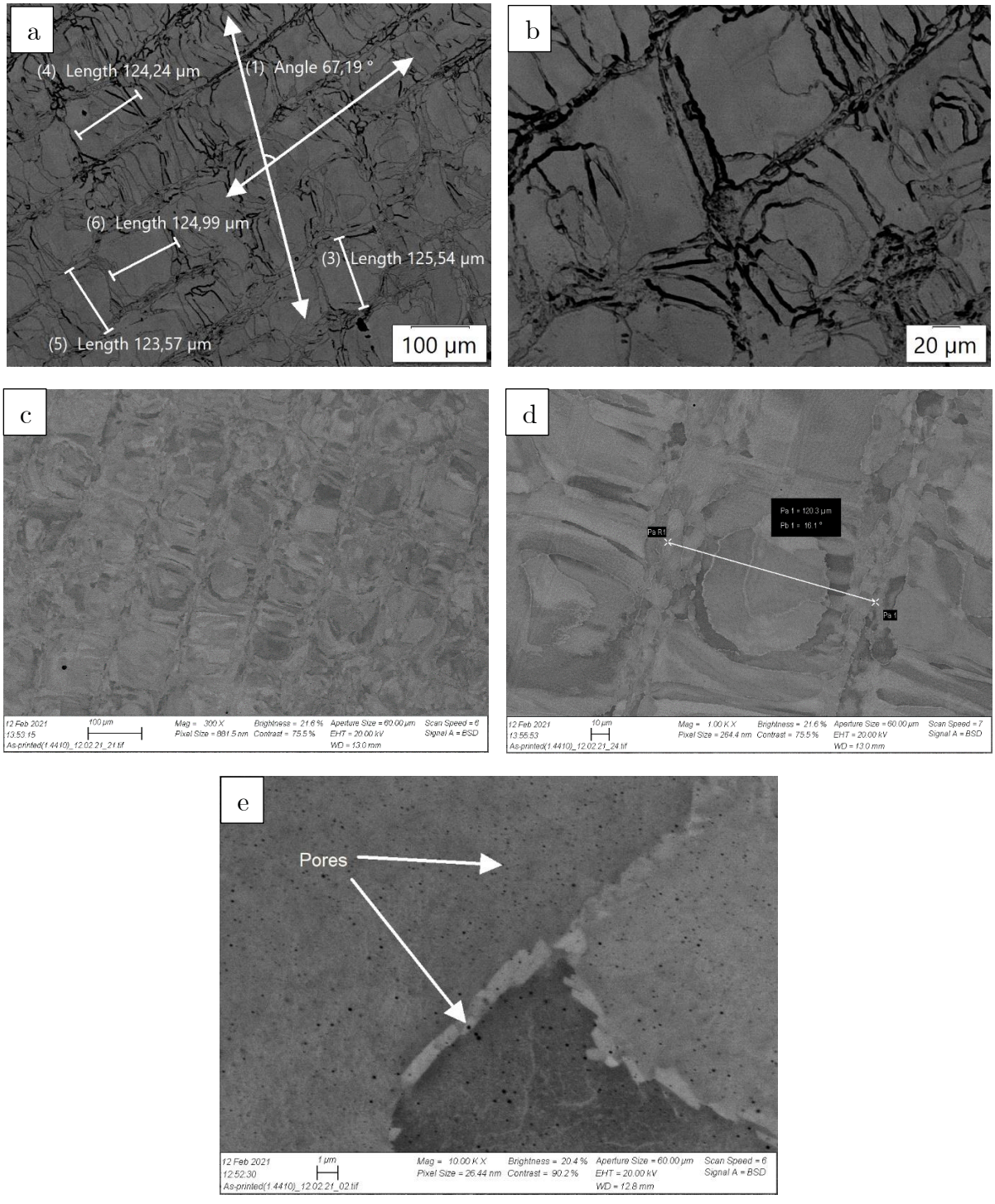

Figure 67: As-printed sample etched with oxalic acid (a) Magnification 326x (b) Magnification 722x. As-printed sample without etching (c) Magnification 300x (d) Magnification 1000x (e) Magnification 10,000x

4.2.2 EDS Analysis

4.2.2.1 SAF 2507 Powder Study

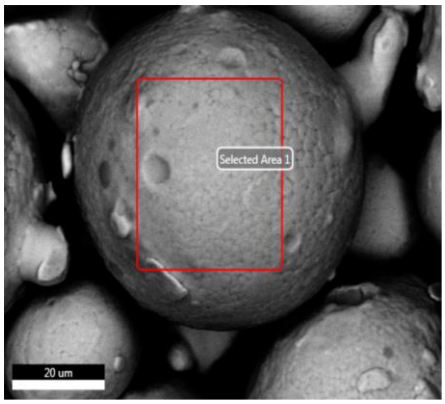

Figure 68: EDS analysis of AISI SAF 2507 powder at selected area 1

The selected area 1 was chosen for EDS analysis, as shown in Figure 68. After EDS analysis, the result is displayed in graphical form (Figure 69) and tabular form (Table 14). The percentage of chromium, carbon, and manganese present in powder is more than the nominal range of SAF 2507 presented in Table 3.

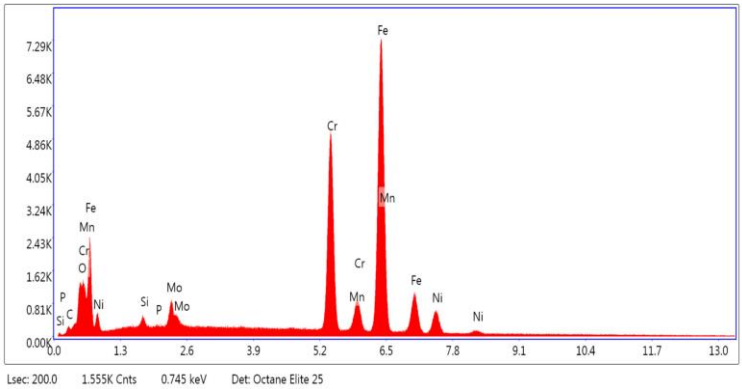

Figure 69: X-ray Spectrum result from selected area 1

Table 14: EDS Analysis result for selected area 1

Element	Weight %	Atomic %	Error %
C K	0.26	1.12	69.30
O K	1.42	4.70	8.82
Si K	0.35	0.66	15.25
P K	0.00	0.00	99.99
Mo L	2.38	1.31	5.37
Cr K	27.50	27.98	2.11
Mn K	1.29	1.24	10.52
Fe K	60.34	57.16	2.19
Ni K	6.46	5.82	4.86

4.2.2.2 As-printed Sample

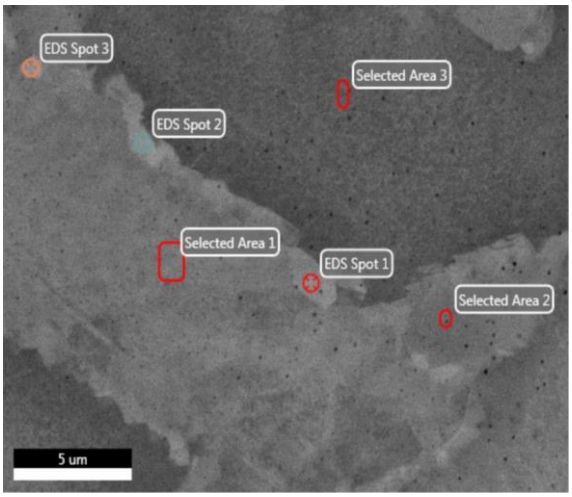

Figure 70: EDS analysis was done at various spot and locations of as-printed sample

The EDS analysis is done at different spots and areas, as shown in Figure 70. The EDS results of spot 1, selected area 1, and selected area 3 are presented in tabular form (Table 15).

Table 15: EDS Analysis result for (a) EDS Spot 1 (b) Selected area 1 (b) Selected area 3

a

Element	Weight %	Atomic %	Error %
C K	0.00	0.02	99.99
O K	1.12	3.75	9.59
N K	0.67	0.61	3.02
Si K	0.31	0.59	17.63
Mo L	2.31	1.30	5.13
Cr K	27.30	28.24	2.09
Fe K	61.70	59.45	2.14
Ni K	6.58	6.03	4.82

b

Element	Weight %	Atomic %	Error %
C K	0.14	0.64	73.51
O K	1.20	4.00	8.77
Al K	0.06	0.13	66.59
Si K	0.49	0.94	15.67
N K	0.56	0.21	42.04
Mo L	2.46	1.37	6.78
Cr K	27.32	28.02	2.08
Fe K	61.30	58.84	2.13
Ni K	6.46	5.86	4.78

c

Element	Weight %	Atomic %	Error %
N K	0.88	0.81	4.66
Si K	0.31	0.61	19.11
Mo L	2.31	1.33	5.66
Cr K	27.69	29.42	2.09
Fe K	62.14	61.48	2.14
Ni K	6.67	6.28	4.83

4.2.2 Phase Analysis using EBSD

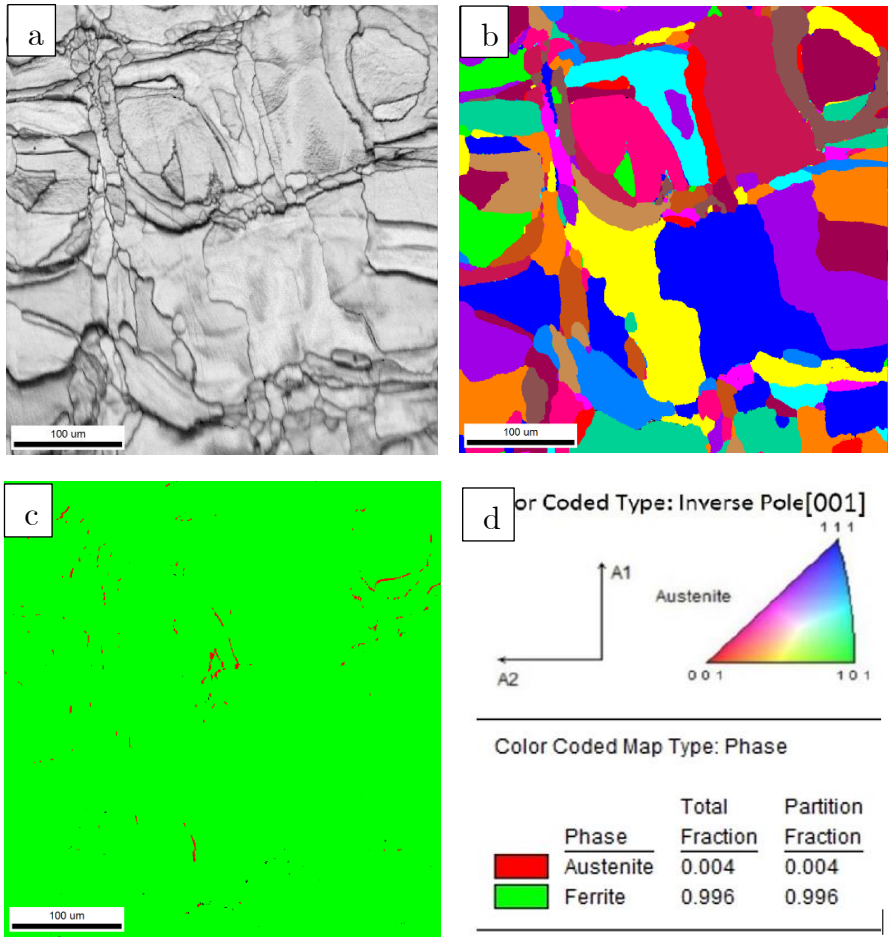

Figure 71: (a) EBSD phase map of as-printed sample (b) Inverse pole figure of EBSD showing grain orientation of as-printed (c) Phase analysis (d) Color-coded map of grain orientation and phase

The EBSD phase map and grain orientation map were taken from the same area to visualize the microstructure of the as-printed sample and identify the nature of tesserae, as shown in Figures 71(a) and 71(b), respectively. The phase map and grain orientation map grain exist inside each tessera, with grains inside tesserae having different orientations than grains inside neighboring tiles. The phase analysis of the same area of the as-printed sample was done as shown in Figure 71(c), and then δ-ferrite & austenite was found to be 99.6% & 0.4%, respectively. This indicates that the as-printed sample was almost ferritic.

4.3 TEM

The TEM analysis was needed to confirm the different phases present in the various samples and observe dislocation. But after analyzing 2-3 samples, It was concluded that it was time-consuming and challenging to find all the phases present because it scans a tiny area (in nanometer-scale) for investigation.

4.3.1 As-printed Sample

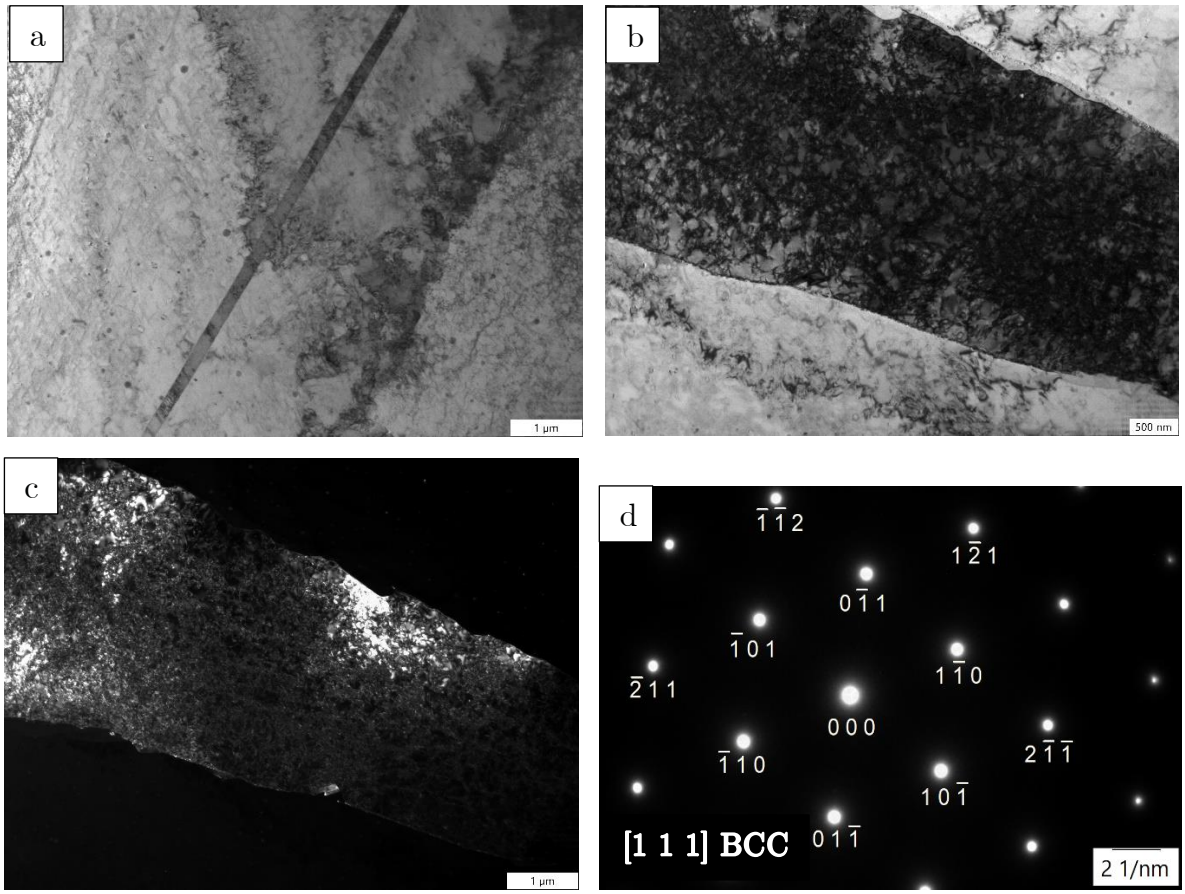

Figure 72: (a) TEM showing dislocation inside tesserae (b)TEM Bright Field image (c) TEM Darkfield Image (d) SAD pattern recorded from the dark region of (b) along zone axis [011]

A lot of dislocation lines are produced in the precipitate-free ferritic region, as shown in Figure 72(a). These dislocations are induced during SLM processing due to high cooling rates. The fast heating leads to high stresses and resulting in the occurrence of dislocation. The bright field and dark field images are shown in Figures 72(b) and (c), respectively. The bright-field image shows a high concentration of entangled concentrated loops. The selected area diffraction pattern (Figure 72(d)) indicates the presence of δ-ferrite based on the BCC unit cell. Since the as-printed sample is almost ferritic, it wasn't easy to find the austenite phase using TEM.

4.3.2 Heat-treated sample at 1100 ° C for 1hour and then Air cooled

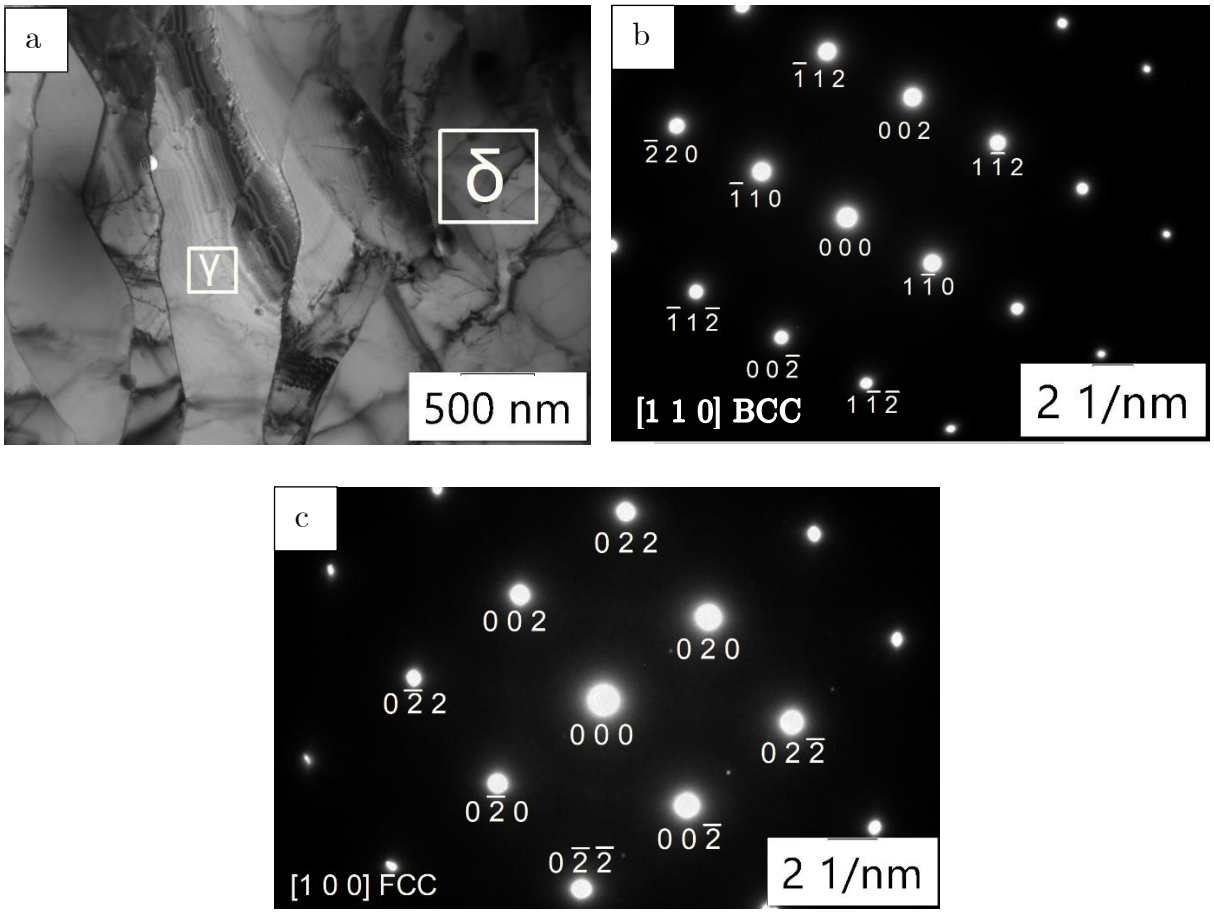

Figure 73: (a)TEM image of the heat-treated sample at 1000 ° C for 1hour and then Air-cooled (b) SAD pattern of δ marked region with big rectangle along [112] zone axis (c) SAD pattern of γ marked region with small rectangle along [022] zone axis

In heat-treated samples at 1100 ° C, fewer dislocations are observed than as-printed samples, as shown in Figure 73(a). The diffraction pattern was studied in two regions represented by small and big rectangular boxes in Figure 73(a). After analyzing the selected area diffraction pattern, it shows the presence of δ-ferrite and austenite based on BCC and FCC unit cell as shown in Figure 73(b) and (c), respectively. There was no precipitate observed at this temperature by the air cooling method.

4.3.3 Heat-treated sample at 1300 ° C for 1hour and then water quenched

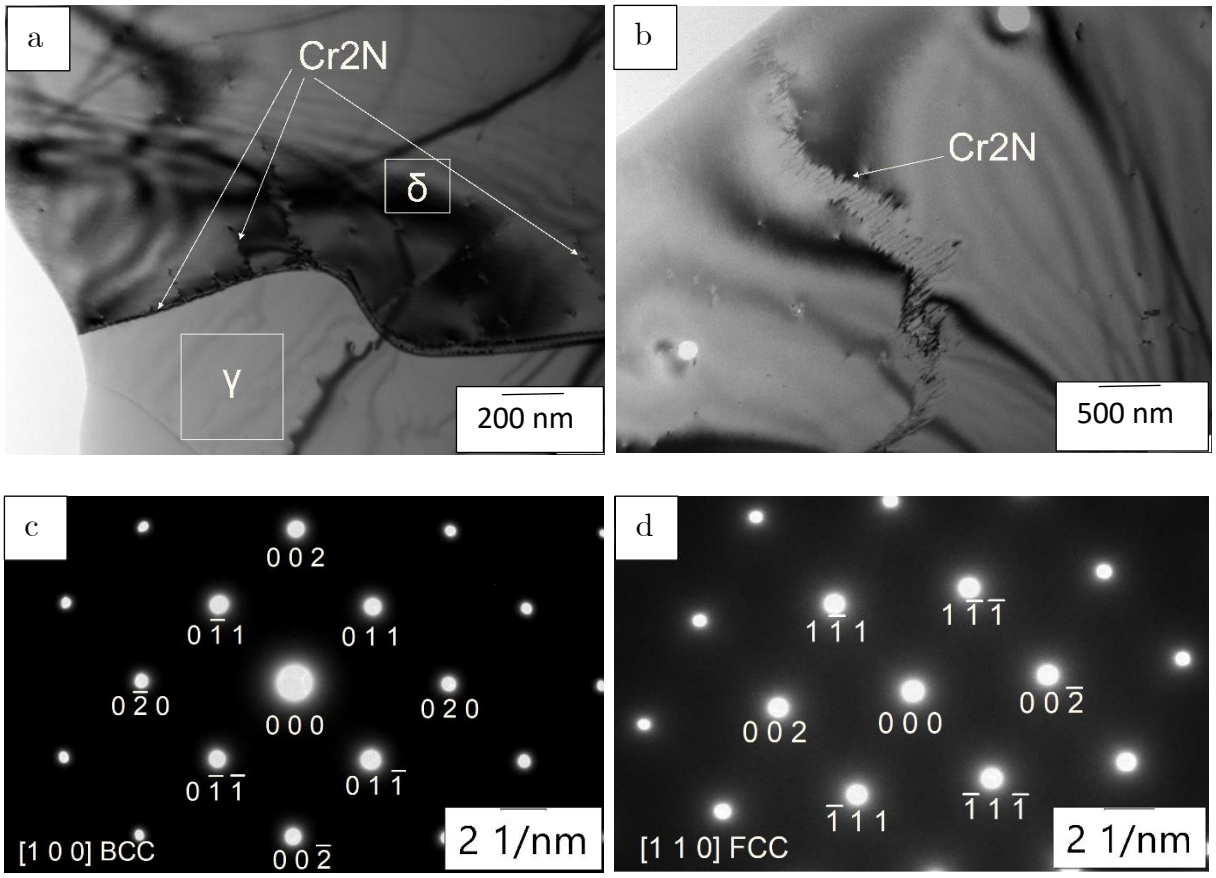

Figure 74: (a)TEM image of the heat-treated sample at 1300 ° C for 1hour and then water quenched (b) zoomed view of Cr_2N precipitation at grain boundary (c) SAD pattern of δ marked region with small rectangle along [011] zone axis (d) SAD pattern of γ marked region with small rectangle along [111] zone axis

In this sample, the dislocation dimension has become shorter, and its morphology has changed from lines to loops, as shown in Figure 74 (a)&(b). Selective area diffraction pattern (SADP)was taken from the region marked as smaller and bigger rectangular box as shown in Fig. 74(a). The results show that δ-ferrite with BCC crystal exists in a small rectangular area (Figure 74(c)) while the bigger rectangular area is an austenite phase with FCC crystal lattice (Figure 74(d)).

As marked in Figure 74(a) and (b), fine needle-shaped may be chromium nitrides formed at the grain boundary and inside ferrite grain due to rapid cooling. It wasn't easy to extract diffraction patterns to prove it. Similarly, Hegsbach also had performed a similar TEM analysis and found identical sharp fine needles at the grain boundary and inside the ferrite phase [5].

4.4 Hardness Measurement

4.4.1 As-printed Sample

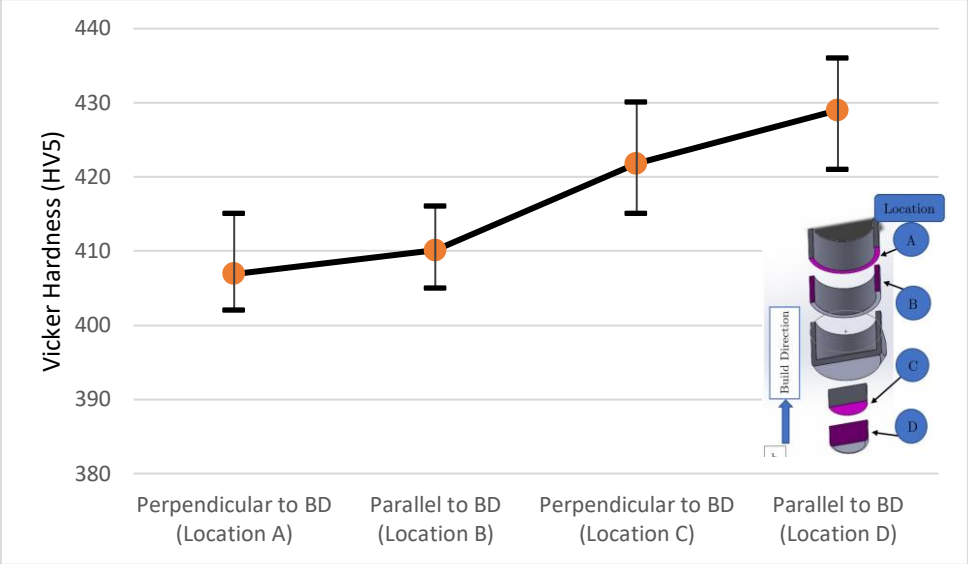

Figure 75: Hardness measurement of As-printed sample at a different location

The hardness value at the solid part is found higher than the hollow part of the as-printed sample, as shown in Figure 75. Similarly, it can also be observed that the hardness of the surface parallel to build direction is higher than the surface perpendicular to build direction. The average Vickers hardness (HV5) at location A, B, C, and D are 406.9±4.1, 410.1±3.3, 421.8±5.6, and 429±4.7, respectively (Appendix D1). The hardness value decreases from bottom to top of the sample.

The average Vickers hardness of the as-printed sample is found about 417 ± 4.4.

4.4.2 Heat-treated sample at 1000 ° C for 1hour and Water quenched & Air cooled

The average Vickers hardness (HV5) of heat-treated at 1000 ° C then water quenched sample at location A, B, C, and D are 380.2±3.7, 385±3.7, 388±3.7, and 391±3.9, respectively, as shown in Figure 76 (Appendix D2). While, the average Vickers hardness (HV5) of heat-treated at 1000 ° C then air-cooled sample at location A, B, C and D are 330.5±3.2, 336.3±3.1, 342.6±4, and 345.5±3.3 respectively, as shown in Figure 77 (Appendix D3). The water-quenched sample has a higher hardness than the air-cooled sample.

The average Vickers hardness (HV5) of heat-treated at 1000 ° C then water quenched sample is 386.1±3.7. While the average Vickers hardness (HV5) of heat-treated at 1000 ° C, then an air-cooled sample is 338.7±3.4.

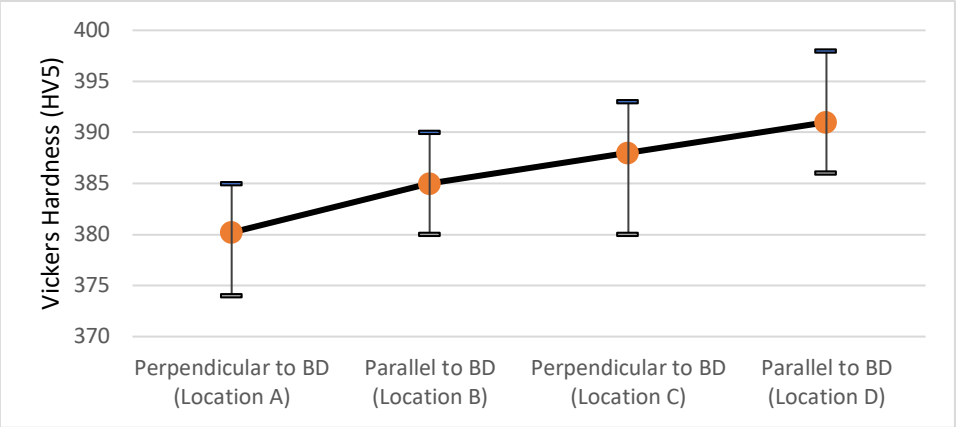

Figure 76: Hardness measurement of HT at 1000 ° C for 1hour then water quenched sample at a different location

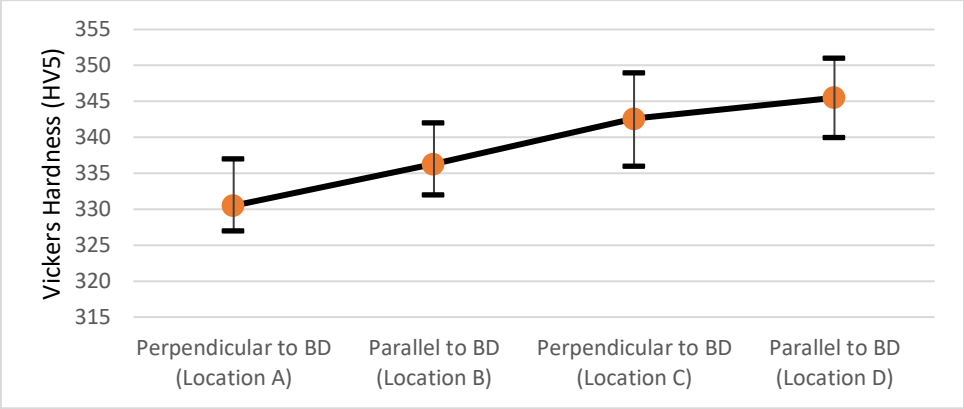

Figure 77: Hardness measurement of HT at 1000 ° C for 1hour then air-cooled sample at a different location

4.4.3 Heat-treated sample at 1100 ° C for 1hour and Water quenched & Air cooled

The average Vickers hardness (HV5) of heat-treated at 1100 ° C then water quenched sample at location A, B, C, and D are 280.7±3.6, 284.3±3.3, 286.1±3.4, and 288.3±4.6, respectively, as shown in Figure 78 (Appendix D4). While the average Vickers hardness (HV5) of heat-treated at 1100 ° C then air-cooled sample at location A, B, C and D are 275.3±3.2, 276.2±3.8, 277.5±3.9, and 278.3±4.2 respectively, as shown in Figure 79 (Appendix D5).

The average Vickers hardness (HV5) of heat-treated at 1100 ° C then water quenched sample is 284.9±3.7. While the average Vickers hardness (HV5) of heat-treated at 1100 ° C then air-cooled sample is 276.8±3.8. The water-quenched sample has a higher hardness than the air-cooled sample.

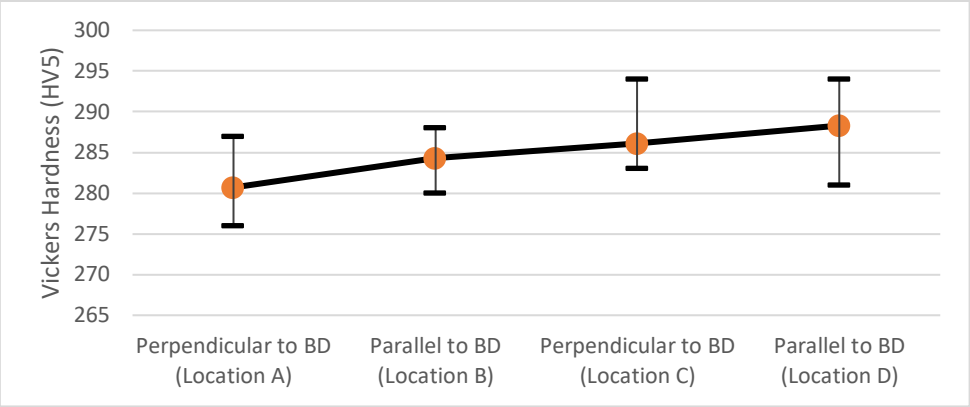

Figure 78: Hardness measurement of HT at 1100 ° C for 1hour then water quenched sample at a different location

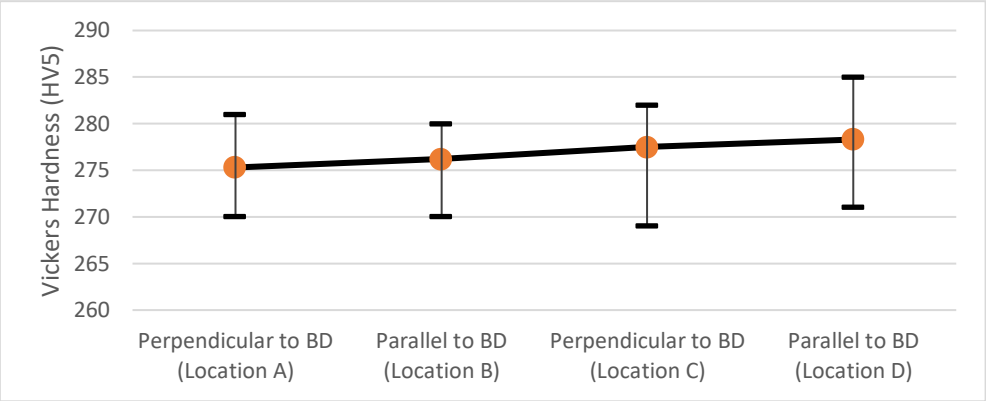

Figure 79: Hardness measurement of HT at 1100 ° C for 1hour then air-cooled sample at a different location

4.4.4 Heat-treated sample at 1200 ° C for 1hour and Water quenched & Air cooled

The average Vickers hardness (HV5) of heat-treated at 1200 ° C then water quenched sample at location A, B, C, and D are 290.4±4.5, 292.5±5.1, 295.1±3.6, and 297.2±4 respectively, as shown in figure 80 (See Appendix D6). While, the average Vickers hardness (HV5) of heat-treated at 1200 ° C then air-cooled sample at location A, B, C and D are 266±3.4, 268.3±4, 270.1±3.3, and 272.2±4.1 respectively, as shown in Figure 81 (See Appendix D7). The water-quenched sample has a higher hardness than the air-cooled sample.

The average Vickers hardness (HV5) of heat-treated at 1200 ° C then water quenched sample is 293.7±4.3. While the average Vickers hardness (HV5) of heat-treated at 1200 ° C then an air-cooled sample is 269.2±3.7.

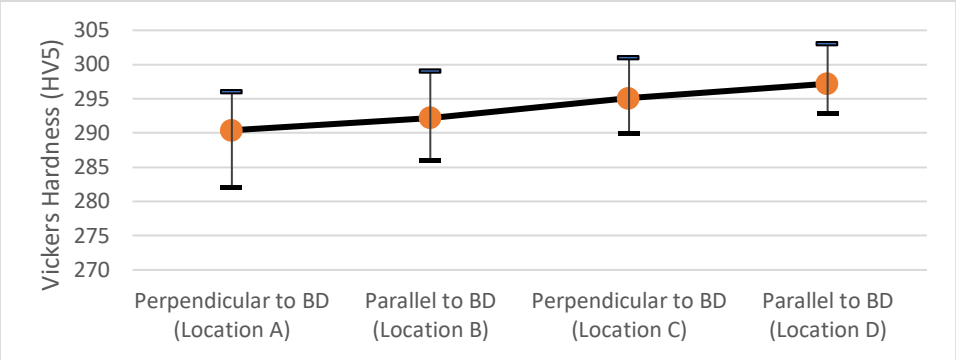

Figure 80: Hardness measurement of HT at 1200 ° C for 1hour then water quenched sample at a different location

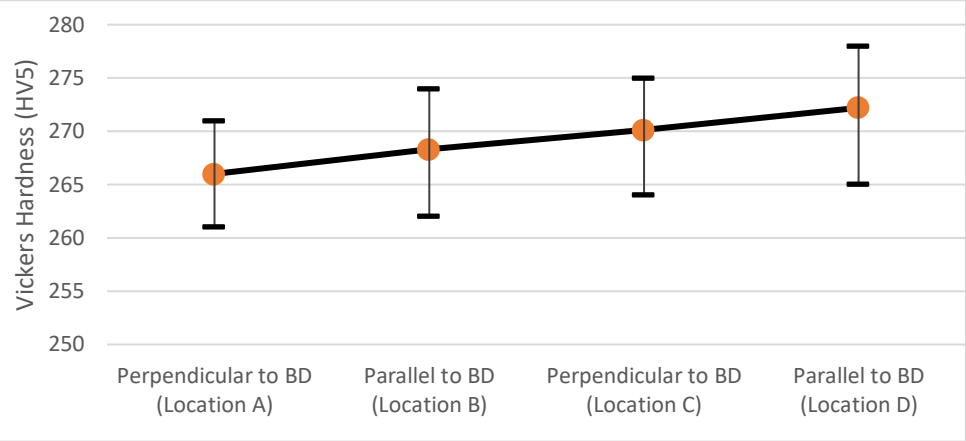

Figure 81: Hardness measurement of HT at 1200 ° C for 1hour then air-cooled sample at a different location

4.4.5 Heat-treated sample at 1300 ° C for 1hour and Water quenched & Air cooled

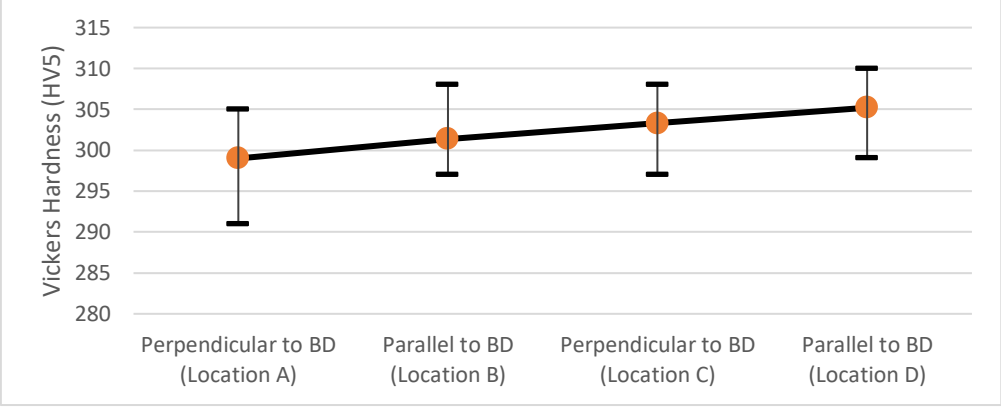

Figure 82: Hardness measurement of HT at 1300 ° C for 1hour then water quenched sample at a different location

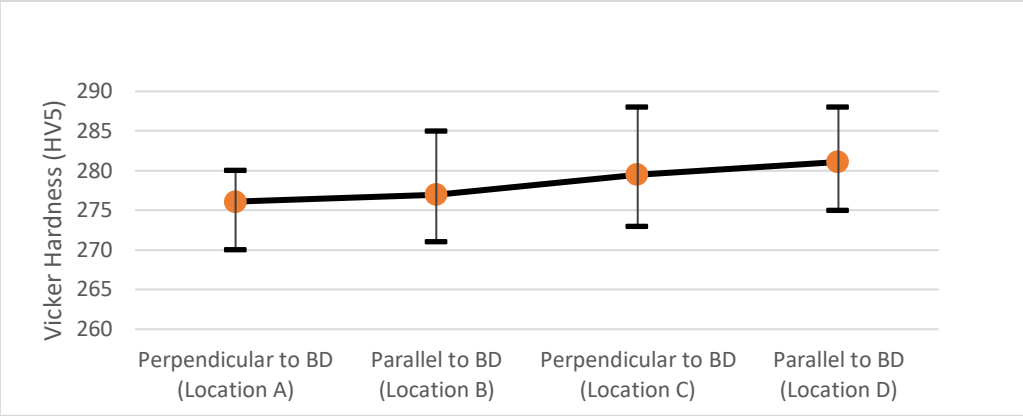

Figure 83: Hardness measurement of HT at 1300 ° C for 1hour then air-cooled sample at a different location

The average Vickers hardness (HV5) of heat-treated at 1300 ° C then water quenched sample at location A, B, C, and D are 299±4.6, 301.4±3.4, 303.3±3.6, and 305.2±3.5 respectively, as shown in Figure 82 (Appendix D8). While, the average Vickers hardness (HV5) of heat-treated at 1300 ° C then air-cooled sample at location A, B, C and D are 276.1±3.9, 277±4.6, 279.5±4.6, and 281±4, respectively, as shown in Figure 83 (Appendix D9). The water-quenched sample has a higher hardness than the air-cooled sample.

The average Vickers hardness (HV5) of heat-treated at 1300 ° C then water quenched sample is 302.2±3.2. While the average Vickers hardness (HV5) of heat-treated at 1300 ° C then air-cooled sample is 278.4±4.3.

4.4.6 Summary of Hardness Measurement

Table 16: Summary of the hardness of all samples of this thesis

Material	Average Vickers Hardness Number
As Printed SLM 2507	417 ± 4.4
Heat Treated at 1000 ° C then, Water Quenched	386.1 ± 3.7
Heat Treated at 1000 ° C then, Air-cooled	338.7 ± 3.4
Heat Treated at 1100 ° C then, Water Quenched	284.9 ± 3.7
Heat Treated at 1100 ° C then, Air-cooled	276.8 ± 3.8
Heat Treated at 1200 ° C then, Water Quenched	293.7 ± 4.3
Heat Treated at 1200 ° C then, Air-cooled	269.2 ± 3.7
Heat Treated at 1300 ° C then, Water Quenched	302.2 ± 3.2
Heat Treated at 1300 ° C then, Air-cooled	278.4 ± 4.3

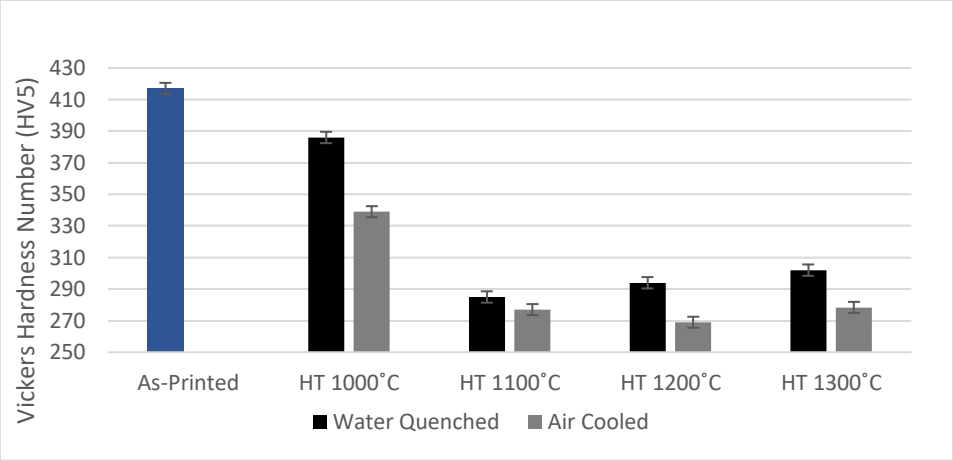

Figure 84: Summary of hardness measured of as printed and heat-treated samples in this thesis

The as-printed sample has the highest hardness compared to heat-treated samples, as shown in Table 16 and Figure 84. Likewise, water quenched samples also have a higher hardness number in comparison with air-cooled samples. The hardness of the heat-treated sample is highest at 1000 ° C than at other temperatures, as shown in figure 84. The hardness of water quenched samples decreases as temperature increases from 1000 ° C to 1100 ° C, and then hardness increases as temperature rise till 1300 ° C. But, the hardness of air-cooled samples decreases as temperature increases till 1200 ° C, then it increases till 1300 ° C.

4.5 Pitting Corrosion Test

The pitting corrosion test ASTM G48; method A was carried out. The sample was semicircular with curved edges, so there may be some error in the exposed area calculation. The weight of the sample before and after the pitting corrosion test was measured as shown in Table 17. There were no significant changes in weight observed, so it is concluded that no corrosion had taken place. So, it justifies its property that it is super duplex material that has high corrosion resistance.

Table 17: Physical measurement data of specimen used for corrosion test

Sample Name	Exposed Area (mm^2)	Weight before the test (g)	Weight after the test (g)
As Printed	706.92	2.8164	2.8163
Heat Treated at 1000 ° C then, Water Quenched	596.22	2.6267	2.6265
Heat Treated at 1000 ° C then, Air-cooled	536.68	2.2079	2.2077
Heat Treated at 1100 ° C then, Water Quenched	605.82	2.7959	2.7956
Heat Treated at 1100 ° C then, Air-cooled	563.93	2.4156	2.4155
Heat Treated at 1200 ° C then, Water Quenched	579.01	2.0128	2.0126
Heat Treated at 1200 ° C then, Air-cooled	576.00	2.3564	2.3561
Heat Treated at 1300 ° C then, Water Quenched	593.98	2.6835	2.6833
Heat Treated at 1300 ° C then, Air-cooled	569.45	2.4528	2.4525

5. Discussion

The results are briefly discussed and compared with theoretical results in this section.

5.1 Macrostructure and Microstructure

The macrostructure of as-printed material is a mosaic-type structure (square-like), as shown in Figures 51(b) and 67(a). The formation of mosaic structure is due to the scanning strategy used during the SLM process [113, 114]. The as-printed material was fully ferritic in composition. The austenite was mainly formed near the grain boundary, which was finer. But δ-ferrite has coarser grains morphology. After etching the sample surface parallel to build direction with oxalic acid, the melt pool was easily visible with an average depth of 90µm. The melt pool made it easy to determine the laser direction and the building direction in the material. The oxalic acid is efficient at revealing grain boundaries and provides good contrast of ferrite and austenite in DSS [115]. So, the dark line visible on the melt pool is supposed to be grain boundary, as shown in figure 53, and white lines are supposed to be austenite, as shown in Figure 52.

After heat treatment, the material resulted in an increase in austenite content. The volumetric fraction of δ-ferrite & austenite depends on heat treatment temperature and the correlation between ferrite & austenite stabilizer elements [91]. The water quenched sample, which was HT at 1000 ° C, shows the presence of austenite, delta ferrite, chromium nitride, and sigma phase (inside ferrite grain). The ferrite grain size is narrowed because of sigma precipitation which consumes chromium and molybdenum in delta ferrite. At this temperature, intermetallic phases like the sigma phase and chromium nitride were observed by light microscopy and were also reported by other authors [116-118]. After using the air cooling method at the same 1000 ° C temperature, the sigma phase was still observed due to incomplete dissolution, as shown in Figure 55. Sigma phase formation occurs by consumption of δ-ferrite phase, which decomposes by reactions $\delta \rightarrow \sigma + \gamma_2$, where γ_2 is secondary austenite.

At the temperature ranging from 1000-1300 ° C, chromium nitride was observed along with austenite and delta ferrite phase due to rapid cooling. The chromium nitride was observed inside the ferrite grain and at the grain boundary. As heat treatment temperature increased, the volume fraction of chromium nitrides and delta ferrite has also increased. The nitrogen content was observed in the as-printed EDS result. Nitrogen is more soluble in austenite than in ferrite. This difference in nitrogen solubility has a significant impact on nitride precipitation in duplex stainless steel. When the amount of ferrite is high, nitride precipitation occurs during rapid cooling because the ferrite's solubility limit is exceeded [71]. Because nitrogen does not have

enough time to diffuse and contribute to austenite stabilization, some of it forms the nitride phase while the rest remains as a nitrogen-enriched region [74].

When the cooling rate is decreased (i.e., air-cooling method), there was the presence of only austenite and delta ferrite at temperature range 1100-1300 ° C. It means it was free from intermetallic or secondary phases. This air cooling was slow enough that the nitrogen had time to diffuse, and trapped chromium nitrides in the ferrite grains were avoided.

In water quenched sample, as HT temperature increases from 1000-1300 ° C, the grain size of austenite grows larger, and the surrounding δ-ferrite band becomes wider. Similar was the case in the air-cooled samples too. But grain size of austenite was a little bigger in an air-cooled sample than the water quenched sample at the same temperature due to slow cooling [116].

Thus, it was difficult to avoid chromium nitrides precipitation even at higher temperatures by the water quenching cooling method. So, heat treatment temperature should be kept as low as possible without risking precipitation of intermetallic phases. The air cooling method provides precipitation-free and pure dual-phase microstructure at a temperature ranging from 1100-1300 ° C, so air cooling is preferred for this material.

5.2 Phase Analysis

The as-printed parts were fully ferritic, and after heat treatment, there was a transition to the duplex microstructure. The ferrite was found about 94% using a light microscope and about 99.6% using EBSD in as-printed SLM SAF 2507. Similarly, Seidi performed phase analysis in as-printed SLM SAF 2507, and ferrite was found about 98% [114].

Then heat treatment was performed at a temperature ranging from 1000-1300 ° C for 1 hour, and it was cooled by two different methods, i.e., water quenching and air-cooling method. The volume fraction of austenite was higher in air-cooled samples than the water-quenched sample at all heat treatment temperatures, as shown in Figure 85. This is because the cooling rate is slower in the air cooling method, allowing more delta ferrite to be transformed to austenite [116]. If the cooling rate is fast, very little ferrite can transform to austenite at room temperature, resulting in an excessive ferrite phase and precipitation of Cr_2N within the ferrite grains [119, 120]. So, the cooling rate of DSS must be sufficiently slow to allow approximately 50% of the ferrite to be converted to austenite and, simultaneously, sufficiently fast to avoid the formation of intermetallic phases [10, 78, 116].

In water quenched material, as heat treatment increased from 1000 ° C to 1300 ° C, the ferrite percentage had increased with a reduction in austenite volume. The intermetallic phase was highest at 1000 ° C (about 14%), then it decreased to 3% at 1100 ° C; finally, it increased to 5.5% at 1300 ° C. The chromium nitride was found to be increased with an increase in temperature. It was difficult to avoid chromium nitrides even at higher temperatures. So, heat treatment temperature should be kept as low as possible without risking precipitation of intermetallic phases [111, 120]. At 1000 ° C, the sigma phase was found in both water quenched and air-cooled samples of about 14% and 15.6%, respectively.

In air-cooled samples, there were not any precipitates found at a heat-treatment temperature from 1100 ° C to 1300 ° C. The best phase balance was found at 1200 ° C with about 61% δ-ferrite and 39% austenite. At 1100 ° C and 1300 ° C, there was almost the same percentage of δ-ferrite and austenite of about 63% and 37% respectively, as shown in Figure 85. So, it can be concluded that good ferrite and austenite proportion was obtained by using the air cooling method, which is free from secondary phases.

The relative proportions of ferrite and austenite in SLM printed material are determined by the steel's composition and heat-treatment temperature. As the phase diagram (Figure 18) shows, small changes in composition can have a huge influence on the relative volume percentage of these two phases(ferrite & austenite) [70]. However, the cooling rate influences the quantity of ferrite that may transform to austenite. Cooling rates after high-temperature exposures affect the phase balance. The fast cooling rates encourage ferrite retention, and it is possible to have more ferrite than the equilibrium level [70, 90, 116].

The as-printed material has about 62 wt. % of Fe and the phase diagram in Figure 18 is for 63.5 wt. % Fe. So, Figure 18 can be used for the prediction of phases at various temperatures. However, phase diagrams are rarely sufficient to predict the resulting microstructure after solidification because it shows the presence of only three solid phases: austenite (γ), ferrite, and sigma phase (σ) [70]. The phase diagram (Figure 18) shows that about 50/50 phase balance can be obtained between 850-950 ℃ for 27.32 % chromium. But, secondary phases like sigma phases and chromium nitrides were present at a heat treatment temperature of 1000 ℃ even after rapid cooling. So, if we heat treat at a temperature between 850-950 ℃, then it is 100% guaranteed that more secondary phases will be visible in the material, and this can also be verified from Table 4. So, I heat treated all the samples above 1000 ℃ (i.e., 1100, 1200 and 1300 ℃) to obtain a pure duplex structure (free from secondary phases). However, it wasn't easy to obtain nearer to 50/50 phase balance at a temperature above 1000 ℃. It is clear from the experiment that the cooling rate affects grain morphology and phase balance of duplex

stainless steel. By trying a more different cooling rate, it is possible to obtain a better phase balance above 1000 ℃ temperature, but I couldn't try it due to lack of samples and time. So, the best phase balance was found at 1200 ° C with about 61% δ-ferrite and 39% austenite by air cooling method.

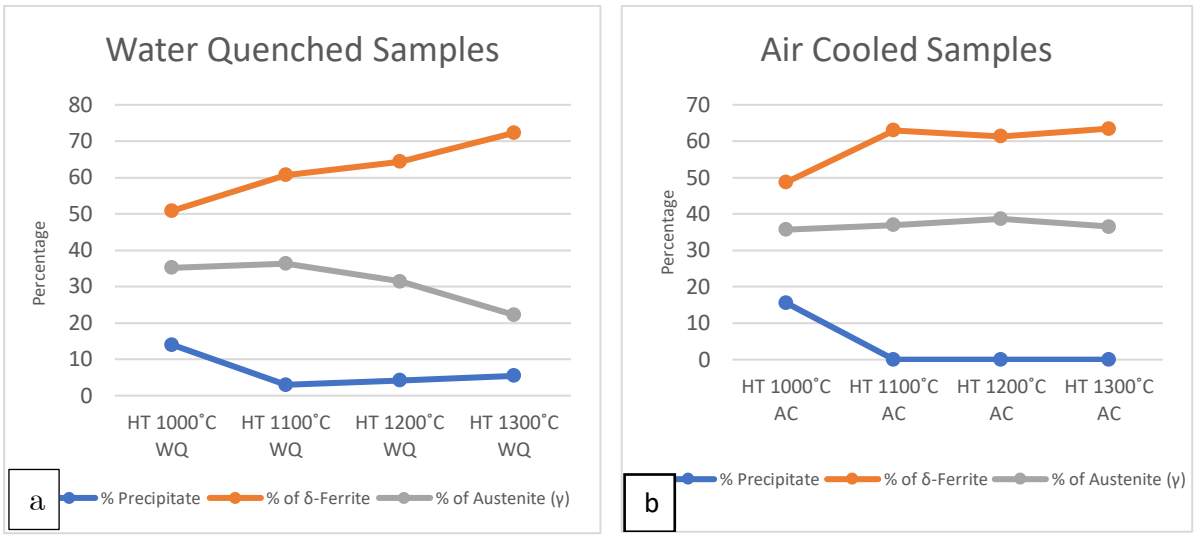

Figure 85: Phase content of heat-treated samples (a) Water quenched (b) Air-cooled

5.3 EDS Analysis

The EDS result of the powder used for printing the material is presented in table 14. Sandvik Osprey LTD analyzed the same powder, and its result is presented in Appendix E. The EDS result shows around 27.5% Cr, 2.38% Mo, 1.2% Mn, 6.46% Ni, 1.42% O, 60.34% Fe and others element, whereas Sandvik result shows around 24.7% Cr, 3.97% Mo, 0.9% Mn, 7% Ni, 0.08% O ,0.27% N, 62.01% Fe and other elements. While comparing the results, there is a lot of variation in the percentage of composition between them. There is around 3% difference in Cr content, and nitrogen content is not presented in the EDS result. It means EDS results are inaccurate and can't be relied upon, but it gives some approximate results.

The EDS analysis of the as-printed sample was done at three different locations, as shown in Figure 70 and Table 15. The as-printed samples showed Cr-enrichment coupled with a high reduction in Ni and Mo. The nitrogen content was present in the as-printed sample at a range of 0.56-0.88% in all 3 locations, which is exceeding the possible maximum nitrogen concentration of ferrite that is 0.07% weight nitrogen [121]. As a result, the formation of nitride phases or nitrogen-enriched areas in the ferrite matrix is possible in rapid cooled heat-treated material. While comparing EDS results

of powder and as-printed samples, the weight percentage of major elements like Cr, Mo, Fe, Ni, O, and Si are almost identical and within the standard range.

The weight percentage of chromium in SAF 2507 is supposed to be in the range of 24-26 [57]. But EDS result shows about 27.5% Cr, which seems to be out of range. This means that results can be varied and misleading since they only address a small point in the sample, while ferrite is magnetic and can cause deflection of the electron beam in SEM. The nitrogen content is difficult to map exactly with X-rays, but we can still look at the difference of this element in the points. Despite this, it seems that the results are credible with what is expected.

5.4 TEM

The examination of the as-printed sample in a transmission electron microscope does not reveal any precipitates, but there is the presence of dislocation. In that sample, only the ferrite phase with BCC crystal structure was revealed using the selected area diffraction pattern as shown in Fig.72. Since only around 1% volume fraction of austenite having FCC crystal structure was present in as printed which was evaluated by EBSD. Hence, it was challenging to find an austenite phase using TEM as it scans a tiny area. Inside the tesserae and smaller recrystallized micron grains in between the mosaic boundaries, nano-sized dislocation loops were found in abundance in the as-printed sample. A large amount of dislocation is observed in as printed sample; this dislocation is responsible for the nucleation of new grains during the solution heat-treatment process. As a result, the practically balanced phase distribution of delta ferrite and secondary austenite is produced. [122].

In the heat-treated sample at 1100 °C and then cooled by air, no precipitate was observed, as shown in Figure 73. The austenite and delta ferrite were observed from the selected area diffraction pattern based on FCC and BCC crystal structure. There is less dislocation observed in this sample as compared to the as-printed sample.

In the water-quenched heat-treated sample at 1300 °C, delta ferrite and austenite phases were observed along with precipitate observed at the grain boundary and inside the delta ferrite phase. These fine needle-shaped precipitates are supposed to be β-Cr_2N, as shown in Figure 74. These precipitates are believed to be the same as those observed at the grain boundaries of the delta ferrite and inside the delta ferrite phase in the light microscope. In combination with a nitrogen super-saturated delta ferrite phase, the rapid cooling leads to chromium nitride precipitation in this heat-treated sample. Large amounts of intergranular deposits were also detected in the ferrite.

Similarly, Hegsbach also had performed a similar TEM analysis and found identical sharp fine needles at the grain boundary and inside the ferrite phase [5]. These were too small to get a diffraction pattern, so that identification from diffraction could not be done. The growth and nucleation of chromium nitride are governed by the diffusion of chromium and nitrogen atom, as discussed by Wilms [123]. The nucleation of these precipitates is due to extra energy associated with dislocations.

Thus, it can be concluded that dislocation's dimension has become shorter, and its morphology had changed from lines to loop with an increase in heat treatment temperature. And in water quenched sample, it is difficult to avoid chromium nitrate precipitate due to nitrogen content present in the as-printed sample.

5.5 Hardness Analysis

Hardness is an important property of super-alloy that needs to be considered while manufacturing materials. The Vickers hardness number of hollow parts is always lower than the solid part of the sample for as printed and all heat-treated samples (see fig. 75 to 83). It means the hollow part is softer than the solid part of the material. It was also found that the surface of the sample that is parallel to build direction is harder than the surface of the sample perpendicular to build direction of as printed and heat-treated samples. This may be due to grain orientation, which shows grain elongation along the build direction of the sample.

The as-printed material has the highest average Vickers hardness number (417 HV) compared to all heat-treated samples, as shown in figure 84. The hardness of as-printed obtained is twice as high as casted duplex material and comparable with as-built SLM 2507 duplex material (see table 18). The hardness of heat-treated SLM built materials is almost 45% higher than heat-treated conventional duplex material, as shown in Table 18. The average hardness decreased in the material by 30-35% after heat treatment was carried out.

The hardness value of the water quenched sample is greater than an air-cooled sample, as shown in figure 84. This is because in all water quenched samples, more precipitates like sigma and chromium nitride are present, and the percentage of austenite is less, as shown in Table 13 [62]. This intermetallic precipitate is hard, resulting in a huge increase in hardness from a macroscopic perspective [124]. The austenite phase is softer than the ferrite phase. It means that material hardness increases with an increase in ferrite & precipitate [62, 91, 117, 125]. The hardness of water quenched samples decreases as HT temperature increases from 1000 °C to 1100 °C and then hardness increases as HT temperature increases from 1100 °C to 1300 °C. This is because the

percentage of precipitate and delta ferrite decreases as HT temperature increases from 1000 ° C to 1100 ° C, and then the percentage of precipitate and delta ferrite increases as temperature rises till 1300 ° C.

The sigma phase precipitate was found in an air-cooled sample, which is HT at 1000 ° C. But in the temperature range 1100-1200°C of an air-cooled sample, the microstructure is free from other precipitation, so the hardness decreased with increasing heat treatment temperature. This is because of the increase in austenite volume, which is the softer of the two phases [10, 91]. Similarly, at a temperature of 1300°C, the hardness of the air-cooled sample was increased because the volume fraction of austenite was decreased, and the volume fraction of delta ferrite was increased.

In conclusion, it can be stated that Vickers hardness is directly proportional to the volume fraction of precipitate (sigma and chromium nitride) & ferrite present and indirectly proportional to the volume fraction of austenite present [62, 91, 117, 125].

Table 18: Microhardness result of SAF 2507 by another Author [113, 114, 126]

Material	Microhardness
As-built SLM 2507 [114]	450 HV
Heat treated at 1000 ° C then, Water Quenched [113]	400 HV
As casted Conventional Duplex [126]	235 HV
Heat treated Conventional duplex [126]	227 HV

5.6 Pitting corrosion

The difference in weight before and after the test is negligible, as shown in table 17. This small deviation in weight may be due to inaccuracy in scale (±0.0001), and the next factor is that the scale was placed on a vibrating table at the workshop. The sample was also inspected with a light microscope, but there was no sign of pits available. There may be few pits present in pores and dents already on the sample's grinded surface. So, it was not possible to completely assure that there haven't been pitting.

As mentioned in ASTM standard [112], 120 grit size paper is suggested for grinding operation. But the sample was grinded with SiC paper of grit 120,220 and 500 to achieve a better surface finish. The pitting resistance of the stainless steel surface increases as the roughness of the surface decreases [127]. This also might be the reason that pitting corrosion was not observed.

6. Conclusion

Super Duplex stainless steel EN 1.4410/ AISI SAF 2507 material was successfully built via the selective laser melting process. Two subsequent studies were done on the material. The first focused on the macrostructure and microstructure. The second determined the mechanical properties, such as the Vickers hardness test and pitting corrosion performance of the material. After the investigation of SLM printed super duplex stainless steel of grade EN 1.4410 / AISI SAF 2507, the conclusive results are summarized below:

1. Because of the specific laser scanning pattern, a unique macroscopic texture was formed. A mosaic-type macrostructure with tesserae of 123–126 µm was obtained after SLM in an as-printed sample. The grains inside each tessera had a different crystallographic orientation than grains in adjacent tesserae.
2. The microstructure of as-printed material was almost entirely ferritic, but the desired dual-phase microstructure was achieved through post-processing heat treatment.
3. In water quenched sample, as HT temperature increases from 1000-1300 ° C, the grain size of austenite grows larger, and the surrounding δ-ferrite band becomes wider. Similar was the case in the air-cooled sample too. But grain size of austenite was a little bigger in an air-cooled sample than the water quenched sample at the same temperature due to slow cooling.
4. Heat treatment temperature or alloy modification and different cooling methods can control the microstructure of duplex stainless steels, particularly the balance between the ferrite and austenite phases. This is especially true for microstructure trends, which rely heavily on thermodynamic transformations.
5. At 1000 ° C, the sigma phase was found in both waters quenched and air-cooled samples. The chromium nitride was observed inside ferrite grain and at the grain boundary in all water quenched samples. As heat treatment temperature increased from 1000 ° C to 1300 ° C, the volume fraction of chromium nitrides has also increased from 1% to 5.5%.
6. When the cooling rate is decreased (i.e., air-cooling method used), there was the presence of only austenite and delta ferrite at temperature range 1100-1300 ° C. It means it was free from intermetallic or secondary phases.
7. At 1000 ° C, the sigma phase was found about 14-15% in both water quenched and air-cooled samples. In contrast, the sigma phases vanished after heat treatment temperature above 1100 ° C. It was difficult to avoid chromium nitrides precipitation even at higher temperatures by the water quenching

cooling method. So, heat treatment temperature should be kept as low as possible without risking precipitation of intermetallic phases.

8. The air cooling method provides precipitation-free and pure dual-phase microstructure at a temperature ranging from 1100-1300 ° C, so air cooling is preferred for this material. The best phase balance was found at 1200 ° C with about 61% δ-ferrite and 39% austenite.
9. The chemical composition of the material refers to a PREN of over 40, which makes it defined as a super duplex stainless steel. After the heat treatment, we see that the mechanical properties and the chemical properties comply with the standard specifications for stainless steel.
10. EDS result shows that all the elemental composition was within the standard SAF 2507 range in powder and in the as-printed sample except chromium, which was found out of range (about 27.5% wt.).
11. The nitrogen content was present in the as-printed sample at a range of 0.56-0.88%, which gives a probability of formation of nitride phases or nitrogen-enriched areas in the ferrite matrix during rapid cooling in heat-treated material.
12. The nano-sized dislocation loops were abundant in the as-printed sample, both within the tesserae and within smaller recrystallized micron grains in between the mosaic boundaries.
13. TEM result also shows a decrease in dislocation density after heat treatment of SLM manufactured parts. As heat treatment temperature increases, dimension of dimension has become shorter, and its morphology had changed from lines to loop with an increase in heat treatment temperature.
14. The solid part of the sample was found harder than a hollow part. The surface of the sample that is parallel to build direction is harder than the surface of the sample perpendicular to build direction. This may be due to grain orientation, which shows grain elongation along the build direction of the sample.
15. The average hardness of as-built SAF 2507 is 417 and decreases with heat treatment. The average hardness decreased in the material by 30-35% after heat treatment was carried out.
16. The hardness of material increases with an increase in the percentage of delta ferrite and percentage of a precipitate. This means that the formation of the sigma phase, chromium nitride, and increase in ferrite content are the main reasons for the increase in hardness.
17. No visible pits were observed in any sample while performing a pitting corrosion test at room temperature of 22±2 ° C for 72 hours. This proves its characteristics that super duplex stainless steel is highly corrosive resistant.

7. Future Work

The following points are my suggestion that can be proposed for future work in additive manufacturing for the production of super duplex stainless steel.

- The material can be printed with different additive manufacturing methods, and its microstructure & mechanical properties can be studied and compared. This will provide information about the impact of AM methods on microstructure & mechanical properties.
- The printing parameter like laser power, printing strategy, hatch distance, layer thickness, and scanning speed can be varied. After that, their microstructure & mechanical properties like hardness, impact test, tensile test, and different corrosion test can be performed on this material compared.
- The different heat treatment methods and different heat treatment temperatures can be tried. After that, their microstructure & mechanical properties can be studied and compared. The heat treatment applied, followed by HIP, can improve mechanical properties, which need to be tested.
- The different cooling methods like oven cooling, oil quenching, pressurized air cooling, brine quenching, and many more methods can be tried on this material after solution heat treatment. Then their microstructure & mechanical properties can be studied and compared.
- Heating the base material before beginning the superalloy printing process can aid in maintaining uniform mechanical properties throughout the alloy specimen, which must also be tested.
- An entire research might be devoted to transmission electron microscopy (TEM) under SLM circumstances to investigate the type, composition, and density of any secondary phases or inclusions present.

References

[1] W. E. Frazier, "Metal additive manufacturing: a review," *Journal of Materials Engineering and performance,* vol. 23, no. 6, pp. 1917-1928, 2014.

[2] M. Bogers, R. Hadar, and A. Bilberg, "Additive manufacturing for consumer-centric business models: Implications for supply chains in consumer goods manufacturing," *Technological forecasting and social change,* vol. 102, pp. 225-239, 2016.

[3] K. V. Wong and A. Hernandez, "A review of additive manufacturing," *International scholarly research notices,* vol. 2012, 2012.

[4] D. D. Gu, W. Meiners, K. Wissenbach, and R. Poprawe, "Laser additive manufacturing of metallic components: materials, processes and mechanisms," *International materials reviews,* vol. 57, no. 3, pp. 133-164, 2012.

[5] F. Hengsbach *et al.*, "Duplex stainless steel fabricated by selective laser melting-Microstructural and mechanical properties," *Materials & Design,* vol. 133, pp. 136-142, 2017.

[6] L. E. Murr *et al.*, "Metal fabrication by additive manufacturing using laser and electron beam melting technologies," *Journal of Materials Science & Technology,* vol. 28, no. 1, pp. 1-14, 2012.

[7] H. D. Solomon and T. Devine Jr, "Duplex Stainless Steels--A Tale of Two Phases," in *Duplex stainless steels*, 1982, pp. 693-756.

[8] A. Steels, "Stainless Steel Grade Datasheets," *Atlas Steels Technical Department: Melbourne, Australia,* 2013.

[9] J. Olsson and M. Snis, "Duplex—A new generation of stainless steels for desalination plants," *Desalination,* vol. 205, no. 1-3, pp. 104-113, 2007.

[10] S. Sharafi, "Microstructure of super-duplex stainless steels," University of Cambridge, 1993.

[11] D. Herzog, V. Seyda, E. Wycisk, and C. Emmelmann, "Additive manufacturing of metals," *Acta Materialia,* vol. 117, pp. 371-392, 2016.

[12] R. Velu, T. Calais, A. Jayakumar, and F. Raspall, "A Comprehensive Review on Bio-Nanomaterials for Medical Implants and Feasibility Studies on Fabrication of Such Implants by Additive Manufacturing Technique," *Materials,* vol. 13, no. 1, p. 92, 2020.

[13] J. Z. Li, M. R. Alkahari, N. A. B. Rosli, R. Hasan, M. N. Sudin, and F. R. Ramli, "Review of Wire Arc Additive Manufacturing for 3D Metal Printing," *International Journal of Automation Technology,* vol. 13, no. 3, pp. 346-353, 2019.

[14] T. Kurzynowski, E. Chlebus, B. Kuźnicka, and J. Reiner, "Parameters in Selective Laser Melting for processing metallic powders," *Proceedings of SPIE,* vol. 8239, p. 823914, 02/09 2012, doi: 10.1117/12.907292.

[15] D. S. Nguyen, H. S. Park, and C. M. Lee, "Optimization of selective laser melting process parameters for Ti-6Al-4V alloy manufacturing using deep learning," *Journal of Manufacturing Processes,* vol. 55, pp. 230-235, 2020.

[16] I. Buj-Corral, A. Tejo-Otero, and F. Fenollosa-Artés, "Development of AM Technologies for Metals in the Sector of Medical Implants," *Metals,* vol. 10, no. 5, p. 686, 2020.

[17] P. Bartolo *et al.*, "Biomedical production of implants by additive electro-chemical and physical processes," *CIRP annals,* vol. 61, no. 2, pp. 635-655, 2012.

[18] W. J. Sames, F. List, S. Pannala, R. R. Dehoff, and S. S. Babu, "The metallurgy and processing science of metal additive manufacturing," *International materials reviews,* vol. 61, no. 5, pp. 315-360, 2016.

[19] C. Emmelmann, J. Kranz, D. Herzog, and E. Wycisk, "Laser additive manufacturing of metals," in *Laser technology in biomimetics*: Springer, 2013, pp. 143-162.

[20] B. Nagarajan, Z. Hu, X. Song, W. Zhai, and J. Wei, "Development of micro selective laser melting: The state of the art and future perspectives," *Engineering,* vol. 5, no. 4, pp. 702-720, 2019.

[21] C. Y. Yap *et al.*, "Review of selective laser melting: Materials and applications," *Applied physics reviews,* vol. 2, no. 4, p. 041101, 2015.

[22] S. Kumar, "10.05 - Selective Laser Sintering/Melting," in *Comprehensive Materials Processing*, S. Hashmi, G. F. Batalha, C. J. Van Tyne, and B. Yilbas Eds. Oxford: Elsevier, 2014, pp. 93-134.

[23] J.-P. Kruth, J. Duflou, P. Mercelis, J. Van Vaerenbergh, T. Craeghs, and J. De Keuster, "On-line monitoring and process control in selective laser melting and laser cutting," in *Proceedings of the 5th Lane Conference, Laser Assisted Net Shape Engineering*, 2007, vol. 1, pp. 23-37.

[24] T. Craeghs, F. Bechmann, S. Berumen, and J.-P. Kruth, "Feedback control of Layerwise Laser Melting using optical sensors," *Physics Procedia,* vol. 5, pp. 505-514, 2010.

[25] J. P. Kruth and S. Kumar, "Statistical analysis of experimental parameters in selective laser sintering," *Advanced Engineering Materials,* vol. 7, no. 8, pp. 750-755, 2005.

[26] M. Rombouts, J.-P. Kruth, L. Froyen, and P. Mercelis, "Fundamentals of selective laser melting of alloyed steel powders," *CIRP annals,* vol. 55, no. 1, pp. 187-192, 2006.

[27] L. Thijs, K. Kempen, J.-P. Kruth, and J. Van Humbeeck, "Fine-structured aluminium products with controllable texture by selective laser melting of pre-alloyed AlSi10Mg powder," *Acta Materialia,* vol. 61, no. 5, pp. 1809-1819, 2013.

[28] L. N. Carter, M. M. Attallah, and R. C. Reed, "Laser powder bed fabrication of nickel-base superalloys: influence of parameters; characterisation, quantification and mitigation of cracking," *Superalloys,* vol. 2012, pp. 577-586, 2012.

[29] G. A. Granta Park, Cambridge, CB21 6AL, UK, ". TWI. What is hot cracking (solidification cracking)?, 2015.," p. 1, 2020 (Accessed 12 Jan 2021). [Online]. Available: https://www.twi-global.com/technical-knowledge/faqs/faq-what-is-hot-cracking-solidification-cracking.

[30] K. Kempen, L. Thijs, B. Vrancken, S. Buls, J. Van Humbeeck, and J. Kruth, "Producing crack-free, high density M2 Hss parts by selective laser melting: pre-

heating the baseplate," in *Proc. 24th Int. Solid Free. Fabr. Symp*, 2013, pp. 131-139.

[31] A. Dass and A. Moridi, "State of the art in directed energy deposition: from additive manufacturing to materials design," *Coatings,* vol. 9, no. 7, p. 418, 2019.

[32] A. Wimmer *et al.*, "Investigations on the influence of adapted metal-based alloys on the process of laser beam melting," *Journal of Laser Applications,* vol. 32, no. 2, p. 022029, 2020.

[33] J.-P. Kruth, L. Froyen, J. Van Vaerenbergh, P. Mercelis, M. Rombouts, and B. Lauwers, "Selective laser melting of iron-based powder," *Journal of materials processing technology,* vol. 149, no. 1-3, pp. 616-622, 2004.

[34] M. F. Zäh and S. Lutzmann, "Modelling and simulation of electron beam melting," *Production Engineering,* vol. 4, no. 1, pp. 15-23, 2010.

[35] A. Hussein, L. Hao, C. Yan, R. Everson, and P. Young, "Advanced lattice support structures for metal additive manufacturing," *Journal of Materials Processing Technology,* vol. 213, no. 7, pp. 1019-1026, 2013.

[36] W. Sames, F. Medina, W. Peter, S. Babu, and R. Dehoff, "Effect of process control and powder quality on Inconel 718 produced using electron beam melting," in *8th Int. Symp. Superalloy 718 Deriv*, 2014, pp. 409-423.

[37] P. Prabhakar, W. J. Sames, R. Dehoff, and S. S. Babu, "Computational modeling of residual stress formation during the electron beam melting process for Inconel 718," *Additive Manufacturing,* vol. 7, pp. 83-91, 2015.

[38] P. Mercelis and J. P. Kruth, "Residual stresses in selective laser sintering and selective laser melting," *Rapid prototyping journal,* 2006.

[39] R. Heim, "Structural Durability: Methods and Concepts," ed: Springer.

[40] C. Li, Z. Liu, X. Fang, and Y. Guo, "Residual stress in metal additive manufacturing," *Procedia Cirp,* vol. 71, pp. 348-353, 2018.

[41] R. Moat, A. Pinkerton, L. Li, P. Withers, and M. Preuss, "Residual stresses in laser direct metal deposited Waspaloy," *Materials Science and Engineering: A,* vol. 528, no. 6, pp. 2288-2298, 2011.

[42] M. F. Zaeh and G. Branner, "Investigations on residual stresses and deformations in selective laser melting," *Production Engineering,* vol. 4, no. 1, pp. 35-45, 2010.

[43] R. Acevedo, P. Sedlak, R. Kolman, and M. Fredel, "Residual stress analysis of additive manufacturing of metallic parts using ultrasonic waves: State of the art review," *Journal of Materials Research and Technology,* 2020.

[44] R. Chakrabarti, P. Biswas, and S. Saha, "A Review on Welding Residual Stress Measurement by Hole Drilling Technique and its Importance," *Journal of Welding and Joining,* vol. 36, no. 4, pp. 75-82, 2018.

[45] M. E. Fitzpatrick, A. T. Fry, P. Holdway, F. Kandil, J. Shackleton, and L. Suominen, "Determination of residual stresses by X-ray diffraction," 2005.

[46] M. Strøm, "Microstructural Analysis of Selective Laser Melted AlSi10Mg," University of Stavanger, Norway, 2020.

[47] S. Map, "X-ray diffraction for residual stress measurement," p. 1, 2020 (accessed Feb 19, 2021). [Online]. Available: https://www.stressmap.co.uk/x-ray-diffraction-for-measuring-residual-stress/.

[48] L. U. University College, "Crystallite Size and Strain," p. 1, 2004 (accessed Feb 28, 2021). [Online]. Available: http://pd.chem.ucl.ac.uk/pdnn/peaks/size.htm.

[49] G. Dieter, "Mechanical Metallurgy, McGraw-Hill, New York, 1986."

[50] A. P. Mouritz, *Introduction to aerospace materials*. Elsevier, 2012.

[51] D. Klarstrom, "Characteristics of nickel and nickel-base alloys," *ASM Handbook,* vol. 13, pp. 641-43, 1992.

[52] D. Peckner, I. M. Bernstein, and D. Peckner, *Handbook of stainless steels*. McGraw-Hill New York, 1977.

[53] I. Alvarez-Armas and S. Degallaix-Moreuil, *Duplex stainless steels*. John Wiley & Sons, 2013.

[54] J.-O. Nilsson, A. Wilson, B. Josefsson, and T. Thorvaldsson, "Relationship between pitting corrosion, toughness and microstructure for isothermally heat treated super duplex stainless steel," *Applications of Stainless Steel'92.,* vol. 1, pp. 280-289, 1992.

[55] Z. Brytan and J. Niagaj, "Corrosion resistance and mechanical properties of TIG and A-TIG welded joints of lean duplex stainless steel S82441/1.4662," *Archives of Metallurgy and Materials,* vol. 61, no. 2A, pp. 771--784, 2016.

[56] S. D. Kahar, "Duplex stainless steels-an overview," *International Journal of Engineering Research and Application,* vol. 7, no. 4 Pt 4, pp. 27-36, 2017.

[57] C. International, "An Introduction to Super-Duplex Stainless Steels," pp. 1-2, 2020. [Online]. Available: https://www.corrotherm.co.uk/hubfs/resources/corrotherm-introduction-super-duplex-stainless-steels.pdf.

[58] J. R. Davis, *Nickel, cobalt, and their alloys*. ASM international, 2000.

[59] T. Chen and J. Yang, "Microstructural characterization of simulated heat affected zone in a nitrogen-containing 2205 duplex stainless steel," *Materials Science and Engineering: A,* vol. 338, no. 1-2, pp. 166-181, 2002.

[60] X. Xie *et al.*, "The role of phosphorus and sulfur in inconel 718," *Superalloys 1996,* vol. 599, 1996.

[61] K. Davidson and S. Singamneni, "Selective laser melting of duplex stainless steel powders: an investigation," *Materials and Manufacturing Processes,* vol. 31, no. 12, pp. 1543-1555, 2016.

[62] K. P. Davidson and S. B. Singamneni, "Metallographic evaluation of duplex stainless steel powders processed by selective laser melting," *Rapid Prototyping Journal,* 2017.

[63] U. S. Bertoli, A. J. Wolfer, M. J. Matthews, J.-P. R. Delplanque, and J. M. Schoenung, "On the limitations of volumetric energy density as a design parameter for selective laser melting," *Materials & Design,* vol. 113, pp. 331-340, 2017.

[64] S. Papula *et al.*, "Selective laser melting of duplex stainless Steel 2205: Effect of post-processing heat treatment on microstructure, mechanical properties, and corrosion resistance," *Materials,* vol. 12, no. 15, p. 2468, 2019.

[65] W. D. Callister and D. G. Rethwisch, *Materials science and engineering: an introduction*. Wiley New York, 2018.

[66] K. Corporation., "Probing and Mapping the Mechanical Properties of 2205 Duplex Stainless Steel," pp. 1-2, Jul 1 2016 (acessed 19 jan 2021). [Online]. Available: https://www.azonano.com/article.aspx?ArticleID=4247.

[67] A. T. 938-C, "Use of Duplex Stainless Steels in the Oil Refining Industry," 2015.

[68] B. Messer, V. Oprea, and A. Wright, "Duplex stainless steel welding: best practices," *Stainless Steel World,* vol. 53, 2007.

[69] "Practical Guidelines for the Fabrication of Duplex Stainless Steels," 2014. [Online]. Available: https://www.imoa.info/molybdenum-media-centre/downloads/practical-guidelines/fabrication-series.php.

[70] I. m. association, "Practical Guidelines for the Fabrication of Duplex Stainless Steels," pp. 25-35, 2014 (acessed on 21 jan 2021). [Online]. Available: https://www.imoa.info/molybdenum-media-centre/downloads/practical-guidelines/fabrication-series.php.

[71] J.-O. Nilsson, "Super duplex stainless steels," *Materials science and technology,* vol. 8, no. 8, pp. 685-700, 1992.

[72] K. Easterling, *Introduction to the physical metallurgy of welding*. Elsevier, 2013.

[73] S. Heino, *Precipitation behaviour in superaustenitic stainless steel with emphasis on welding*. 1998.

[74] J.-O. Nilsson and G. Chai, "The physical metallurgy of duplex stainless steels," *Proceedings duplex stainless steel,* vol. 97, no. 5, pp. 73-82, 1997.

[75] M. Pohl, O. Storz, and T. Glogowski, "Effect of intermetallic precipitations on the properties of duplex stainless steel," *Materials characterization,* vol. 58, no. 1, pp. 65-71, 2007.

[76] T. Børvik *et al.*, "Pipe fittings in duplex stainless steel with deviation in quality caused by sigma phase precipitation," *Materials Science and Engineering: A,* vol. 527, no. 26, pp. 6945-6955, 2010.

[77] C. Oernek and D. L. Engelberg, "Correlative EBSD and SKPFM characterisation of microstructure development to assist determination of corrosion propensity in grade 2205 duplex stainless steel," *Journal of Materials Science,* vol. 51, no. 4, pp. 1931-1948, 2016.

[78] R. Gunn, *Duplex stainless steels: microstructure, properties and applications*. Elsevier, 1997.

[79] A. Ramirez, J. Lippold, and S. Brandi, "The relationship between chromium nitride and secondary austenite precipitation in duplex stainless steels," *Metallurgical and materials transactions A,* vol. 34, no. 8, pp. 1575-1597, 2003.

[80] P. Chavdarov, "Electron Beam Welding of Super duplex Stainless Steel UNS S32750," *Stainless Steel World,* 2007.

[81] P. Southwick and R. Honeycombe, "Precipitation of M23C6 at austenite/ferrite interfaces in duplex stainless steel," *Metal Science,* vol. 16, no. 10, pp. 475-482, 1982.

[82] T. Thorvaldsson, H. Eriksson, J. Kutka, and A. Salwén, "Influence of microstructure on mechanical properties of a duplex stainless steel," *Stainless Steel'84, Chalmers University of Technology,* pp. 101-105, 1984.

[83] H. Okada and R. Staehle, "Predictive Methods for Assessing Corrosion Damage to BWR Piping and PWR Steam Generators," *H. Okada and R. Staehle, Eds., 400 pages, 8. 5 x 11 inches(21. 5 x 28 cm), hard cloth. 1982. NACE, Houston, Tx,* 1982.

[84] P. Auger, F. Danoix, A. Menand, S. Bonnet, J. Bourgoin, and M. Guttmann, "Atom probe and transmission electron microscopy study of aging of cast duplex stainless steels," *Materials Science and Technology,* vol. 6, no. 3, pp. 301-313, 1990.

[85] D. Henriet, P. Lacombe, B. Baroux, and G. Beranger, "Stainless steel," *Phys Les Ulis,* p. 823, 1993.

[86] J. Charles, "Proceedings Conf. Duplex Stainless Steels," *Beaune, France, Les editions de physique,* vol. 1, pp. 3-48, 1991.

[87] J. Charles, "Proceedings Conf. Duplex Stainless Steels," *Beaune, France, Les editions de physique,* vol. 1, pp. 151-168, 1991.

[88] R. Gunn, *Duplex stainless steels: microstructure, properties and applications*. Elsevier, 1997, pp. 20-50.

[89] S. David, J. Vitek, R. Reed, and T. Hebble, "Effect of rapid solidification on stainless steel weld metal microstructures and its implications on the Schaeffler diagram," Oak Ridge National Lab., TN (USA), 1987.

[90] D. Steiner Petrovič, M. Pirnat, G. Klančnik, P. Mrvar, and J. Medved, "The effect of cooling rate on the solidification and microstructure evolution in duplex stainless steel: A DSC study," *Journal of thermal analysis and calorimetry,* vol. 109, no. 3, pp. 1185-1191, 2012.

[91] M. Martins and L. C. Casteletti, "Effect of heat treatment on the mechanical properties of ASTM A 890 Gr6A super duplex stainless steel," *Journal of ASTM International,* vol. 2, no. 1, pp. 1-14, 2005.

[92] l. alloys, "SAF2507 (Alloy 32750)," blog p. 2, 2020. [Online]. Available: https://www.langleyalloys.com/en/products/saf2507/.

[93] R. E. Smallman and A. Ngan, *Physical metallurgy and advanced materials*. Elsevier, 2011.

[94] G. Mohamed and R. Hegazy, "Comparison of GUM and Monte Carlo methods for the uncertainty estimation in hardness measurements," *International Journal of Metrology and Quality Engineering,* vol. 8, p. 14, 01/01 2017, doi: 10.1051/ijmqe/2017014.

[95] G. N. Nigon, O. B. Isgor, and S. Pasebani, "The effect of annealing on the selective laser melting of 2205 duplex stainless steel: Microstructure, grain orientation, and manufacturing challenges," *Optics & Laser Technology,* vol. 134, p. 106643, 2021.

[96] Z. Ahmad, *Principles of corrosion engineering and corrosion control*. Elsevier, 2006.

[97] P. Pohjanne, L. Carpén, T. Hakkarainen, and P. Kinnunen, "A method to predict pitting corrosion of stainless steels in evaporative conditions," *Journal of constructional steel research,* vol. 64, no. 11, pp. 1325-1331, 2008.

[98] A. J. Sedriks, "Corrosion of stainless steel, 2," pp. 156-210, 1996.

[99] M. Honarvar Nazari and X. Shi, "Vehicle Risks of Winter Road Operations and Best Management Practices," 2018, pp. 241-272.

[100] N. Perez, "Electrochemistry and Corrosion Science. 2004, Hingham, MA," ed: USA: Kluwer Academic Publishers.

[101] S. D. Cramer *et al.*, *ASM handbook*. ASM international Materials Park, Ohio, 2003.

[102] Y. Hu *et al.*, "Effects of Micro-Sized Ferrite and Austenite Grains on the Pitting Corrosion Behavior of Lean Duplex Stainless Steel 2101," *Metals,* vol. 7, no. 5, p. 168, 2017.

[103] A. Di Gianfrancesco, "Technologies for chemical analyses, microstructural and inspection investigations," in *Materials for ultra-supercritical and advanced ultra-supercritical power plants*: Elsevier, 2017, pp. 197-245.

[104] N. I. P. FOCUS, "SEM Technology Overview – Scanning Electron Microscopy," vol. 1, no. 1, p. 3, 12.03.2021 2018. [Online]. Available: https://www.nanoimages.com/sem-technology-overview/.

[105] P. J. Goodhew and J. Humphreys, *Electron microscopy and analysis*. CRC Press, 2000.

[106] J. I. Goldstein, D. E. Newbury, J. R. Michael, N. W. Ritchie, J. H. J. Scott, and D. C. Joy, *Scanning electron microscopy and X-ray microanalysis*. Springer, 2017.

[107] P. Goodhew, "General introduction to transmission electron microscopy (TEM)," *Aberration-Corrected Analytical Transmission Electron Microscopy,* pp. 1-19, 2011.

[108] J. W. Eccles, *An electron energy loss spectroscopy study of metallic nanoparticles of gold and silver*. The University of Manchester (United Kingdom), 2010.

[109] D. B. Williams and C. B. Carter, "The transmission electron microscope," in *Transmission electron microscopy*: Springer, 1996, pp. 3-17.

[110] M. A. Anam, J. Dilip, D. Pal, and B. Stucker, "Effect of scan pattern on the microstructural evolution of Inconel 625 during selective laser melting," in *Proceedings of 25th Annual International Solid Freeform Fabrication Symposium*, 2014.

[111] T. H. Iversen, "Intragranular chromium nitride precipitates in duplex and superduplex stainless steel," pp 14, Institutt for materialteknologi, 2012.

[112] A. Designation, "Standard test methods for pitting and crevice corrosion resistance of stainless steels and related alloys by use of ferric chloride solution," *ASTM International,* p. 4, 2011.

[113] K. Saeidi, S. Alvi, F. Lofaj, V. I. Petkov, and F. Akhtar, "Advanced mechanical strength in post heat treated SLM 2507 at room and high temperature promoted by hard/ductile sigma precipitates," *Metals,* vol. 9, no. 2, p. 199, 2019.

[114] K. Saeidi, L. Kevetkova, F. Lofaj, and Z. Shen, "Novel ferritic stainless steel formed by laser melting from duplex stainless steel powder with advanced mechanical properties and high ductility," *Materials Science and Engineering: A,* vol. 665, pp. 59-65, 2016.

[115] J. C. Lippold, *Welding metallurgy and weldability*. pp 389-391 Wiley Online Library, 2015.

[116] B.-H. Shin, J. Park, J. Jeon, S.-b. Heo, and W. Chung, "Effect of cooling rate after heat treatment on pitting corrosion of super duplex stainless steel UNS S 32750," *Anti-Corrosion Methods and Materials,* 2018.

[117] D. Zou, Y. Han, W. Zhang, and J. Yu, "Sigma phase precipitation and properties of super-duplex stainless steel UNS S32750 aged at the nose temperature," *Journal of Wuhan University of Technology-Mater. Sci. Ed.,* vol. 26, no. 2, pp. 182-185, 2011.

[118] D. Fellicia, B. Kurniawan, D. Wulanari, A. Purniawan, and A. Wibisono, "Study of sigma phase in duplex SAF 2507," in *IOP Conference Series: Materials Science and Engineering*, 2017, vol. 202, no. 1: IOP Publishing, p. 012039.

[119] Z. Zhang, H. Jing, L. Xu, Y. Han, L. Zhao, and J. Zhang, "Influence of microstructure and elemental partitioning on pitting corrosion resistance of duplex stainless steel welding joints," *Applied Surface Science,* vol. 394, pp. 297-314, 2017.

[120] N. Pettersson, R. F. Pettersson, and S. Wessman, "Precipitation of chromium nitrides in the super duplex stainless steel 2507," *Metallurgical and Materials Transactions A,* vol. 46, no. 3, pp. 1062-1072, 2015.

[121] I. Moreno, J. F. Almagro, and X. Llovet, "Determination of nitrogen in duplex stainless steels by EPMA," *Microchimica Acta,* vol. 139, no. 1-4, pp. 105-110, 2002.

[122] A. F. Padilha, C. F. Tavares, and M. A. Martorano, "Delta ferrite formation in austenitic stainless steel castings," in *Materials Science Forum*, 2013, vol. 730: Trans Tech Publ, pp. 733-738.

[123] Z. Wei, J. Laizhu, H. Jincheng, and S. Hongmei, "Effect of ageing on precipitation and impact energy of 2101 economical duplex stainless steel," *Materials characterization,* vol. 60, no. 1, pp. 50-55, 2009.

[124] M. Davanageri, S. Narendranath, and R. Kadoli, "Influence of ageing time on hardness, microstructure and wear behaviour of AISI2507 super duplex stainless steel," *Materials Research Express,* vol. 4, no. 8, p. 086506, 2017.

[125] F. Tehovnik, B. Arzensek, B. Arh, D. Skobir, B. Pirnar, and B. Zuzek, "Microstructure evolution in SAF 2507 super duplex stainless steel," *Mater. Technol,* vol. 45, no. 4, pp. 339-345, 2011.

[126] S. Ghosh and S. Mondal, "Effect of heat treatment on microstructure and mechanical properties of duplex stainless steel," *Transactions of the Indian Institute of Metals,* vol. 61, no. 1, pp. 33-37, 2008.

[127] T. Hong and M. Nagumo, "Effect of surface roughness on early stages of pitting corrosion of type 301 stainless steel," *Corrosion science,* vol. 39, no. 9, pp. 1665-1672, 1997.

Appendix

Appendix A: Microstructure Analysis using OM

A1. As-printed sample

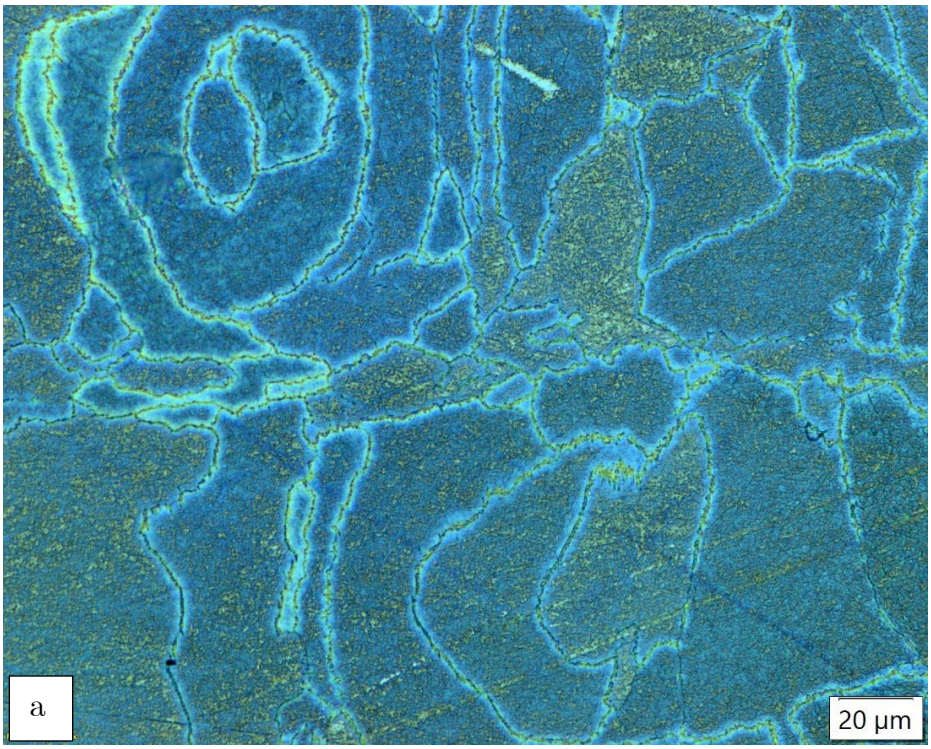

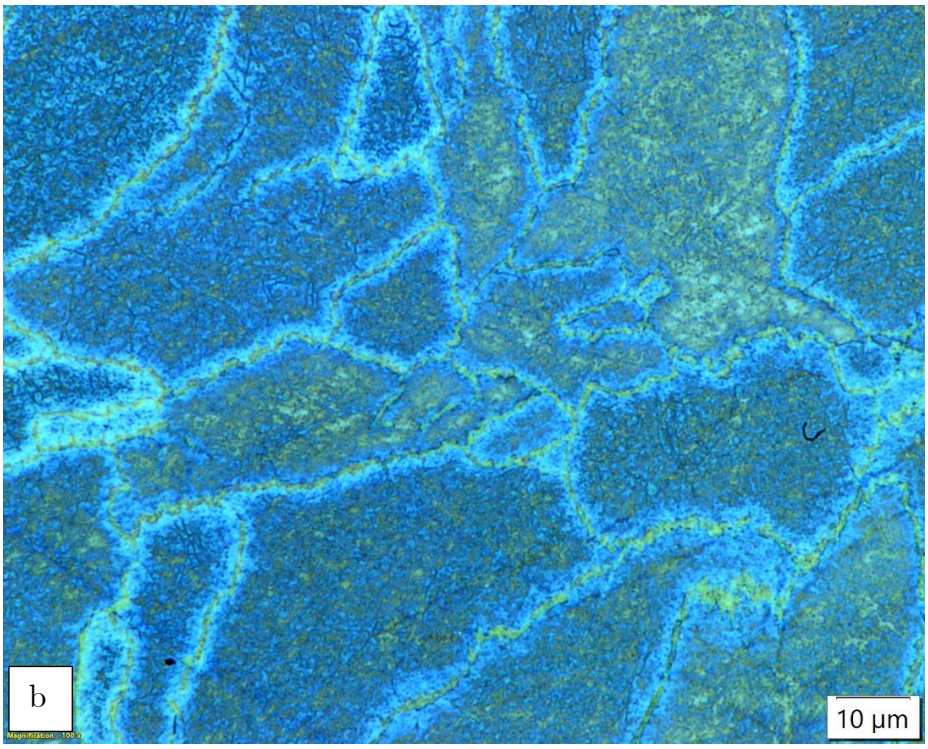

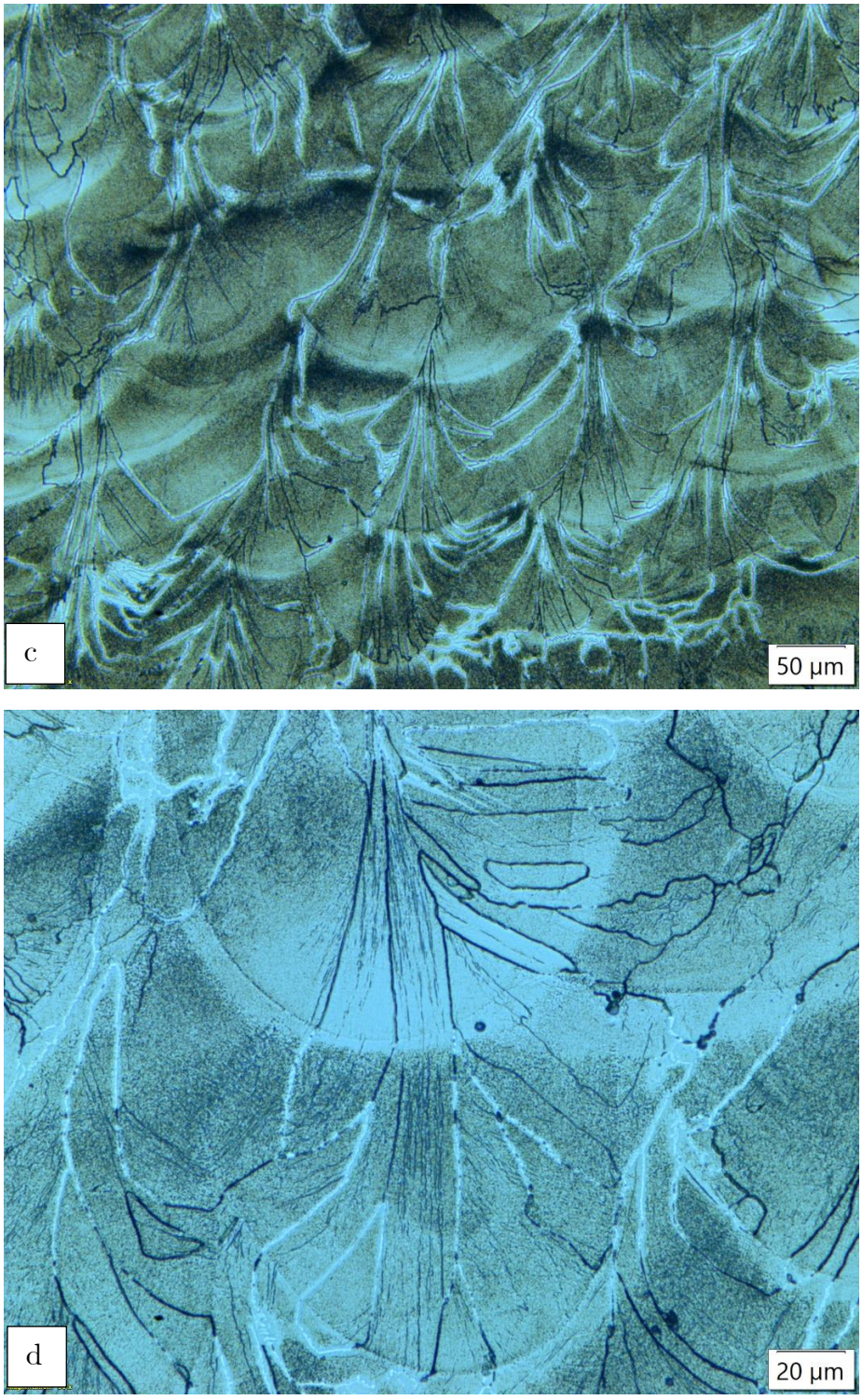

Figure I: *Microstructure of As-printed Sample (a) Perpendicular to Build Direction of Magnification 50x (b) Perpendicular to Build Direction of Magnification 100x (c) Parallel to Build Direction of Magnification 20x (d) Parallel to Build Direction of Magnification 50x*

Melt pool Depth Measurement

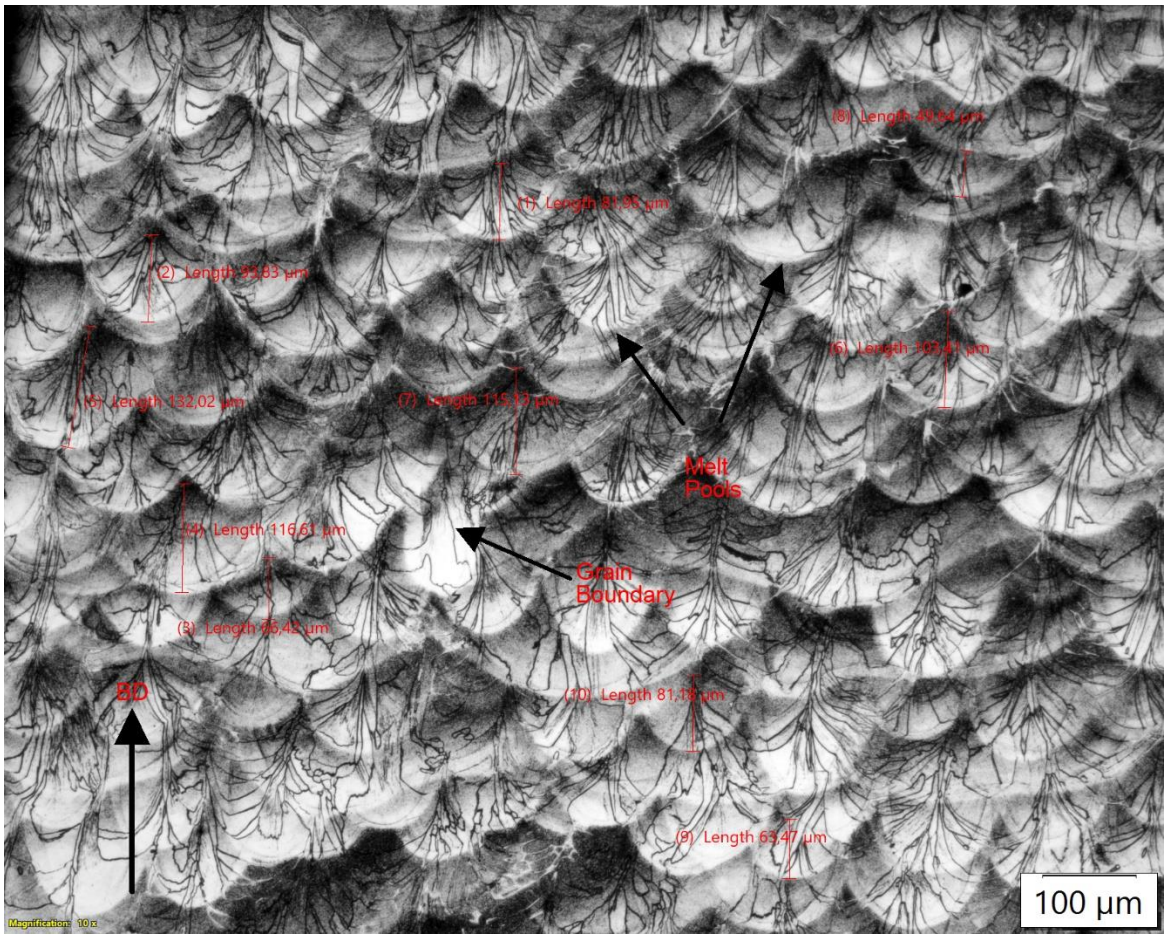

Figure II: *Melt pool Depth Measurement*

Table I: *Measurement of Melt pool Depth*

Type	Melt pool Depth [µm]
Arbitrary Line 1	81.95
Arbitrary Line 2	93.83
Arbitrary Line 3	66.42
Arbitrary Line 4	116.61
Arbitrary Line 5	132.02
Arbitrary Line 6	103.41
Arbitrary Line 7	115.13
Arbitrary Line 8	49.64
Arbitrary Line 9	63.47
Arbitrary Line 10	81.18
Count	10
Minimum	49.64
Maximum	132.02
Average	90.37

Grain Size Measurement

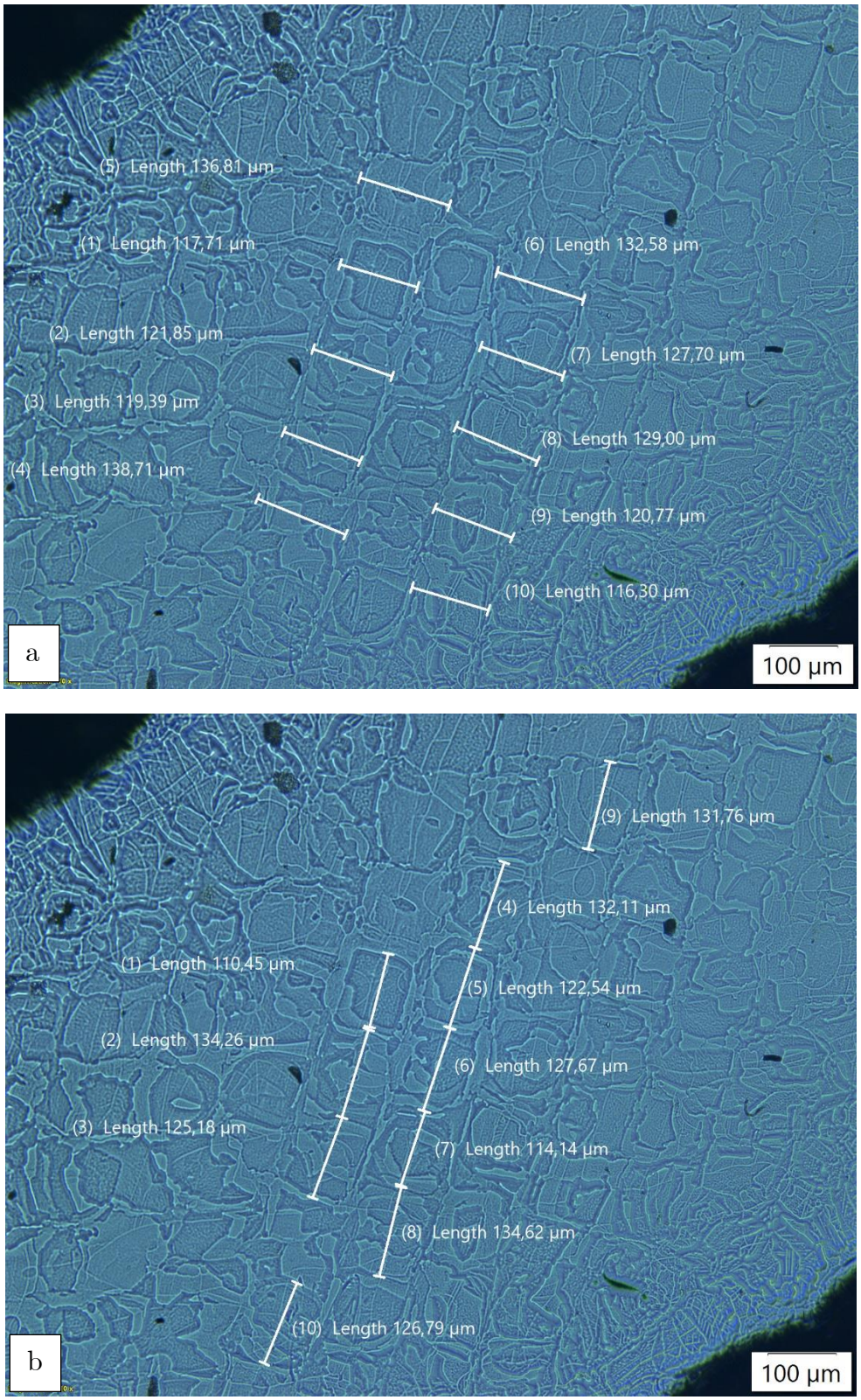

Figure III: *Grain size measurement (a) length measurement (b) width measurement*

Table II: *Grain size measurement*

Type	Length [µm]	width [µm]
Arbitrary Line 1	117.71	110.45
Arbitrary Line 2	121.85	134.26
Arbitrary Line 3	119.39	125.18
Arbitrary Line 4	138.71	132.11
Arbitrary Line 5	136.81	122.54
Arbitrary Line 6	132.58	127.67
Arbitrary Line 7	127.70	114.14
Arbitrary Line 8	129.00	134.62
Arbitrary Line 9	120.77	131.76
Arbitrary Line 10	116.30	126.79
Average Value	**126.08**	**125.95**
Standard Deviation	**7.65**	**7.82**

A2. Heat-treated sample at 1000 ° C for 1hour and water Quenched

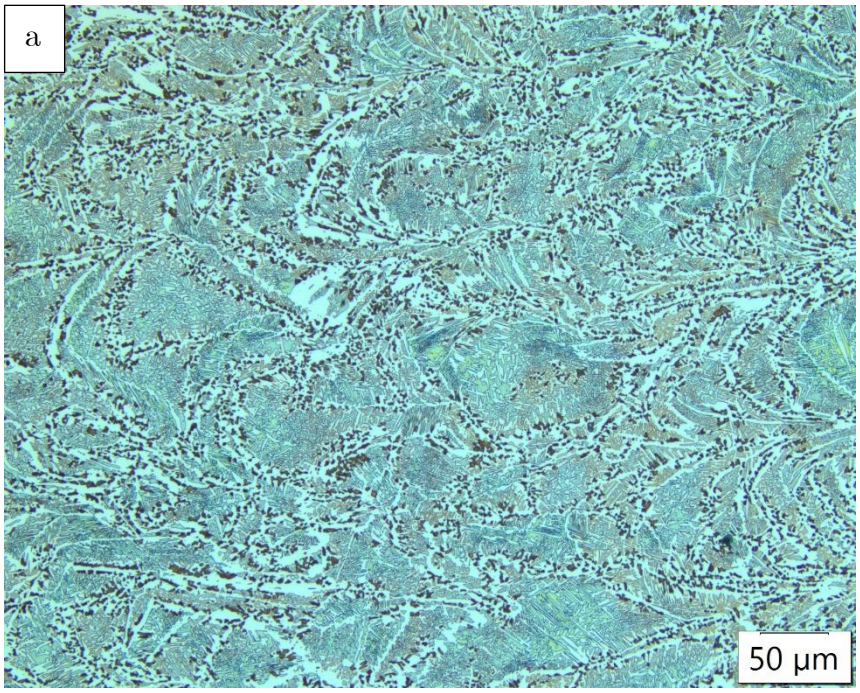

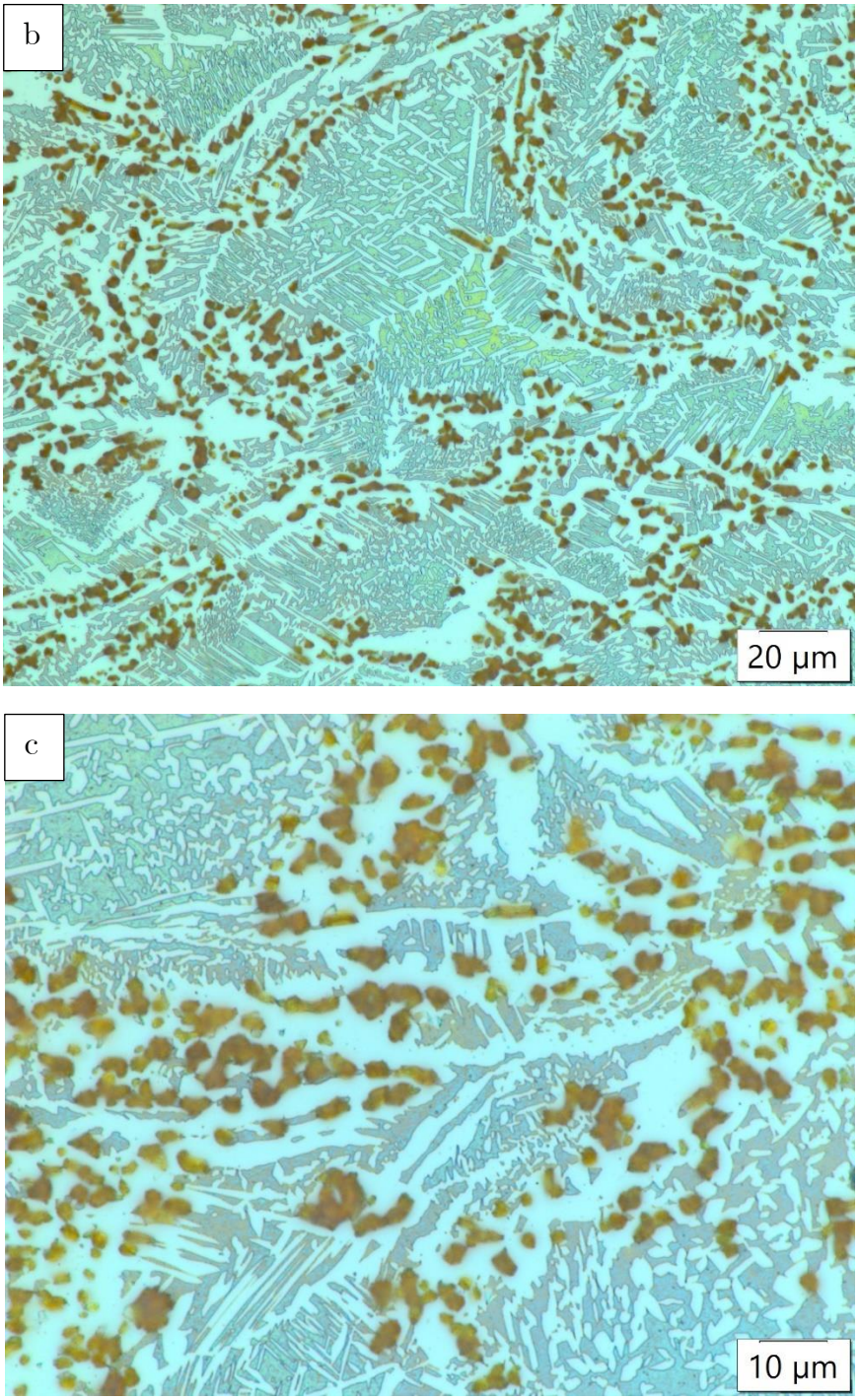

Figure IV: *Microstructure of heat-treated sample at 1000 ° C for 1hour and water Quenched (a) Magnification 20x (b) Magnification 50x (c) Magnification 100x*

A3. Heat-treated sample at 1000 ° C for 1hour and Air-cooled

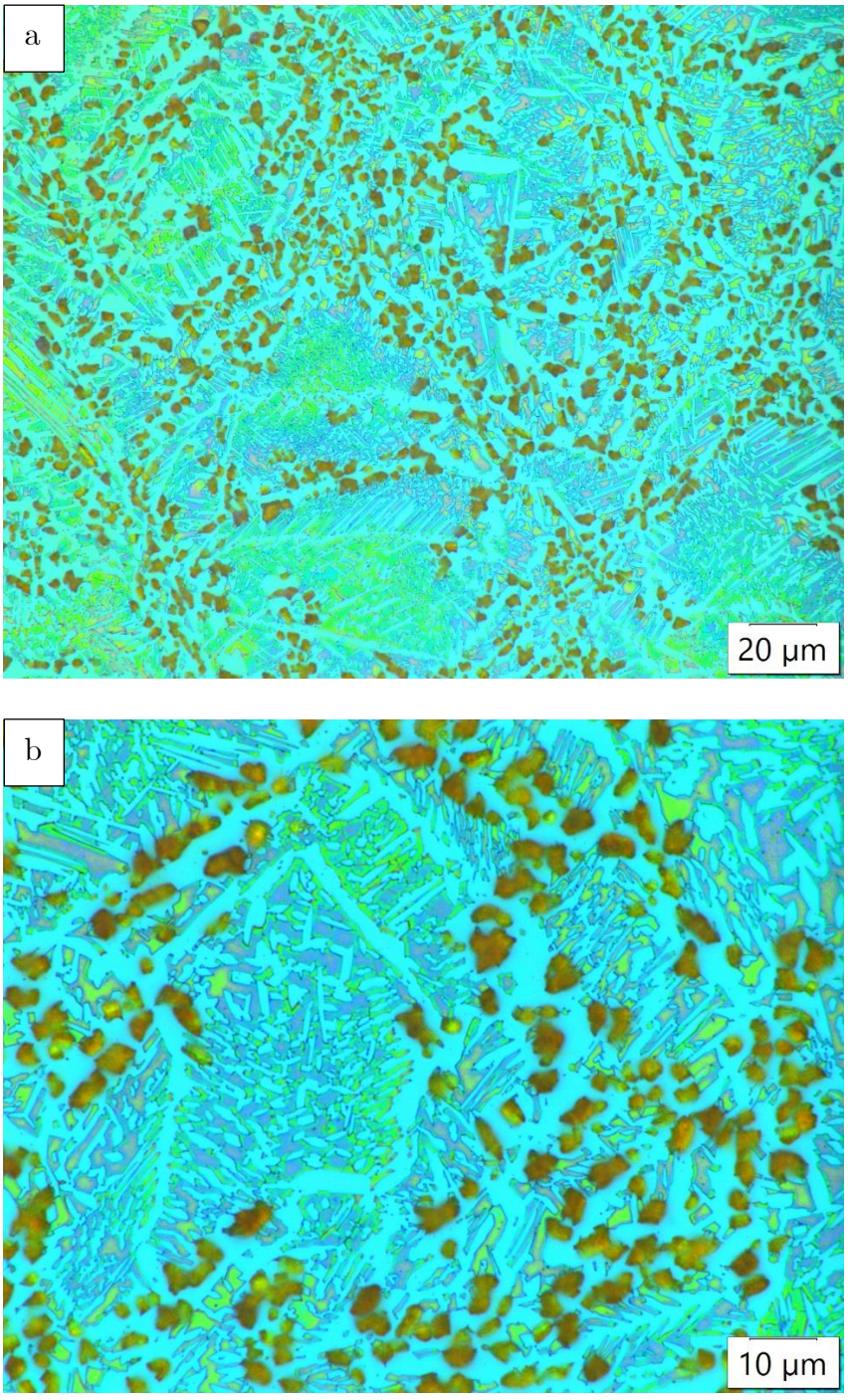

Figure V: *Microstructure of heat-treated sample at 1000 ° C for 1hour and air-cooled (a) Magnification 50x (b) Magnification 100x*

A4. Heat-treated sample at 1100 ° C for 1hour and water Quenched

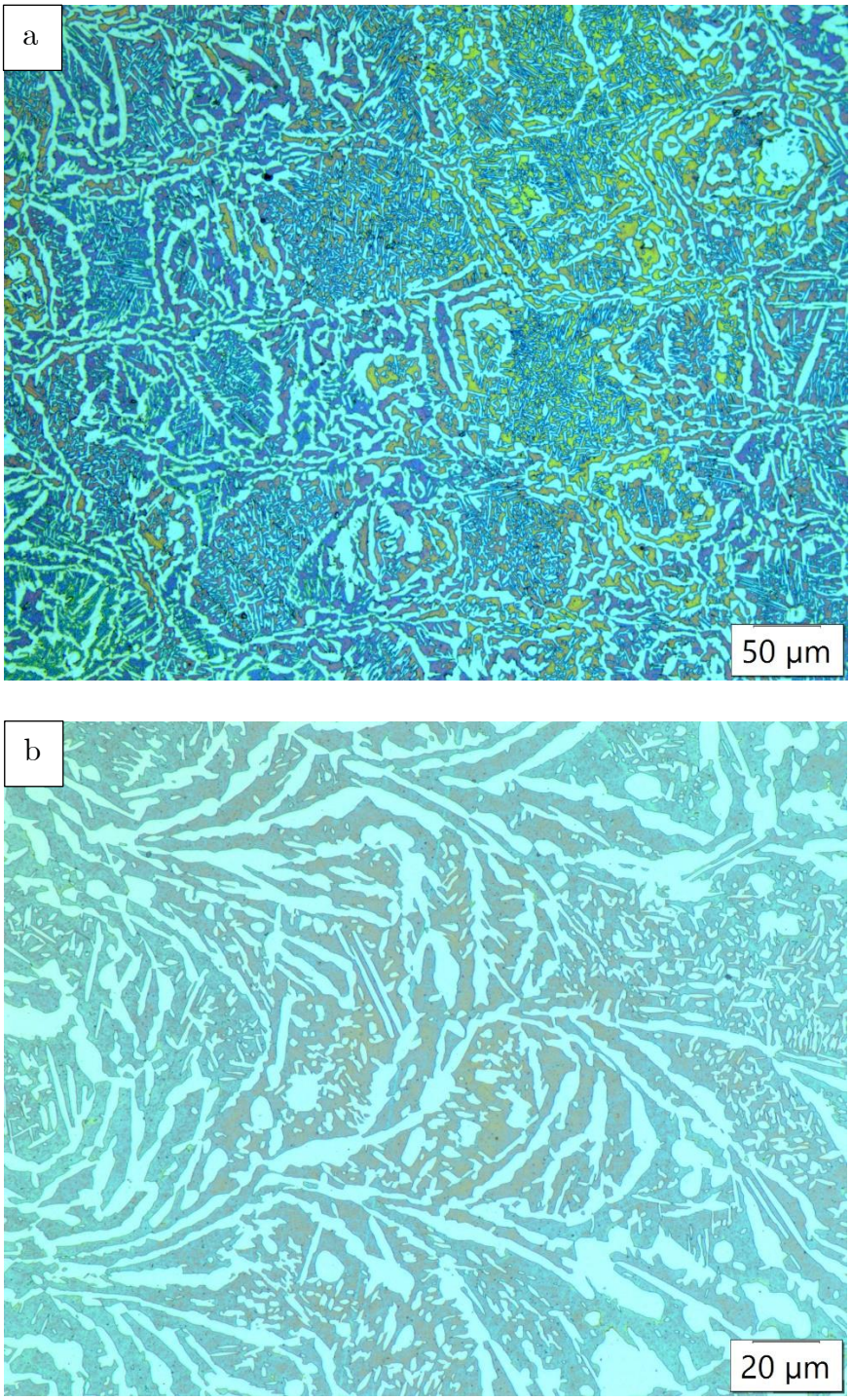

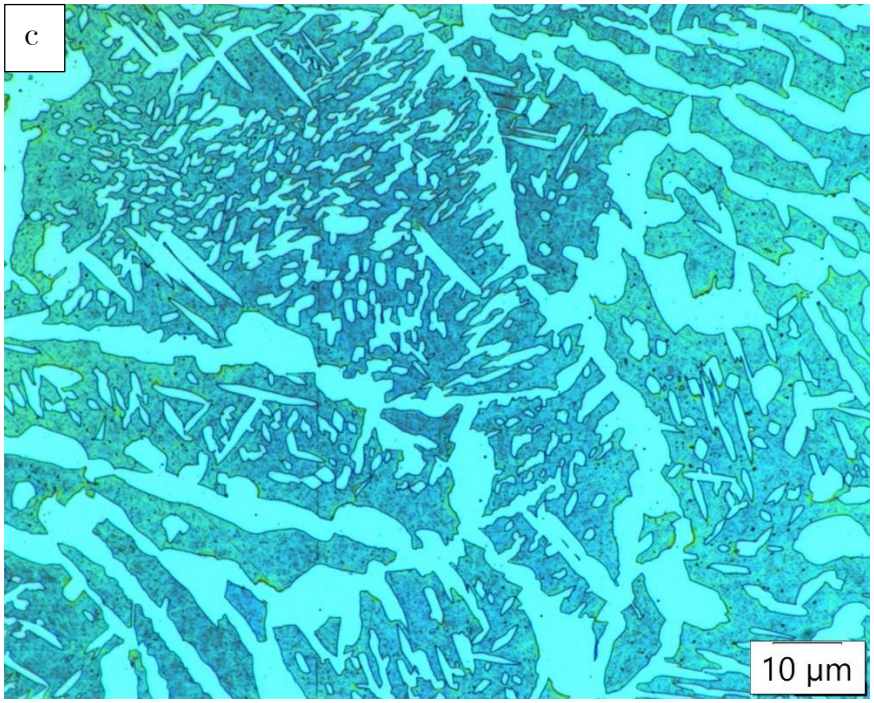

Figure VI: *Microstructure of heat-treated sample at 1100 ° C for 1hour and water Quenched (a) Magnification 20x (b) Magnification 50x (c) Magnification 100x*

A5. Heat-treated sample at 1100 ° C for 1hour and Air-cooled

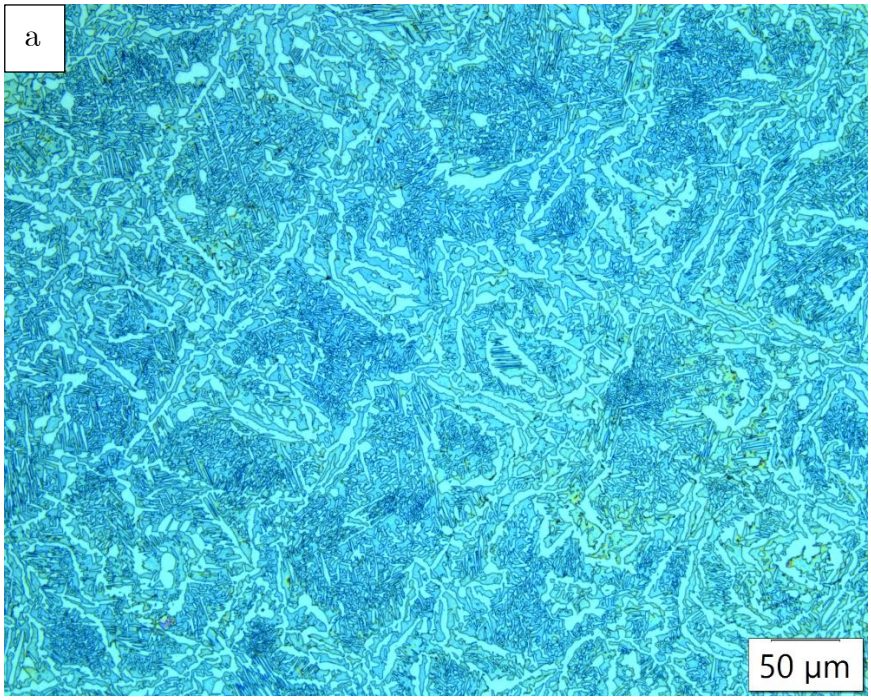

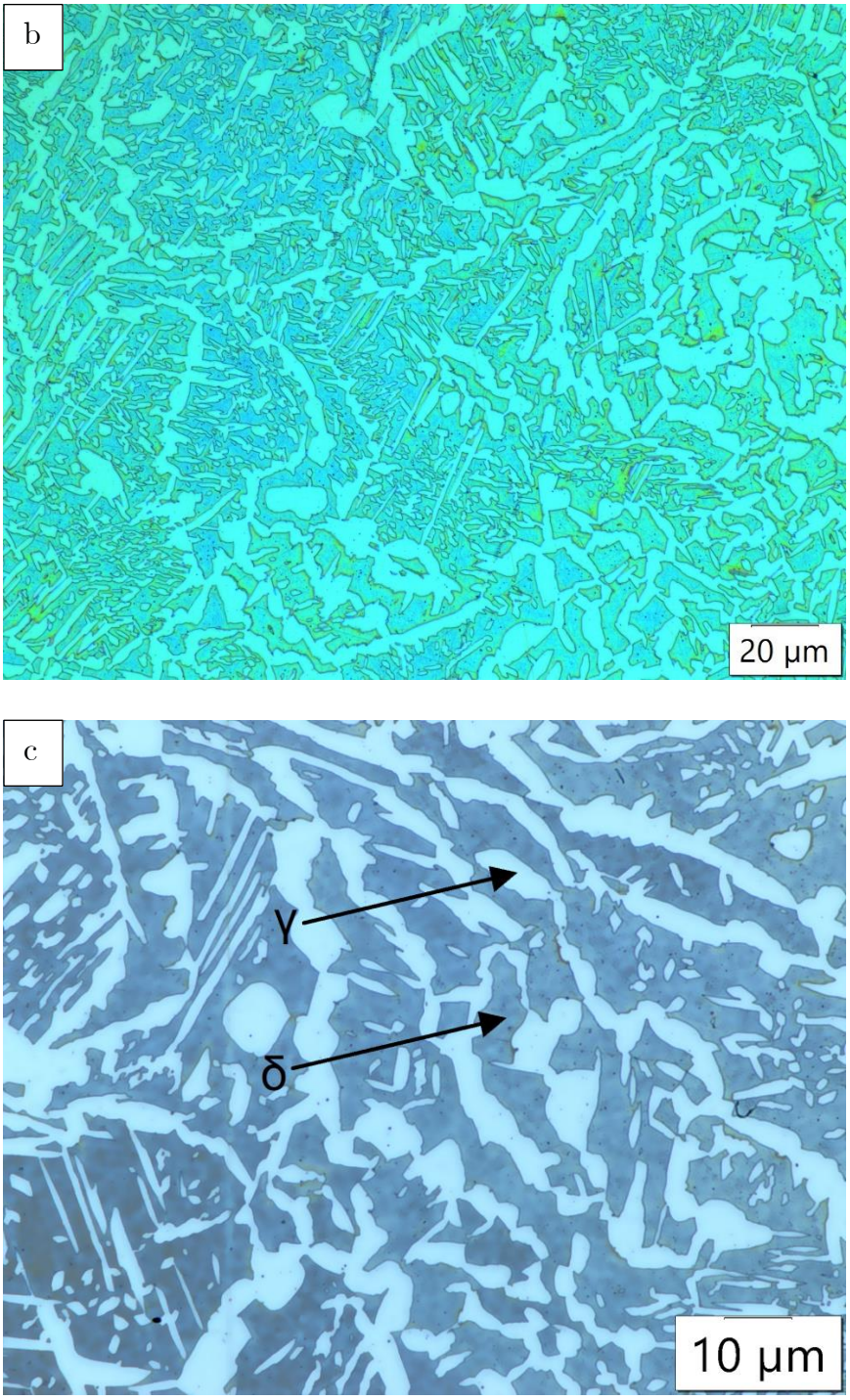

Figure VII: *Microstructure of heat-treated sample at 1100 ° C for 1hour and air-cooled (a) Magnification 20x (b) Magnification 50x (c) Magnification 100x*

A6. Heat-treated sample at 1200 ° C for 1hour and water Quenched

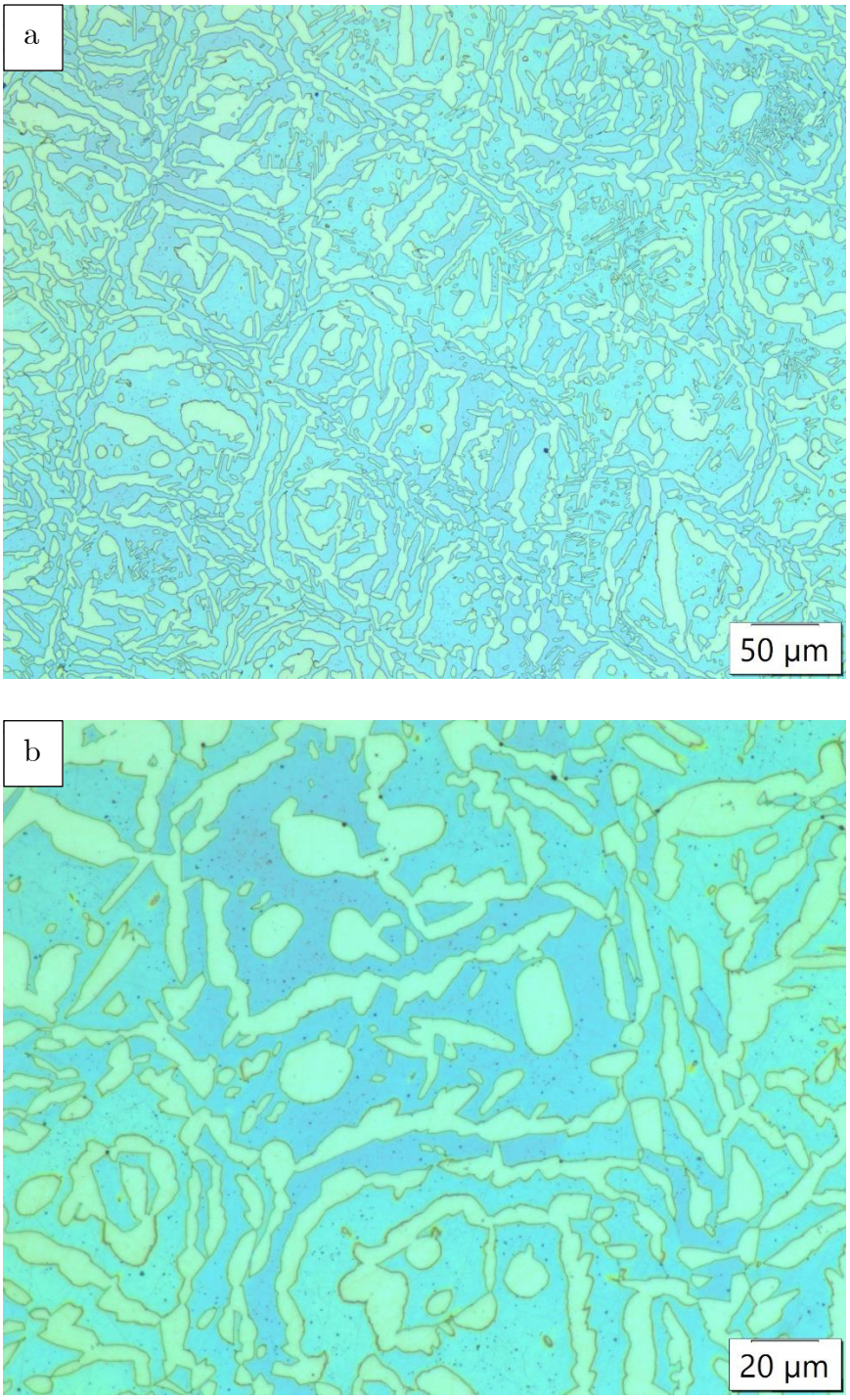

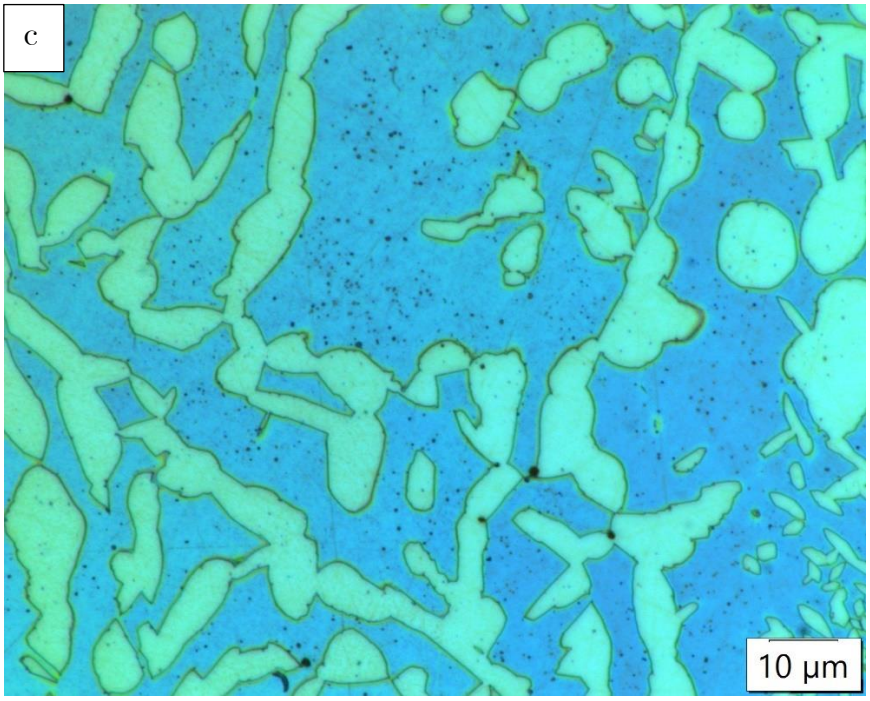

Figure VIII: *Microstructure of heat-treated sample at 1200 ° C for 1hour and water quenched (a) Magnification 20x (b) Magnification 50x (c) Magnification 100x*

A7. Heat-treated sample at 1200 ° C for 1hour and Air-cooled

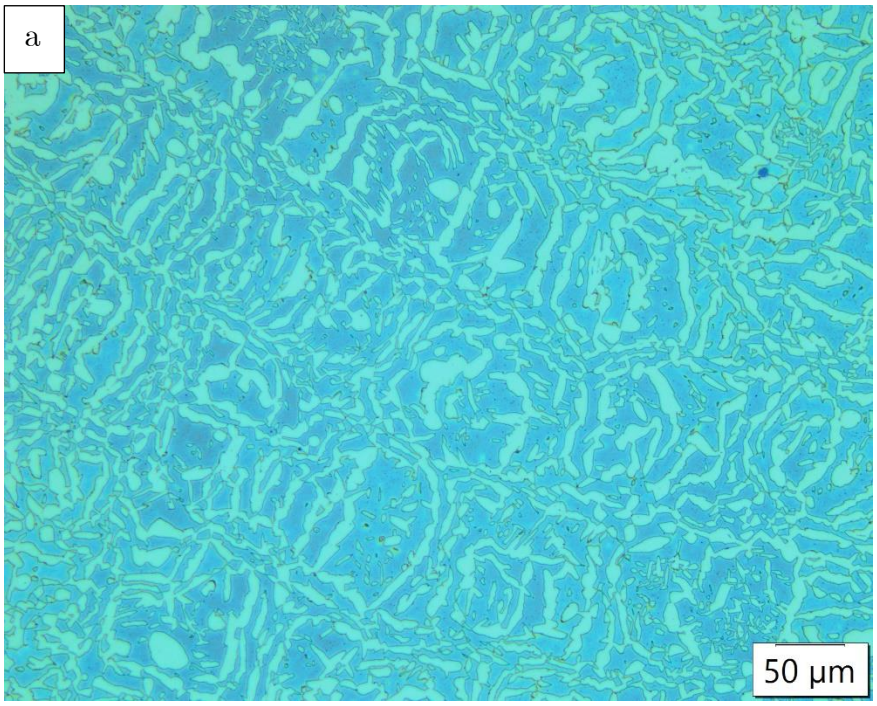

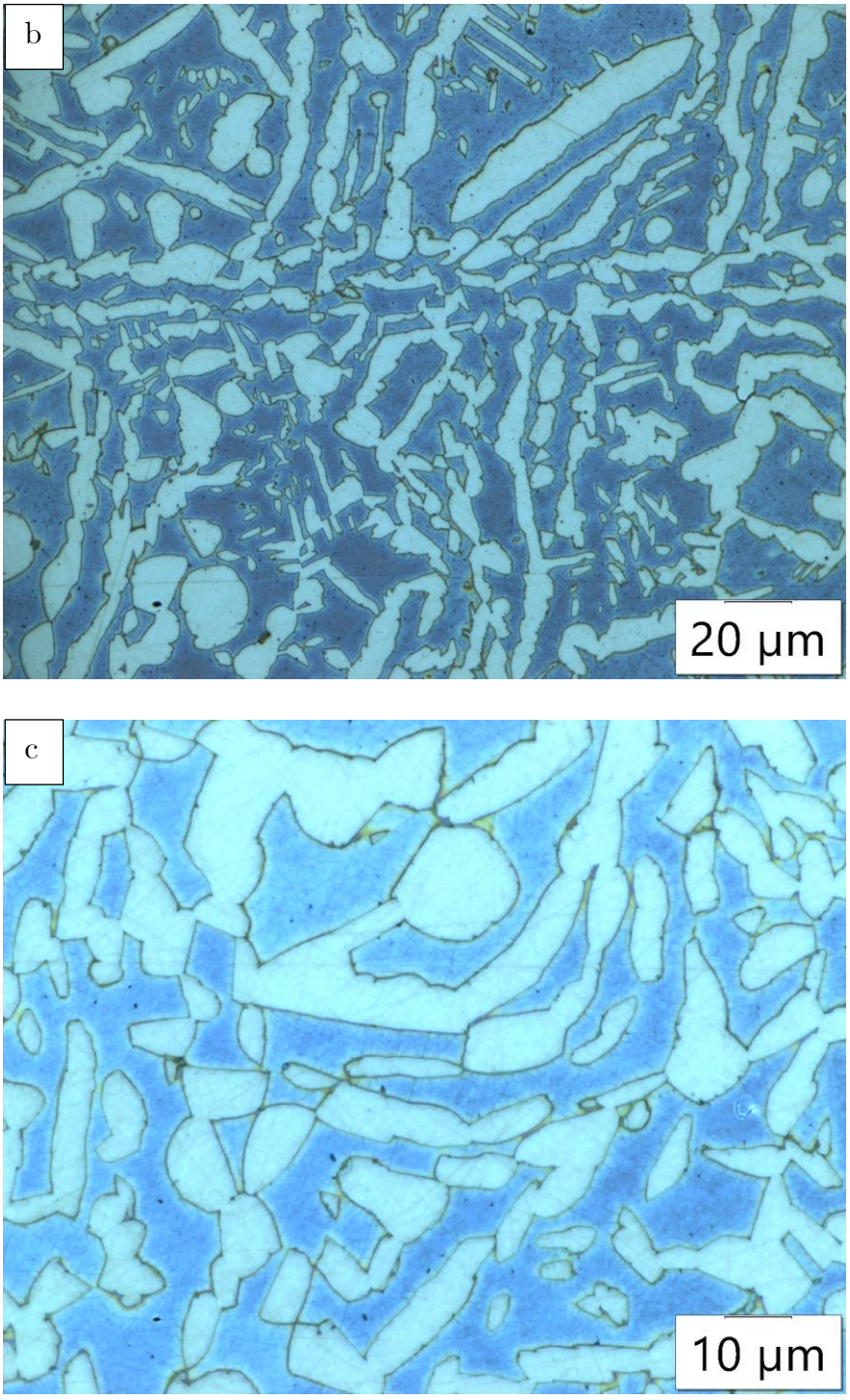

Figure IX: *Microstructure of heat-treated sample at 1200 ° C for 1hour and air cooled (a) Magnification 20x (b) Magnification 50x (c) Magnification 100x*

A8. Heat-treated sample at 1300 ° C for 1hour and water Quenched

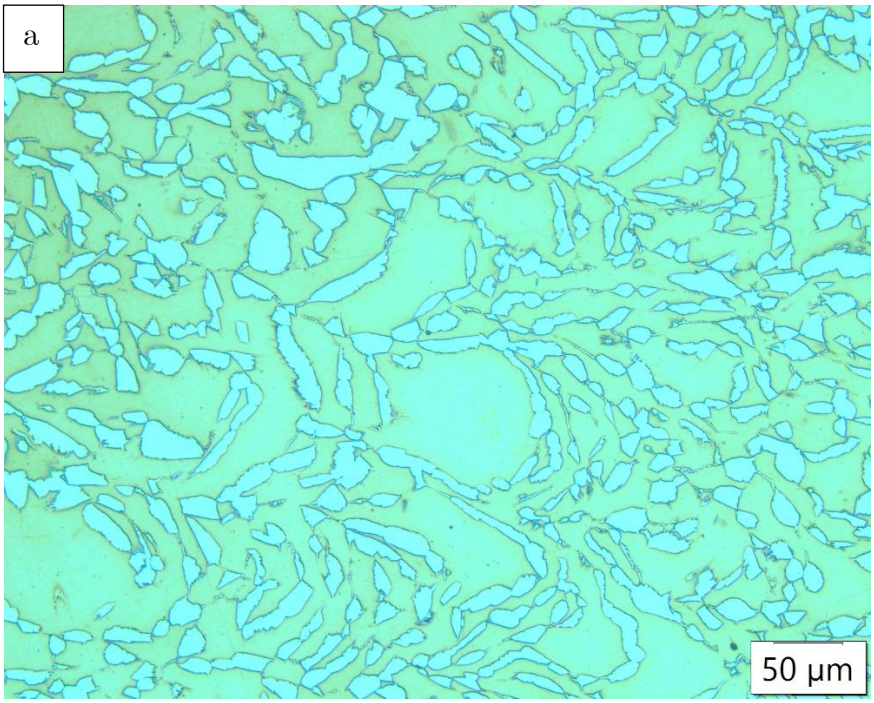

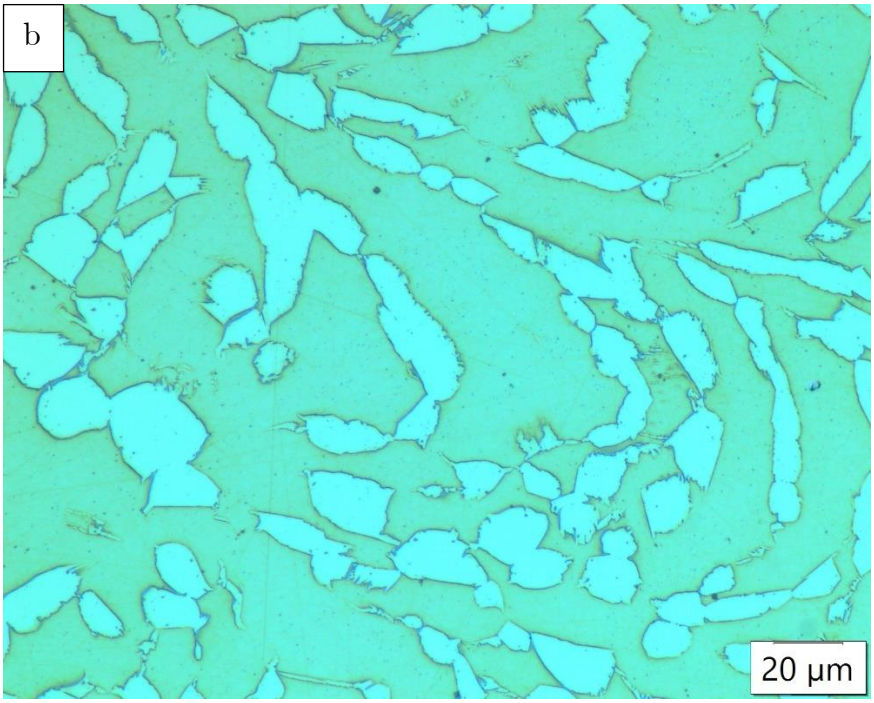

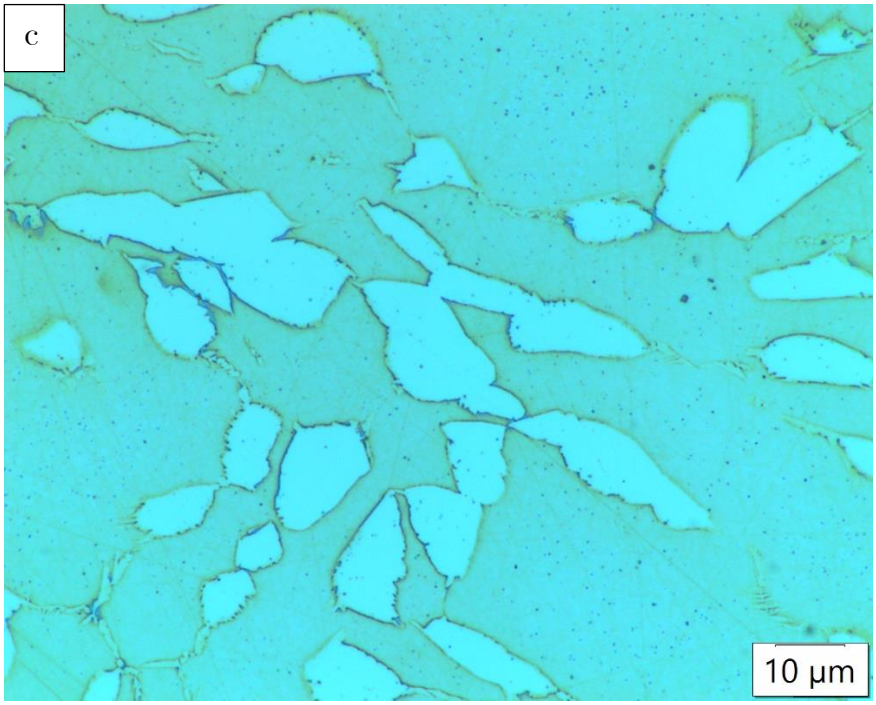

Figure X: *Microstructure of heat-treated sample at 1300 ° C for 1hour and water quenched (a) Magnification 20x (b) Magnification 50x (c) Magnification 100x*

A9. Heat-treated sample at 1300 ° C for 1hour and Air-cooled

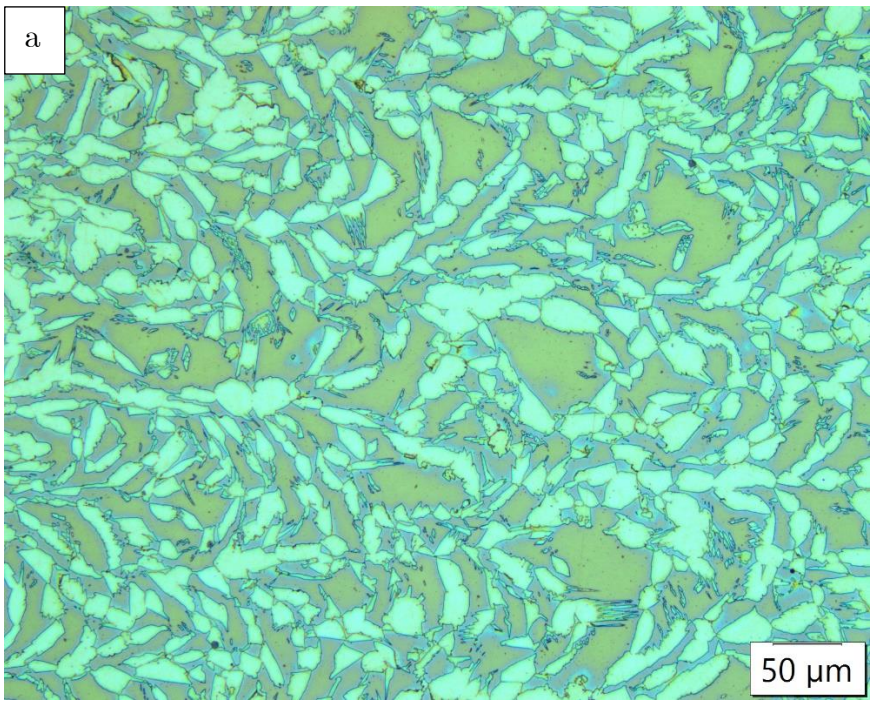

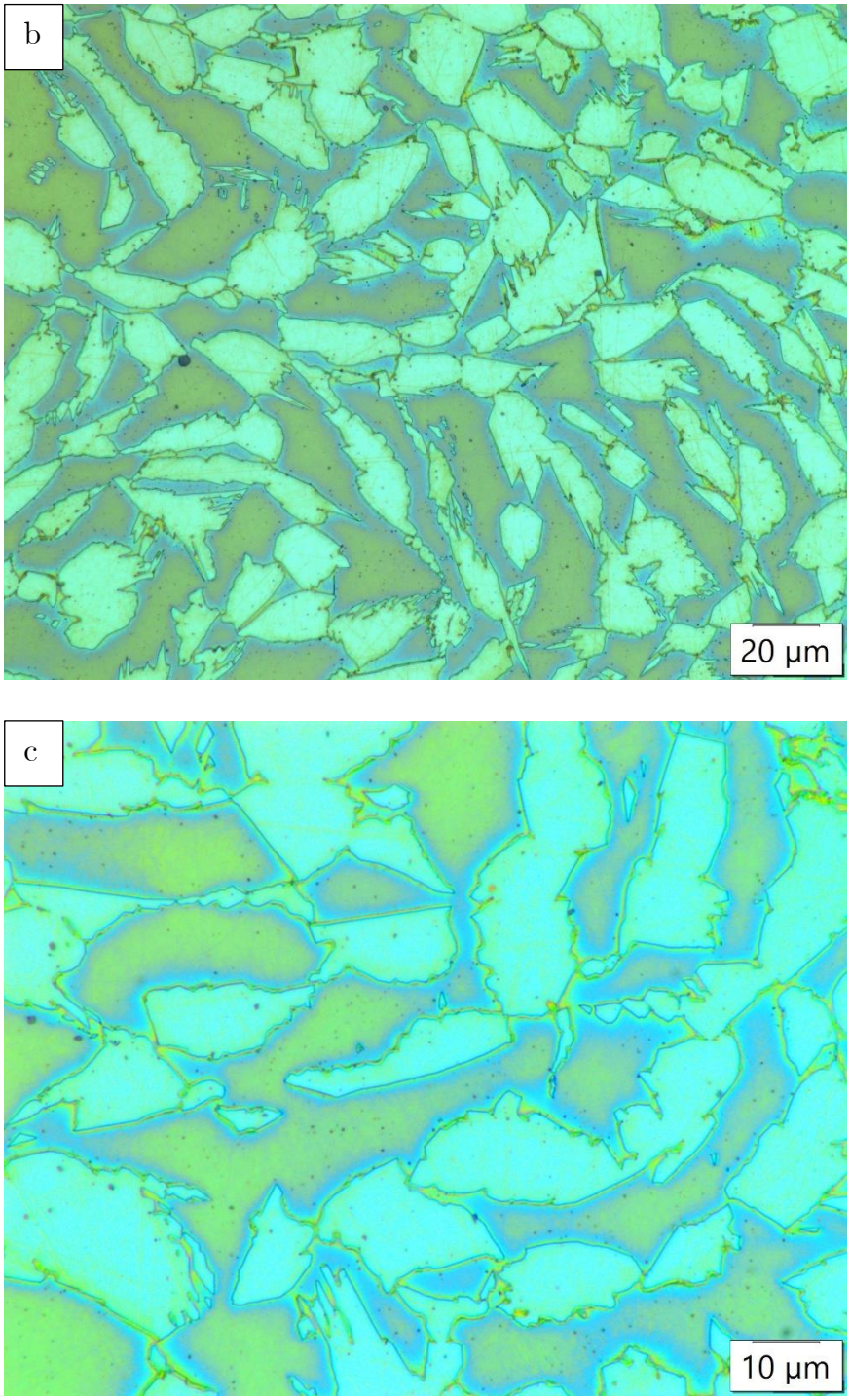

Figure XI: *Microstructure of heat-treated sample at 1200 ° C for 1hour and air cooled (a) Magnification 20x (b) Magnification 50x (c) Magnification 100x*

Appendix B: Phase Analysis using OM

B1. As-printed sample

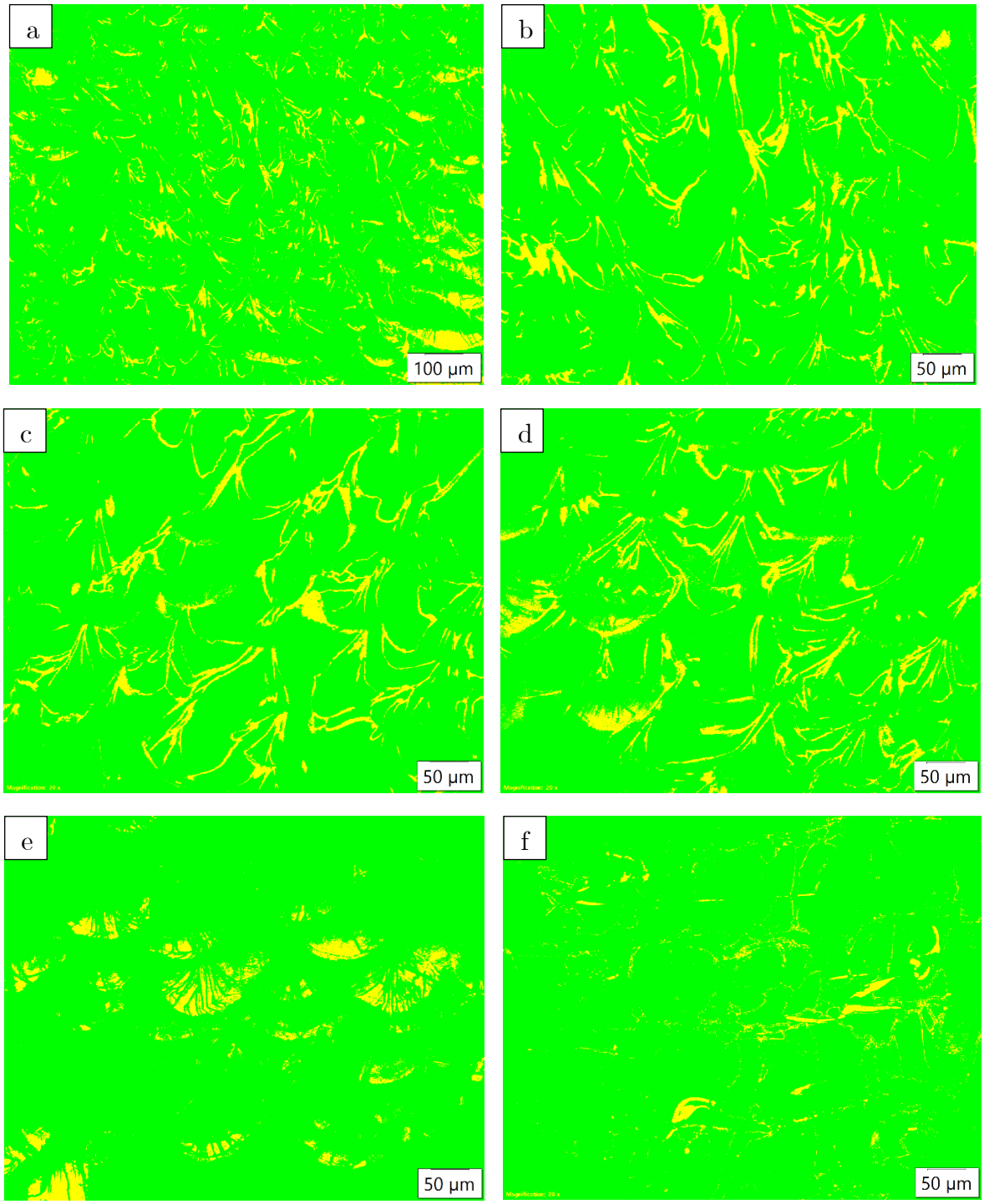

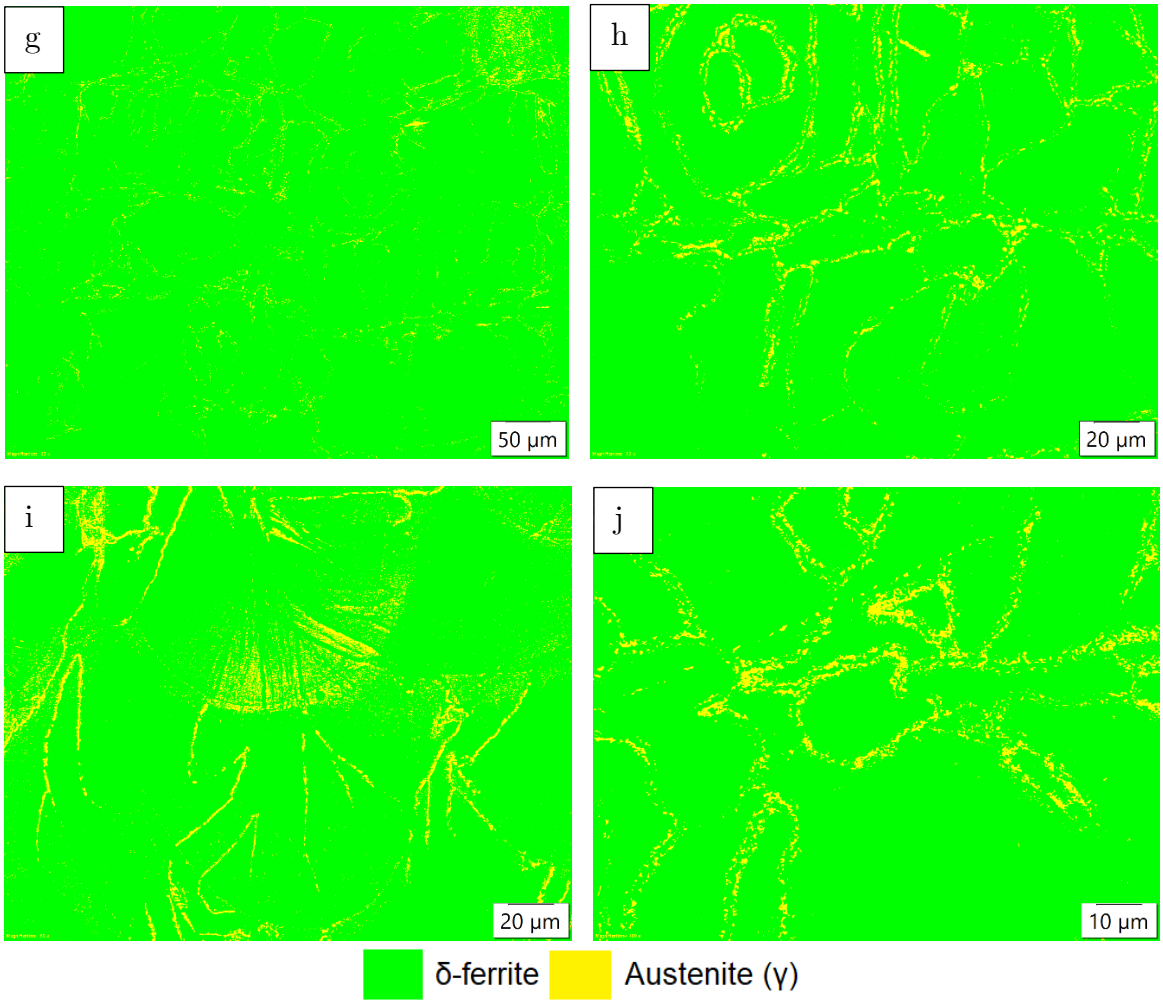

Figure XII: *Phase analysis of as-printed sample (a) Magnification 10x (b) Magnification 20x (c) Magnification 20x (d)Magnification 20x (e) Magnification 20x (f) Magnification 20x (g) Magnification 20x (h)Magnification 50x (i)Magnification 50x (j) Magnification 100x*

Table III: *Summary of Phase Balance of As-printed Specimen*

Figure No.	Magnification	% of δ-Ferrite	% of Austenite (γ)
XII (a)	10x	91.66	8.34
XII (b)	20x	91.13	8.87
XII (c)	20x	91.59	8.41
XII (d)	20x	90.86	9.14
XII (e)	20x	94.19	5.81
XII (f)	20x	96.22	3.78
XII (g)	20x	96.62	3.38
XII (h)	50x	95.01	4.99
XII (i)	50x	93.44	6.56
XII (j)	100x	94.81	5.19
Average Value		**93.55**	**6.45**
Standard Deviation		**2.14**	**2.14**

B2. Heat-treated sample at 1000 ° C for 1hour and water Quenched

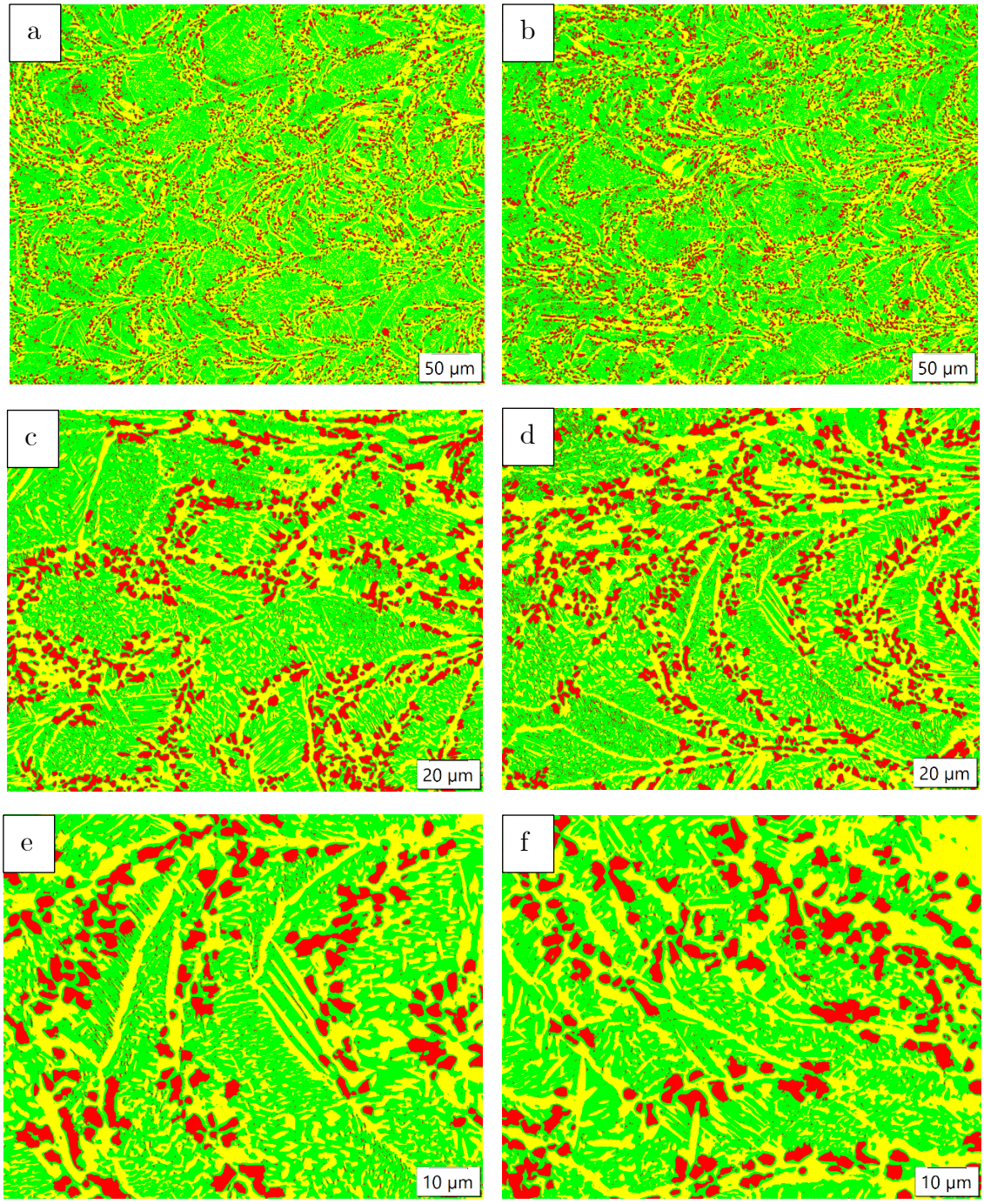

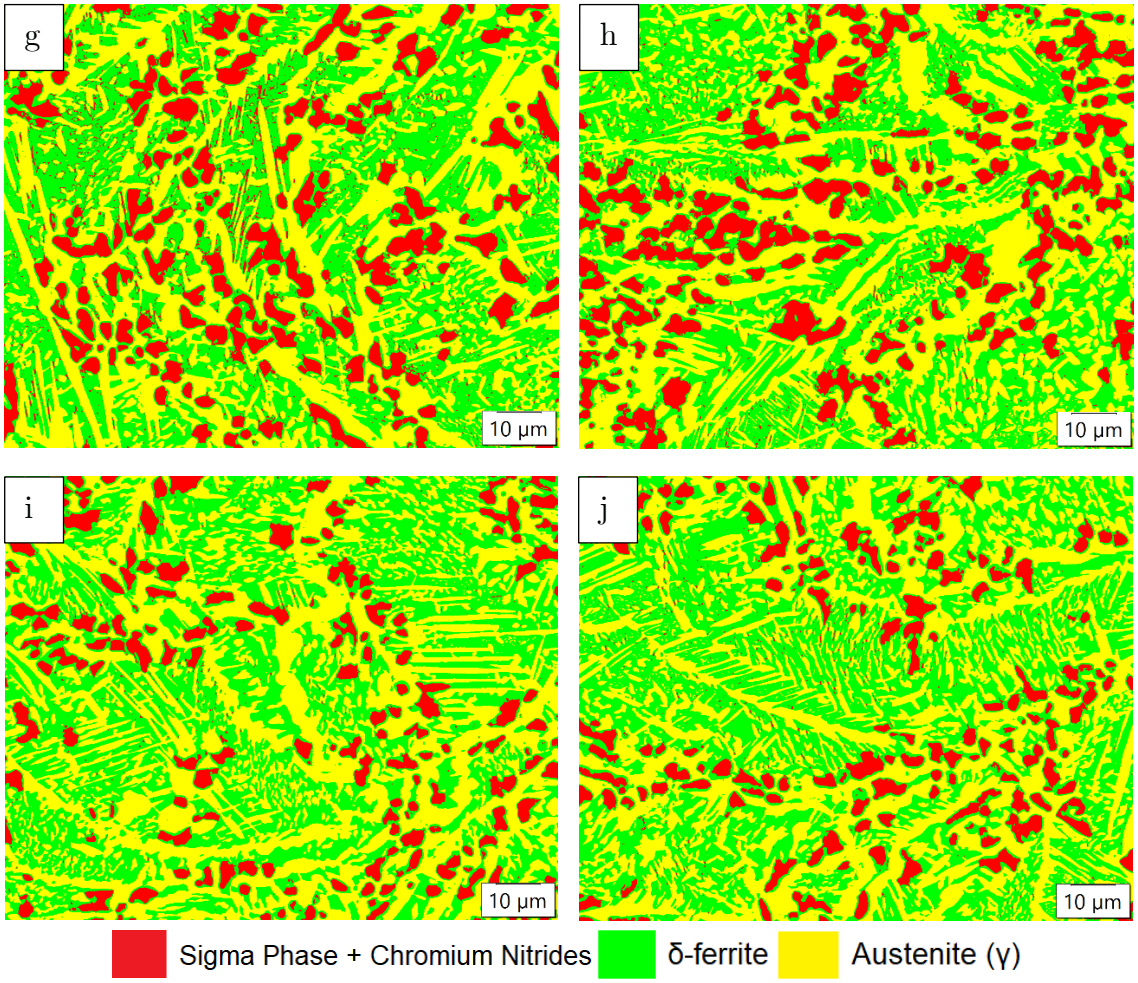

Figure XIII: *Phase analysis heat-treated sample at 1000 °C for 1hour and water Quenched (a) Magnification 20x (b) Magnification 20x (c) Magnification 50x (d)Magnification 50x (e) Magnification 100x (f) Magnification 100x (g) Magnification 100x (h)Magnification 100x (i)Magnification 100x (j) Magnification 100x*

Table IV: *Summary of Phase Balance of HT sample at 1000 °C for 1hour and water Quenched*

Figure No.	Magnification	% of σ + β-Cr_2N	% of δ-Ferrite	% of Austenite (γ)
XIII (a)	20x	10.47	57.72	31.81
XIII (b)	20x	13.05	59.21	27.74
XIII (c)	50x	15.96	51.83	32.21
XIII (d)	50x	16.19	49.29	34.53
XIII (e)	100x	14.37	51.13	34.50
XII (f)	100x	15.52	49.31	35.17
XIII (g)	100x	15.96	45.92	38.12
XIII (h)	100x	15.52	44.94	39.53
XIII (i)	100x	12.00	49.97	38.03
XIII (j)	100x	11.18	48.91	39.91
Average Value		**14.02**	**50.82**	**35.16**
Standard Deviation		**2.17**	**4.55**	**3.87**

B3. Heat-treated sample at 1000 ° C for 1hour and Air-cooled

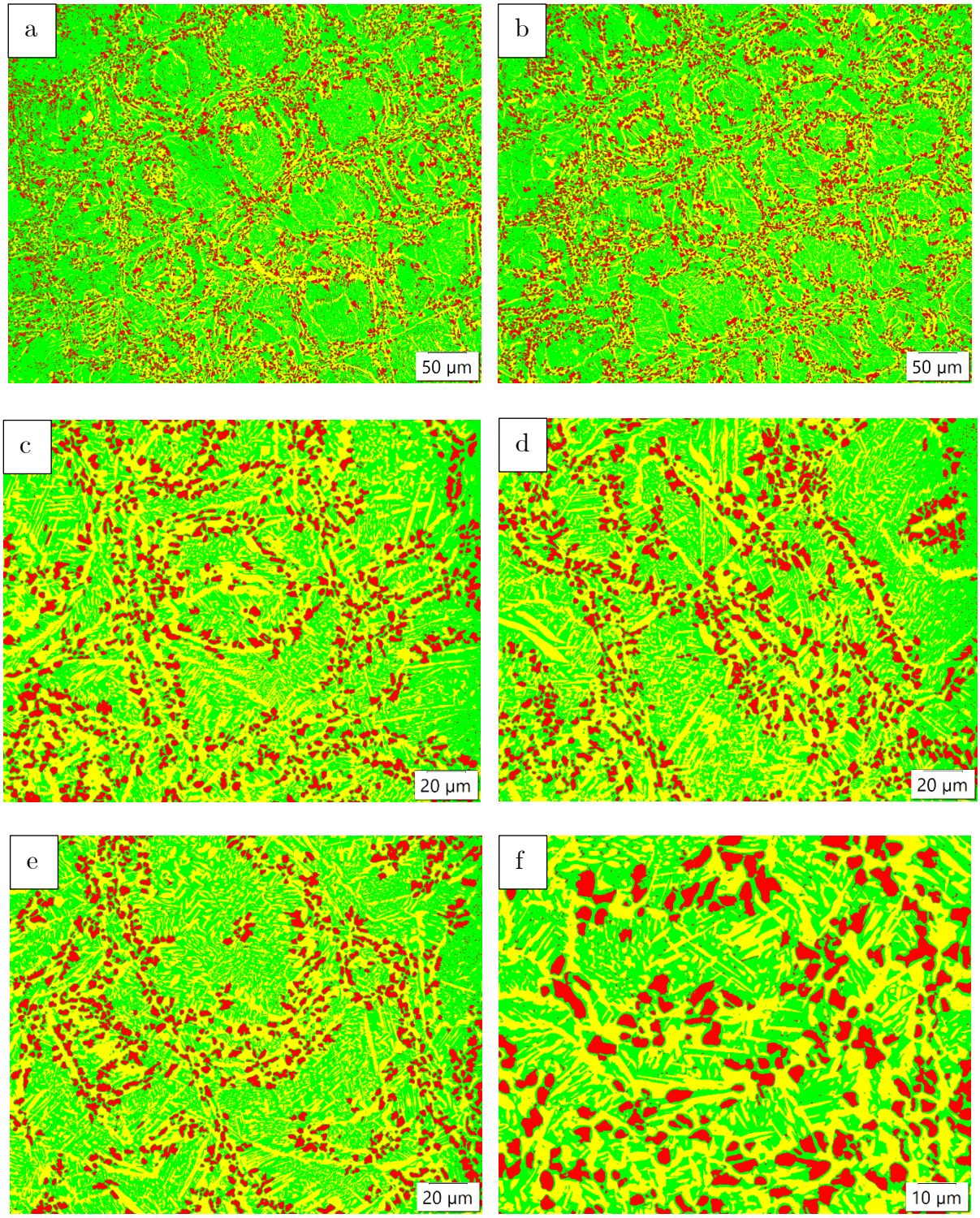

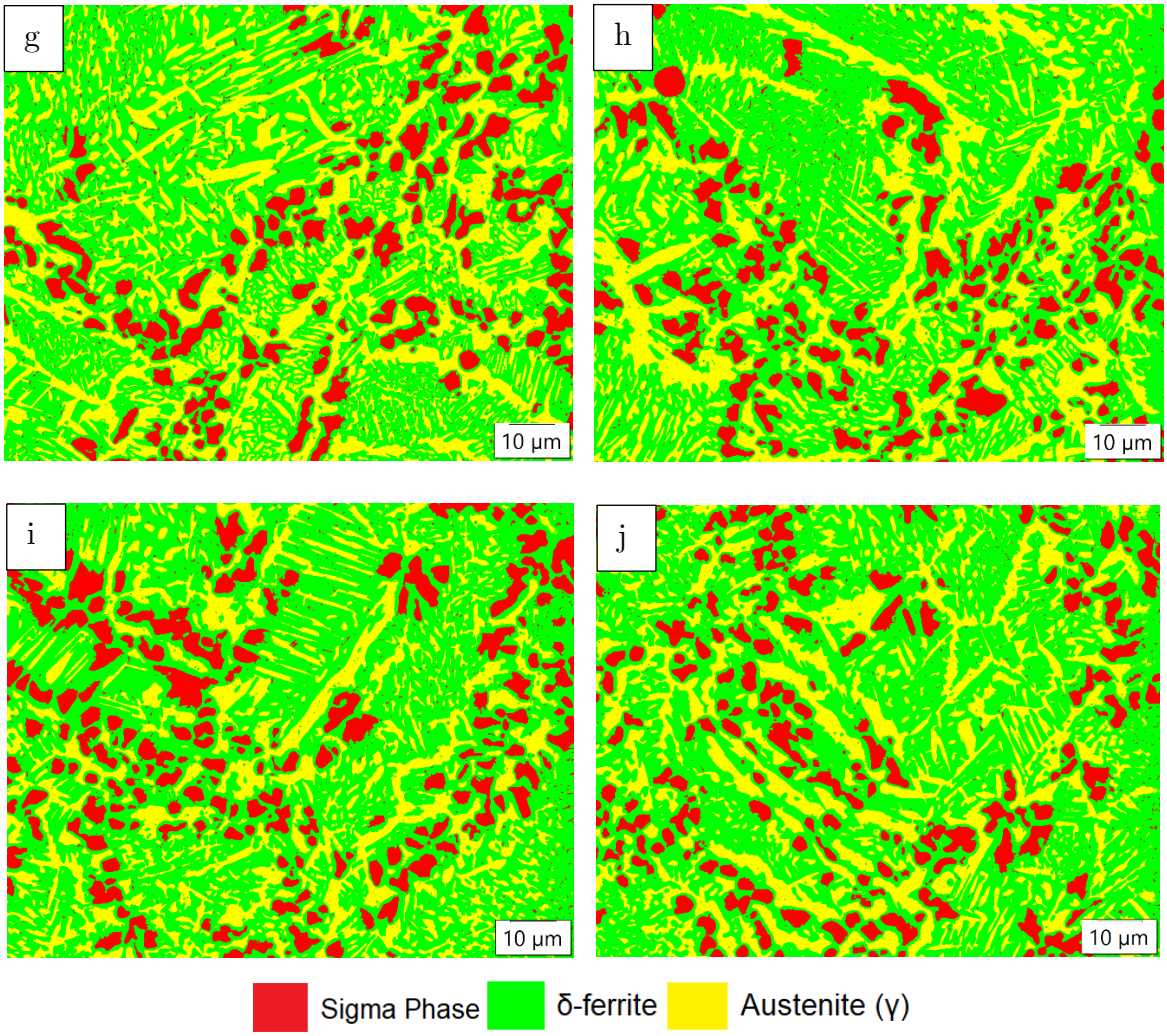

Figure XIV: *Phase analysis HT sample at 1000 ° C for 1hour and air cooled (a) Magnification 20x (b) Magnification 20x (c) Magnification 50x (d)Magnification 50x (e) Magnification 50x (f) Magnification 100x (g) Magnification 100x (h)Magnification 100x (i)Magnification 100x (j) Magnification 100x*

Table V: *Summary of Phase Balance of HT sample at 1000 ° C for 1hour and air-cooled*

Figure No.	Magnification	% of σ	% of δ-Ferrite	% of Austenite (γ)
XIV (a)	20x	16.61	51.92	31.47
XIV (b)	20x	17.04	50.99	31.97
XIV (c)	50x	14.90	45.15	39.95
XIV (d)	50x	15.38	46.70	37.91
XIV (e)	50x	14.59	46.88	38.53
XIV (f)	100x	18.43	42.70	38.87
XIV (g)	100x	13.89	51.08	35.03
XIV (h)	100x	13.01	51.23	35.75
XIV (i)	100x	17.34	48.95	33.72
XIV (j)	100x	14.57	51.62	33.80
Average Value		**15.58**	**48.72**	**35.70**
Standard Deviation		**1.71**	**3.20**	**3.00**

B4. Heat-treated sample at 1100 ° C for 1hour and water Quenched

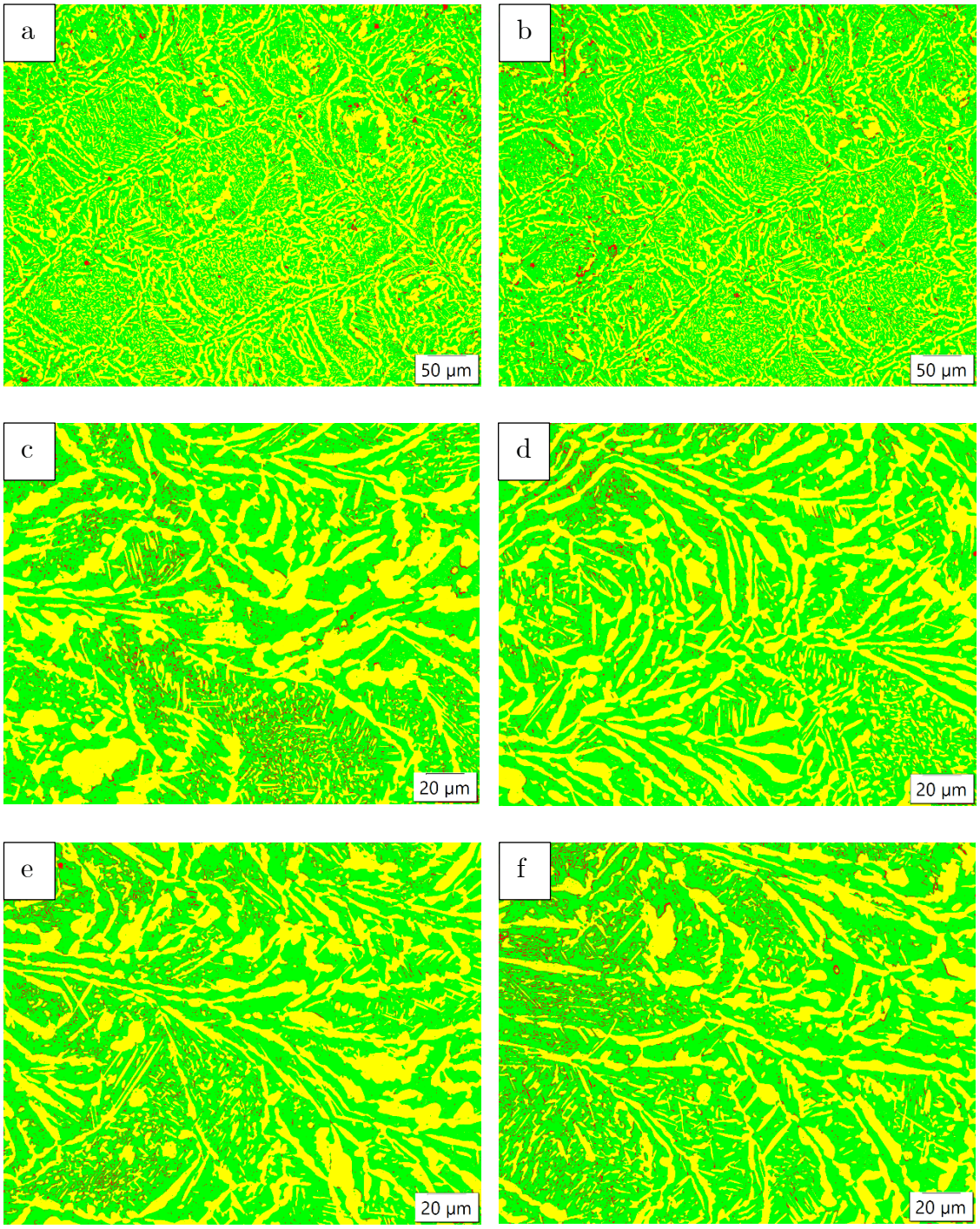

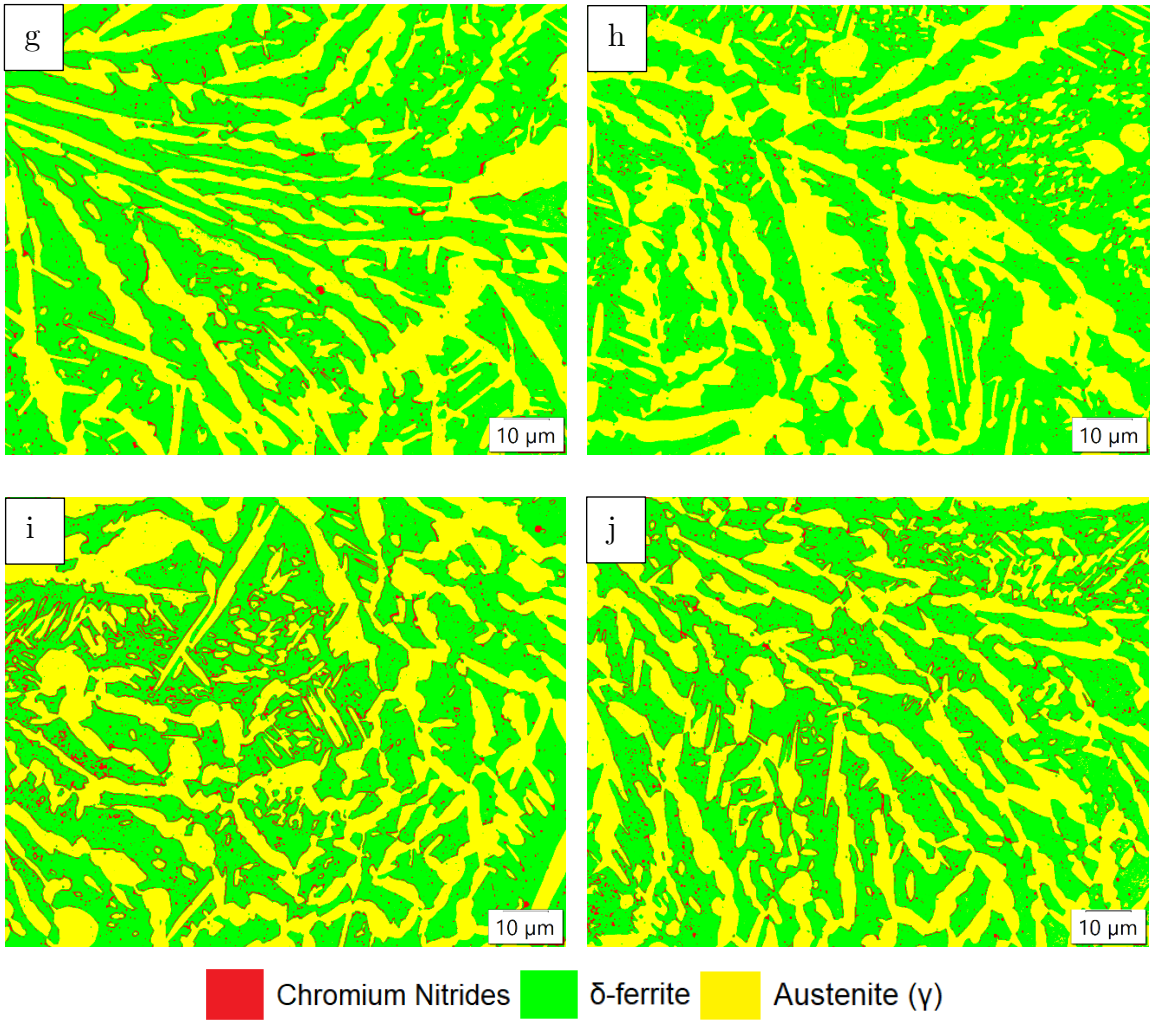

Figure XV: *Phase analysis HT sample at 1100 ° C for 1hour and water quenched (a) Magnification 20x (b) Magnification 20x (c) Magnification 50x (d)Magnification 50x (e) Magnification 50x (f) Magnification 50x (g) Magnification 100x (h)Magnification 100x (i)Magnification 100x (j) Magnification 100x*

Table VI: *Summary of Phase Balance of HT sample at 1100 ° C for 1hour and water quenched*

Figure No.	Magnification	% of β-Cr_2N	% of δ-Ferrite	% of Austenite (γ)
XV (a)	20x	1.74	61.05	37.21
XV (b)	20x	2.48	65.25	32.27
XV (c)	50x	3.58	63.10	33.32
XV (d)	50x	2.13	59.28	38.59
XV (e)	50x	2.85	61.16	35.99
XV (f)	50x	4.15	63.82	32.03
XV (g)	100x	2.98	58.85	38.17
XV (h)	100x	1.51	59.48	39.01
XV (i)	100x	4.54	56.34	39.12
XV (j)	100x	4.08	58.54	37.38
Average Value		**3.00**	**60.69**	**36.31**
Standard Deviation		**1.06**	**2.73**	**2.78**

B5. Heat-treated sample at 1100 ° C for 1hour and Air-cooled

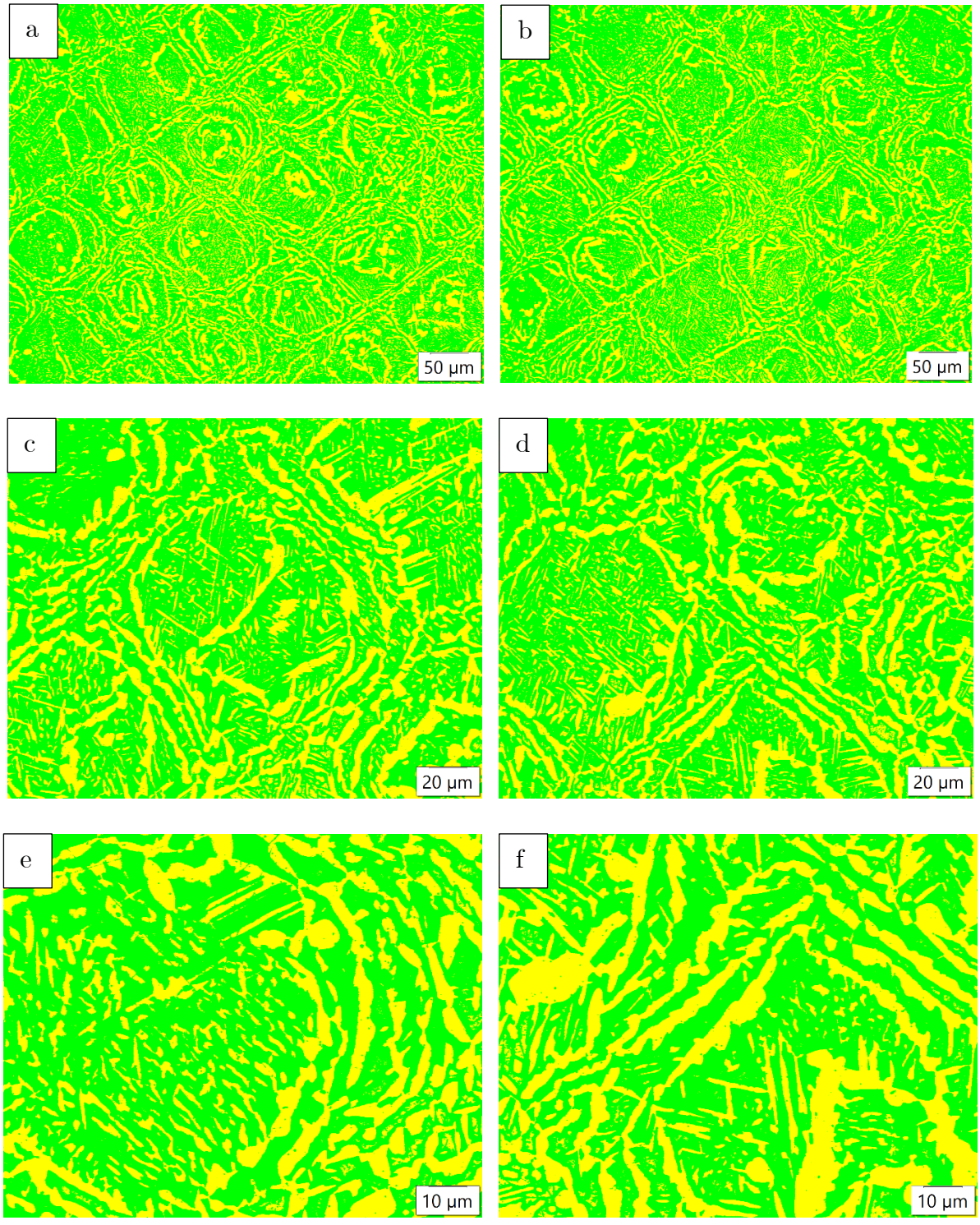

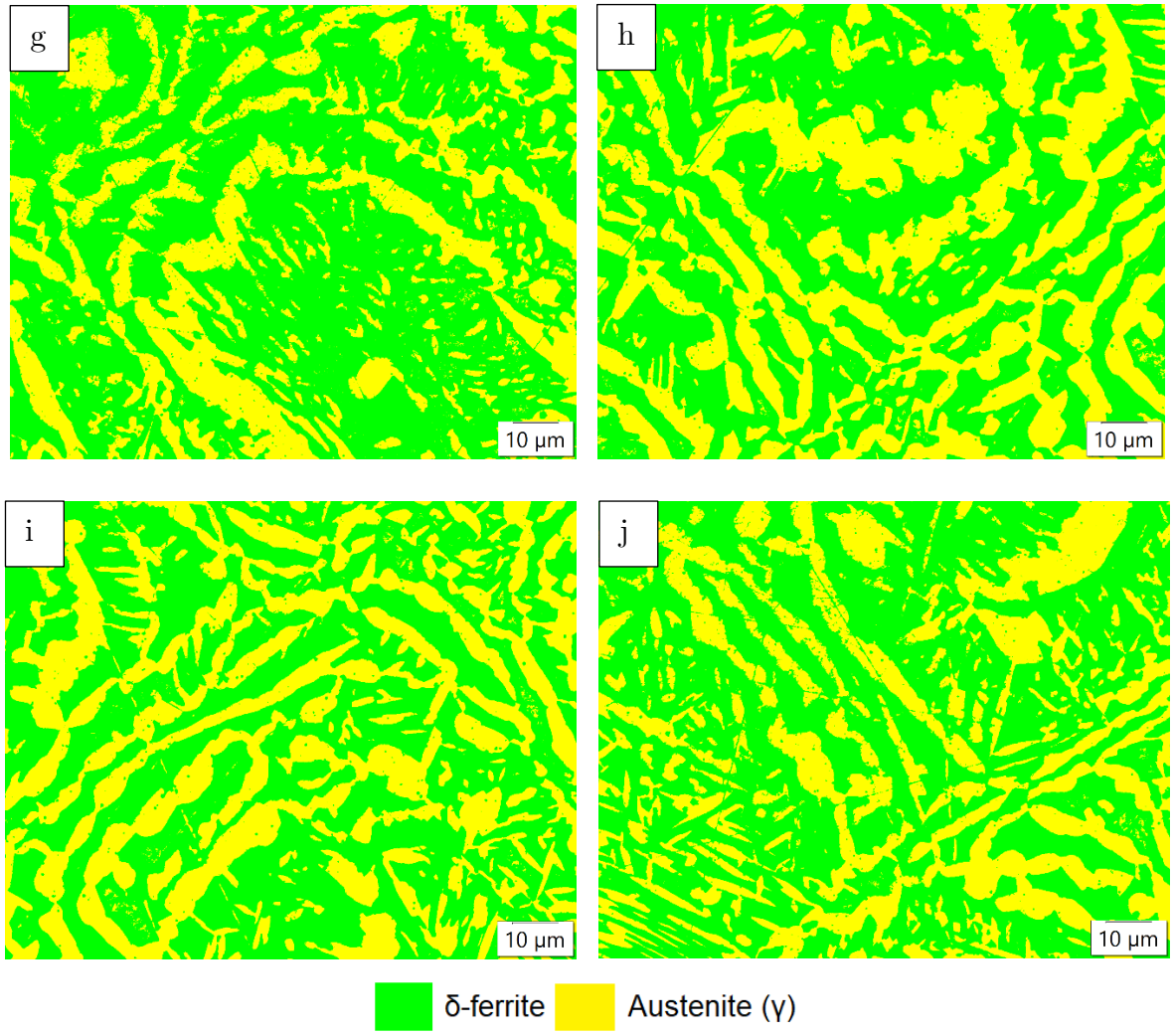

Figure XVI: *Phase analysis HT sample at 1100 ° C for 1hour and air cooled (a) Magnification 20x (b) Magnification 20x (c) Magnification 50x (d)Magnification 50x (e) Magnification 100x (f) Magnification 100x (g) Magnification 100x (h)Magnification 100x (i)Magnification 100x (j) Magnification 100x*

Table VII: *Summary of Phase Balance of HT sample at 1100 ° C for 1hour and air-cooled*

Figure No.	Magnification	% of δ-Ferrite	% of Austenite (γ)
XVI (a)	20x	63.15	36.85
XVI (b)	20x	65.61	34.39
XVI (c)	50x	64.93	35.07
XVI (d)	50x	64.53	35.47
XVI (e)	100x	64.09	35.91
XVI (f)	100x	59.14	40.86
XVI (g)	100x	67.60	32.40
XVI (h)	100x	57.96	42.04
XVI (i)	100x	59.82	40.18
XVI (j)	100x	63.47	36.53
Average Value		**63.03**	**36.97**
Standard Deviation		**3.09**	**3.09**

B6. Heat-treated sample at 1200 ° C for 1hour and water Quenched

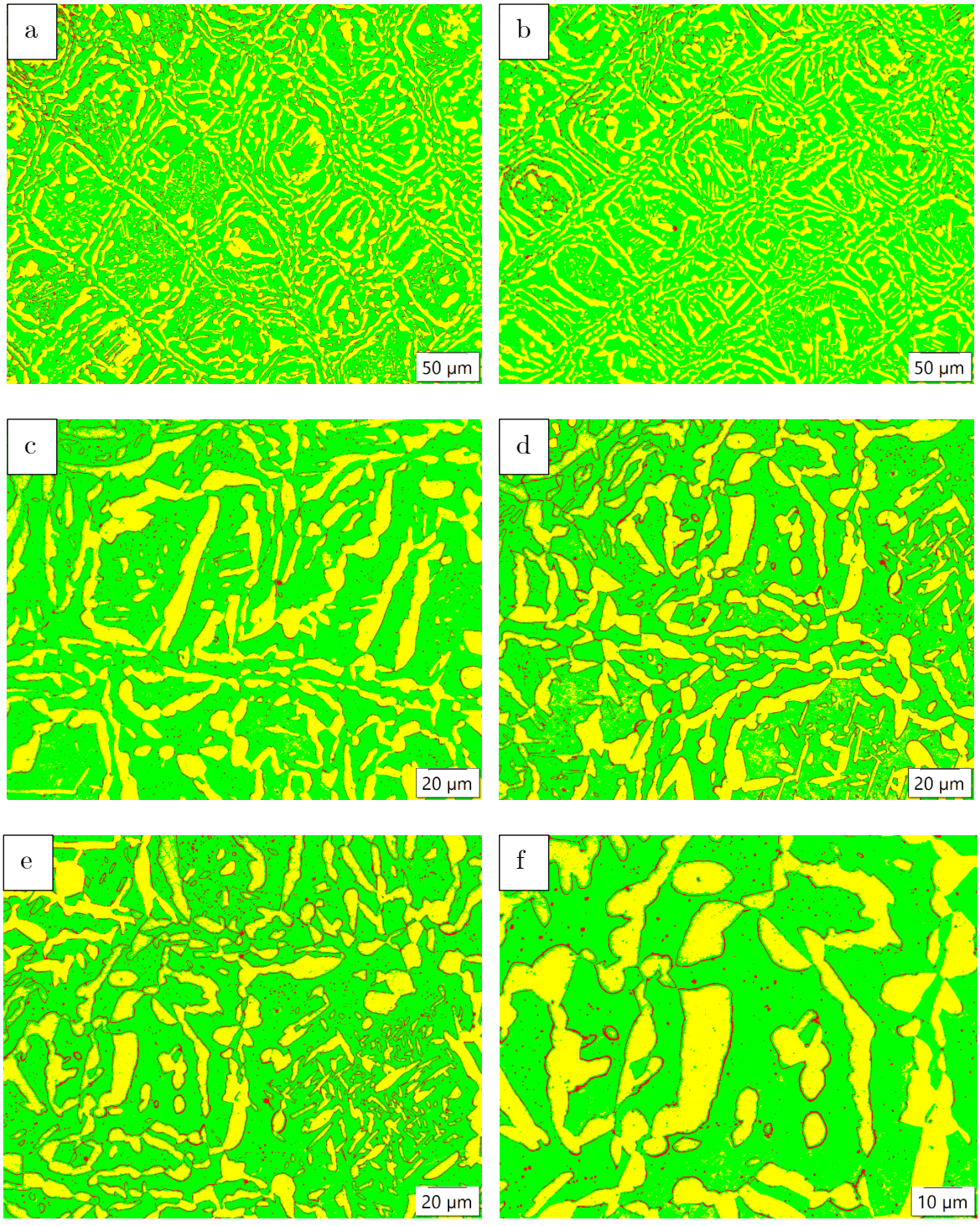

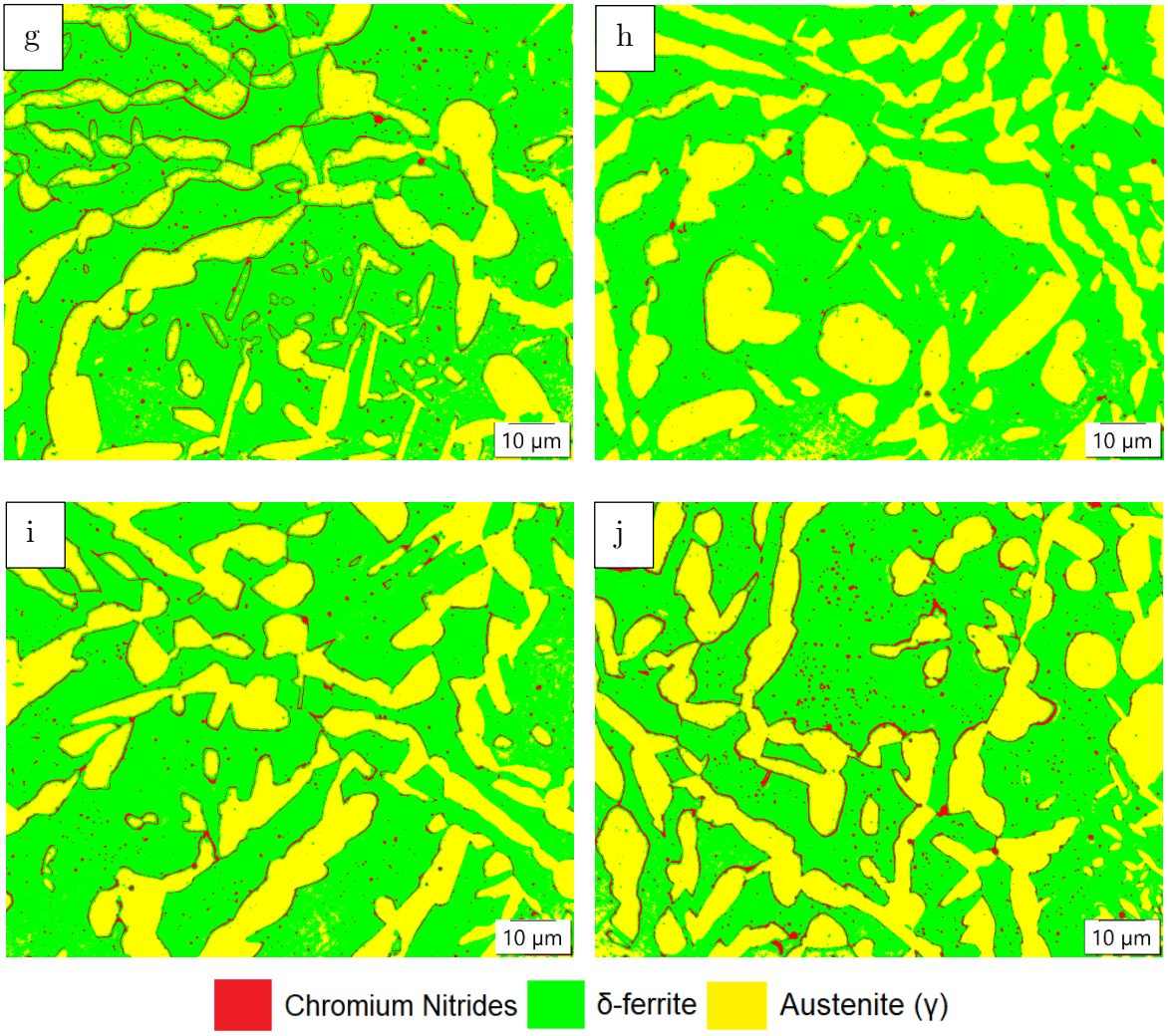

Figure XVII: *Phase analysis HT sample at 1200 ° C for 1hour and water quenched (a) Magnification 20x (b) Magnification 20x (c) Magnification 50x (d)Magnification 50x (e) Magnification 50x (f) Magnification 100x (g) Magnification 100x (h)Magnification 100x (i)Magnification 100x (j) Magnification 100x*

Table VIII: *Summary of Phase Balance of HT sample at 1200 ° C for 1hour and water quenched*

Figure No.	Magnification	% of β-Cr_2N	% of δ-Ferrite	% of Austenite (γ)
XVII (a)	20x	4.75	63.69	31.56
XVII (b)	20x	3.59	64.26	32.15
XVII (c)	50x	3.26	67.35	29.39
XVII (d)	50x	6.03	63.40	30.57
XVII (e)	50x	5.75	65.70	28.55
XVII (f)	100x	3.79	63.66	32.55
XVII (g)	100x	4.13	67.63	28.24
XVII (h)	100x	2.94	63.05	34.01
XVII (i)	100x	3.36	64.31	32.33
XVII (j)	100x	4.15	60.59	35.26
Average Value		**4.18**	**64.36**	**31.46**
Standard Deviation		**1.04**	**2.09**	**2.29**

B7. Heat-treated sample at 1200 ° C for 1hour and Air-cooled

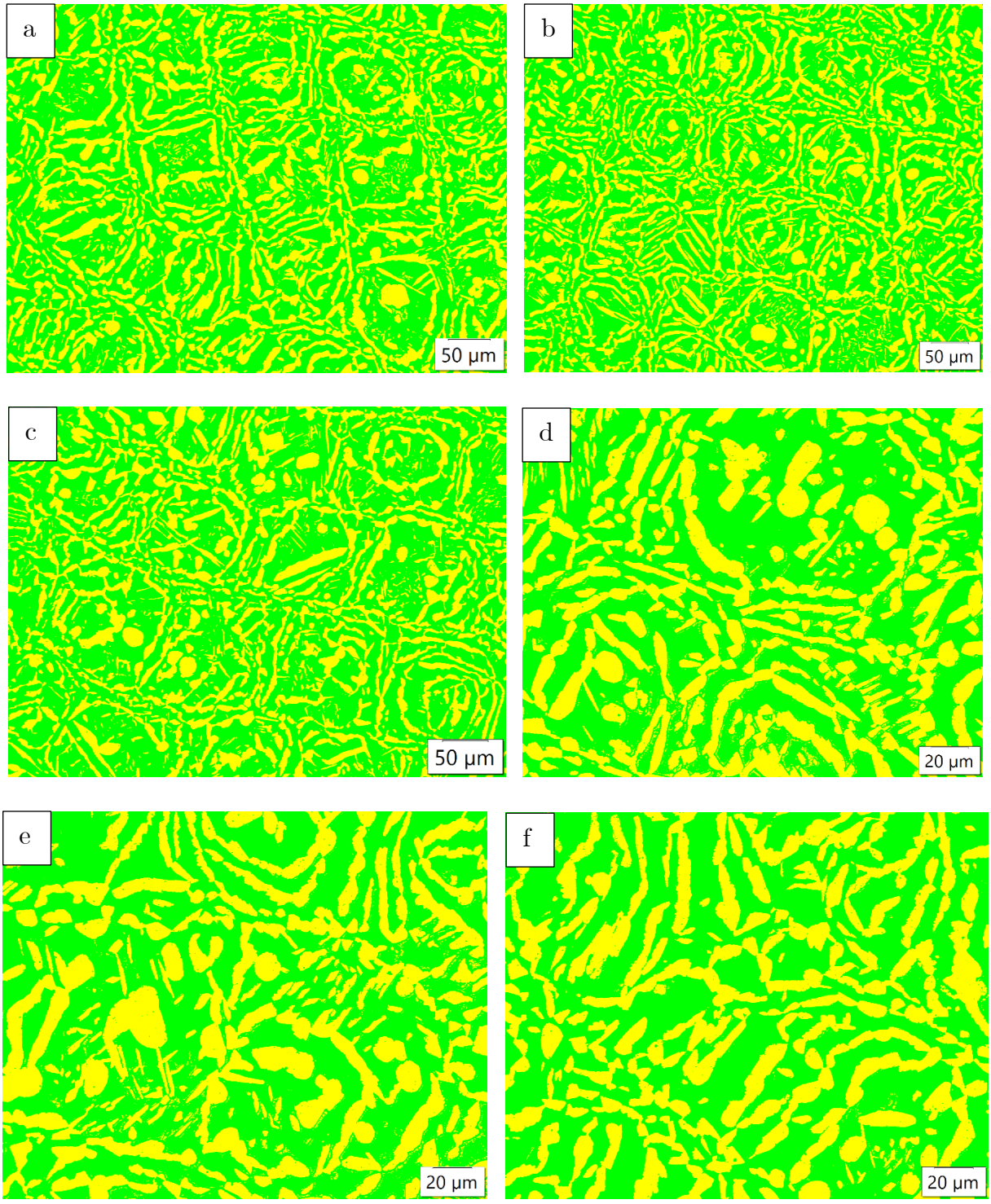

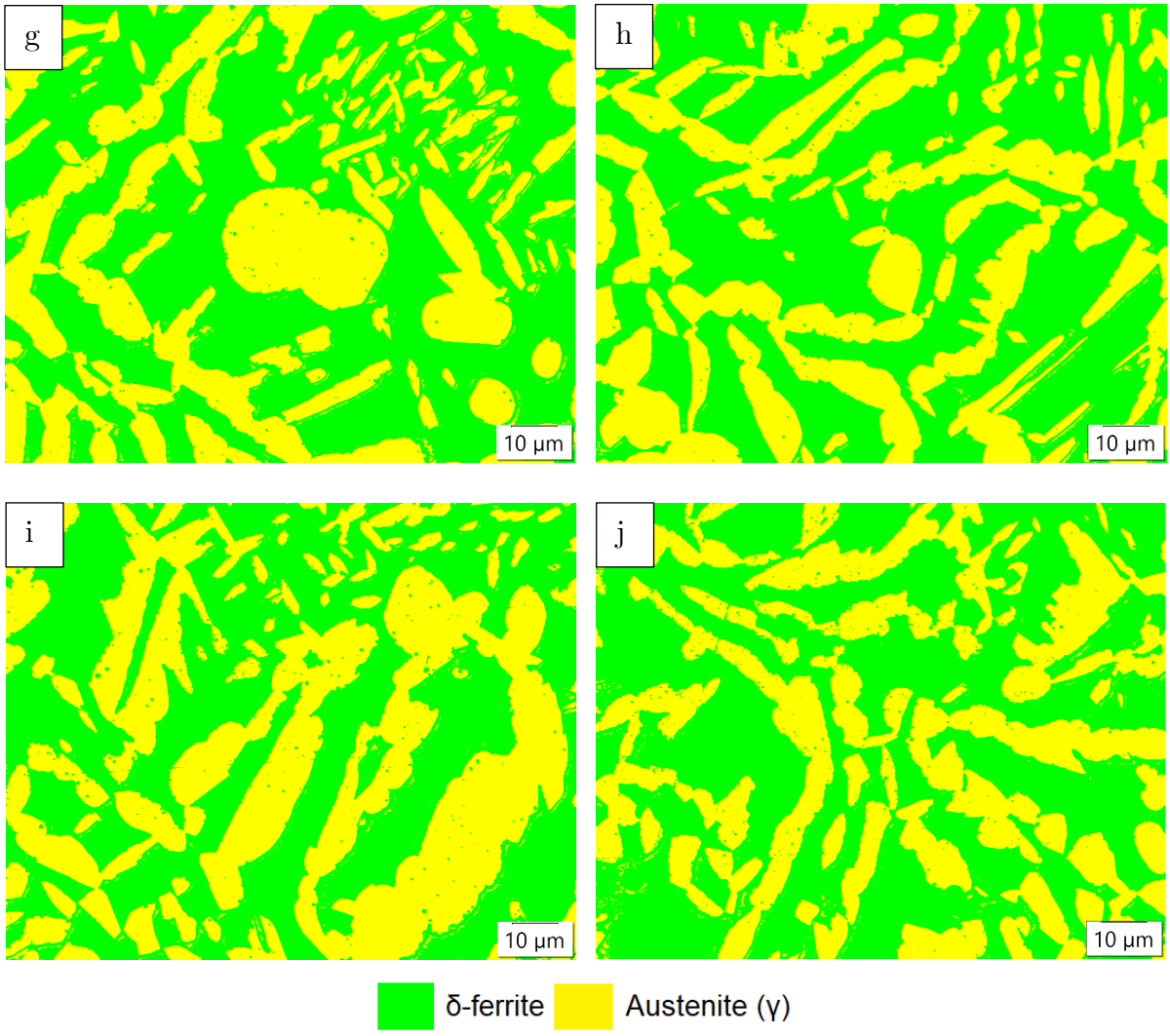

Figure XVIII: *Phase analysis HT sample at 1200 ° C for 1hour and air cooled (a) Magnification 20x (b) Magnification 20x (c) Magnification 20x (d)Magnification 50x (e) Magnification 50x (f) Magnification 50x (g) Magnification 100x (h)Magnification 100x (i)Magnification 100x (j) Magnification 100x*

Table IX: *Summary of Phase Balance of HT sample at 1200 ° C for 1hour and air-cooled*

Figure No.	Magnification	% of δ-Ferrite	% of Austenite (γ)
XVIII (a)	20x	64.58	35.42
XVIII (b)	20x	63.82	36.18
XVIII (c)	20x	66.29	33.71
XVIII (d)	50x	59.81	40.19
XVIII (e)	50x	60.13	39.87
XVIII (f)	50x	61.18	38.82
XVIII (g)	100x	59.85	40.15
XVIII (h)	100x	59.36	40.64
XVIII (i)	100x	57.45	42.55
XVIII (j)	100x	60.89	39.11
Average Value		**61.34**	**38.66**
Standard Deviation		**2.72**	**2.72**

B8. Heat-treated sample at 1300 ° C for 1hour and water Quenched

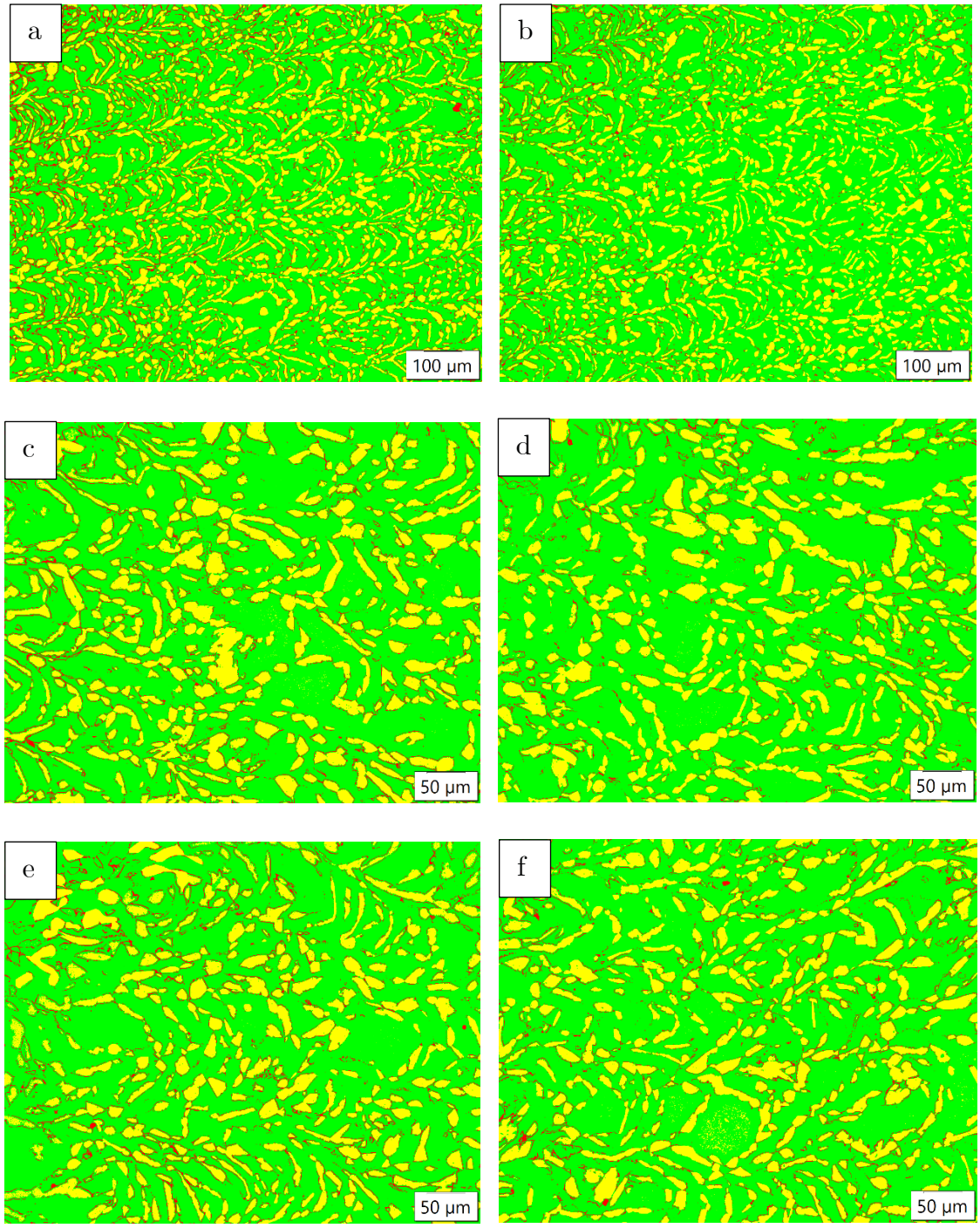

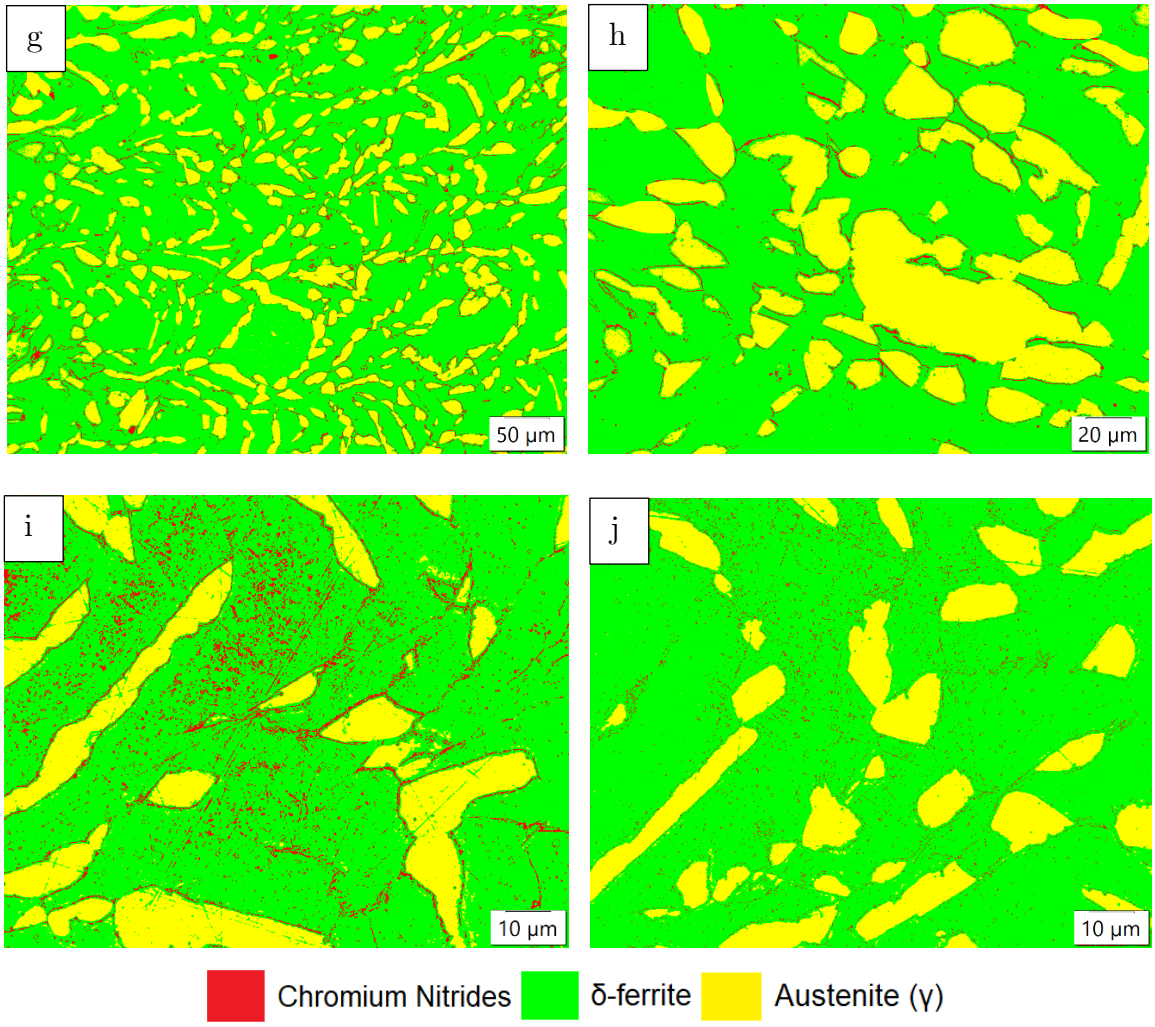

Figure XIX: *Phase analysis HT sample at 1300 ° C for 1hour and water quenched (a) Magnification 10x (b) Magnification 10x (c) Magnification 20x (d)Magnification 20x (e) Magnification 20x (f) Magnification 20x (g) Magnification 20x (h)Magnification 50x (i)Magnification 100x (j) Magnification 100x*

Table X: *Summary of Phase Balance of HT sample at 1300 ° C for 1hour and water quenched*

Figure No.	Magnification	% of β-Cr_2N	% of δ-Ferrite	% of Austenite (γ)
XIX (a)	10x	8.67	69.09	22.24
XIX (b)	10x	6.51	73.09	20.40
XIX (c)	20x	5.68	72.13	22.19
XIX (d)	20x	5.01	73.05	21.94
XIX (e)	20x	6.05	72.84	21.11
XIX (f)	20x	5.93	71.73	22.34
XIX (g)	20x	4.98	73.54	21.48
XIX (h)	50x	3.68	71.13	25.19
XIX (i)	100x	5.38	69.43	25.19
XIX (j)	100x	3.27	76.86	19.87
Average Value		**5.52**	**72.29**	**22.20**
Standard Deviation		**1.51**	**2.21**	**1.77**

B9. Heat-treated sample at 1300 ° C for 1hour and Air-cooled

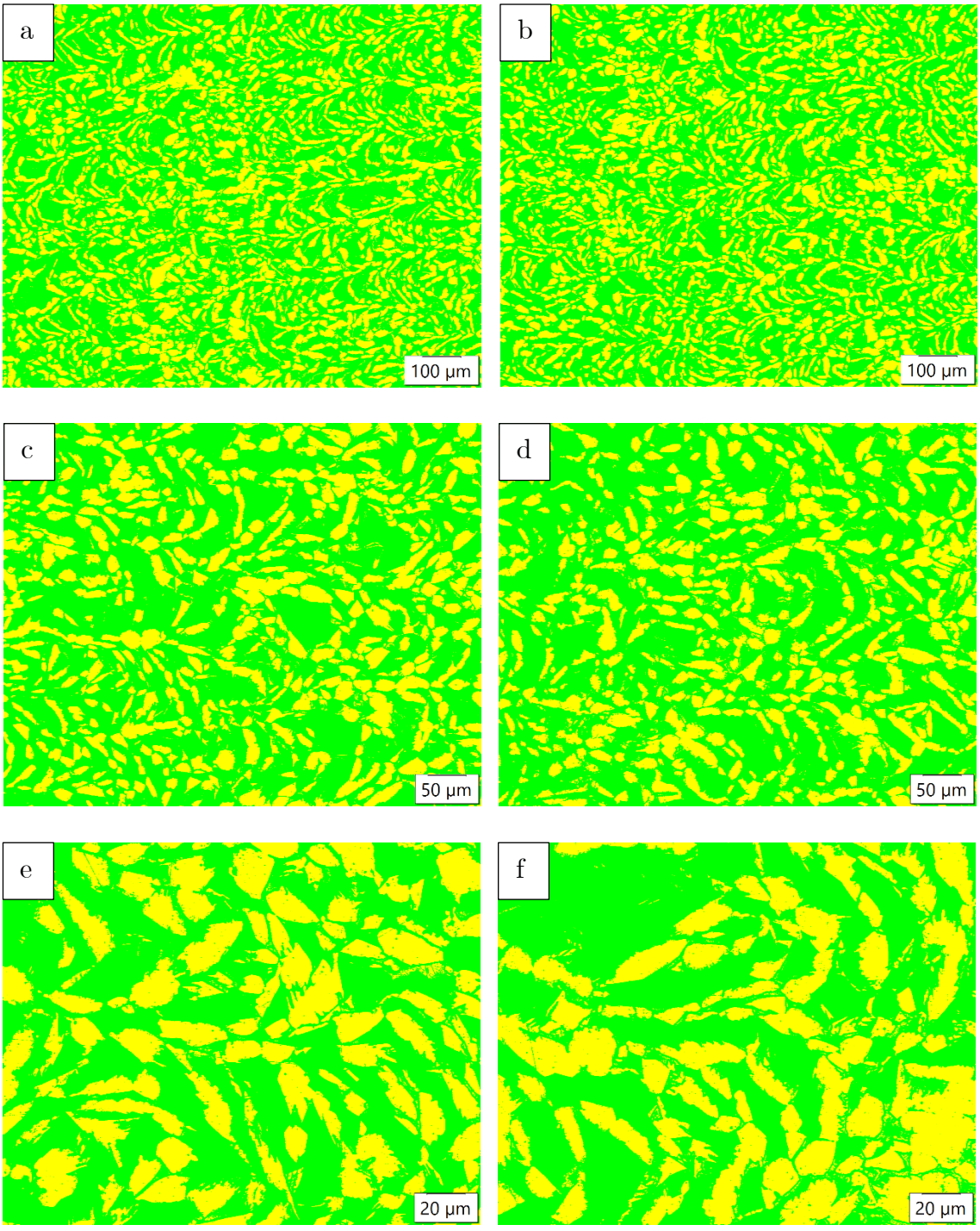

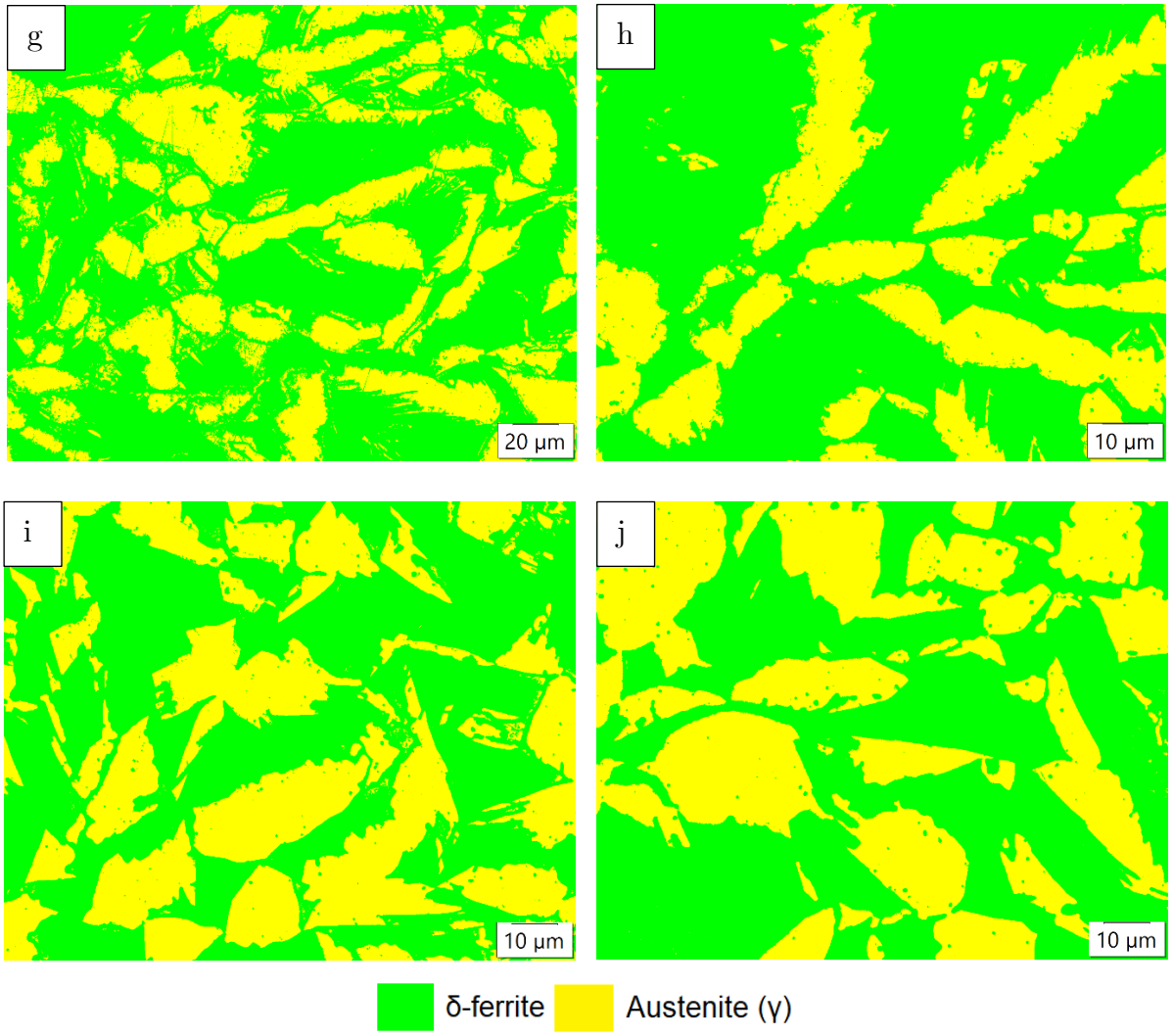

Figure XX: *Phase analysis HT sample at 1300 ° C for 1hour and air cooled (a) Magnification 10x (b) Magnification 10x (c) Magnification 20x (d)Magnification 20x (e) Magnification 50x (f) Magnification 50x (g) Magnification 50x (h)Magnification 100x (i)Magnification 100x (j) Magnification 100x*

Table XI: *Summary of Phase Balance of HT sample at 1300 ° C for 1hour and air-cooled*

Figure No.	Magnification	% of δ-Ferrite	% of Austenite (γ)
XX (a)	10x	63.94	36.06
XX (b)	10x	63.70	36.30
XX (c)	20x	66.54	33.46
XX (d)	20x	67.24	32.76
XX (e)	50x	61.13	38.87
XX (f)	50x	60.90	39.10
XX (g)	50x	64.26	35.74
XX (h)	100x	67.85	32.15
XX (i)	100x	59.87	40.13
XX (j)	100x	59.13	40.87
Average Value		**63.46**	**36.54**
Standard Deviation		**3.12**	**3.12**

B10. Summary of Phase Analysis

Table XII: *Summary of Phase Analysis*

Sample Name	% Precipitate	% of δ-Ferrite	% of Austenite (γ)
As Printed	-	93.55 ± 2.14	6.45 ± 2.14
HT at 1000 ° C for 1hr then water quenched	14.02 ± 2.17	50.82 ± 4.55	35.16 ± 3.87
HT at 1000 ° C for 1hr then air-cooled	15.58 ± 1.71	48.72 ± 3.2	35.70 ± 3
HT at 1100 ° C for 1hr then water quenched	3.00 ± 1.06	60.69 ± 2.73	36.31 ± 2.78
HT at 1100 ° C for 1hr then air-cooled	-	63.03 ± 3.09	36.97 ± 3.09
HT at 1200 ° C for 1hr then water quenched	4.18 ± 1.04	64.36 ± 2.09	31.46 ± 2.29
HT at 1200 ° C for 1hr then air-cooled	-	61.34 ± 2.72	38.66 ± 2.72
HT at 1300 ° C for 1hr then water quenched	5.52 ± 1.51	72.29 ± 2.21	22.20 ± 1.77
HT at 1300 ° C for 1hr then air-cooled	-	63.46 ± 3.12	36.54 ± 3.12

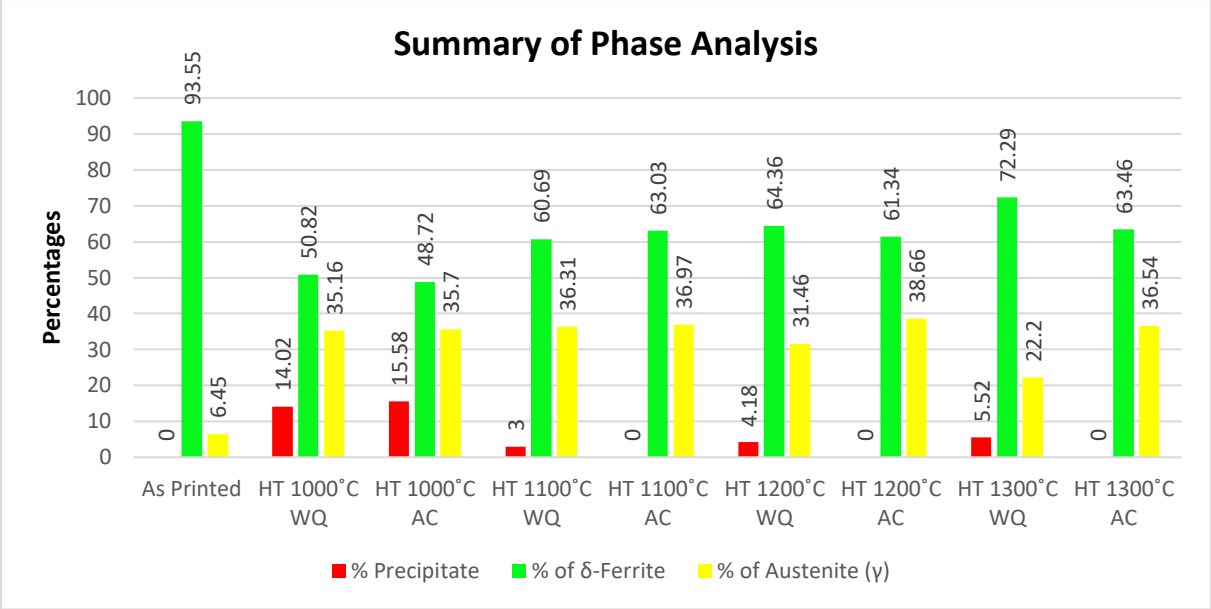

Figure XXI: *Summary of phase analysis*

Appendix C: Microstructure Analysis using SEM

C1. As-printed sample final polished with OP-S

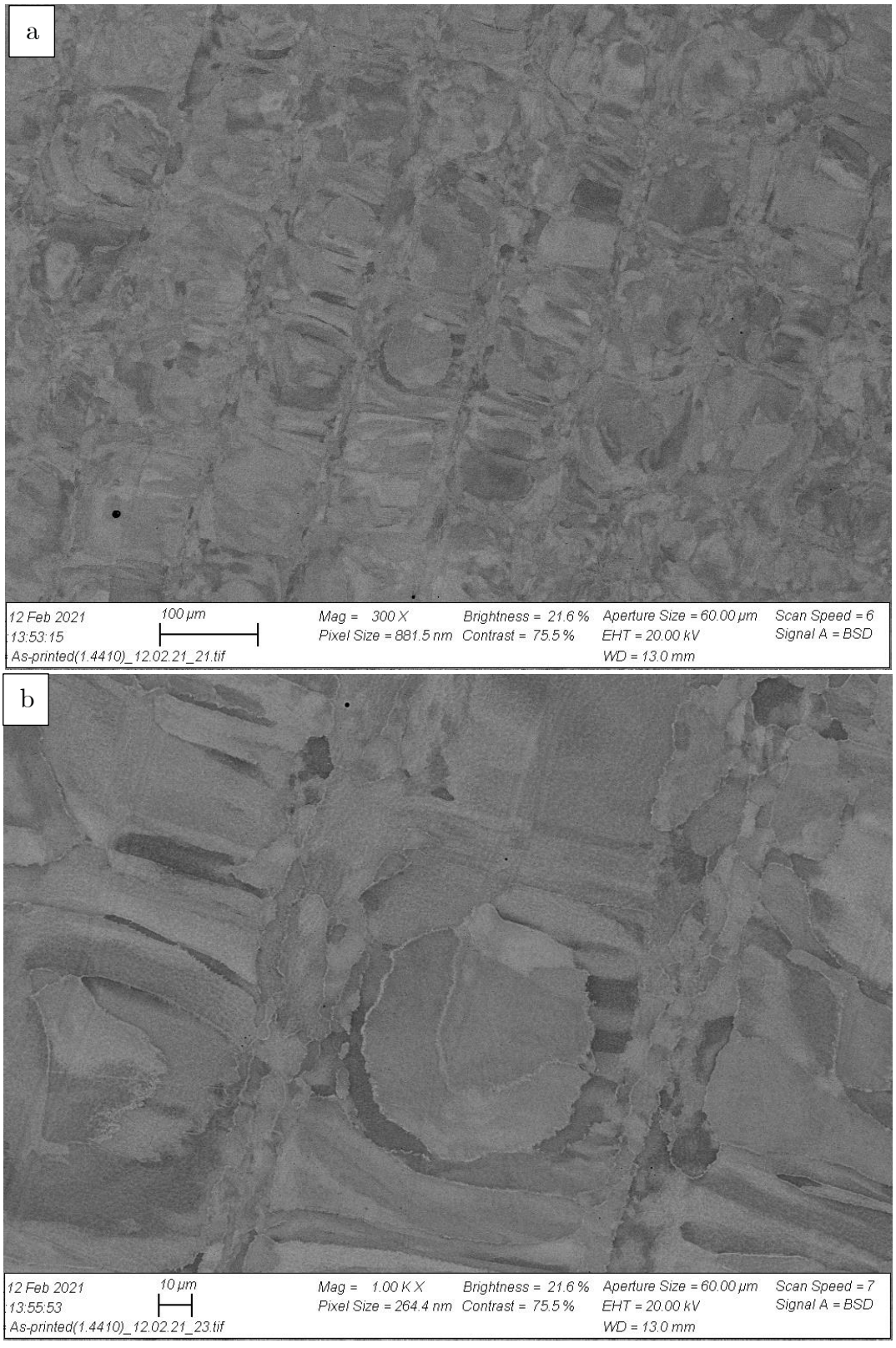

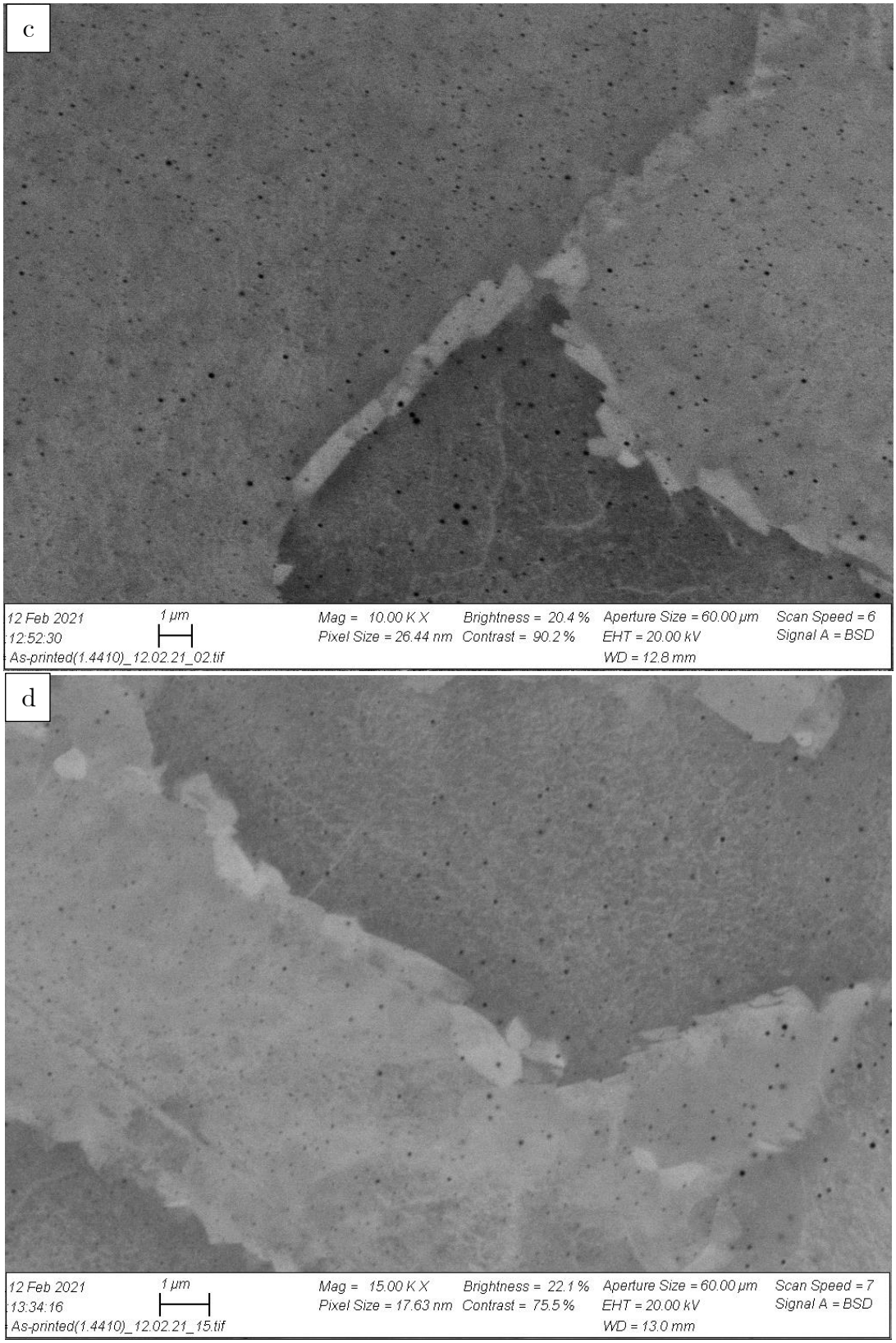

Figure XXII: *Microstructure of as-printed sample final polished with OP-S (a) Magnification 300x (b) Magnification 1000x (c) Magnification 10,000x (d) Magnification 15,000x*

C1. As-printed sample etched with oxalic acid

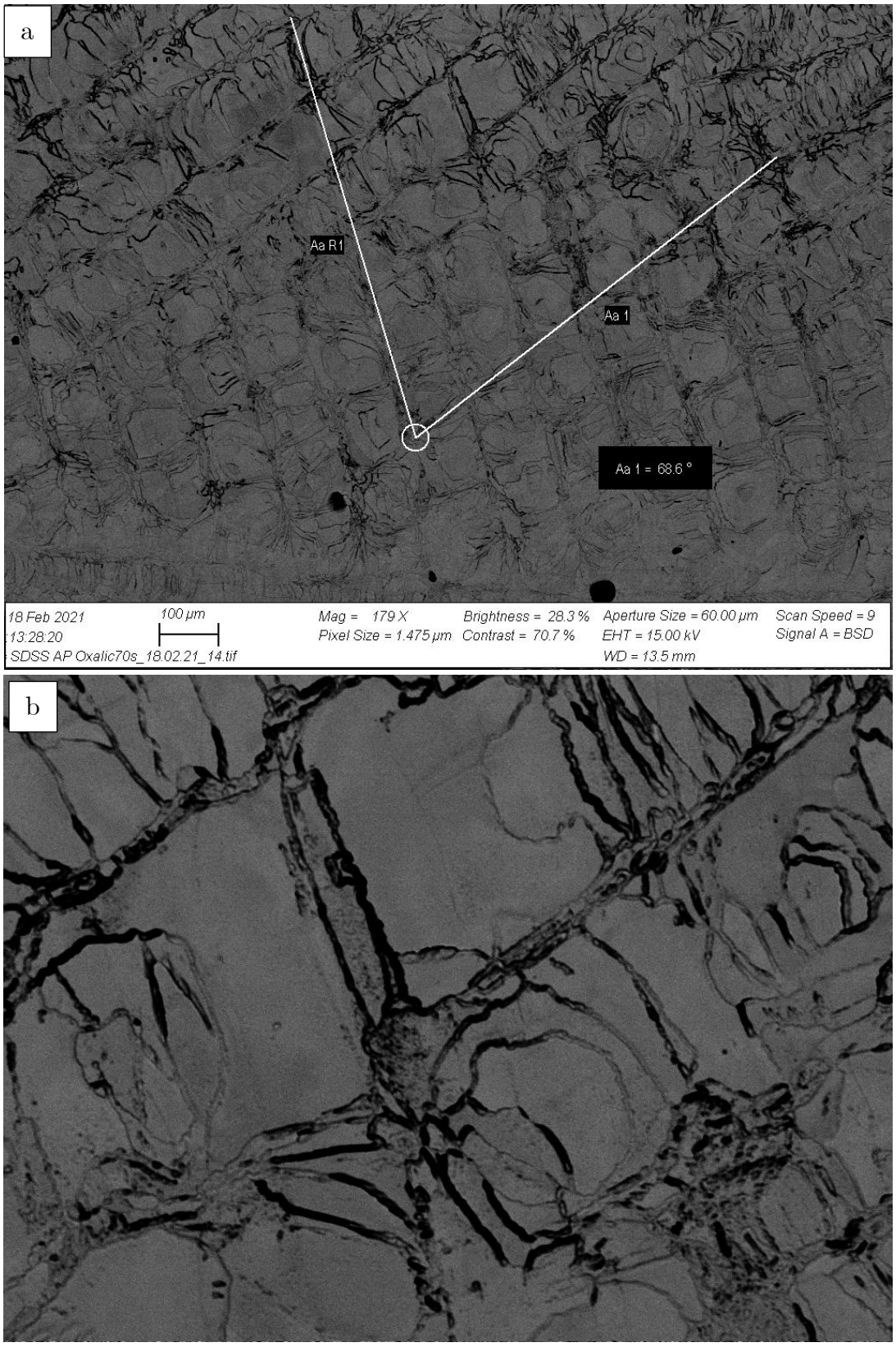

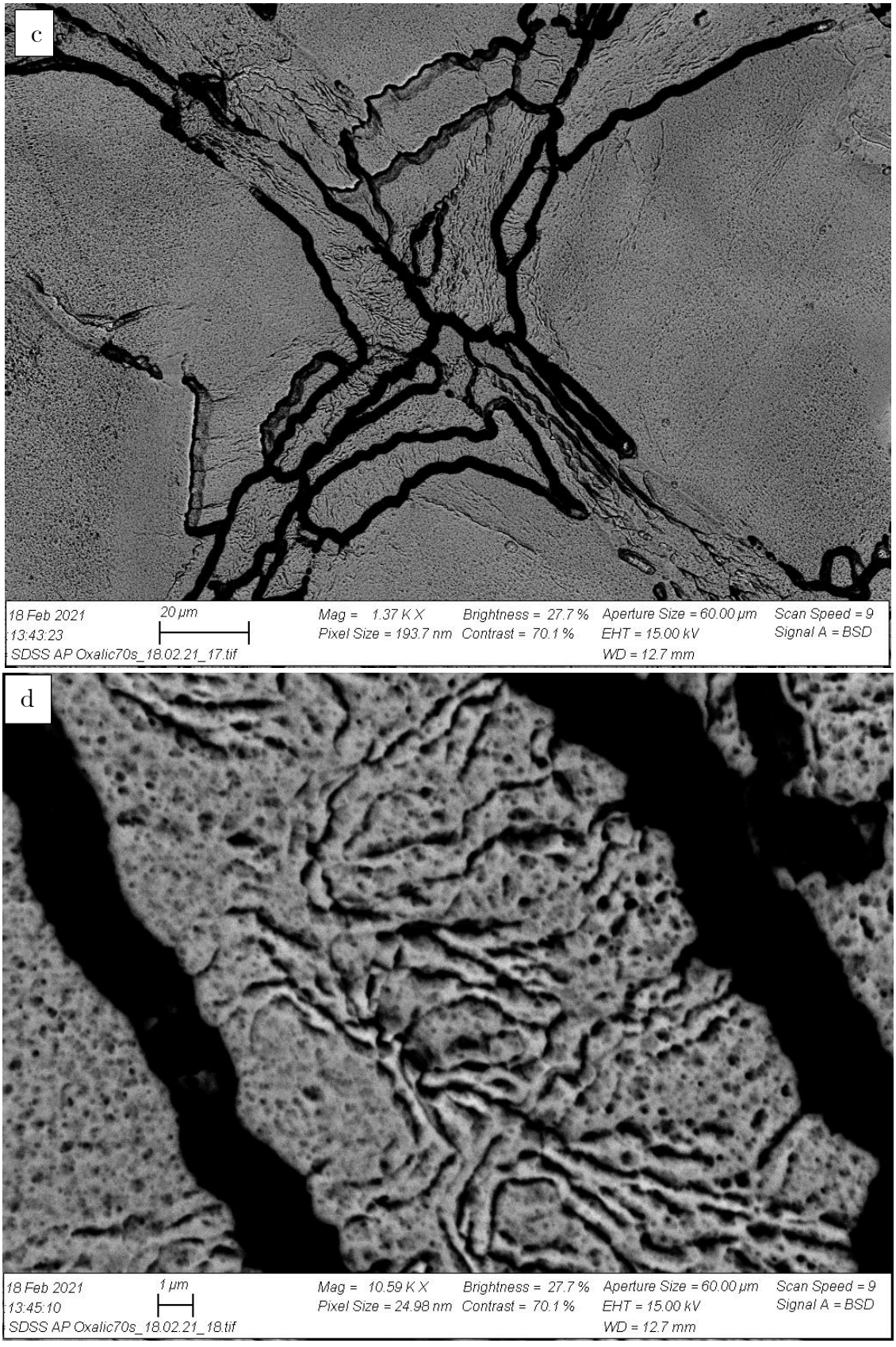

Figure XXIII: *Microstructure of as-printed sample etched with oxalic acid (a) Magnification 179x (b) Magnification 768x (c) Magnification 1,370x (d) Magnification 10,590x*

Appendix D: Hardness Measurement

D1. As-printed sample

Table XIII: *Vickers hardness Measurement (HV5) of as-printed sample*

Trial No.	Hollow Part		Solid Part	
	Perpendicular to BD (Location A)	Parallel to BD (Location B)	Perpendicular to BD (Location C)	Parallel to BD (Location D)
1	408	405	415	424
2	403	416	420	421
3	408	412	416	426
4	405	411	430	430
5	415	408	423	435
6	412	413	422	432
7	407	406	418	428
8	405	409	417	436
9	402	410	429	431
10	404	411	428	427
Average Value	406.9	410.1	421.8	429.0
Standard Deviation	4.1	3.3	5.6	4.7
Range	13	11	15	15
Maximum Value	415	416	430	436
Minimum Value	402	405	415	421

D2. Heat-treated sample at 1000 ° C for 1hour and water Quenched

Table XIV: *Vickers hardness Measurement (HV5) of HT sample at 1000 ° C for 1hour and water Quenched*

Trial No.	Hollow Part		Solid Part	
	Perpendicular to BD (Location A)	Parallel to BD (Location B)	Perpendicular to BD (Location C)	Parallel to BD (Location D)
1	384	386	380	386
2	375	380	389	391
3	379	381	393	388
4	374	384	387	396
5	385	387	384	398
6	381	390	391	387
7	378	385	389	390
8	382	388	388	393
9	381	380	390	389
10	383	389	389	392
Average Value	380.2	385.0	388.0	391.0
Standard Deviation	3.7	3.7	3.7	3.9
Range	11	10	13	12
Maximum Value	385	390	393	398
Minimum Value	374	380	380	386

D3. Heat-treated sample at 1000 ° C for 1hour and Air-cooled

Table XV: *Vickers hardness Measurement (HV5) of HT at 1000 ° C for 1hour and air-cooled*

Trial No.	Hollow Part		Solid Part	
	Perpendicular to BD (Location A)	Parallel to BD (Location B)	Perpendicular to BD (Location C)	Parallel to BD (Location D)
1	327	336	348	347
2	329	332	339	349
3	330	336	342	348
4	331	335	345	342
5	330	336	336	344
6	337	339	344	345
7	328	339	349	340
8	327	342	342	345
9	332	332	341	344
10	334	336	340	351
Average Value	**330.5**	**336.3**	**342.6**	**345.5**
Standard Deviation	3.2	3.1	4.0	3.3
Range	10	10	13	11
Maximum Value	337	342	349	351
Minimum Value	327	332	336	340

D4. Heat-treated sample at 1100 ° C for 1hour and Air-cooled

Table XVI: *Vickers hardness Measurement (HV5) of HT sample at 1100 ° C for 1hour and water Quenched*

Trial No.	Hollow Part		Solid Part	
	Perpendicular to BD (Location A)	Parallel to BD (Location B)	Perpendicular to BD (Location C)	Parallel to BD (Location D)
1	277	288	283	294
2	282	280	284	283
3	280	280	285	293
4	286	280	288	287
5	278	287	294	288
6	279	286	284	281
7	281	288	289	291
8	287	283	286	283
9	276	285	285	291
10	281	286	283	292
Average Value	**280.7**	**284.3**	**286.1**	**288.3**
Standard Deviation	3.6	3.3	3.4	4.6
Range	11	8	11	13
Maximum Value	287	288	294	294
Minimum Value	276	280	283	281

D5. Heat-treated sample at 1100 ° C for 1hour and Air-cooled

Table XVII: *Vickers hardness Measurement (HV5) of HT sample at 1100 ° C for 1hour and air-cooled*

Trial No.	Hollow Part		Solid Part	
	Perpendicular to BD (Location A)	Parallel to BD (Location B)	Perpendicular to BD (Location C)	Parallel to BD (Location D)
1	277	276	281	271
2	270	271	275	275
3	272	277	276	278
4	279	278	282	285
5	281	280	269	283
6	275	272	279	282
7	276	270	275	279
8	274	279	278	278
9	275	280	279	277
10	274	279	281	275
Average Value	**275.3**	**276.2**	**277.5**	**278.3**
Standard Deviation	3.2	3.8	3.9	4.2
Range	11	10	13	14
Maximum Value	281	280	282	285
Minimum Value	270	270	269	271

D6. Heat-treated sample at 1200 ° C for 1hour and Water Quenched

Table XVIII: *Vickers hardness Measurement (HV5) of HT sample at 1200 ° C for 1hour and water Quenched*

Trial No.	Hollow Part		Solid Part	
	Perpendicular to	Parallel to BD	Perpendicular to	Parallel to BD
1	285	286	296	301
2	289	288	290	293
3	288	288	294	301
4	282	286	300	294
5	294	295	301	293
6	292	291	296	294
7	296	294	295	301
8	290	299	292	303
9	293	296	291	294
10	295	299	296	298
Average Value	**290.4**	**292.2**	**295.1**	**297.2**
Standard Deviation	4.5	5.1	3.6	4.0
Range	14	13	11	10
Maximum Value	296	299	301	303
Minimum Value	282	286	290	293

D7. Heat-treated sample at 1200 ° C for 1hour and Air-cooled

Table XIX: *Vickers hardness Measurement (HV5) of HT sample at 1200 ° C for 1hour and air-cooled*

Trial No.	Hollow Part		Solid Part	
	Perpendicular to BD (Location A)	Parallel to BD (Location B)	Perpendicular to BD (Location C)	Parallel to BD (Location D)
1	267	274	272	270
2	267	273	273	272
3	264	265	270	278
4	268	269	268	270
5	271	272	264	278
6	264	262	267	274
7	261	269	275	271
8	261	269	273	265
9	270	264	268	275
10	267	266	271	269
Average Value	**266.0**	**268.3**	**270.1**	**272.2**
Standard Deviation	3.4	4.0	3.3	4.1
Range	10	12	11	13
Maximum Value	271	274	275	278
Minimum Value	261	262	264	265

D8. Heat-treated sample at 1300 ° C for 1hour and Water Quenched

Table XX: *Vickers hardness Measurement (HV5) of a heat-treated sample at 1300 ° C for 1hour and water Quenched*

Trial No.	Hollow Part		Solid Part	
	Perpendicular to	Parallel to BD	Perpendicular to	Parallel to BD
1	301	300	303	310
2	302	302	297	299
3	305	308	299	304
4	298	297	308	305
5	291	301	306	307
6	292	302	301	308
7	300	306	302	303
8	299	299	304	301
9	298	298	306	306
10	304	301	307	309
Average Value	**299.0**	**301.4**	**303.3**	**305.2**
Standard Deviation	4.6	3.4	3.6	3.5
Range	14	11	11	11
Maximum Value	305	308	308	310
Minimum Value	291	297	297	299

D9. Heat-treated sample at 1300 ° C for 1hour and Air-cooled

Table XXI: *Vickers hardness Measurement (HV5) of HT sample at 1300 ° C for 1hour and air-cooled*

Trial No.	Hollow Part		Solid Part	
	Perpendicular to BD (Location A)	Parallel to BD (Location B)	Perpendicular to BD (Location C)	Parallel to BD (Location D)
1	280	277	273	281
2	279	275	278	283
3	270	285	285	275
4	278	275	283	279
5	277	273	279	277
6	279	285	277	279
7	279	278	275	288
8	270	276	288	286
9	272	275	278	283
10	277	271	279	280
Average Value	**276.1**	**277**	**279.5**	**281.1**
Standard Deviation	3.9	4.6	4.6	4
Range	10	14	15	13
Maximum Value	280	285	288	288
Minimum Value	270	271	273	275

Appendix E: EDS

The EDS analysis of AISI SAF 2507 powder that was used for SLM printing of sample is shown below, which was done by Sandvik osprey LTD.

SANDVIK OSPREY LTD.,

RED JACKET WORKS,
MILLAND ROAD,
NEATH SA11 1NJ,
UNITED KINGDOM.

Telephone: 01639.634121
Fax: 01639.630100
E-Mail: powders.osprey@sandvik.com

CERTIFICATE OF ANALYSIS: 31554

Revision: 2

Customer:	**METALL-MASKIN AS**
Customer Order:	6832724
Customer Alloy Name:	SAF2507
Osprey Order Number:	200708/02 CALL:01
Osprey Alloy Name:	SAF2507
Dispatch Number:	20D1034
Weight:	50.00Kg (110lb)
Powder Size:	-45micron +10micron
Atomise Gas:	Nitrogen

Physical Test Data

	Minimum	Actual	Maximum
Tap Density, g/cc		4.89	
App Density, g/cc		4.0	
Hall Flow, s/50g		16.0	25.0

Particle Size Data

Sieve Analysis

+45µm	1.15%
-45µm	98.85%

Laser Diffraction Analysis
Malvern 2000 Instrument

	Minimum	Actual	Maximum
d10 µm		22.0	
d50 µm		33.4	
d90 µm		50.8	

-10.0 µm = %

Chemical Analysis(wt %)

El	Minimum	Actual	Maximum
Cr	24.6	**24.7 %**	25.4
Ni	6.8	**7.0 %**	7.2
Mo	3.76	**3.97 %**	4.24
Mn	0.7	**0.9 %**	1.1
Si	0.2	**0.4 %**	0.6
N	0.26	**0.27 %**	0.31
O		**0.08 %**	
Cu	0.00	**0.02 %**	0.20
C	0.00	**0.02 %**	0.02
Co	0.00	**0.02 %**	0.54
Al	0.000	**0.015 %**	0.025
P	0.000	**0.012 %**	0.025
Sn	0.000	**0.010 %**	0.019
Ti	0.000	**0.010 %**	0.025
W	0.00	**0.01 %**	0.05
S	0.000	**0.007 %**	0.008
B	0.000	**0.001 %**	0.003
Fe	**BALANCE**		

SAF2507 is a super duplex stainless steel.

Test Type	Standard	Method	Elements
Chemical Analysis	UKAS Accredited Laboratories compliant with ISO/IEC 7025:2017 Refer to UKAS 0012/0038/1091 for details	ICP-OES	Al, As, B, Be, Ca, Cd, Co, Cr, Cu, Fe, Hf, In, Mg, Mn, Mo, Ni, Nb, P, Sb, Si, Sn, Ti,Ta, V, W, Y, Zn, Zr
		Leco, Eltra Combustion	C, H, N, O, S
	Laboratory compliant with ISO/IEC 17025:2017	GD-MS	Bi, Ga, Pb, Te, Ti

Test Type	Method	Standard
Physical Analysis	Tap Density	In house method SWP-019 (based on ISO 3953)
	Apparent Density	In house method SWP-019 (based on ASTM B703)
	Pycnometric Density	In house method SWP-228 (based on ASTM B923-16)
	Laser Particle Size Analysis	In house method SWP-015 (based on ISO 13320)
	Sieve	In house method SWP-223 (based on ASTM B214-16)
	Hall or Carney Flow	In house method SWP-019 (based on ISO 4490/ASTM B213-03)

This certificate was produced electronically by HERAULT SYLVIE in accordance with Sandvik Osprey's Integrated Management System. No other signature is required to validate this document.

Printed on: 20/08/2020

Dispatch Group Ref: 20E1002

Page 2 of 2